

Berichte

zur Polar-
und Meeresforschung

586

2009

**Reports
on Polar and Marine Research**



**The Expedition of the Research Vessel "Polarstern"
to the Antarctic in 2006 (ANT-XXIII/7)**

**Edited by
Peter Lemke
with contributions of the participants**

 **HELMHOLTZ
| GEMEINSCHAFT**

**ALFRED-WEGENER-INSTITUT FÜR
POLAR- UND MEERESFORSCHUNG**
In der Helmholtz-Gemeinschaft
D-27570 BREMERHAVEN
Bundesrepublik Deutschland

ISSN 1866-3192

Hinweis

Die Berichte zur Polar- und Meeresforschung werden vom Alfred-Wegener-Institut für Polar- und Meeresforschung in Bremerhaven* in unregelmäßiger Abfolge herausgegeben.

Sie enthalten Beschreibungen und Ergebnisse der vom Institut (AWI) oder mit seiner Unterstützung durchgeführten Forschungsarbeiten in den Polargebieten und in den Meeren.

Es werden veröffentlicht:

- Expeditionsberichte (inkl. Stationslisten und Routenkarten)
- Expeditionsergebnisse (inkl. Dissertationen)
- wissenschaftliche Ergebnisse der Antarktis-Stationen und anderer Forschungs-Stationen des AWI
- Berichte wissenschaftlicher Tagungen

Die Beiträge geben nicht notwendigerweise die Auffassung des Instituts wieder.

Notice

The Reports on Polar and Marine Research are issued by the Alfred Wegener Institute for Polar and Marine Research in Bremerhaven*, Federal Republic of Germany. They appear in irregular intervals.

They contain descriptions and results of investigations in polar regions and in the seas either conducted by the Institute (AWI) or with its support.

The following items are published:

- expedition reports (incl. station lists and route maps)
- expedition results (incl. Ph.D. theses)
- scientific results of the Antarctic stations and of other AWI research stations
- reports on scientific meetings

The papers contained in the Reports do not necessarily reflect the opinion of the Institute.

The „Berichte zur Polar- und Meeresforschung“
continue the former „Berichte zur Polarforschung“

* Anschrift / Address

Alfred-Wegener-Institut
Für Polar- und Meeresforschung
D-27570 Bremerhaven
Germany
www.awi.de

Editor in charge:
Dr. Horst Bornemann

Assistant editor:
Birgit Chiaventone

Die "Berichte zur Polar- und Meeresforschung" (ISSN 1866-3192) werden ab 2008 ausschließlich elektronisch als Open-Access-Publikation herausgegeben (URL: <http://epic.awi.de>).

**The Expedition ANTARKTIS-XXIII/7
of the Research Vessel "Polarstern" in 2006**

**Edited by
Peter Lemke
with contributions of the participants**

**Ber. Polarforsch. Meeresforsch. 586 (2009)
ISSN 1866-3192**

ANT-XXIII/7

25 August 2006 - 29 October 2006

Cape Town - North-Western Weddell Sea - Cape Town

Fahrtleiter / Chief Scientist

Peter Lemke

Koordinator / Coordinator

Eberhard Fahrbach

CONTENTS

1.	Expedition ANT-XXIII/7: Fahrtverlauf und Zusammenfassung	7
	Itinerary and summary	10
2.	Weather conditions	12
3.	Physical and chemical oceanography	16
3.1	Water mass variability in the north-western Weddell Sea: A continuation of the DOVETAIL project	16
3.2	Water mass variability in the north-western Weddell Sea: Trace measurements – helium isotopes, neon, CFC's, and tritium	21
3.3	Iceberg drifter deployment (freshwater export in the north-western Weddell Sea)	24
3.4	Uptake of anthropogenic CO ₂ by the Weddell Sea	27
3.5	Dissolved organic carbon sequestration in the deep Weddell Sea	30
3.6	Oceanic mass variability in the Antarctic Circumpolar Current observed by bottom pressure sensors and GRACE satellites	31
4.	Regional variability of sea ice properties and thickness in the northwestern Weddell Sea obtained by in-situ and satellite measurements	36
4.1	General ice conditions in the study region	37
4.2	Sea ice thickness distribution	43
4.3	Snow thickness distribution	56
4.4	Ice types and properties derived from ice coring	61
4.5	Snow properties	68
4.6	Floe size distribution	70
5.	Weddell Sea air-ice chemistry interaction study	75

6.	Biology	86
6.1	Sea ice biogeochemistry and biodiversity in winter and early spring	86
6.2	Life cycle strategy of pelagic and sympagic zooplankton	102
6.3	Dynamics of organic sulphur compounds in sea ice	113
7.	Bathymetry	117
7.1	Sea floor morphology and topography of the northern Weddell Sea	117
7.2	Regional bathymetric studies	119
 APPENDIX		123
A.1	Beteiligte Institute / participating institutions	124
A.2	Fahrtteilnehmer / cruise participants	127
A.3	Schiffsbesatzung / ship's crew	129
A.4	Station list	130

1. EXPEDITION ANT-XXIII/7: FAHRTVERLAUF UND ZUSAMMENFASSUNG

Peter Lemke
Alfred-Wegener-Institut

Das Forschungsschiff *Polarstern* verließ den Hafen von Kapstadt (Südafrika) früh morgens am 25. August 2006, um im nordwestlichen Weddellmeer südlich der Süd-Orkney Inseln Forschungsprojekte im Bereich Ozeanografie, Meereis, Biologie, Luftchemie und Bathymetrie zu bearbeiten (Abbildung 1.1).

Die ozeanografischen Arbeiten widmeten sich der Erforschung der Winterbedingungen in den dominanten Regionen der Tiefen- und Bodenwasserproduktion, die verantwortlich sind für den Wassermassenexport in die Tiefseebecken der Weltmeere. Die hydrografischen Aktivitäten mit dem Ziel, die Bildung, die Verteilung, den Verlauf und den Export der Tiefenwassermassen zu verstehen, bezogen sich auf die Hauptpassagen östlich und westlich der Süd-Orkney-Inseln sowie auf einen Abschnitt südlich der Larsen-A-Region (Abbildung 3.1). Diese Arbeiten wurde ergänzt durch Spurenstoffmessungen (Heliumisotope ^3He und ^4He , Neon und FCKWs), die auch genutzt werden, um Wassermassenbildung und Wassermassentransport zu beschreiben, und durch Eisbergmarkierung, um deren Driftverlauf sowie den Süßwassereintrag ins Weddellmeer aufgrund von Eisbergschmelze besser abschätzen zu können. Außerdem wurden während der Reise Gesamtkohlendioxid und -alkalinität gemessen, die es in Verbindung mit zusätzlichen Daten ermöglichen werden, das anthropogene CO_2 -Signal im Weddellmeer abzuleiten. Man erwartet, anhand dieser Daten die gesamte jährliche Aufnahme von anthropogenem CO_2 durch die Wassermassen des Weddellmeeres abschätzen zu können.

Außerdem wurden im Gebiet des Antarktischen Zirkumpolarstroms (ACC) sechs Bodendruckensensoren am Meeresboden ausgesetzt, um über mehrere Jahre Zeitserien des Meeresbodendrucks und der akustischen Laufzeiten zur Oberfläche zu bekommen, um Messungen der Schwerefeldvariationen durch die GRACE-Satellitenmission zu validieren und damit die Veränderlichkeit der Meeresströmungen und des Wärme- und Massentransports im südantlantischen Teil des ACC einschätzen zu können.

Meereis spielt eine wichtige Rolle bei der Bestimmung des Austauschs zwischen Ozean und Atmosphäre in den Polarregionen und beeinflusst das Klimasystem weltweit. Die Eigenschaften des Meereises im Weddellmeer im Winter sind kaum bekannt und wurden detailliert erforscht, besonders die regionale und zeitliche Veränderlichkeit der Dicke von Schnee und Meereis, die mit Hilfe eines hub-

schraubergestützten Dickensensors, des schiffseigenen Eisbeobachtungssystems und durch *in-situ* Messungen auf dem Eis bestimmt wurde. Das Hauptaugenmerk wurde auf die Eigenschaften von ein- und zweijährigem Eis gerichtet und besonders auf die Veränderung des Ökosystems nach dem Überleben der Sommerschmelze.

In zunehmendem Maße unterstützen Beobachtungen die Hypothese, dass salzige Eisblumen auf neu gebildetem Meereis die lang gesuchte Hauptquelle für polares troposphärisches Brom darstellen. Um dies genauer zu beleuchten, wurden Spurengasmessungen über der Meereisoberfläche durchgeführt, und Proben von Eisblumen gesammelt, um die Ergebnisse anhand von Oberflächeninformationen von Schiffsbeobachtungen und Satelliten zu analysieren. Ziel war der Nachweis der potentiellen Bromquellen und die Quantifizierung und Parametrisierung der Bromflüsse.

Der Schwerpunkt der Meereis-Arbeiten zu Biogeochemie und Biodiversität war auf die Darstellung der physikalischen, chemischen und biologischen Wechselwirkungen im winterlichen Weddellmeer gerichtet, um die Entwicklung der Produktion von Biomasse in diesem Teil des Jahreszyklus zu verstehen. Als Teil dieser Aktivitäten wurden fotosynthetische Parameter und biooptische Eigenschaften des Meereises bestimmt, um den Einfluss und die Antriebsfaktoren der Primärproduktion des Meereises zu untersuchen.

Die Verteilung von Organismen im und unter dem Meereis wurde hinsichtlich Artenzusammensetzung, vertikaler Verteilung, Abundanz, Biomasse und deren Lebensbedingungen, physiologischer Funktion und Anpassungsstrategien erforscht. Besonders wichtig waren Meereiskopepoden und deren pelagische Gegenstücke. Untersuchungen wurden durchgeführt, um die jeweilige physiologische und biochemische Anpassung, den Energiebedarf und die Lebensstrategien zur Nutzung von kurzfristigen Nahrungsimpulsen und zum Überstehen von Perioden der Nahrungsknappheit zu verstehen. Ein weiteres Thema war die Produktion von Dimethylsulfid (DMS) durch biophysikalische Prozesse im Meereis und an der Meeresoberfläche. DMS wird in Form von Aerosolen in die Atmosphäre transportiert und spielt eine wichtige Rolle bei der Entwicklung von Nebel und Wolken, mit Auswirkungen auf Niederschlag, Strahlungseigenschaften und Energieaufnahme in der Atmosphäre. Die Untersuchungen werden eine ausgedehnte Grundlage für das Verstehen von Prozessen, Parametrisierungen von Klimamodellen und die Interpretation von Eiskernen bieten.

Die Polarmeere spielen im weltweiten Kohlenstoffzyklus eine zentrale Rolle. Die Bildung von Tiefen- und Bodenwasser in diesen Regionen entfernt für Tausende von Jahren große Mengen gelösten organischen Materials (DOM) aus den aktiven Kohlenstoffkreisläufen. Das Wissen um die chemische Struktur von DOM ist besonders wichtig, weil nur biogeochemisch stabile und schwer abbaubare Substanzen den Transport in die Tiefsee überleben. DOM im Gebiet der antarktischen Bodenwasserbildung wurde auf molekularem Niveau anhand moderner Analysetechniken analysiert. Umwandlungsprozesse von DOM, die schwer abbaubare organische Substanzen zur Folge haben, wurden zur Quantifizierung der

sogenannten „DOM-Pumpe“ identifiziert. Dieses Wissen wird helfen, die Modelle zum weltweiten Kohlenstoffkreislauf zu verbessern.

Während der gesamten Reise wurden bathymetrische Untersuchungen durchgeführt, um Fächerlotdaten zur Erweiterung der Datenbasis für verschiedene Ozeankartierungsprogramme zu sammeln und die Seekarten in antarktischen Gewässern zu verbessern. Die hydrografischen Arbeiten wurden durch Vermessungen an Stellen ozeanografischer Probenahme unterstützt, vor allem in den Bereichen der Ozeanpassagen. Eine spezielle Untersuchung wurde in der Nähe eines Erdbebenepizentrums durchgeführt, um eine eventuelle Veränderung der Bodentopografie zu entdecken.

Nach Abschluss des Arbeitsprogramms fuhr *Polarstern* in Richtung Kapstadt und erreichte den Hafen am Morgen des 29. Oktober 2006.

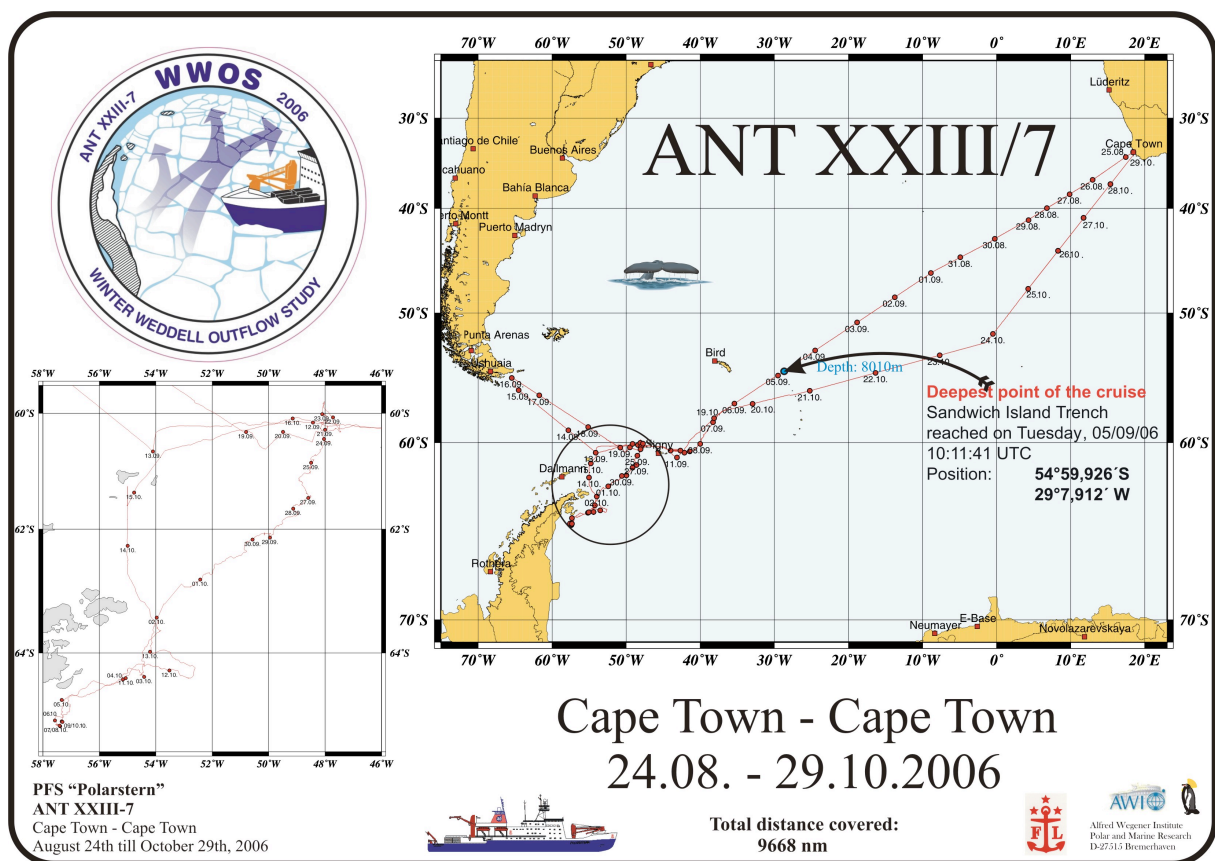


Fig.1.1: Cruise map of ANT XXIII/7

ITINERARY AND SUMMARY

The research vessel *Polarstern* left port in Cape Town (South Africa) early morning on 25 August 2006 to perform oceanographic, sea ice, biological, air chemistry and bathymetric investigations in the north-western Weddell Sea southward of the South Orkney Islands (Fig .1.1).

The oceanographic work was dedicated to investigate the winter conditions in the dominant regions of deep and bottom water production and export to the world's oceans. Dense sections across the main passages east and west of the South Orkney Islands and a section to the south to the Larsen-A region comprised the main hydrographic activities (Fig. 3.1), which were aimed at the understanding of the formation, the distribution, the pathways and the export of the deep water masses. The hydrographic work was complemented by tracer measurements (Helium isotopes ^3He and ^4He , Neon and CFCs), which will also be used to characterise water mass formation and transport, and by iceberg marking to provide a better estimate on their drift trajectories and the freshwater input to the Weddell Sea from iceberg melting. In addition, total CO_2 and total alkalinity were measured during the cruise which, in combination with auxiliary data, will allow deriving the anthropogenic CO_2 signal in Weddell Sea waters. It is expected that these data will provide an estimate of the total annual anthropogenic CO_2 uptake by the Weddell Sea water masses.

Furthermore, six bottom pressure sensors were deployed on the sea floor in the area of the Antarctic Circumpolar Current (ACC) to acquire multi-year time-series of ocean bottom pressure and acoustic travel time to the surface for the validation of gravity field variability measurements by the GRACE satellite mission, for estimates of the variability of ocean currents and the transport of heat and mass in the South Atlantic part of the ACC.

Sea ice plays a major role in determining the exchange between ocean and atmosphere in polar regions and affects the climate system also on the global scale. The sea ice characteristics in winter in the Weddell Sea are poorly known and were investigated in detail, especially concerning the regional and temporal variability of snow and sea ice thickness, which were determined from a helicopter-borne thickness sensor, from the ship's sea ice monitoring system and from *in-situ* measurements on the ice. The main emphasis was given to the characteristics of first-year and second-year ice and especially to the modification of the ecosystem after survival of the summer melt.

Increasing evidence supports the hypothesis that salty frost flowers on newly formed sea ice represent the long-sought major source of polar tropospheric bromine. In

order to shed light on this, trace gas measurements over the sea ice surface were performed, samples of frost flowers were collected, and the results will be analysed using surface information from both ship observations and from satellite. The aim was to verify the potential bromine sources and to possibly quantify and parameterize the bromine fluxes.

The main focus of the sea ice – biogeochemistry and biodiversity work was directed towards the characterization of the physical, chemical and biological interactions in the Weddell Sea during winter, in order to understand the evolution of the biomass production in this part of the seasonal cycle. As part of these activities photosynthetic parameters and bio-optical properties of sea ice were determined to understand the influence and forcing factors on sea ice primary production.

The distribution of organisms in and below the sea ice was investigated with respect to species composition, vertical distribution, abundance, biomass, as well as their living conditions, physiological performance and adaptation strategies. Of special importance were sea ice copepods and their pelagic counterparts. Investigations were performed in order to understand the respective physiological and biochemical adaptation, energy requirements and life strategies to utilize short-term food-pulses and to endure periods of food scarcity. Another topic was the production of dimethyl sulphide (DMS) through biophysical processes in the sea ice and the surface ocean layer. DMS is transported into the atmosphere as aerosol and plays a major role in the development of fog and clouds, with effects on precipitation, on radiative properties and energy absorption in the atmosphere. The investigations will provide an extended basis for process understanding, climate model parameterizations, and interpretation of ice cores.

The polar oceans play a central role in the global carbon cycle. The formation of deep and bottom water in these regions removes high amounts of dissolved organic matter (DOM) from the active carbon cycles for thousands of years. The knowledge of the chemical structure of DOM is of major importance because only biogeochemically stable, refractory substances survive the transport to the deep ocean. DOM in the area of Antarctic Bottom Water Formation was analyzed on a molecular level by modern analytical techniques. Transformation processes of DOM resulting in refractory organic substances were identified for the quantification of the so-called “DOM-pump”. This knowledge will help to improve models for the global carbon cycle.

During the entire cruise bathymetric investigations have been undertaken to collect multi-beam data to enlarge the data bases for different ocean mapping programmes and to improve Nautical Charts in the Antarctic. The hydrographic work was supported through surveys around oceanographic sampling sites, especially in the regions of ocean passages. A special survey was performed in the vicinity of an earth quake epicentre to detect a possible change in bottom topography.

After the conclusion of the work programme *Polarstern* steamed towards Cape Town and reached port in the morning of 29 October 2006.

2. WEATHER CONDITIONS

Rüdiger Hartig, Hartmut Sonnabend
Deutscher Wetterdienst

Polarstern left Cape Town in the morning of 25 August 2006 bound to the scientific research area: “northwestern Weddell Sea”. The cruise started with fair skies, fresh breeze from southeast and moderate sea swell. As soon as the next day, however, the weather turned worse. Frequent development of intense depressions over the Southern Atlantic ocean produced winds of near gale and gale force as well as rough seas. In this early period *Polarstern* was hit twice (26 August and 30 August) by storms with gusts up to force 9 Bft. With the beginning of September weather conditions improved. West- and northwesterly winds around force 6 Bft and sea swell between 4 m and 7 m were observed. Just in time the research area near the South Orkney Islands was reached on 6 September.

The weather here was very unsettled. Several low pressure systems developed at the northern tip of the Antarctic Peninsula and moved eastward across the Weddell Sea. Ahead of these depressions moist and mild oceanic air moved into the working area, followed by cold and dry polar air in their rear. Thus periods with overcast sky and occasional snowfall changed with fair weather. The temperature ranged between freezing level and $-17\text{ }^{\circ}\text{C}$, the wind was between 5 Bft and 8 Bft from various directions.

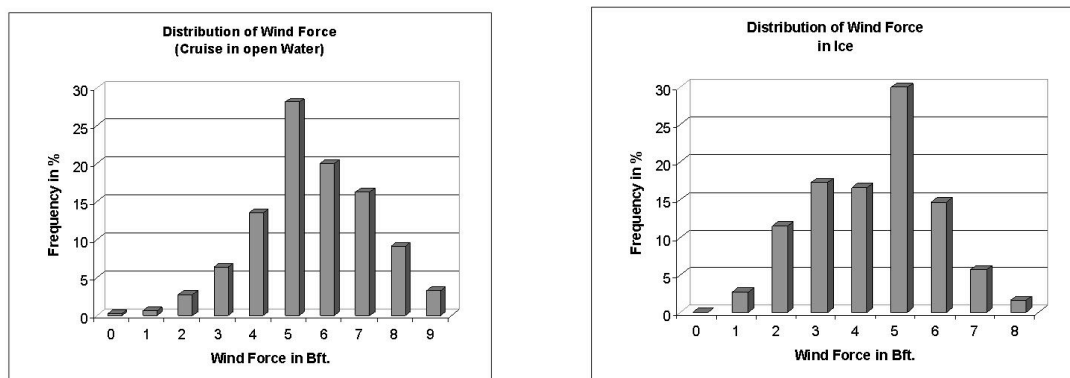


Fig. 2.1: Distribution of wind force during cruise in open water and cruise in ice

A medical emergency case interrupted the scientific programme between 11 September and 18 September. The vessel changed the course to King George Island, attempting to fly the patient via Teniente Marsh airfield to Punta Arenas, Chile. This trip started with weak winds and smooth sea, but approaching the peninsula on

13 September the weather turned worse. Finally, visibility and ceiling improved by the afternoon and the patient was flown by helicopter to the airfield. As the connecting flight to Punta Arenas could not be organized, the patient was returned to *Polarstern* for evacuation in Ushuaia (Argentina). The Drake Passage was crossed at southwest winds force 6 Bft. The swell started with 8 - 11 m in the southern portion and decreased to 5 - 6 m in the northern portion of the passage. On 15 September *Polarstern* took waiting position approx. 80 miles off the coast of Tierra del Fuego. A first attempt to fly to Ushuaia failed, as severe showers (snow, grain) and icing occurred within the flight corridor. Afternoon conditions improved and the patient was successfully flown to Ushuaia. Due to darkness the return had to be postponed to the next day. On 16 September frequent showers and gusts between force 8 Bft and force 11 Bft (Fig. 2.1) delayed the return flight until 18:00 h local time. After the return of the helicopter, *Polarstern* sailed back to Antarctica. Crossing the Drake Passage again moderate southerly airflow, moderate swell and decreasing temperatures were observed.

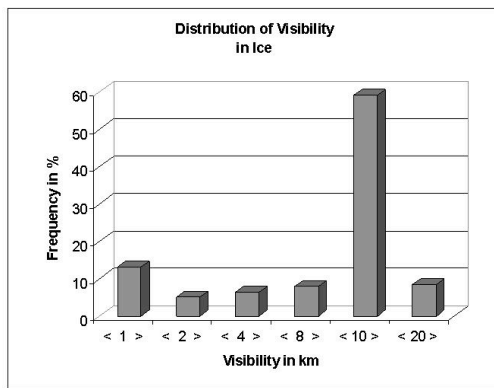


Fig. 2.2: Distribution of visibility

On 19 September the scientific work continued west of the South Orkney Islands. The general atmospheric circulation until 24 September was given by high pressure west of the peninsular and low pressure east of the Weddell Sea. This led to cold air advection from southwest and south with force 4 - 7 Bft and temperatures between -14°C and -22°C . The weather frequently changed between sunny and overcast periods, snowfall occurred occasionally. On 25 September an anticyclone turned the flow to northwest and west. Broken to overcast skies, windforce still from 4 to 7 Bft and temperatures between

-5°C and freezing level prevailed for several days. Low ceiling, poor visibility and icing obstructed the flight activities those days (Fig.2.2). The west and northwest surface winds enhanced the pressure on the sea ice, increased ridges and closed leads. As the vessel made no significant progress against the icedrift, the work in the Powell Basin had to be shortened and *Polarstern* sailed west to positions near Joinville Island and the Larsen Ice Shelf.

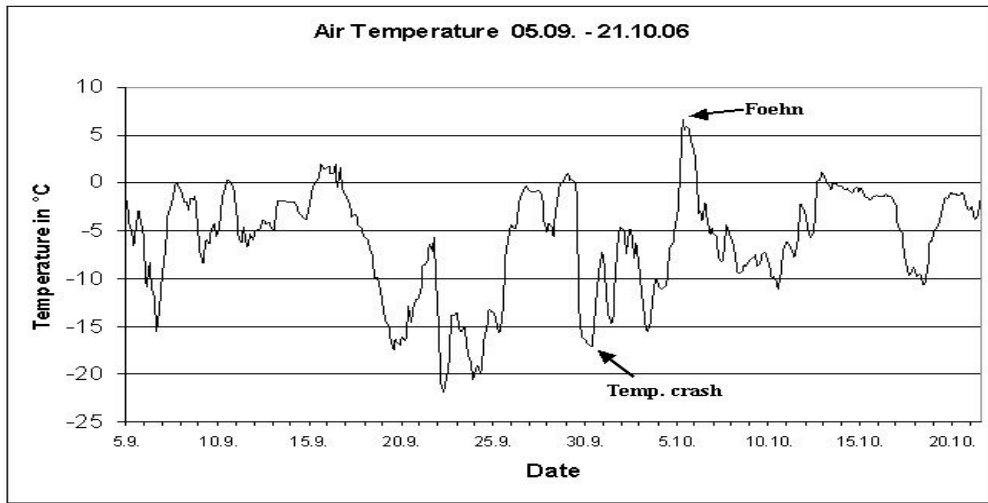


Fig. 2.3: Temperature time series ANT-XXIII/7

Marambio (60 km distance) observed 0 °C! From 6 October to 12 October high pressure determined the weather with variable winds around force 3 Bft and temperatures from -4 °C to -11 °C. Overcast skies and periods with fog were interrupted by two sunny days. Due to dense and thick sea ice *Polarstern* could not get as near to the ice shelf as planned. Therefore several helicopter flights were required to support the scientific work. Even though the conditions were not optimal, the flight schedule was almost completed. Only two “long distance flights” to the ice shelf had to be cancelled due to bad visibility and low ceiling.

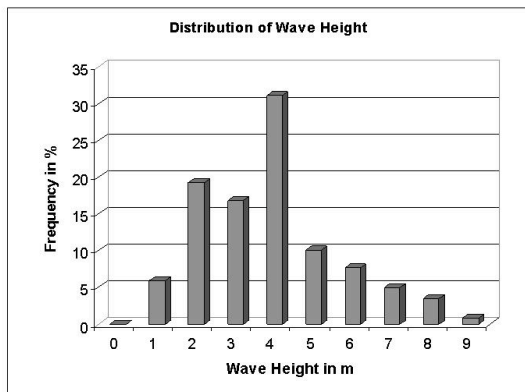


Fig. 2.4: Distribution of wave height

From 13 October to 15 October stations in the Bransfield Strait along 55°W were covered. The sea ice was less dense in this area, so the northwest of force 5 to 8 Bft was able to produce a swell of approx. 3 m (Fig. 2.4). Low cloud cover, poor visibility and temperatures around freezing level did not prevent the scientific work.

On October 15 *Polarstern* sailed east to perform final works near the South Orkney Islands and South Sandwich Islands. This period started with gale from south. After 3 days the wind finally turned to west and decreased to force 3-5 Bft. Poor visibility, low cloud cover and temperatures near -2 °C were the most frequent conditions. Only 17 and 18 October appeared with fair skies and -10 °C, allowing extended flight activity. A

flight to the South Sandwich Islands on 21 October, however, had to be cancelled due to fog.

On 21 October the vessel left the sea ice starting the return voyage to Cape Town. This leg started with moderate winds from west to northwest and temperatures near freezing level. Visibility was poor or moderate. On the way north the wind intensified to near gale and gale force. On 26 October a violent storm passed the cruise track in the south, but did not increase the windspeed above force 8 at *Polarstern*. The final approach to Cape Town was determined by a subtropic high giving moderate southwest winds and fair weather. On 29 October this cruise leg finished.

3. PHYSICAL AND CHEMICAL OCEANOGRAPHY

3.1 Water mass variability in the north-western Weddell Sea: A continuation of the DOVETAIL project

Hartmut Hellmer¹⁾, Mathias van Caspel³⁾, Andreas Macrander¹⁾, Dirk Olbers¹⁾, Lutz Sellmann¹⁾, Mauricio Mata²⁾, Vagner Da Silva Duarte²⁾, Rodrigo Kerr Duarte Perreira²⁾, Nuno Nuez³⁾, Michael Schodlock¹⁾

¹⁾Alfred-Wegener-Institut

²⁾Fundação Universidade Federal do Rio Grande, Brasil

³⁾University of East Anglia

Objectives

- Acquisition of wintertime hydrographic conditions in key regions for the composition and advection of globally relevant newly formed water masses to reduce the summer bias in temporal interpretations.
- Continuation of long-term observations in the north-western (NW) Weddell Sea as part of the international DOVETAIL (Deep Ocean Ventilation Through Antarctic Intermediate Layers) project to monitor the flow of deep and bottom waters out of the Weddell Sea.
- Estimation of the wintertime export rates through main passages in the South Scotia Ridge connecting the Weddell Sea with the global ocean.
- Acquisition of hydrographic conditions on the continental shelf under the influence of drastic changes due to the decay of Larsen-B Ice Shelf.
- Monitoring of the large-scale upper-ocean structure by means of ARGO drifting floats.

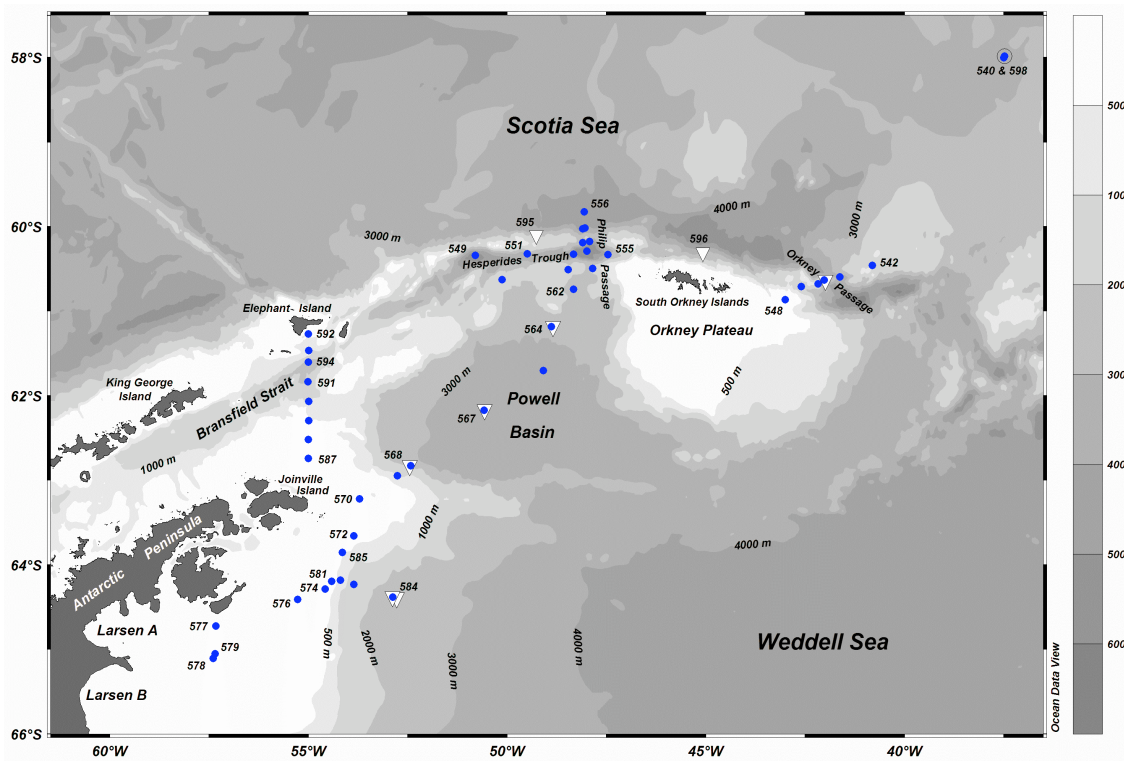


Fig. 3.1: CTD station distribution map for the north-western Weddell Sea including deployment sites for ARGO drifting floats (white triangles)

Work at Sea

The hydrographic work was focused on CTD (Conductivity-Temperature-Depth) measurements in combination with LADCP (Lowered Acoustic Doppler Current Profiler) observations and bottle rosette sampling for tracer and biogeochemical studies. A total of 46 stations were conducted in three main areas (Fig. 3.1):

- the South Scotia Ridge with the passages to the east (South Orkney – 41°W 61°S) and to the west (Philip – 49°W 61°S) of the South Orkney Plateau,
- the north-western Weddell Sea continental shelf and slope, and
- the eastern Bransfield Strait Basin.

Although a high or equally spaced distribution was desired, the actual position of the stations was strongly influenced by local bathymetry, which often had to be determined first by means of a Hydrosweep survey, and winter sea ice conditions. As a consequence 6 stations were conducted across the South Orkney passage and 13 stations on two sections following the main axes of the Hesperides Trough (including the confining ridges) and the passage itself from the deep Scotia Sea into Powell Basin. On the transit from Philip Passage to the NW continental shelf the Powell Basin was sampled from NE to SW with 6 stations. In the shallow waters (down to 440 m depth) off the northern tip of the Antarctic Peninsula 9 casts were conducted on the way in and out, while only 4 additional stations covered the continental slope at ca. 64.2°S down to 2,500 m depth because of a compact sea ice cover further east. The

section across Bransfield Strait at 55°W from Joinville to Elephant Islands (Fig 3.1) represents one of the long-term observations maintained by the Federal University of Rio Grande (FURG), Brazil. It was originally planned as the Brazilian contribution to the DOVETAIL programme but became a repeat section in the scope of the Brazilian Antarctic Survey (PROANTAR) GOAL project. Since in open water, none of the 8 stations had to be re-located from the original position.

Preliminary results

In the following, the preliminary results are presented according to the above mentioned main areas:

3.1.1 South Scotia Ridge

The bathymetric survey to the west of Philip Passage revealed that all previous hydrographic cruises had sampled the southern crest of a ridge system which confines the two major basins of the Hesperides Trough (see Fig. 3.1). With a depth of more than 5500 m the eastern basin serves as a “trap” for dense water masses escaping from Powell Basin across the less than 1850 m deep southern sill. The northern sill with a depth of 2800 m, connecting the eastern basin with the Scotia Sea, does not serve as a major outflow because with temperatures less than -0.3 °C the waters crossing the northern sill are 0.1 °C warmer than those in the southern Scotia Sea (Fig. 3.2). Therefore, in the past the contribution of Philip Passage to the Weddell Sea outflow might have been overestimated emphasizing even more the importance of South Orkney Passage for the export of deep and bottom waters formed in the Weddell Sea. Using the pre-processed LADCP measurements this export amounts to 1.7 Sv (1 Sv = $1 \times 10^6 \text{ m}^3 \text{ s}^{-1}$).

3.1.2 North-western Continental Shelf and Slope

The more or less meridional section on the shallow (< 500 m) continental shelf from the tip of the Antarctic Peninsula to the former area of Larsen-B Ice Shelf revealed a high spatial variability in shelf water characteristics. Pronounced features are the core of Modified Warm Deep Water (MWDW) with a maximum temperature of -0.78 °C and a salinity of 34.57 (# 581) in combination with a salinity minimum at the surface, and high salinities (34.59) at both southernmost stations (Fig. 3.2). Because of the inaccessibility of the area due to a compact sea ice cover, we can only assume that the stations are located on the northern slope of a trough extending toward the coast where a water depth of 963 m was previously measured.

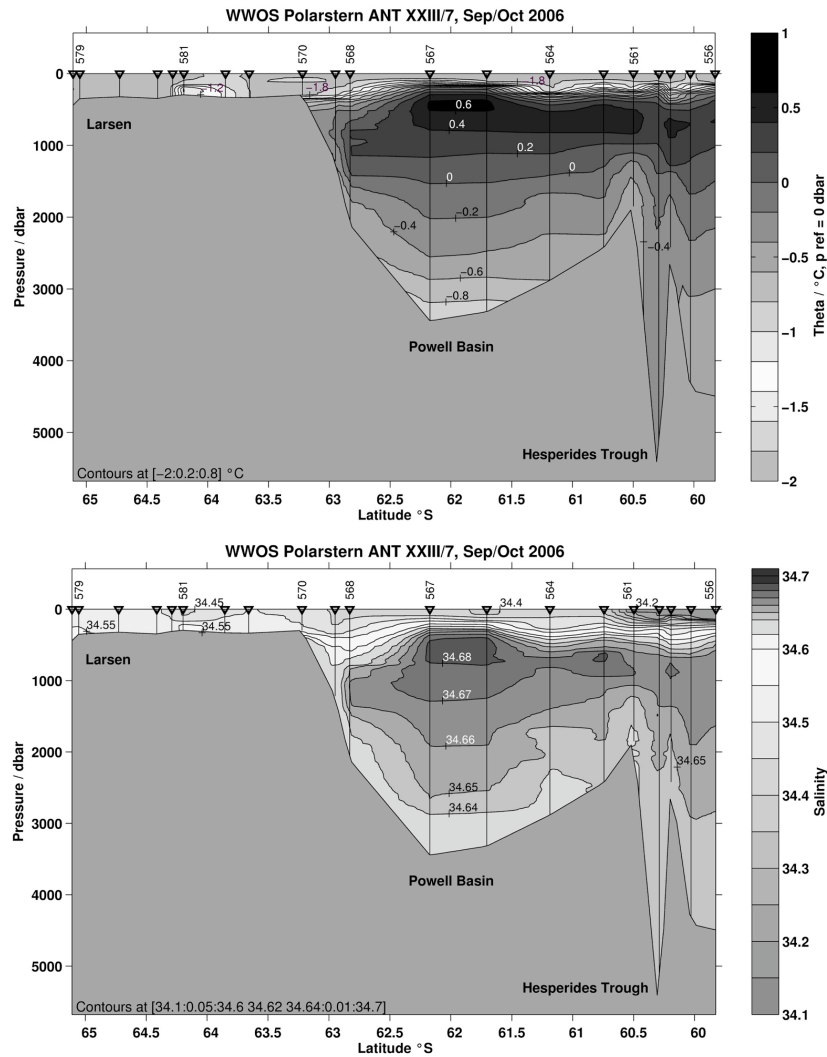


Fig. 3.2: Potential temperature (upper) and salinity (lower panel) section extending from the southernmost station (# 579) on the Larsen-continental shelf (left) across Basin to the southern Scotia Sea (# 556, right). For station locations see Fig. 3.1.

The section perpendicular to the continental slope (Fig. 3.3) showed that local shelf waters cannot contribute to the formation of deep water. Due to its low salinity, probably caused by melting of the numerous grounded icebergs, this shelf water interleaves at a depth of roughly 450 m. However, as the temperature/salinity distribution indicates, the bottom layer at the easternmost station (# 584) with very low temperatures of $-1.55\text{ }^{\circ}\text{C}$ might originate from the shelf stations (# 578 und 579) just 80 km to the south. The comparison with stations from the central Powell Basin (e.g., # 567) suggests that these bottom waters do not contribute to the near-bottom layer in Powell Basin. However, the differences in the characteristics between both sites could be simply caused by temporal variability in the composition of the western bottom waters.

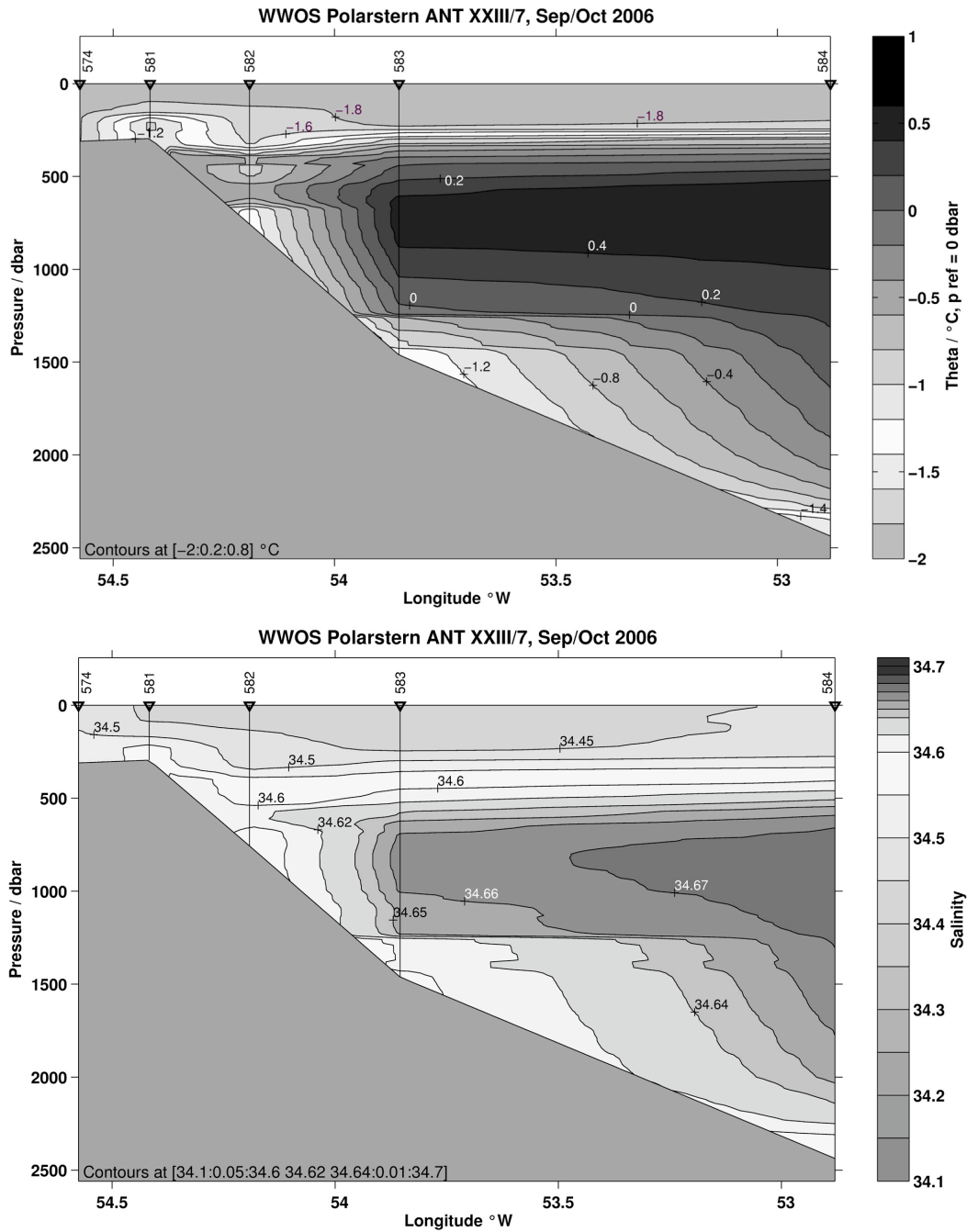


Fig. 3.3: Potential temperature (upper) and salinity (lower panel) section extending from the Larsen-continental shelf (# 574) across the continental slope (# 584). For station locations see Fig. 3.1.

3.1.3 Eastern Bransfield Strait Basin

First results show relatively high salinity ($S > 34.55$; $\theta < -1.6$ °C) waters present at the bottom of stations on the continental shelf and at the shelf break to the north of Joinville Island. This is a quite different situation compared to the summertime cruises which always found a strong melt water signal near Joinville Island. Although these shelf waters are the densest found along the entire section, they are not

observed in the deeper parts of the eastern basin, where warmer waters ($S < 34.55$, $\theta > -1$ °C) from the northern Powell Basin via the north-eastern channel seem to dominate. Obviously, the relatively high salinity waters do not predominantly contribute to the deep water of the eastern Bransfield Strait basin. Instead, they ought to continue westward to ventilate the bottom waters of the central basin.

Waters with higher salinities ($S > 34.55$) are also found at intermediate levels (1,250 m) near the southern slope (# 591), associated with relatively high temperatures ($\theta > -0.68$ °C) and low oxygen values ($DO_2 < 5.9$ ml/l). This suggests that they represent cold MWDW present in the northern Powell Basin and the north-eastern channel. Along the section, the warmest waters are found near Elephant Island ($\theta > -0.35$ °C) at around 380 m. The low oxygen values ($DO_2 < 5.9$ ml/l) indicate a CDW origin from incursions near Elephant Island which were also observed during the GOAL high resolution summer cruises.

3.2 Water mass variability in the north-western Weddell Sea: Trace measurements – helium isotopes, neon, CFC's, and tritium

Oliver Huhn
Institut für Umweltphysik, Bremen

Objectives

Measurements of noble gases (helium isotopes ^4He and ^3He , and neon), tritium, and chlorofluorocarbons (CFCs) complement the hydrographic programme. These tracers provide additional and independent information to identify and to compute fractions of contributing source water masses to the formation of Weddell Sea Deep and Bottom Waters and the time scales of their spreading. Furthermore, comparable tracer measurements from previous cruises exist from 1996 (section west of Joinville Island), from 1998 (Philip Passage/Powell Basin, section west of Joinville Island, South Orkney Passage), and from the ISPOL cruise in 2004/2005 (in the vicinity of Larsen-C Ice Shelf). A comparison of these data sets might allow assessing the variability in formation and distribution of deep and bottom waters which partly escape from the Weddell Basin towards the north contributing to Antarctic Bottom Water and, thus, the deep and cold branch of the global thermohaline circulation.

Main objectives of the repeated and new tracer measurements are to:

- extend the tracer time series, particularly after large parts of the northern Larsen-Ice Shelf had disintegrated,
- assess changes in deep and bottom water distribution in the area where they leave the Weddell Basin,
- quantify the deep and bottom water composition, i.e., changes in contributing shelf water types, particularly Ice Shelf Water or glacial melt water, respectively, and
- estimate the time scales of the water mass formation and conversion processes.

Work at sea

During the cruise a total of 550 samples on 37 CTD stations were collected for chlorofluorocarbons (CFC-11 and CFC-12). The water samples from the rosette were collected into 100 ml glass ampoules and sealed off after a CFC free headspace of pure nitrogen had been applied. The CFC samples will be analysed later at the IUP-Bremen. The amount of CFC degassing into the headspace will be accounted for during the measurement procedure in the lab. The determination of CFC concentration will be accomplished by purge and trap sample pre-treatment followed by gas chromatographic (GC) separation on a capillary column and electron capture detection (ECD). The system will be calibrated by analyzing several different volumes of a known standard gas. Additionally, the blank of the system will be analyzed regularly.

Furthermore, 310 samples from 30 stations were collected for helium isotopes (^3He , ^4He) and neon (Ne). The water samples from the Niskin bottles were stored in clamped off copper tubes. They will be analysed later using the IUP-Bremen noble gas mass spectrometer, after the gases were extracted from the sea water samples.

Finally, 110 samples from 16 stations (in the western part of the cruise only) were collected for tritium (^3H). Additionally, several snow samples were collected. Since tritium is part of the water molecule, the water samples were filled into water vapour tight glass bottles. At the IUP-Bremen, all gasses will be extracted and the water samples will be stored for at least half a year. During that time a sufficient part of the ^3H has decayed to ^3He . Finally, the ^3He is measured with the same IUP-Bremen mass spectrometer as mentioned above.

3.2.1 Tracer methods and expected results

Atmospheric air with a constant composition of helium and neon is trapped in the ice matrix during the formation of meteoric ice or shelf ice, respectively. Due to the enhanced hydrostatic pressure at the base, these low soluble gases are completely dissolved in water when the ice shelf ice is melting at its base. Thus, pure glacial melt water is supersaturated by roughly 1,060 % in helium and 770 % in neon. Noble gas observations allow for calculating even small fractions of glacial melt water (or Ice Shelf Water) contributing to the formation of deep and bottom water. Furthermore, at the mid-ocean ridges of the deep Pacific helium with an enhanced $^3\text{He}/^4\text{He}$ ratio (8 times larger than the atmospheric ratio) is released into the deep water. These waters contribute to Circumpolar Deep Water (South Pacific Deep Slope Water) of which parts are advected into the Weddell Sea forming Warm Deep Water (WDW).

Chlorofluorocarbons (CFCs) are transient tracers due to their atmospheric time evolution. Atmospheric concentrations of the entirely anthropogenic CFC-11 and CFC-12 increased almost monotonously between 1940 and 1990. Afterwards they leveled off (CFC-12) or even decreased (CFC-11). The ocean surface (i.e., the mixed layer) in which they are dissolved by gas exchange is the only source for the ocean

interior. Thus, CFC measurements provide information whether a water mass observed in the inner ocean contains fractions of recently ventilated (surface) water and, furthermore, allow to estimate the time elapsed since this water mass was in contact with the atmosphere (i.e., the internal transit time or "age").

Tritium is a radioactive tracer which decays to ^3He . The only source of tritium for the inner ocean is the ocean surface via precipitation and water vapour exchange. The major pool of tritium in the atmosphere lasts from hydrogen bomb tests in the 50s and 60s of the last century, even if this "bomb peak" declines rapidly due to the radioactive decay of tritium. However, different spatial precipitation rates and different spatial water vapour exchange rates (e.g., due to sea ice coverage) imprint locally a different surface water saturation of tritium. Thus, the observed tritium concentration in the ocean interior provides information about the source region of deep and bottom waters (therefore we additionally take snow samples from different regions). Moreover, since the decay time of tritium is known (12.4 years) and the amount of ^3He is measured as well (sea above) the ratio of tritium and ^3He allows a complementary estimate of the "age" of a water mass observed in the ocean interior.

Major aims of the (partly repeated) tracer measurements are to compare the contemporary distribution, the composition from different source water masses and their spatial origins, and the time scales of the spreading of deep and bottom water which is partly able to escape from the Weddell Basin through gaps in the South Scotia Ridge. Furthermore, they will allow comparisons with tracer measurements from previous cruises. Since large parts of the Larsen Ice Shelf had collapsed in the past (Larsen A in 1998 and Larsen B in 2002), a change in the boundary conditions might have caused a modification of the deep and bottom water formation and its distribution and spreading, particularly concerning possible changes in the contributing fractions of different shelf water types, i.e., Ice Shelf Water or glacial melt water.

3.3 Iceberg drifter deployment (freshwater export in the north-western Weddell Sea)

Michael Schodlok
Alfred-Wegener-Institut

Objectives

The calving of icebergs from Antarctic ice shelves and their subsequent drift causes a significant transport and input of freshwater from the ice sheet into the upper ocean. Calving events of gigantic icebergs are known to occur infrequently, but the drift and life times of these giants can be easily monitored by satellite. However, a large amount of freshwater is transported away from the Antarctic ice sheet through medium and small-size icebergs with lengths of the order of a few kilometres and less. Since 1999, 69 of medium and small-sized icebergs have been tagged with GPS buoys in the Weddell Sea to monitor their positions and subsequent drift. The analysis of these drifts indicates:

- an export of icebergs to the west of the South Orkney Islands,
- an export of icebergs to the east of the South Sandwich Islands, and
- the possibility that icebergs remain within the Weddell Sea
- the importance of sea ice concentration on iceberg drift.

Only a small number of sea ice and iceberg buoys have been deployed on the western Weddell Sea continental shelf to date to reveal predominant drift patterns. And although sea ice cover above 90 % concentration in the western Weddell Sea dominates iceberg drift, the pathways of sea ice and iceberg buoys in this area are different. Sea ice buoys mainly follow the Weddell Gyre eastwards whilst iceberg buoys show a separation of drift pathways at the southern edge of Powell Basin partly drifting towards the north and partly following the Weddell Gyre. Thus, the objective during ANT-XXIII/7 is to study this drift separation and in turn prevalent iceberg drift patterns, and the freshwater export in the north-western Weddell Sea.

Work at sea

During ANT-XXIII/7, 8 icebergs with edge sizes between 300 m and 3,000 m and up to 50 m freeboard were tagged at the southernmost part of the cruise on the western Weddell Sea continental shelf. The iceberg buoys transmit the daily (12:00 h) GPS position (given with an accuracy of less than 15 m) using the ARGOS satellite system. Buoys with additional air pressure recorders have a higher transmission frequency of 3 hours. Iceberg deployment specification such as dimension and dates are presented in table 3.1. Figure 3.4 shows the deployment positions relative to the cruise track, and iceberg A53A which broke of Larsen-C Ice Shelf in 2005 with an initial size of 29 nm x 14 nm.

The icebergs in the vicinity of A53A were tagged in an area dominated by first-year ice (see also contribution of the sea ice group, C. Haas et al.) while the easterly icebergs were drifting in an area of heavily deformed multi-year ice. The

northernmost iceberg (#10812) was part of a cluster of grounded icebergs with large areas of open water. This assembly of large icebergs with edge sizes of more than 1 km are the remnants of iceberg A53B which broke off of Larsen-C Ice Shelf also in 2005. While consecutive SAR images show the drift of parts of this cluster (not shown here), iceberg 10812 remained fairly stationary with a mean speed of 0.2 km/day \pm 0.3 km/day during the first 14 days of drift.

Tab. 3.1: Details of iceberg buoy deployments during ANT-XXIII/7

No.	ARGOS ID	Date	Time (UTC)	Latitude	Longitude	Length	Width	Freeboard
1	8061	07.10.2006	14:00 h	65°17.31'S	57°13.07'W	830 m	610 m	49 m
2	8065	07.10.2006	16:30 h	65°44.15'S	58°07.98'W	1350 m	630 m	49 m
3	9367	07.10.2006	17:35 h	65°24.78'S	57°32.17'W	3110 m	1685 m	46-56 m
4	9360	10.10.2006	13:28 h	65°06.55'S	56°20.92'W	830 m	520 m	39 m
5	9831	10.10.2006	14:04 h	65°26.53'S	55°10.04'W	870 m	390 m	55 m
6	3701	10.10.2006	18:52 h	65°04.40'S	56°00.75'W	720 m	390 m	30 m
7	9835	10.10.2006	19:11 h	65°02.79'S	56°00.68'W	390 m	295 m	30 m
8	10812	11.10.2006	13:36 h	64°14.84'S	54°43.71'W	1110 m	815 m	43 m

As mentioned above the buoys were deployed on icebergs drifting in different sea ice concentrations. The icebergs in the vicinity of A53A show a different drift behaviour compared to those further to the east (Fig. 3.5). The mean speed (first 14 days of drift record) of these buoys (8061, 8065, and 9367) of 4.3 km/day \pm 3.7 km/day is smaller compared to 7.9 km/day \pm 4.8 km/day of buoys 9831, 9835, and 3701. Furthermore, the latter buoy array shows a more coherent drift pattern from the start of the drift. With the drift of the northern buoys 9360 and 8061 into the area of multiyear sea ice (SAR images show the changes in ice regimes between 17 and 24 October 2006) their drift pattern became more coherent with the eastern buoy array.

The three snapshots of iceberg A53A were taken from SAR images (Fig. 3.5). Its freeboard was very variable from only a few meters to more than 40 m (the latter is an estimate comparing A53A freeboard height to measured adjacent smaller icebergs). A draft estimate can be inferred from the last position as its north-western edge crossed the *Polarstern* cruise track (7 October 2006), and due to an extensive Hydrosweep survey (see Chapter 7) the bottom depth is well known. As the iceberg is still drifting the draft is not larger than 440 m.

3.4 Uptake of anthropogenic CO₂ by the Weddell Sea

Steven van Heuven
Royal Netherlands Institute for Sea

Background and objectives

In the last 250 years large amounts of CO₂ have been emitted to the atmosphere as a result of human activity. A significant fraction (~50 %) of this 'anthropogenic' CO₂ has subsequently been taken up by the oceans, which in that way have an ameliorating effect on the rate of climate change - predicted as a result of increasing atmospheric CO₂ concentration. The total amount of anthropogenic CO₂ taken up, current and past rates of uptake, the potential decline in uptake due to 'saturation' of the surface ocean, and the deleterious effect on marine life resulting from the increasing total dissolved inorganic carbon content of the oceans are a current focus of the fields of marine chemistry, biogeochemistry, and biology.

Next to laboratory studies aimed at conceptual and mechanistical understanding of the processes involved, a large effort is being made to investigate the state of the carbonate system in all areas of the world ocean. This is performed almost exclusively through research cruises, since no remote sensing or automated profiling systems are currently suitable for the task.

Work at sea

High-precision measurements were made of the total dissolved inorganic carbon (TDIC) content and total alkalinity (TA) of all samples collected on all oceanographic stations, generally excluding the samples from 5 m depth. This yielded a total of ~525 unique samples + ~175 duplicates.

Analysis of TDIC was performed using the "coulometric method". TA analysis was performed with the 'standard' titration, using curve fits along modified Gran plots. Both analyses were performed using a single integrated system: the VINDTA system (Versatile Instrument for Determination of Titration Alkalinity, MARIANDA, Kiel, Germany). Analysis accuracy was set through the use of certified reference material (CRM, supplied by Dr. A. Dickson, Scripps Institute of Oceanography).

3.4.1 Details of methods used

Two VINDTA setups were used concurrently, often running 'duplicates' of the same samples, drawing from the same sample bottle at the same moment. These duplicates will yield an estimate of system inter-comparability, relative drift, and (to some degree) CRM variability.

For the coulometric determination of TDIC, an accurately known amount of sample (~20 ml) is dispensed with an automated, thermostated pipette into a stripper. The sample is acidified, converting the carbonate species into CO₂(aq). The evolving CO₂ is removed from the sample by sparging with N₂. The CO₂-enriched N₂ stream is led through a solution in the coulometric cell, which absorbs the CO₂ and, thereby,

becomes more transparent. The coulo-meter subsequently electrically titrates the solution back to its original opacity. The required amount of charge is a direct and linear measure of the amount of CO₂ absorbed. With knowledge of the sample's volume and density, the concentration of the total of CO₂-species in the sample is easily calculated.

Total alkalinity is mathematically derived from a 4th order curve fit along a 'modified gran plot' of electrode potential versus volume of acid added to an accurately known amount of sample (~100 ml), dispensed with an automated, thermostated pipette. Titration is performed automatically in a thermostated cell.

Approximately every 6th analysis was followed by analysis of CRM in order to set accuracy and to detect and to be able to correct for measurement drift. Every CRM-sample was run on both machines at the same time. A final way of application of corrections is still to be decided upon. The most likely candidate is a best-fit linear correction through all CRM measurements between start-ups of the equipment, i.e., per day.

3.4.2 Data quality

The initial estimate of data quality is "reasonable" to "excellent", with the later stations generally being of higher quality than the earlier ones. For an example of the some of the preliminary results, see Fig. 3.6.

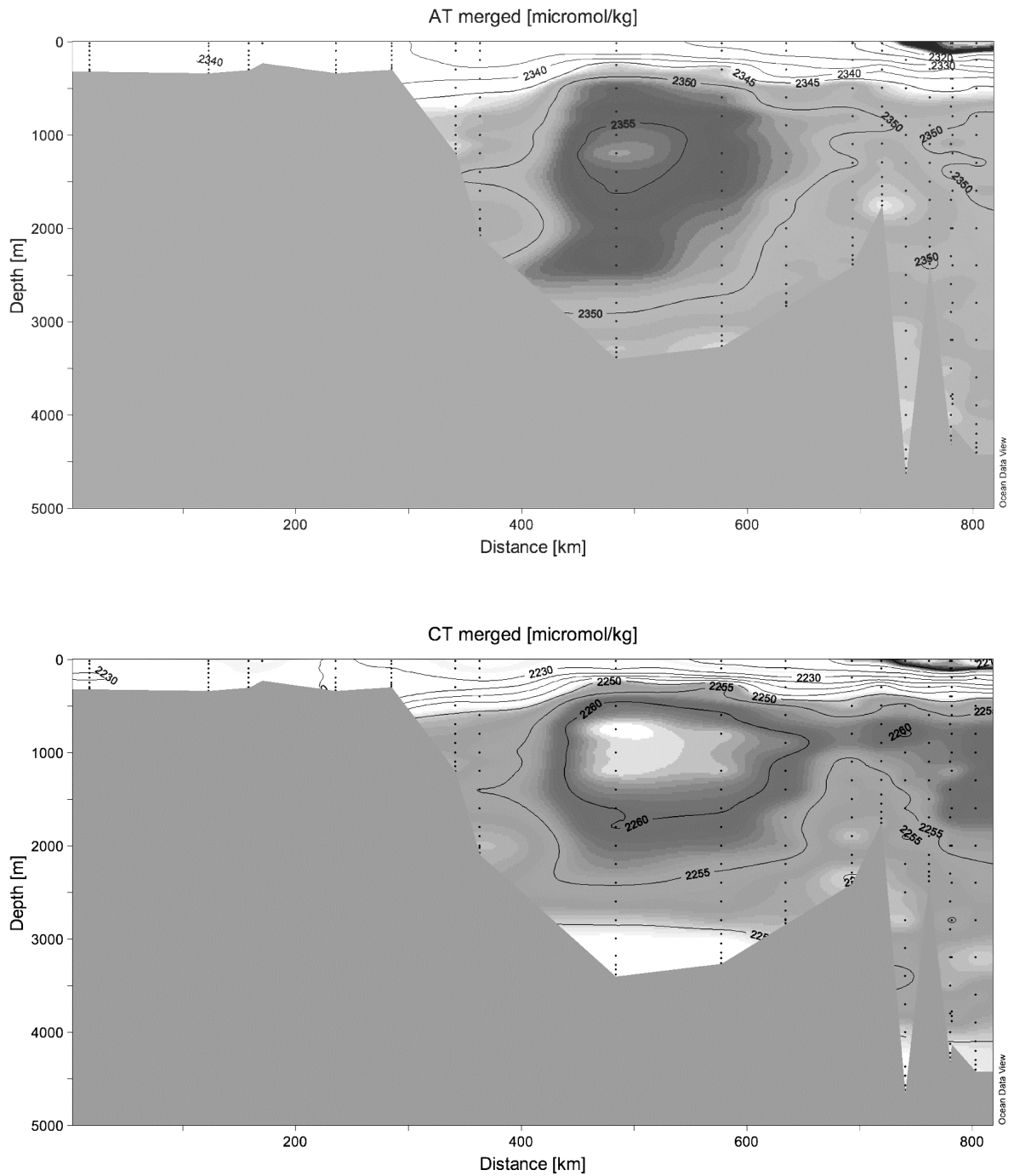


Fig. 3.6: Same transect as Fig. 3.2 but for total alkalinity (upper) and total carbon (lower panel)

3.5 Dissolved organic carbon sequestration in the deep Weddell Sea

Ines Vogel and Anika Friedrich
Alfred-Wegener-Institut

Objectives

Source, diagenesis, and preservation mechanisms of dissolved organic matter (DOM) remain elemental questions in contemporary marine science and represent a missing link in models of global elemental cycles. The polar oceans play a central role in the global carbon cycle. They are probably a primary source of DOM to the deep ocean because these regions are the only places where surface waters are efficiently transported to great depth. Deep-water formation is directly linked to sea ice formation, when salt is rejected and dense, brine-enriched waters penetrate the deep ocean. Sea ice is one of the most productive marine environments, and DOM concentrations in the brine are among the highest measured in marine waters. The biogeochemistry of sea ice is widely unknown and it is not clear whether sea ice DOM is persistent enough to survive downward convection. Broad significance is expected by answering the question: “Do ice-covered oceans act as a DOM pump to the abyssal ocean and so sequester carbon from active cycles?” By combining several molecular tracer techniques we will be able to quantify the concentration of ice-algal derived DOM in different water masses and along diagenetic pathways on a large scale in the Weddell Sea.

Work at sea

A total of 35 CTD casts and large-volume water samples (ca. 60 liters of water for each sample) for the extraction of DOM were taken along transects from the western continental shelf across the slope into the central Weddell Sea and across the eastern Bransfield Strait basin. Large-volume sampling focused on Warm Deep Water (WDW) in order to obtain a suite of samples along a diagenetic sequence of DOM, from less (on the shelf) to highly degraded (central Weddell Sea). This sampling scheme is a continuation of our activities during the ISPOL experiment, where sampling was restricted to mainly one region.

The water samples for the analysis of dissolved organic carbon and nitrogen (DOC, DON) were filtered through 0.2 μm (PTFE) and acidified to pH2. The water for DOM analysis was also filtered through 0.2 μm (PTFE) and acidified to pH2 with HCl before a solid phase extraction followed by elution with methanol. All samples are kept at -30°C and will be analyzed at home for DOC, DON, and molecular constituents with advanced analytical techniques.

Preliminary and expected results

First indications for the existence of a “DOM-pump” in the Weddell Sea were obtained during the ISPOL experiment. WDW is characterized by the highest temperatures ($\sim 0.6^{\circ}\text{C}$, ~ 600 m) and represents the oldest water mass being transported

southwards from the Antarctic Circumpolar Current. The mineralization of sinking organic particles in the history of this water mass causes nutrient accumulation and oxygen depletion in the WDW. The nutrient maximum (~ 1,200 m) is significantly deeper than the temperature maximum (~ 600 m). Hence mixing of WDW with surface and bottom water alone cannot explain the nutrient profiles in the water column. The nutrient increase is rather caused by mineralization of sinking particles. The increasing silicate/nitrate-ratio with depth reflects the slower mineralization rate of silicate compared to nitrate. Bottom water is the densest water with lowest temperatures (-1.55 °C) and the highest salinity (34.6). Contrary to WDW, it is characterized by low nutrient content, high oxygen concentration, and most importantly in the context of our study, increased DOC concentrations. These profiles indicate the formation of bottom water from biologically active surface waters within relatively short periods of time. This is a first indication for DOM being transported from surface to bottom waters.

3.6 Oceanic mass variability in the Antarctic Circumpolar Current observed by bottom pressure sensors and GRACE satellites

Andreas Macrander
Alfred-Wegener-Institut

Objectives

Ocean Bottom Pressure (OBP) represents an integral measure of the water column and the overlying atmosphere. Its variability is affected by sea surface height, changes in the density structure, and geostrophic current variability. Hence, OBP measurements at a few different locations allow integrating estimates of transport and mass flux variability.

The Antarctic Circumpolar Current (ACC), which distributes the dense water masses produced in the Weddell Sea into the oceans, extends over the entire water column. Therefore, large OBP variability is expected in this region, which may also be detected by the GRACE satellite mission that aims to observe surface mass fluxes on the earth by means of space-borne gravity field measurements.

During ANT-XXIII/7, 6 PIES (Pressure sensor equipped Inverted Echo Sounder) have been deployed on the sea floor in the area of the ACC (Fig. 3.7). The objectives are:

- Acquisition of multi-year time series of Ocean Bottom Pressure (OBP) and acoustic travel time (bottom to surface) in a 2-dimensional array in the region 9°W – 13°E / 37°S – 53°S (Fig. 3.7), where a high signal-to-noise ratio is expected.
- Validation of gravity field variability observed by the GRACE satellite mission.
- Observations of sea surface height and integrating estimates of current, transport, heat content, and mass variability of the ACC.
- Validation of the AWI Finite Elements Sea-Ice Model (FESOM).

Work at sea

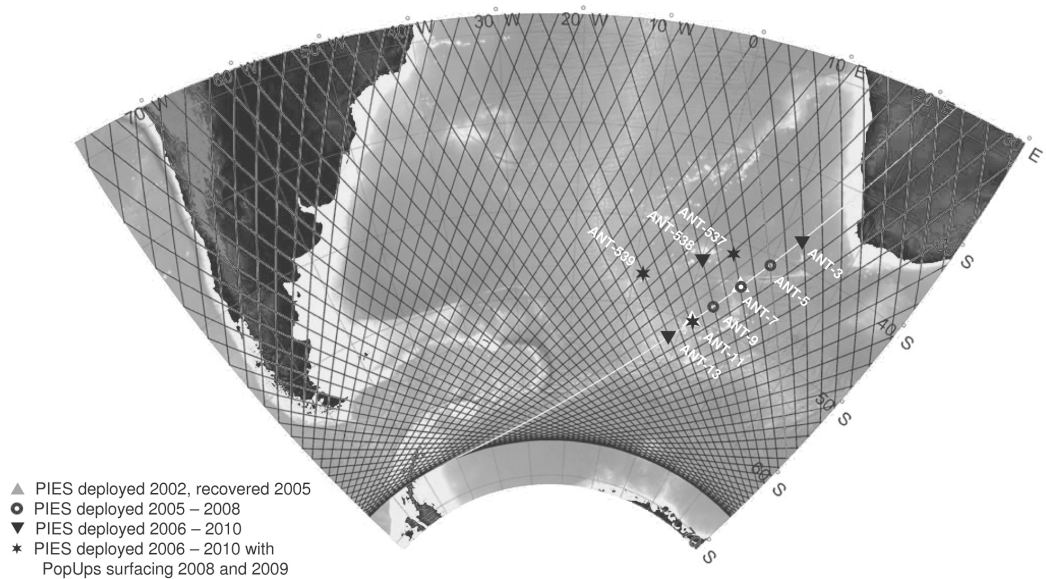
During ANT-XXIII/7, 6 PIES (manufactured by University of Rhode Island) have been deployed by *Polarstern* (see station list).

Since the GRACE gravity field observations have a spatial resolution of $O(500\text{ km})$, a two-dimensional array covering a large region of coherent OBP variability was installed, which allows a comparison between the point-measurements obtained by each PIES and the spatially integrating GRACE data.

The mooring positions were determined by the analysis of GRACE data and time series of two PIES deployed as test moorings from 2002 – 2005. These revealed a large region of coherent OBP variability in the South Atlantic sector of the ACC (Fig. 3.7), which agrees also with the FESOM model at AWI (not shown). Furthermore, the deployment positions are located along Topex/Poseidon radar altimetry ground tracks (Fig. 3.7) to allow additional sea surface height comparisons between PIES and satellite altimetry.

Each mooring consists of an acoustic Posidonia transmitter for relocation purposes, floatation, 50 m of line, and the actual PIES located in a 1.5 m diameter steel stand that ensures a stable position of the PIES at the ocean bottom. All moorings reach the sea floor freely falling. The PIES then collect and store OBP and travel time data until they are acoustically released and recovered as part of future *Polarstern* cruises in 2008 – 2010. To enable an earlier start of data analysis without interrupting the OBP time series, three of the PIES include an additional PopUp buoy module for intermediate data retrieval via an Iridium satellite link.

Hydrographic CTD casts have been taken at all except two of the mooring positions for calibration and referencing of the acoustic travel time and OBP time series.



Correlation GRACE GFZ3 do 1-50, 750 km vs. in-situ OBP at ANT 11-1

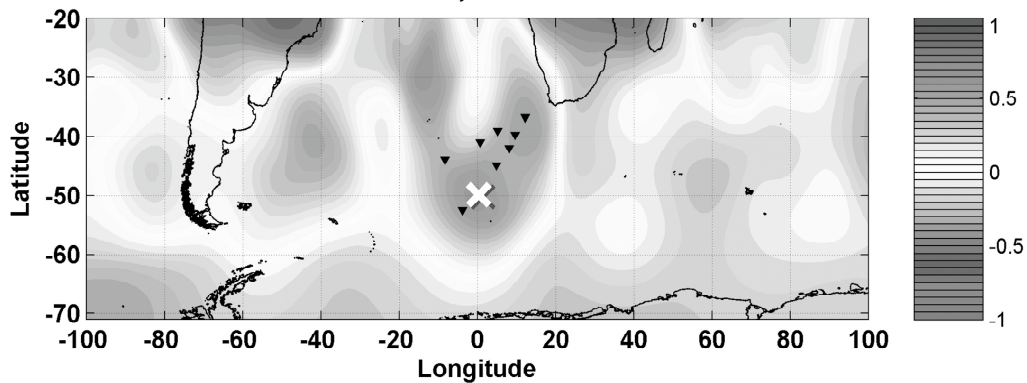


Fig. 3.7: PIES deployment positions during ANT-XXIII/7. Upper panel: \triangle PIES deployed 2002, recovered in 2005 during ANT-XXII/3. \bullet PIES deployed during ANT-XXII/3 (Jan 2005).

\blacktriangledown Deployment positions on ANT-XXIII/7 ($*$ with additional PopUp buoys).

Topex/Poseidon altimetry ground tracks shown as black lines (track #133 in white).

Lower panel: Correlation between monthly GRACE GFZ3 gravity field solutions and in-situ OBP observed by PIES ANT-11-1 (white cross). A region of coherent variability extends to the northeast and northwest of that position (dark shading). The PIES array deployed in 2005 and 2006 (ANT-XXIII/7) is additionally indicated by small black triangles.

Expected results

The GRACE satellite mission provides monthly time series of the gravity field of the earth with unprecedented accuracy. Over the oceans, short-term fluctuations of the gravity field are associated with changes of sea surface height (SSH) or the density structure of the water column.

3.6 Oceanic mass variability in the Antarctic Circumpolar Current observed by bottom pressure sensors and GRACE satellites

The Ocean Bottom Pressure observations obtained by the PIES array will be employed as a ground-truth site to validate GRACE OBP estimates. Since in the ACC large OBP variability and hence a higher signal-to-noise ratio than in other regions is expected, GRACE may perform well to observe oceanic mass variability associated with geostrophic current and mass variations. First results from two PIES deployed from 2002 – 2005 suggest that GRACE in fact captures the dominant modes of OBP variability in the ACC (Fig. 3.8). The extended 2-dimensional array (Fig. 3.7), operating from 2005/2006 to 2010, is expected to improve the detection of large-scale coherent OBP signals and is thus an important contribution to the global ground-truth validation of GRACE in the framework of the BMBF-Geotechnologien project “Improved GRACE level-1 and level-2 products and their validation against ocean bottom pressure”.

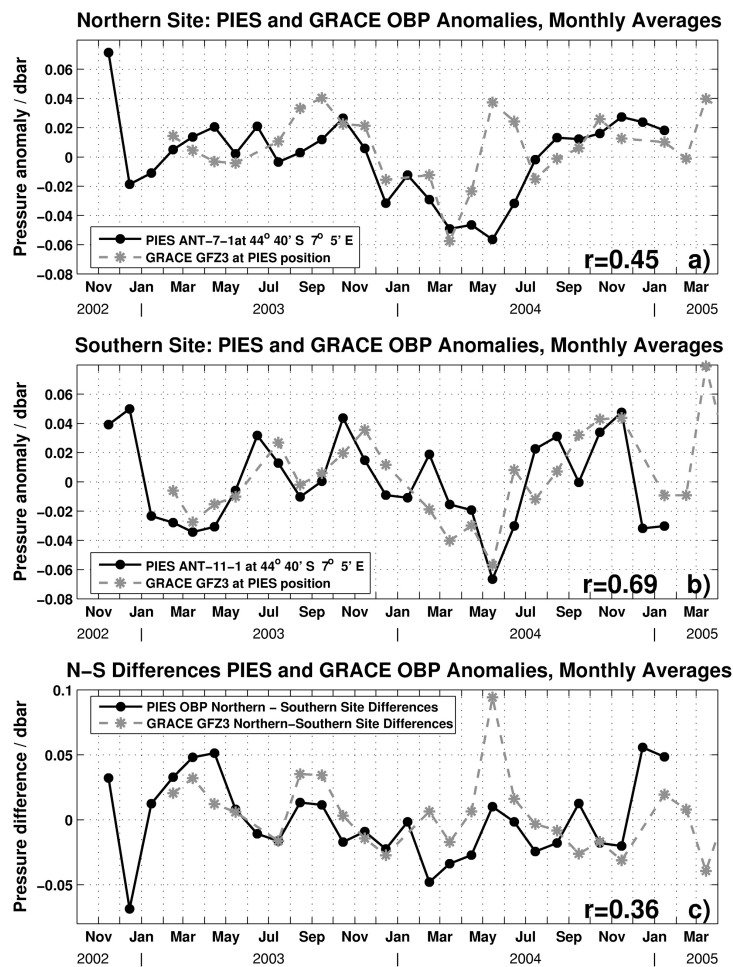


Fig. 3.8: Comparison of in-situ OBP observations by PIES and GRACE satellite data. a, b: Monthly OBP anomalies measured by PIES (black solid lines) and the GRACE satellite mission (grey dashed lines) at the two mooring sites ANT7 and ANT11 in the northern part of the ACC. For locations see Fig. 3.7. The GRACE observations are significantly correlated with the PIES observations ($r=0.45$ at ANT7, $r=0.69$ at ANT11). c: OBP differences between both sites, which correspond to geostrophic current anomalies.

All PIES are deployed on Topex/Poseidon altimeter ground tracks, allowing to combine *in-situ* observations of acoustic travel time and OBP, Topex/Poseidon Sea Surface Height, and GRACE gravity measurements. This dataset will be assessed to determine the variability of geostrophic current velocities, both at the surface and at abyssal depth, and transport and heat content of the ACC. Moreover, the multi-year OBP time series will be used for validation of the German community Finite Elements Sea-Ice Model (FESOM) operated by the group of Jens Schröter at AWI.

4. REGIONAL VARIABILITY OF SEA ICE PROPERTIES AND THICKNESS IN THE NORTHWESTERN WEDDELL SEA OBTAINED BY IN-SITU AND SATELLITE MEASUREMENTS

Christian Haas¹⁾, Anika Friedrich¹⁾,
Zijun Li³⁾, Marcel Nicolaus¹⁾,
Andreas Pfaffling¹⁾, Takenobu
Toyota²⁾

¹⁾Alfred-Wegener-Institut
²⁾Institute of Low Temperature Science,
Sapporo/Japan
³⁾State Key Laboratory of Coastal and
Offshore Engineering, Dalian/China

Objectives

The western Weddell Sea is one of only a few regions of the Southern Ocean covered by perennial sea ice. As such, it is of particular importance for atmosphere-ice-ocean processes and in particular for the oceanic freshwater balance. Therefore, the main objectives of the sea ice geophysical programme were:

1. Quantification of the regional variability of first- and second-year sea ice and snow thickness in the north-western Weddell Sea, and observations of their interannual variability in comparison with earlier measurements of other researchers, obtained by drilling and upward-looking-sonar. In particular, we aimed at continuing observations performed during ISPOL (ANT-XXII/2) in December 2005.
2. Validation of satellite measurements of radar backscatter and surface temperature of different ice types and polynya processes by means of coincident real-time Envisat-SAR and NOAA-AVHRR imagery received on board, and *in-situ* measurements of ice and snow thickness and other physical properties. With an improved understanding of satellite signatures, the results of our *in-situ* measurements can be spatially extrapolated and extended to longer time periods.
3. Investigation of physical and biological ice properties and processes and the fate of perennial ice after surviving one summer melt season. From earlier *Polarstern* cruises including ISPOL it is clear that the ice undergoes significant changes during the summer season. ANT-XXIII/7 offered the opportunity to study the fate of this ice during the following winter, in particular the properties of remnant metamorphous snow, superimposed ice, and refrozen gap layers.

Work at sea

To address those objectives, measurements have been carried out on the ice, from the ship, and by helicopter, including:

4. Regional variability of sea ice properties and thickness in the northwestern Weddell Sea obtained by in-situ and satellite measurements

- Ice coring and analyses of ice temperature, salinity and texture profiles, and snow-pit measurements of snow properties during ice stations. Additionally, ice and snow thickness profiles were measured by means of electromagnetic (EM), ground-penetrating radar (GPR), and drill-hole profiling.
- Ship-based visual and photo observations of general ice conditions, and continuous EM, GPR, and video measurements of ice and snow thickness.
- Helicopter-borne EM ice thickness and GPR snow thickness surveys, laser profiling of surface roughness and ridge distribution, and video-recordings of floe size distributions.

In total, measurements have been performed on 40 days when the ship was travelling through ice. The map in figure 4.1 shows the locations of all 27 ice stations and helicopter EM flight tracks

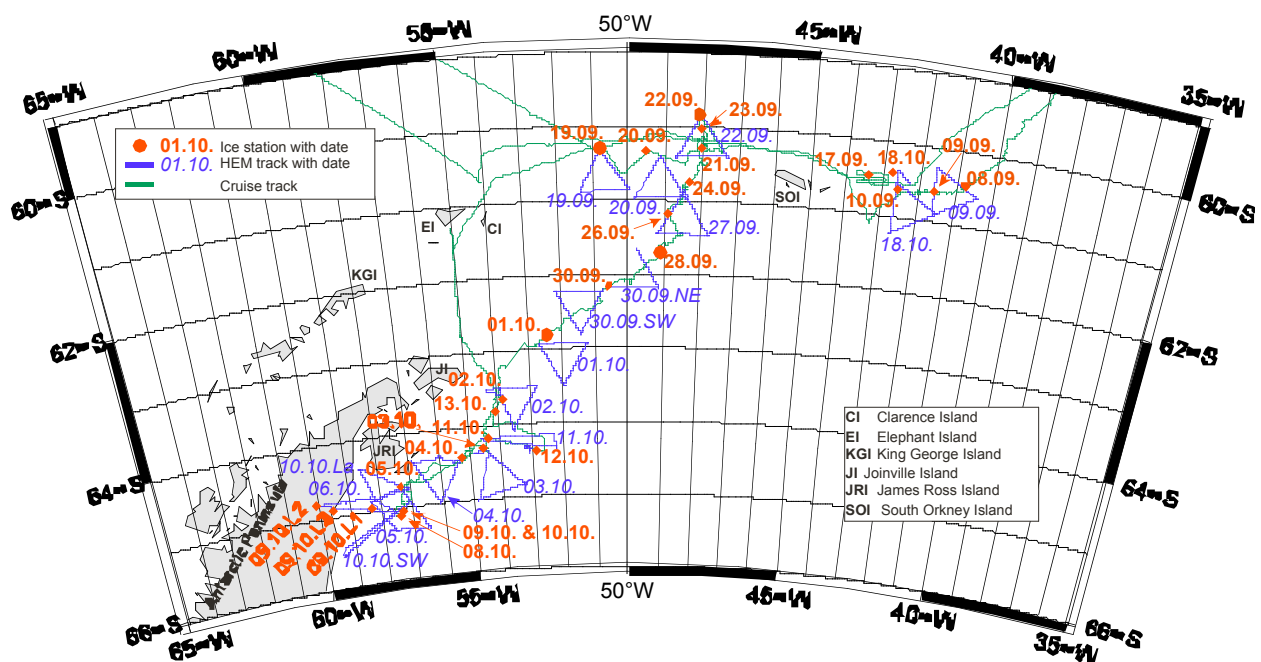


Fig. 4.1: Cruise track, ice stations and HEM profiles of the sea ice geophysics group during ANT-XXIII/7. Labels give the date of the ice station. Ice stations are separated into first-year (smaller dots) and second-year (larger dots) sea ice floes.

4.1 General ice conditions in the study region

4.1.1 Ice conditions and ice types observed with satellite radar and thermal infrared imagery

For the design and interpretation of ANT-XXIII/7 ice and snow measurements the knowledge about the occurrence and regional variability of different ice types and ice regimes is essential. Therefore, we observed the study region by means of real-time satellite radar and thermal infrared imagery. High resolution radar images were also

used together with helicopter reconnaissance flights to support the ship navigation through ice.

The best overview of general ice conditions and ice types was obtained from Quikscat (Ku-band) and Envisat Global-Mode-Mosaics (GMM; C-band) radar backscatter maps. These were received by email from the Technical University of Denmark (DTU, courtesy Leif Toudal) at the same day of the acquisition, or on the following day. The backscatter maps in figure 4.2 were acquired on September 7, 2006, and show ice conditions at the beginning of ANT-XXIII/7. Medium backscatter around Orkney Islands indicates the presence of large amounts of second-year ice in that region. South- and eastwards lower backscatter points to prevailing first-year ice. Along the east side of the Antarctic Peninsula a prominent band of heavily deformed first- and second-year ice with high backscatter extended, covering much of the actually study region (cf. Fig. 4.1). To the east of that band, another south-north extending band of first-year ice exported from the Ronne polynya can be seen. Similarly, between the bright band and the Peninsula a region of low-backscatter first-year ice formed in the bays of the former Larsen-A and –B ice shelves was observed.

The high resolution Envisat Synthetic-Aperture Radar (SAR) Wide-Swath-Mode (WSM) image in figure 4.3 reveals more detail about those different ice regimes, and their relation to our ice measurements shown in figure 4.1. In particular, the band of high-backscatter, thick deformed first and second-year ice can be seen at the right boundary of the image, and different regions of first-year ice along the Peninsula, originating from narrow polynyas in the Larsen-A and –B embayments.

Comparable Envisat imagery was obtained every three days throughout the cruise, allowing close observations of the changes in ice conditions which occurred due to ice drift and surface melting events. Imagery was acquired by European Space Agency (ESA) as part of their so-called background mission. By means of automatic computer scripts (courtesy T. Busche), full resolution WSM images were downloaded to AWI by ftp, enhanced, geocoded and projected, and compressed jpeg-2000 quicklooks were emailed to the ship. Normally, the images were received on board within half a day after the satellite overpass. Unfortunately, due to a failure of the data downlink instrument on board Envisat, no imagery was available between September 26 and October 5.

NOAA-AVHRR imagery was directly received on board with *Polarsterns* HRPT receiving station. Those images, in particular of the thermal infrared channels, revealed further insight into ice conditions, in particular of the thin ice regions in the Larsen embayments. They confirmed the existence of open water in the polynya regions, as well as of the very thick ice in the band with high radar backscatter, which could be identified by the lowest sea ice/snow surface temperatures in some images. AVHRR imagery proved the most useful for supporting *Polarsterns* navigation through heavy ice conditions, as not only leads, but also brash ice regions like those south and east of James Ross Island were clearly identifiable by their higher surface temperatures compared to regions with a more closed ice cover.

4. Regional variability of sea ice properties and thickness in the northwestern Weddell Sea obtained by in-situ and satellite measurements

Radar satellite imagery was very important for the observation of temporal snow melt events. There were several periods during the cruise when air temperatures rose above 0 °C, and where warm snow was observed (see Section 4.4.1 and 4.5). These events occurred predominantly in the marginal ice zone and adjacent southern regions, and caused strong snow metamorphosis, and partial melting. A very prominent event was experienced in the evening of September 28, when air temperatures measured on board *Polarstern* rose up to +1.2 °C and fog and even some rain were observed. At the same time, radar backscatter dropped markedly, as can be seen in the Quickscat map of September 29 (Fig. 4.5). Only one day later, air temperatures dropped to -17.5 °C, causing refreezing of the snow and the formation of ice layers near the surface. As a consequence, volume scattering increased markedly and Ku-band radar backscatter rose to much higher values than before the melting event (Fig. 4.5).

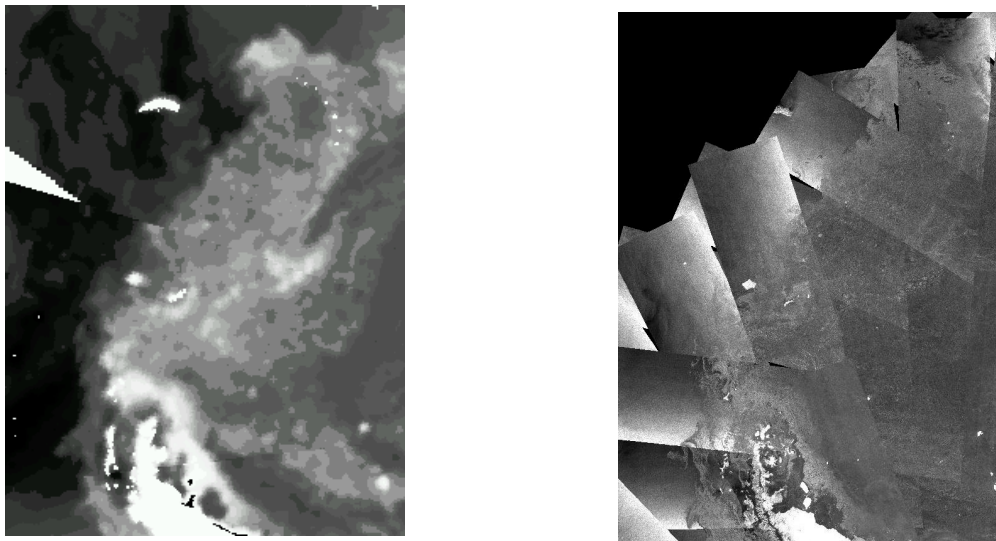


Fig. 4.2: Quickscat Ku-band (left) and Envisat-GMM C-band (right) radar backscatter maps of the northwestern Weddell Sea, showing ice conditions on September 7, 2006 (courtesy L. Toudal, DTU). Bright grey values correspond to high backscatter.

4.1 General ice conditions in the study region

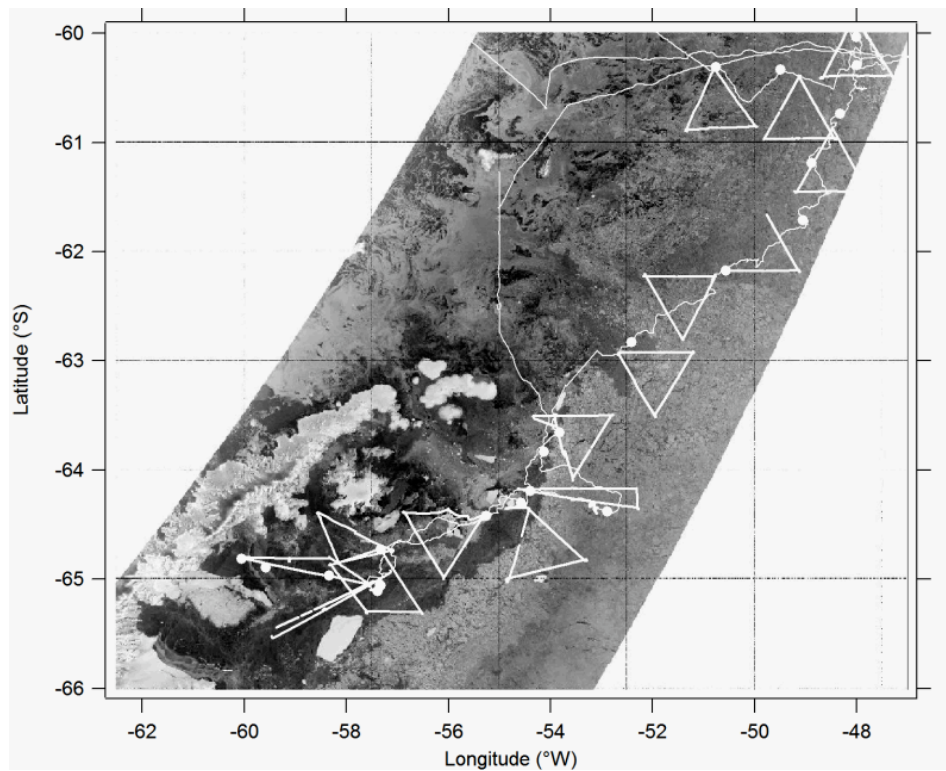


Fig. 4.3: Envisat-SAR image of parts of the study region, acquired by European Space Agency (ESA) on September 19, 2006. The ANT-XXIII/7 cruise track (thin line), helicopter EM flight tracks (thick lines), and locations of ice stations are shown (filled circles).

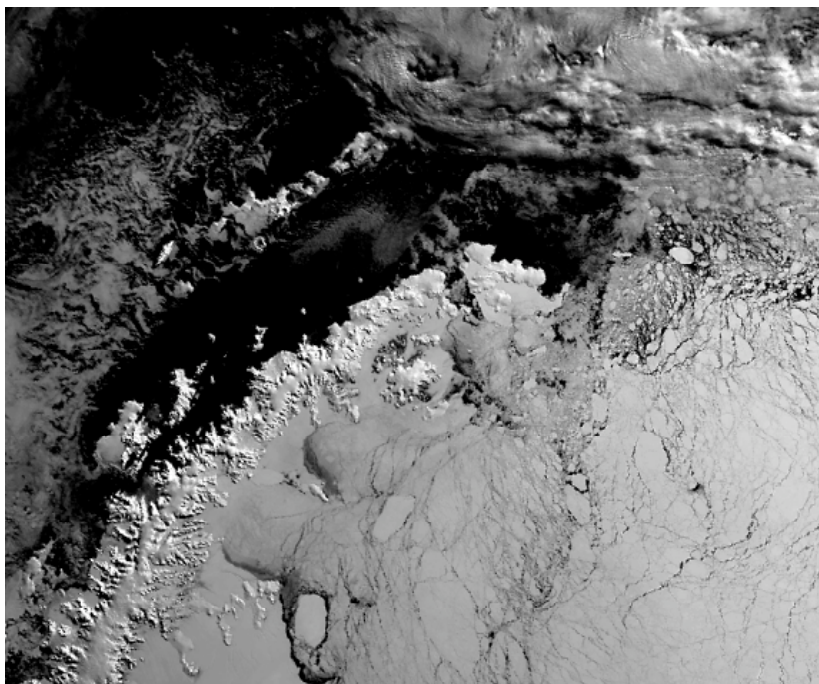


Fig. 4.4: NOAA-AVHRR channel 4 (thermal infrared) image of the study region, acquired on October 3, 2006, at 12:10 UTC



Fig. 4.5: Quikscat Ku-band backscatter maps of September 28 (left), 29 (centre), and 30 (right), showing backscatter changes due to the passage of a region of warm air. Bright grey values indicate high backscatter.

4.1.2 Visual ice observations

During the cruise the general ice conditions were recorded hourly from on the ship's bridge, by visual ice observations following the ASPeCt protocol. All members of the international sea ice research team contributed to the observations. They are important as general background information on ice conditions for later interpretation of other data gathered during the cruise. Observations included the total ice concentration and an estimation of the areal coverage, thickness, floe size, topography and snow cover of the three dominant ice classes. The thickest of these three ice categories is defined as the primary ice type. Photos were taken from the portside, front, and starboardside of the ship and will be published as images on the AWI sea ice web site together with the data. Additionally to the hourly observations meteorological conditions were recorded from the *Polarstern* Data Acquisition System (PODAS) including water temperature, air temperature, true wind speed and direction, total cloud cover, visibility and current weather. The observations are contributed to the SCAR Antarctic Sea Ice Processes and Climate (ASPeCt) data base which is compiling a sea ice climatology from any past and forthcoming ship cruises through Antarctic sea ice. Observations were performed on 41 days.

The data show three distinct ice regimes along the ship's transect. On the way from the Sandwich Islands through the Orkney region to Elephant Island, a heterogeneous ice regime was found until 60°S 48°W with thin first-year ice and multi year ice as its main ice types (Figs. 4.6 and 4.7). This area was followed by a heavily deformed band of mainly thick first-year and multiyear ice reaching from the Powel Basin south to the Larsen-A region. The Larsen-A area itself was dominated by thin and medium first-year ice, and brash.

4.1 General ice conditions in the study region

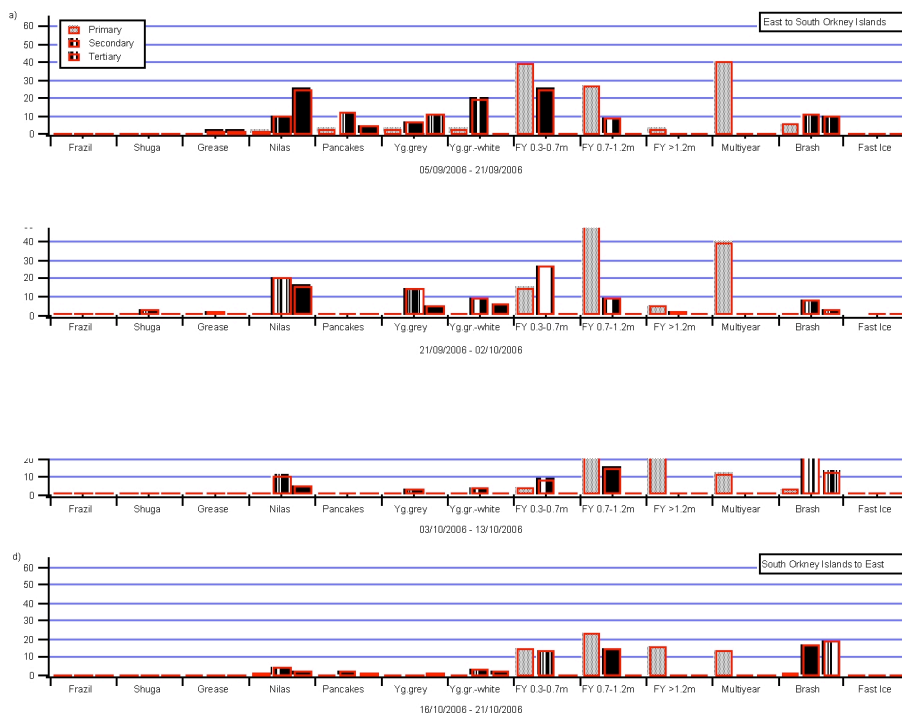


Fig. 4.6: Visually observed ice types and their areal fraction

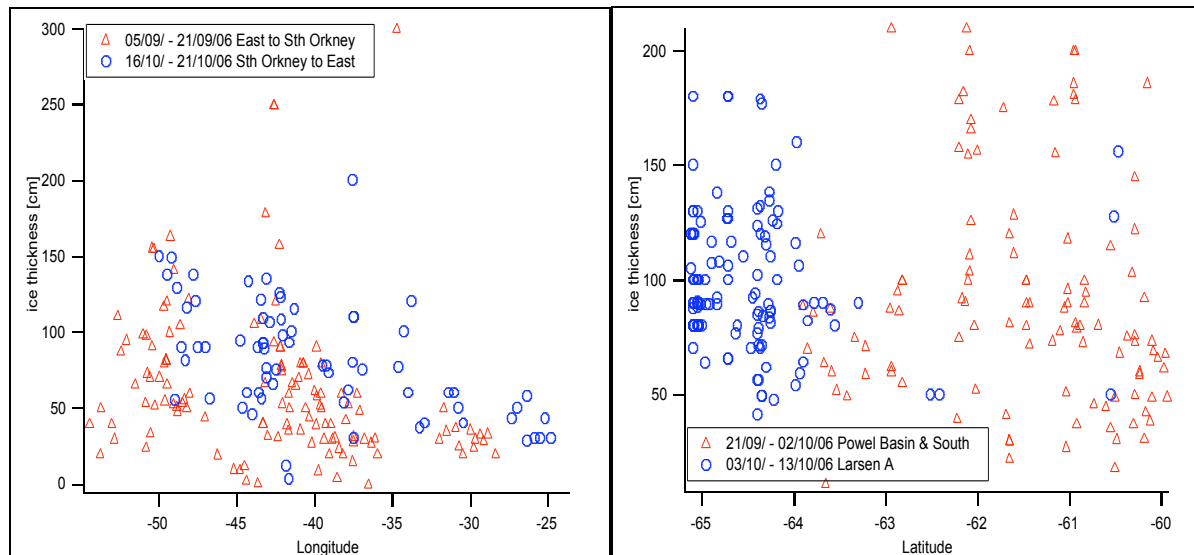


Fig. 4.7 Visually observed ice thickness for different regions along the cruise track

4.2 Sea ice thickness distribution

The ice thickness distribution is one of the most important sea ice properties, as it is a result of the thermodynamic and dynamic growth history of the ice. Therefore, it can be used to observe interannual climate variability as well as to outline different ice regimes with different age and origin.

Here, most measurements were performed by means of electromagnetic (EM) inductive sounding, which is an established technique to measure ice thickness. The accuracy of EM measurements is better than ± 0.1 m over level ice. However, the maximum thickness of ridges and deformed ice can be underestimated by as much as 50 %.

EM ice thickness retrievals yield an estimate of total ice thickness, i.e. the sum of snow and ice thickness. Any EM ice thickness value stated in this Section therefore refers to total thickness. Because it is important to distinguish between snow and ice thickness, much effort was put into measurements of snow thickness, which are reported in Section 4.5. Drill-hole measurements have been performed to confirm the calibration of the EM measurements, and to yield independent estimates of ice thickness, freeboard, and surface elevation.

4.2.1 Ground based thickness measurements

On almost every ice station, an ice and snow thickness profile was obtained, consisting of drill-hole, snow stick, and EM thickness measurements. They served to characterise each station floe as background information for ice core analyses, as well as complementary data to be compared with ship- and airborne thickness observations. Along the first 200 m of each profile, holes were drilled at least every 20 m for measurements of ice and snow thickness, draft, and freeboard. In-between, snow thickness was measured every one or two meters with a ruler stick. Those measurements served as validation for the EM and GPR ice and snow thickness measurements, and for independent studies of ice floe isostasy, in particular for comparisons of snow surface elevation and ice freeboard with ice thickness. Along the 200 m profile and beyond, a Geonics EM31 instrument was pulled to obtain high resolution ice thickness data with a spatial sampling interval of 5 m. Those measurements reached lengths of over 3 km, and in total 21.7 km of thickness profile was acquired on 22 floes. Ruler stick snow thickness measurements were also performed every 20 m along the EM profile to obtain larger-scale snow thickness information than from the 200 m validation line. All EM measurements were recorded together with GPS position data by a data logger. They were subsequently geocoded and corrected for walking speed variations and ice drift by means of ship GPS reference data to obtain an equidistant data set.

Figure 4.8 shows typical profiles of second-year and thick and thin first-year ice floes thus obtained, representative of most sampled ice floes. Note the different level ice thicknesses, which are also less smooth with increasing ice age. Note also the different degree of deformation of each ice type.

The data of every profile and further information on ice type and location is summarized in table 4.1. The thickness distribution of all drill-hole and EM31 data is presented in figure 4.9. It is characterized by a strong mode between 1.2 and 1.4 m, mostly resulting from the first-year ice sampled in the Larsen region. Secondary modes between 2.5 and 3 m represent thick first-year and second-year ice. There was very good agreement between the thickness distributions obtained by drilling and EM surveying (Fig. 4.9), although there were about 200 times more EM than drill-hole measurements (Tab. 4.1). There is also excellent agreement between the ground-based and airborne thickness distributions (Fig. 4.9). The latter also comprise the thin ice and open water fractions in the study region.

Figure 4.10 shows the snow thickness distribution obtained along the full length of the EM profiles, which are also summarized in table 4.1. Snow thicknesses were dominated by a mode between 0.05 and 0.10 m. There were also secondary modes between 0.3 and 0.45 m. While the former mainly resulted from thin first-year ice, particularly on the almost bare ice in the Larsen region, the thicker snow was found on thick first-year and second-year ice. See Section 4.5 for a more comprehensive discussion of regional patterns of the snow thickness distribution.

4. Regional variability of sea ice properties and thickness in the northwestern Weddell Sea obtained by in-situ and satellite measurements

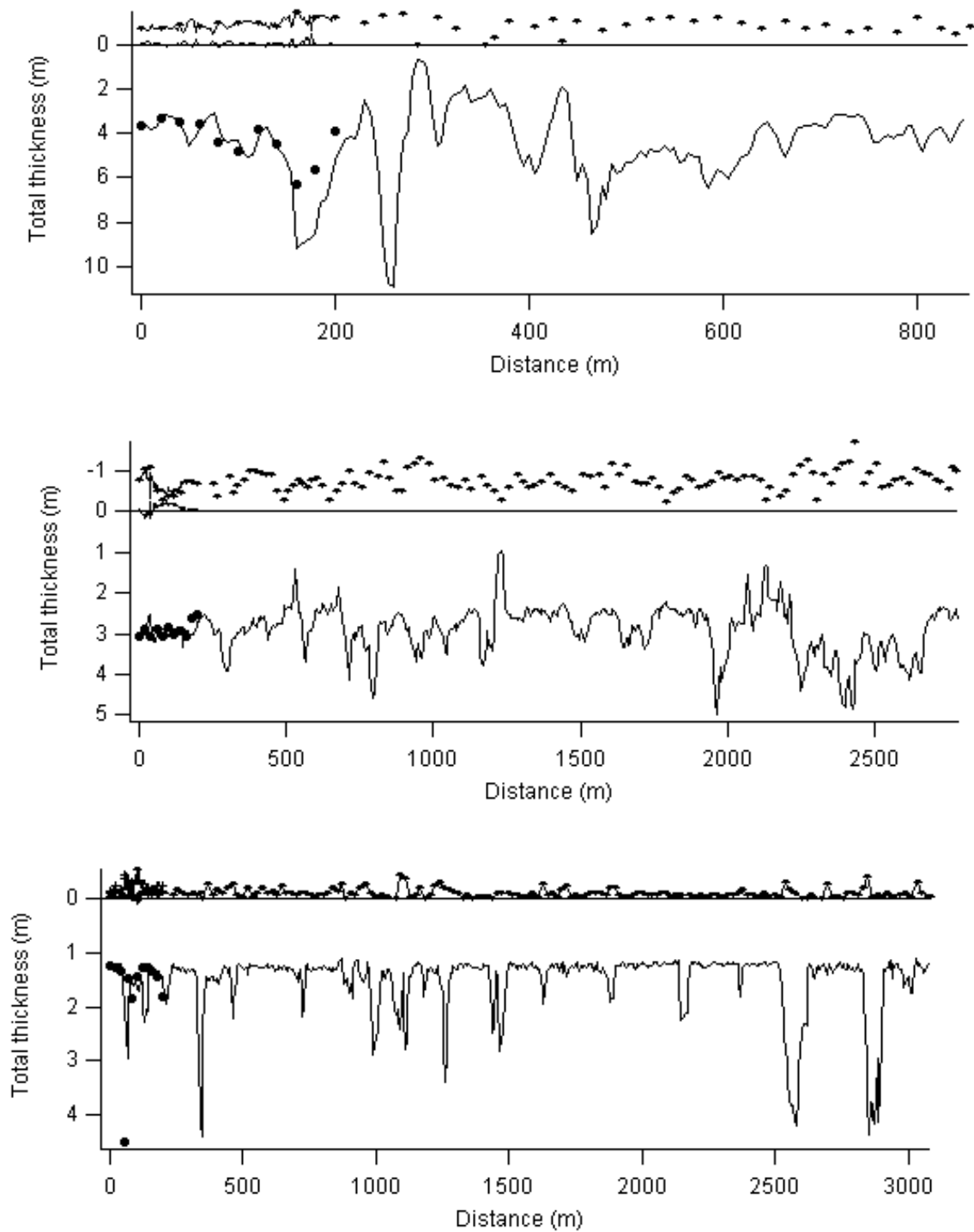


Fig. 4.8: Typical thickness profiles of (top) second-year, (centre) thick first-year, and (bottom) thin first-year ice obtained by drilling (large dots) and EM sounding (solid lines). Note different scales. Ice thickness is plotted downwards, while snow thickness is shown above the 0 m horizontal line. Along the first 200 m of each profile, calculated freeboard and surface elevation is also shown, based on the measured total ice thickness and snow thickness. Profiles were obtained on (top) October 1, (centre) October 12, and (bottom) October 8.

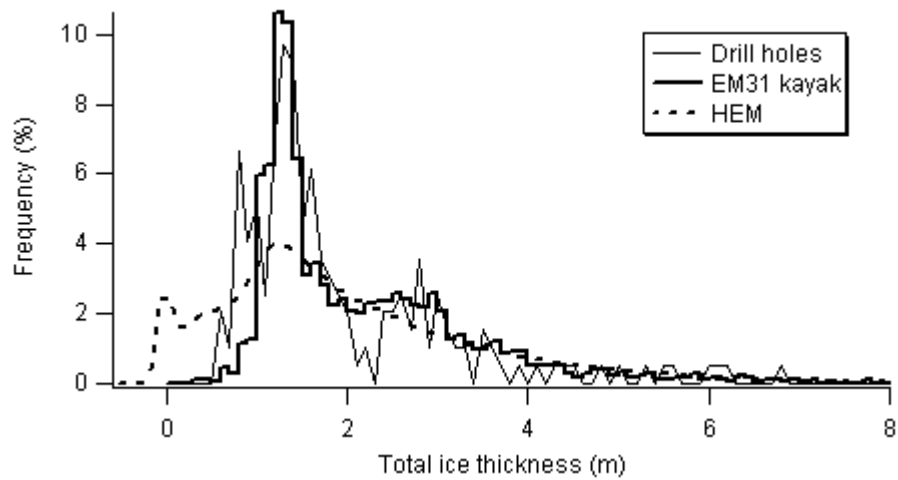


Fig. 4.9: Ice thickness distributions obtained from all drill-hole and ground-based EM31 measurements as well as from airborne EM sounding (Section 4.2.4)

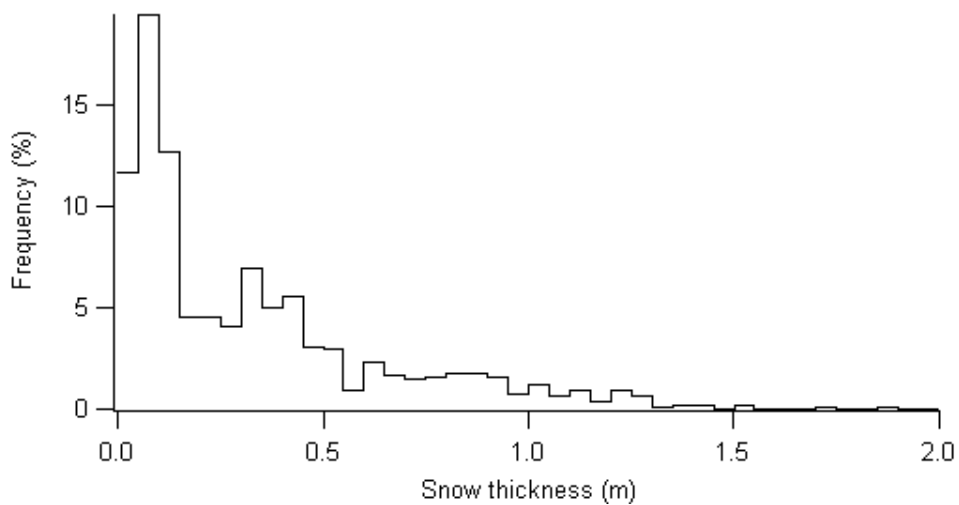


Fig. 4.10: Snow thickness distribution obtained from ruler stick measurements along long ground-based EM thickness profiles

Tab. 4.1: Overview of snow and sea ice thickness of all 28 sea ice stations. Additionally, freeboard from ice coring sites, ice type (FYI: first-year ice; SYI: second-year ice) and mean salinity of the sea ice core are given. “Heli” stations were visited by helicopter in stead of *Polarstern*-gangway. “Night” stations were mainly performed during darkness. L1 to L3 are used to distinguish sea ice stations close to Larsen-A polynya on 09.09.06.

Date	Julian Day	Lon °W	Lat °S	Snow thickness (stick)			Snow thickness (radar)			Snow thickness (EM31)			Sea ice thickness (EM31)			Free-board m	Ice type	Mean salinity	Comment
				Profile length	Mean	stddev	Profile length	Mean	stddev	Profile length	Mean	stddev	Profile length	Mean	stddev				
				M	m	m	m	m	m	m	m	m	m	m	m				
8.9.06	251	40.787	60.465	200	0.13	0.09	200	0.20	0.10				200	0.96	0.51	-0.02	FYI	4.51	
9.9.06	252	41.583	60.597	200	0.37	0.19	200	0.35	0.17	455	0.36	0.15	460	1.73	0.56	0.06	FYI	3.99	
10.9.06	253	42.615	60.615				700	0.65	0.23	600	0.68	0.23	600	2.75	1.09	0.03	FYI	5.06	Night
19.9.06	262	50.769	60.305	60	0.36	0.10	60	0.37	0.12				60	3.07	0.35	0.26	SYI	2.79	
20.9.06	263	49.495	60.331	60	0.10	0.03							55	0.89	0.06	0.05	FYI	5.46	
21.9.06	264	48.002	60.292	65	0.35	0.08							65	1.96	0.56	0.07	FYI	4.40	
22.9.06	265	48.084	59.835	71	1.10	0.41				323	1.00	0.38	340	5.44	0.83	0.06	SYI	1.13	
23.9.06	266	48.014	60.037	100	0.39	0.06							70	1.46	0.05	0.00	FYI	4.20	
24.9.06	267	48.331	60.737	200	0.44	0.27	200	0.46	0.26	600	0.32	0.25	600	1.81	0.81	0.01	FYI	3.71	Night
26.9.06	269	48.892	61.186	100	0.54	0.14	100	0.55	0.07				230	2.26	0.48	0.02	FYI	4.65	
28.9.06	271	49.062	61.709	200	0.68	0.18	200	0.69	0.17	1106	0.74	0.27	1105	4.54	2.16	0.10	SYI	2.89	
30.9.06	273	50.572	62.170	170	0.36	0.11	170	0.48	0.25	784	0.59	0.29	785	3.31	1.80	0.04	FYI	4.19	
1.10.06	274	52.422	62.829	200	0.90	0.27	200	0.92	0.25	854	0.90	0.34	850	4.45	1.69	0.02	SYI	2.80	
2.10.06	275	53.826	63.650	200	0.16	0.11	200	0.22	0.12	1050	0.16	0.16	1050	1.69	0.50	0.10	FYI	5.13	
3.10.06	276	54.578	64.296	200	0.11	0.07				2614	0.14	0.15	2615	1.69	0.63	0.15	FYI	5.28	
4.10.06	277	55.264	64.418	200	0.12	0.10	200	0.17	0.10	1500	0.12	0.10	1500	1.51	0.61	0.14	FYI	5.61	
5.10.06	278	57.331	64.726							571	0.12	0.14	570	2.81	1.01	0.19	FYI	5.02	
8.10.06	281	57.391	65.106	200	0.12	0.12				3087	0.11	0.09	3085	1.51	0.57	0.12	FYI	5.66	
9.10.06	282	57.343	65.052	200	0.05	0.04					0.10	0.11	875	2.29	0.73	0.10	FYI	5.43	
9.10.06	282	58.338	64.964	point	0.03								point	1.22		0.11	FYI	8.34	Heli, L1
9.10.06	282	60.060	64.810	25	0.04	0.01										0.15	FYI	4.92	Heli, L2
9.10.06	282	59.584	64.892	25	0.01	0.07										0.08	FYI	6.29	Heli, L3
10.10.06	283	57.330	65.055	130	0.07	0.06										no core	FYI	no core	Heli
11.10.06	284	54.399	64.189	200	0.10	0.05					0.11	0.09	2770	1.34	0.47	0.06	FYI	5.64	
12.10.06	285	52.896	64.379	200	0.59	0.24	2500	0.72	0.27	2782	0.77	0.25	2790	2.90	0.59	0.08	FYI	3.36	
13.10.06	286	54.130	63.832	200	0.13	0.13				986	0.11	0.11	985	1.64	0.43	0.12	FYI	5.60	
17.10.06	290	43.436	60.469	108	0.56	0.31										Surface core	FYI	Surface core	Heli
18.10.06	291	42.797	60.396	82	0.51	0.08										-0.10	FYI	4.92	Heli
SUM:				3596	0.32	0.13	4930	0.48	0.18	17313.8	0.39	0.19	21660	2.31	0.75	0.08		4.65	

4.2.2 Ship based EM-thickness measurements

During most time in the ice, ship-based along track ice thickness measurements were performed using *Polarstern's* Sea Ice Monitoring System SIMS. This is based on electromagnetic induction sounding of sea ice thickness, using a Geonics EM31 instrument and a sonic distance meter. All measurements were taken with a sampling frequency of 0.5 Hz. In total, measurements were performed on 31 days (09.09. to 13.09. and 23.09. to 11.10. and 13.10. to 19.10.)

Unfortunately, under most ice conditions met during the cruise, where the ship either steamed through open water leads or had to do some serious ramming, SIMS ice thickness retrievals are not well representing the regional ice thickness distribution. However, they still provide complementary, relative information about different ice regimes, can be used for comparison with thickness estimates from video (Section 4.2.3), and for ship-in-ice studies.

The thickness distribution along the cruise track is shown in figure 4.11. The profiles have been split into two east-west sections between Orkney and Philip Passages, and into one north-south section across the Powel Basin and into the Larsen region. Mean ice thicknesses have been computed for data including and excluding measurements over water, which were defined as having thicknesses smaller than 0.2 m. The difference between both values is indicative for the amount of open water at the ships bow. For the east-west profiles, spatial intervals of one degree latitude have been chosen for averaging, and 0.5 degrees for the north-south transect.

Mean ice thicknesses of up to 2 m have been found. On the east-west profiles, ice thickness was least north of the south Orkney Islands, where a large open polynya was frequently observed on satellite imagery, and where much open water was met during the first east-west transect between September 9 and 13 (Fig. 4.11a). East and west of the Islands, ice thickness was much larger due to the presence of thick second-year ice flowing out from the Weddell Sea. Although the ice edge had retreated considerably southward between September 13 and October 16, mean ice thickness was actually larger during the latter transect. This is probably a result of smaller floes of similar thickness, which have resulted in a higher ice concentration and therefore larger mean thickness in front of the bow.

Ice conditions were much more favourable for SIMS measurements on the north-south transect. Mean ice thickness was only around 1 m in the Powel Basin (Fig. 4.11 b), in agreement with other observations and due to the presence of much new ice and leads in a diverging ice cover. However, there was a marked increase when the Larsen region was entered, and ice thicknesses persistently above 1.5 m explain why the ship ultimately came to a stop.

Some of the main thickness characteristics along the north-south transect can be seen from the thickness distributions in figure 4.11c, which were computed for 0.5 degree latitude intervals. They show modal thicknesses of 0.5 to 0.8 m in the northern Powel Basin, and modal thicknesses between 1.2 and 1.4 m in the Larsen

4. Regional variability of sea ice properties and thickness in the northwestern Weddell Sea obtained by in-situ and satellite measurements

region. Both values are in good agreement with some modes in the airborne measurements (Fig. 4.14). However, the thicker ice modes are not clearly distinguishable.

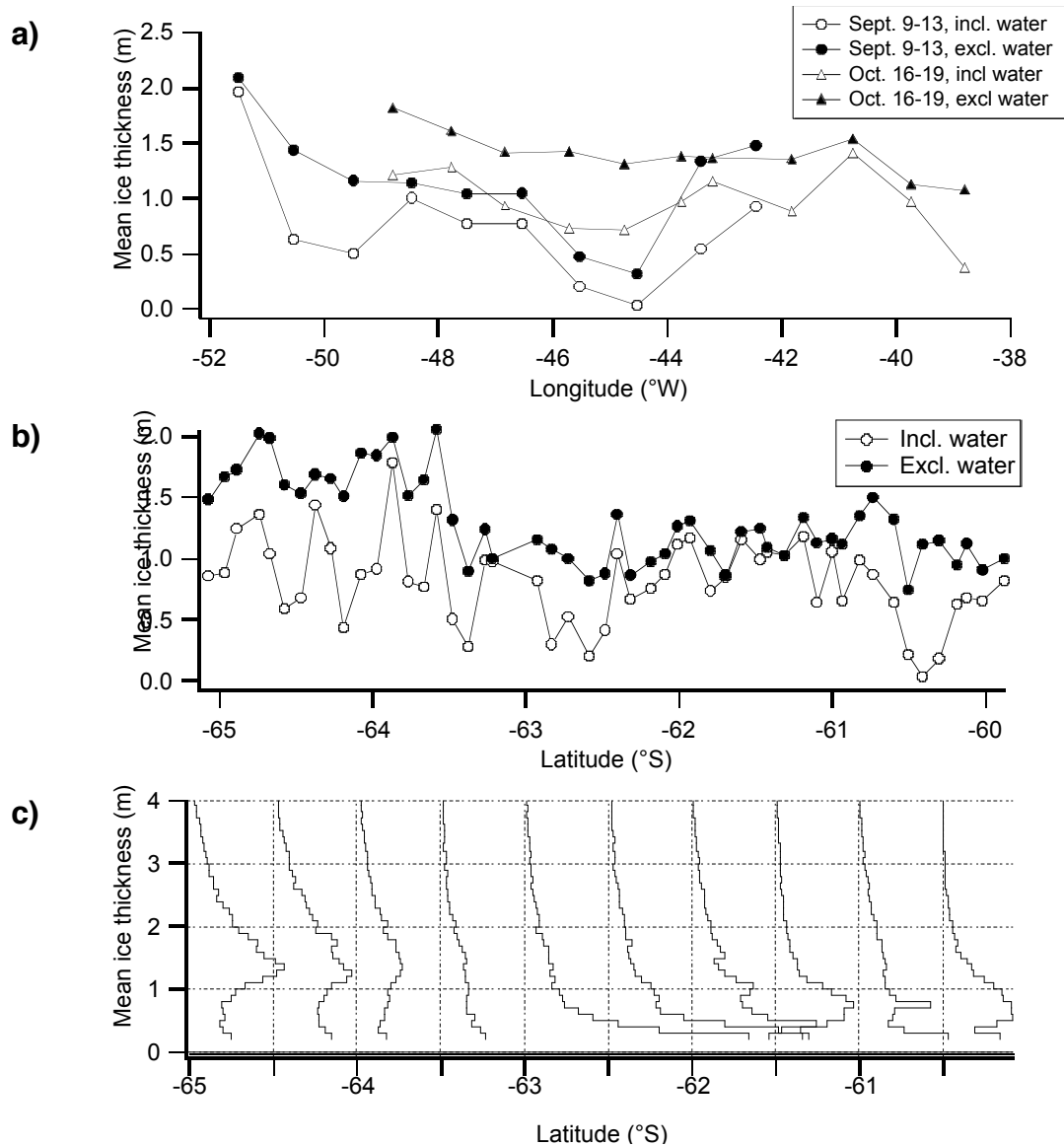


Fig. 4.11: Results of continuous EM ice thickness measurements at the ships bow. Mean ice thickness is shown for all measurements and measurements over ice only (a) along the east-west transects and (b) along the north-south transect (cf. map of cruise track in Fig. 4.1). Ice thickness histograms have been calculated for 0.5 degree latitude intervals along the north-south transect in (c).

4.2.3 Ship based video-thickness measurements

A video monitoring system was also utilized for ice thickness measurements. We mounted a downward-looking video camera on the upper side deck of the ship (Fig. 4.12 a to c) to record the ice floes which were broken at the bow and then turned into side-up positions alongside the hull (Fig. 4.12 d). The monitoring was done principally

for 8 hours per day, from 8 o'clock a.m. to 16 o'clock p.m., with Hi-8 video camera system during the cruise in sea ice area from 9 September to 19 October. We will search for those ice floes that turn at right angles and the ice thickness will be measured manually on each video image. To determine the scale on the video images, a stick of 50 cm length was lowered onto ice floes several times during the cruise. This method has been used to monitor the thickness distribution of the Okhotsk and east Antarctic sea ice for more than 10 years, and it is confirmed that this is useful to obtain the thickness distribution of relatively thin ice.

However, it should be noted that ridged ice is beyond the measuring ability because its greater thickness and roughness prevents it from turning to the side-up position. This method provides the ice thickness distribution principally for level ice. In addition, it should be kept in mind that the obtained ice thickness distribution is biased to thinner ice if the ship selected thinner route.

Despite these drawbacks, this method is considered to provide the useful information in the following points: firstly, it will validate the measurement of the ship-board EM (SIMS) for level ice. Secondly, it can provide some implications on the thickening process of level ice. In general, level ice is thickened through the processes of thermodynamic growth and rafting, and then is used for ridging activities under the compressive forcing. Thus, a rafting process plays a significant role at early stage of ice growth and seems to be important to the modelling of sea ice, especially in the seasonal sea ice zone. However, this process is not understood well at present. Recently, through the measurement for the Okhotsk Sea ice a probabilistic rafting cycle model has been proposed. This theory will be tested for the Weddell Sea ice. In addition, this method also provides some information on biological activities. By observing the brown colour of broken ice, the distribution of ice algae will be estimated to some extent (Fig. 4.12 e). Besides, the depth of ice algae within ice may help us estimate the ice growth history.

4. Regional variability of sea ice properties and thickness in the northwestern Weddell Sea obtained by in-situ and satellite measurements

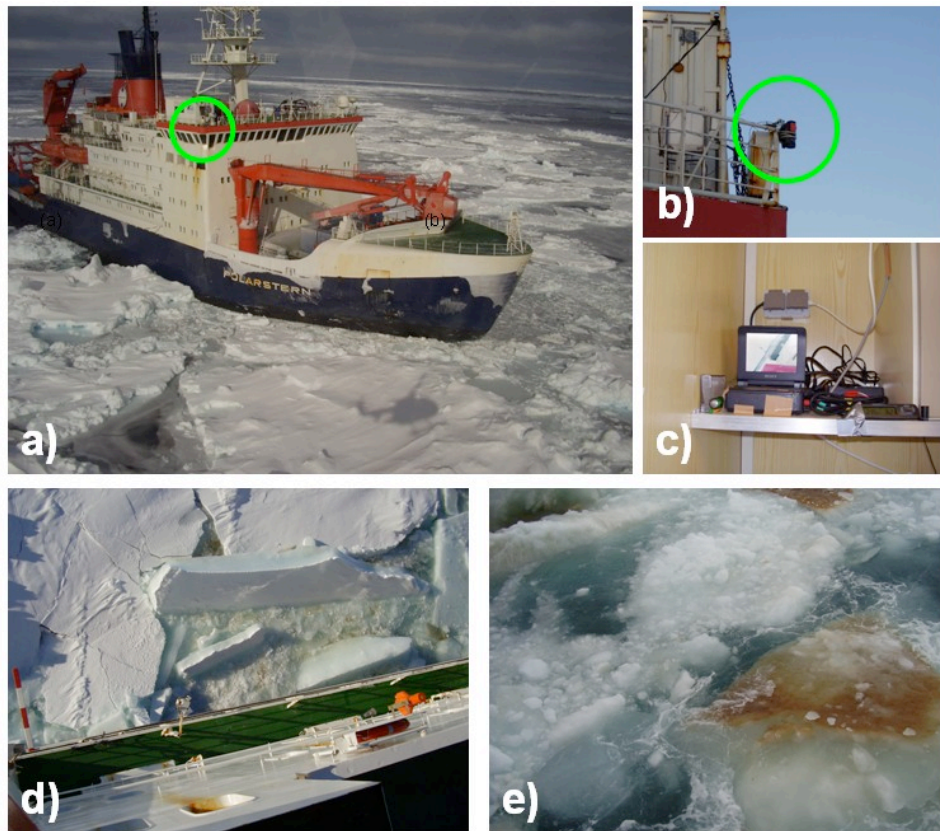


Fig. 4.12 Video monitoring system. (a) Video camera location on Polarstern (b) Video camera (Hi-8). (c) Monitor inside the container. Examples of broken ice floes for (d) ice thickness measurement and (e) observation of ice algae within sea ice

4.2.4 Airborne EM ice thickness measurements

Total ice thickness has been measured by means of helicopter-borne EM thickness sounding with a towed EM ice thickness sensor (EM-Bird). Two instruments were used during ANT-XXIII/7, both 3.5 m long with a diameter of 0.35 m, weighing around 100 kg. The bird was towed 20 m below the helicopter, at an operation altitude of 10 to 15 m above the ice surface with 70 - 80 knots. Geo-referenced digital still photographs were taken to document general ice conditions. Subsequently they were included into an html linked map projection allowing for easy geocoded image browsing. During the flights, seal counts were performed for the German Environmental Agency (Tab. 4.2).

In total, 17 HEM flights with a total length of about 2,040 miles were performed, covering well the different ice types and ice regimes encountered during the cruise (see Maps in Fig. 4.1 and 4.3).

Figure 4.13 shows the thickness distribution obtained from all flights. It is dominated by a strong mode of 1.3 m, with a shoulder at 0.4 m. The fraction of 2.5 % of open water can be seen with an ice thickness of 0 m. Note the large amount of ice thicker than 3 m. The mean thickness of all measurements was 2.11 m.

However, as the EM flights covered so many different ice regimes (Fig. 4.3), the main characteristics of each are hidden in the overall distribution. Therefore, figure 4.14 presents the thickness distributions obtained from each flight individually. It is clear that even this separation is not sufficient, as many flights covered several ice regimes, and thus need further differentiation and merging with other flights. However, figure 4.14 nicely represents the main characteristics of each ice regime:

- Thick first-year and second-year ice in the Orkney and Philip Passages, and first-year ice below thinner than 1 m.
- Very thick ice > 2 m in the Powel Basin, representative of the high backscatter band in the radar imagery, and thin and thick first-year ice with modal thicknesses of 0.9 and 1.5 m.
- Thick first-year ice with modal thicknesses between 1.2 and 1.4 m in the Larsen region, with thinner ice of 0.5 m thickness only close to the Larsen-A polynya. Note that the ice in the Larsen Region was hardly covered by any snow (see Table 4.1 and Section 4.5).

Mean and modal ice thicknesses identified on each flight are summarized in table 4.2. For most flights, several modes of the distribution were obvious. However, some of them were identified subjectively based on knowledge of thickness distributions of shorter sections of each flight, and would not be statistically significant in the distributions shown in figure 4.14. However, many modal thicknesses appear in several flights, identifying ice with the same growth history. This was particularly found with thinner first-year ice (modes of 0.7 to 1.0 m) which appeared on many flights in small fractions.

4. Regional variability of sea ice properties and thickness in the northwestern Weddell Sea obtained by in-situ and satellite measurements

Tab. 4.2: Mean and modal ice thickness, and number of observed seals for every helicopter EM flight

Flight Ids	Latitude (°S)	Longitude (°W)	Number of seals	Mean thickness (m)	Standard deviation (m)	Modal thickness (m)
20060909	-60.62	-41.23	8	1.62	0.91	0.75, 1.6
20060919	-60.69	-50.66	n.o.	1.76	1.59	1.1
20060920	-60.77	-49.11	10	1.36	1.06	0.8
20060922	-60.20	-48.02	8	1.49	1.3	0.7
20060927	-61.28	-48.48	4	1.89	1.08	1, 1.8, 2.3
20060930NE	-62.05	-49.66	28	2.31	1.85	0.3, 1, 2.5
20060930SW	-62.41	-51.44	4	2.31	1.96	0.1, 0.9, 2.7
20061001	-63.12	-51.95	14	2.59	2.11	0.1, 0.9, 2.7
20061002	-63.67	-53.61	48	2.85	2.01	1, 1.5, 2.6
20061003	-64.68	-54.26	30	2.75	1.87	0.1, 0.4, 1, 1.4, 3.2
20061004	-64.59	-56.10	35	2.59	1.79	1, 1.3, 2.4
20061005	-65.04	-57.47	20	2.68	1.97	1.2, 3.2
20061006	-64.89	-58.77	32	1.38	0.88	0.5, 1.2
20061010LA	-64.64	-57.93	15	1.86	1.47	0.1, 1.3
20061010LB	-65.24	-58.34	4	2.17	1.26	1.3
20061011	-64.22	-53.36	184	2.68	1.9	1.5, 3.6
20061018	-60.80	-42.31	11	1.62	1.1	0.7, 1.5

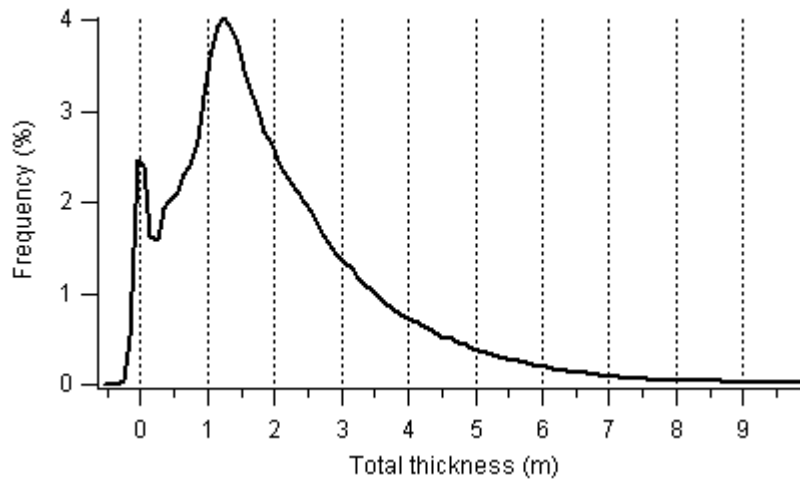
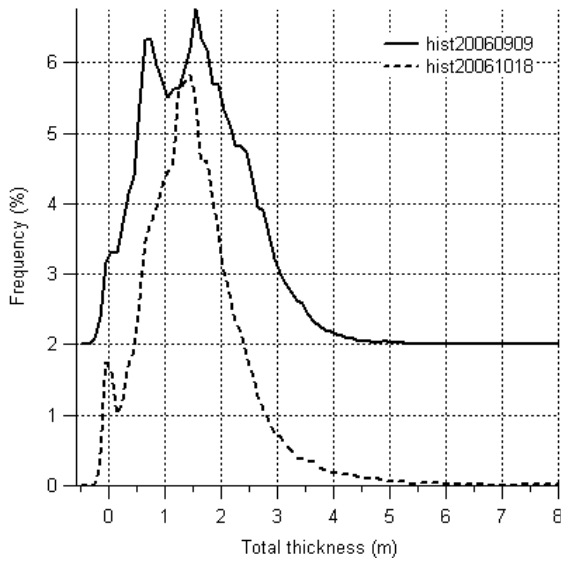
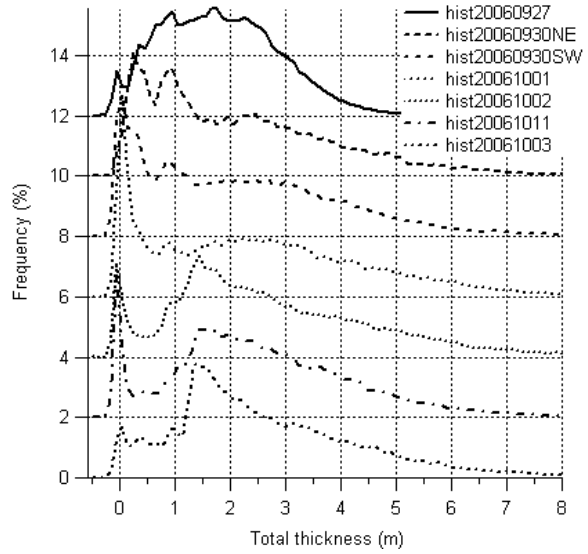


Fig. 4.13: Ice thickness distribution computed from all helicopter EM flights (bin width 0.1 m)

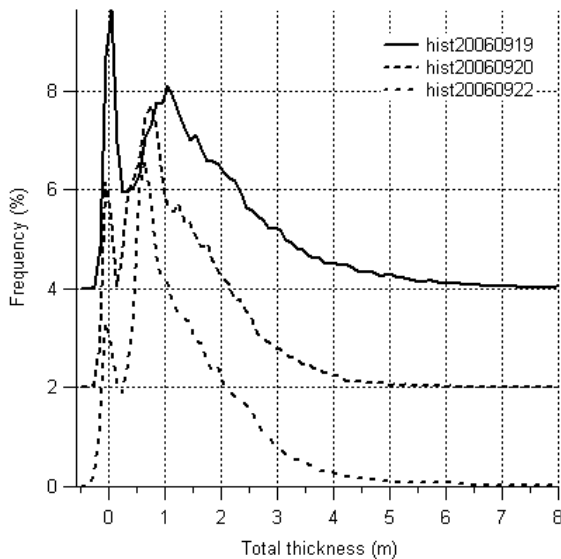
a) Orkney Passage



c) Powel Basin



b) Philip Passage



d) Larsen-A&B

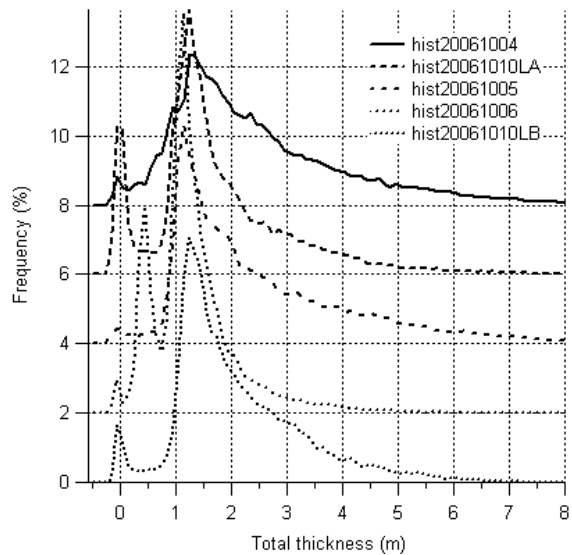


Fig. 4.14: Ice thickness distributions obtained from each helicopter EM flight, separated into different regions with characteristically different ice regimes.

Larsen-A polynya

The recurring Larsen-A polynya is the source of much of the thick first-year ice encountered in the westernmost study region (Fig. 4.15). It is likely that the region has turned into an ice factory since the breakup of the Larsen-A ice shelf, and therefore has fundamental consequences for Weddell Sea ice shelf and bottom water formation. During ANT-XXIII/7, we had the unique opportunity to survey across the polynya region to derive estimates of ice and salt production to be compared with hydrographic measurements. On 6 of October a flight across different zones of the polynya region and onto the shoreward fast ice was performed (Fig. 4.15). The mean

4. Regional variability of sea ice properties and thickness in the northwestern Weddell Sea obtained by in-situ and satellite measurements

and modal ice thickness of approximately 8 km long subsections of the profile along the northern leg is shown in figure 4.16, as well as the resulting thickness distribution of the whole profile in figure 4.17. The fast ice and two distinct regions with modal ice thicknesses of 0.5 and 1.2 m can be seen. These represent different phases of polynya openings, which will be identified later by means of SAR imagery. Interestingly, the 1.2 m thick ice had already attained almost the same modal thickness as ice surveyed much further northeast in the same dark low-backscatter band of sea ice. However, mean ice thicknesses and their standard deviations gradually increase away from the polynya, showing the maturing of the ice cover by deformation and ridge formation.

The satellite images in figure 4.15 also show the locations of ice core retrievals. Note that one core was taken from the high backscatter band on 9 October (Core 061009TEX3). Remarkably, this core was the only core of the whole cruise consisting completely of frazil ice (see Fig. 4.22 ice cores). The frazil was 1 m thick, however, only the uppermost 0.6 m were consolidated, while the lower part was consolidated slush. This is an important observation for the modelling of ice production in polynyas, and will be used together with SAR and weather data to improve the understanding of polynya processes and ice formation.

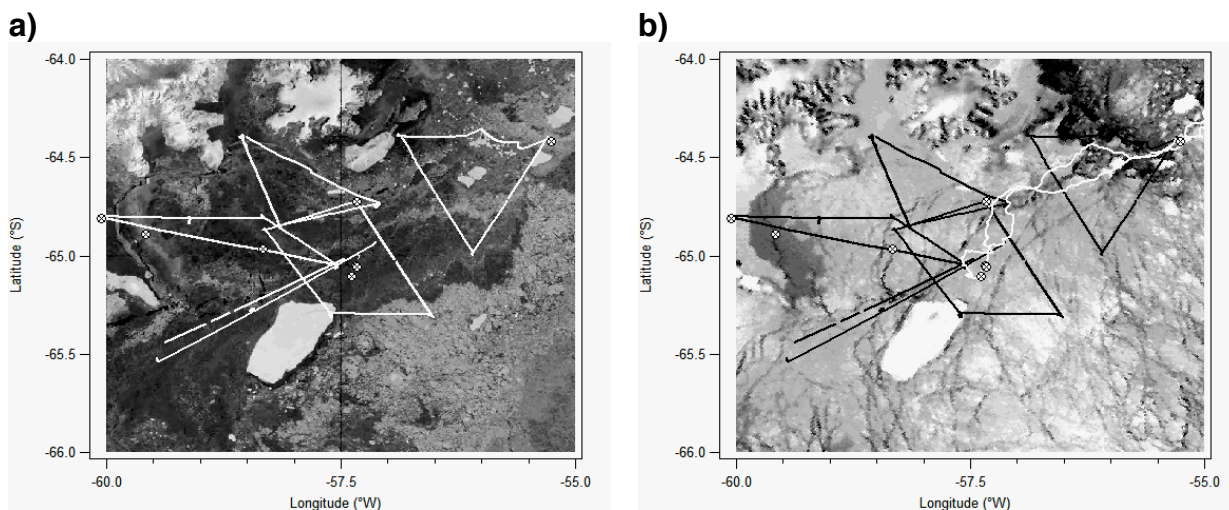


Fig. 4.15: (a) Envisat-SAR (October 05) and (b) NOAA-AVHRR-channel-4 images (October 03) of the Larsen-A region. Straight lines denote helicopter EM ice thickness profiles, and symbols mark locations of ice core retrievals. The track of Polarstern is shown as white line in (b).

4.2 Sea ice distribution

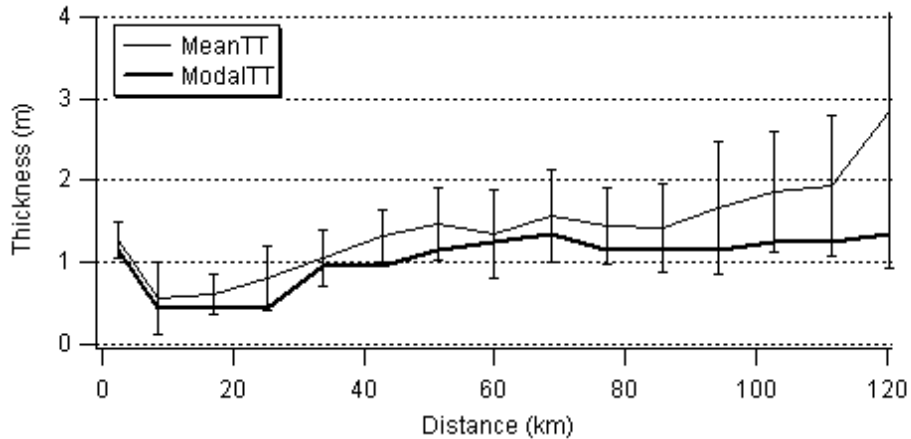


Fig. 4.16: Mean and modal total thickness along the northern leg of the Larsen-A polynya flight on October 6 (cf. Fig. SARAVHRR). Error bars denote standard deviation.

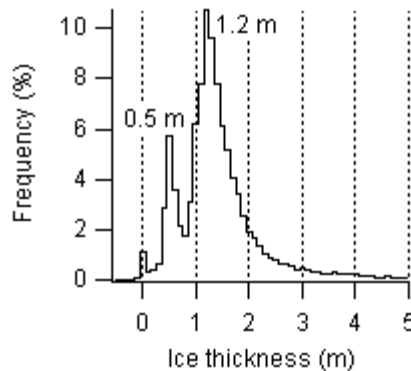


Fig. 4.17: Ice thickness distribution of the northern leg of the Larsen-A flight (cf. Fig.s 4.15 and 4.16)

4.3 Snow thickness distribution

Snow on sea ice plays a key role within the atmosphere-ice-ocean system, since it modifies heat flux from the ocean to the atmosphere, and the sea ice mass balance. Furthermore, all electromagnetic ice thickness measurements (see above) give total (snow + sea ice) thickness only. Hence, snow thickness needs to be measured as well, to compute sea ice thickness from both data sets. Therefore, on ANT-XXIII/7 we have paid particular attention to extensive observations of representative snow thickness distributions.

Snow thickness was measured in three ways:

- 1 and 2) Direct thickness readings were obtained with a metal ruler (snow stick) a) along tape measure profiles with a spacing of 1 m or 2 m, or b) in concert with EM31 ice thickness surveys where snow thickness was measured approximately every 20 m. Tape measure profiles were mostly 200 m long (13 out of 25), with shorter lines when floe size was limited. EM31 profile lengths reached up to several kilometres (see Table 4.1).

4. Regional variability of sea ice properties and thickness in the northwestern Weddell Sea obtained by in-situ and satellite measurements

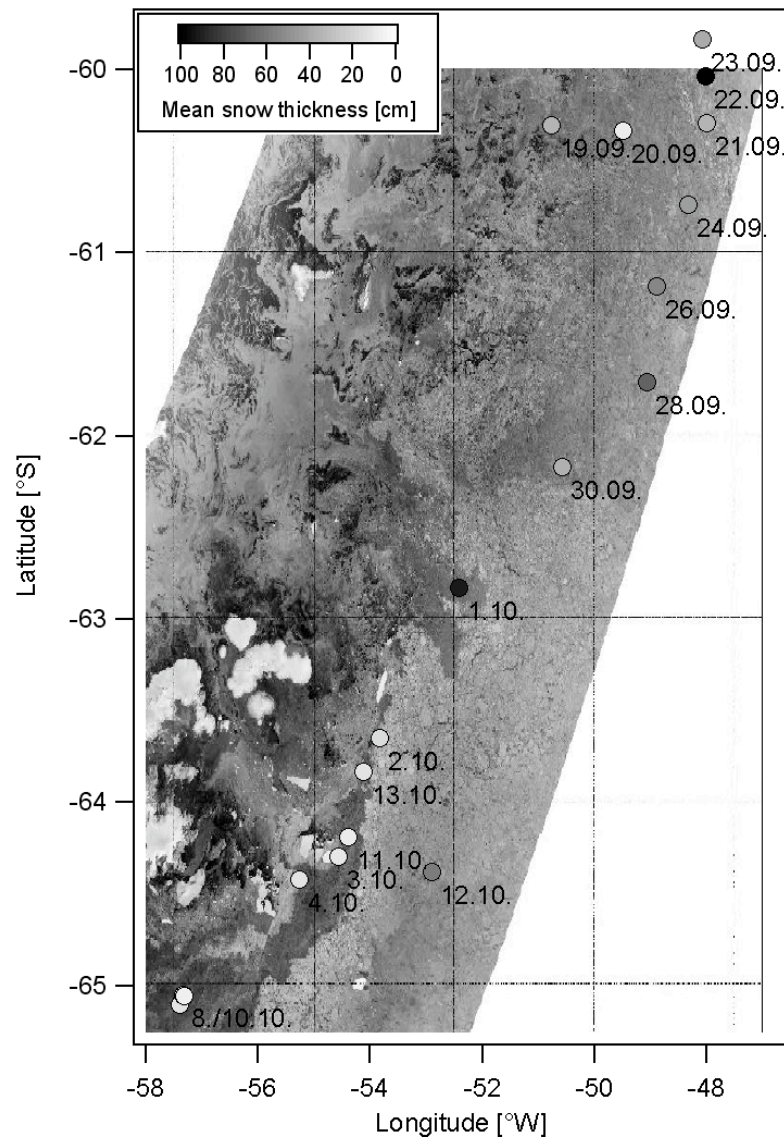


Fig. 4.18: Ice station locations with SAR scene from 19th September in the background. Marker colour coding shows mean snow thickness obtained from direct, snow stick profiles.

- 3) (GSSI SIR-3000 with 400 Mhz antenna) was pulled over ice floes in a pulka (sledge) along the tape measure profiles as well as following or coincident with the EM31 transects. The contrast in dielectric permittivity between snow (~1.5) and sea ice (~2) allows to obtain radar snow thickness profiles with a radar antenna moved along the snow surface. Lateral radar snow thickness sampling is roughly 1 cm, leading to high-resolution snow thickness profiles.

In total a sum of 25 tape measure profiles, 14 EM31 transects and 12 radar surveys have been conducted cumulating to profile lengths of approximately 3.6 km, 17 km and 5 km respectively. Figure 4.18 shows a summary of most ice stations during ANT-XXIII/7 along with dates and mean snow thickness (colour code). The SAR scene in the background was acquired on September 19.

4.3.1 Ruler stick measurements

Figure 4.19 provides an overview on the snow thickness statistics (snow stick, tape measure profiles), mean snow thicknesses of all floes are summarized in table 4.1. As outlined in figure 4.23 for sea ice types, the same three different regions can be distinguished for snow regimes, too: I) moderate thickness of 0.34 m in the MIZ, II) moderately to very thick (mean: 0.53 m), highly variable snow cover on the band of SYI and FYI in the central part of the study area and III) very small snow thickness of 0.09 m (mean of ruler measurements) in the Larsen Polynya area (south-west).

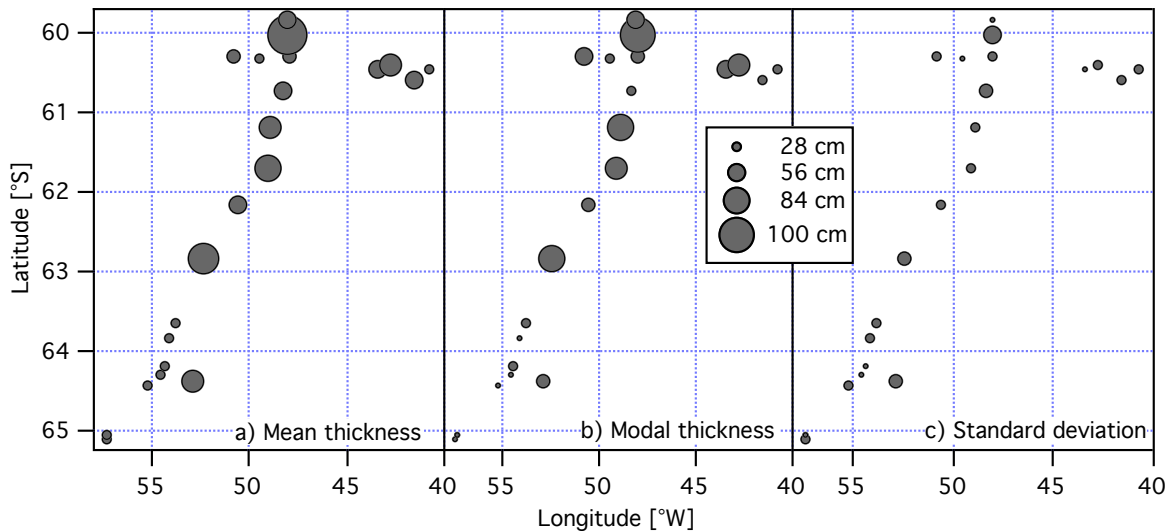


Fig. 4.19: Snow thickness statistics obtained from direct, snow stick measurements. Larsen Polynya stations are not shown for plot scale reasons. The point-size legend is valid for a) to c).

The thick snow on SYI indicates that part of the snow has remained from the last summer. The thin snow cover of less than 0.12 m in the Larsen area is probably due to a) low precipitation b) high evaporation and c) the fact, that the sea ice is comparably young and did not accumulate large snow masses during the observed winter time d) strong winds causing snow drift. These aspects might be discussed including $\delta^{18}\text{O}$ measurements, which were taken from the snow samples (see below).

4.3.2 Ground penetrating radar (GPR) measurements

Snow thickness profiling on sea ice with off-the-shelf geophysical radar devices is a rather innovative approach to snow thickness studies. There is no evidence in literature for any operational application of GPR for snow thickness on sea ice besides our own experiments on ARK-XIX and ARISE 2003. Thus, first results from this cruise set a milestone in the development of radar as a standard geophysical tool in sea ice research.

4. Regional variability of sea ice properties and thickness in the northwestern Weddell Sea obtained by in-situ and satellite measurements

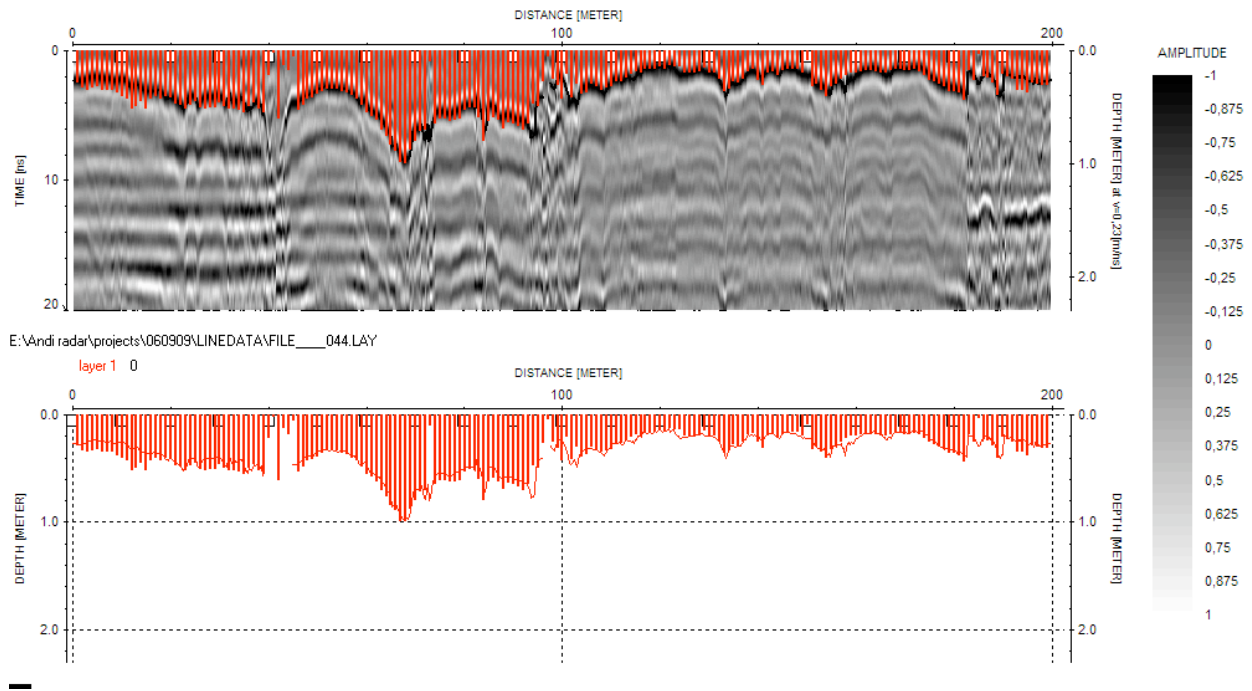


Fig. 4.20: Radar profile from 9 September. Upper panel shows processed radar section along with snow stick results (vertical bars). Picked radar snow thickness along with snow stick thickness is shown in the lower panel.

In eleven out of twelve acquired radar profiles a clear reflector could be identified as the snow/ice interface. The single failure on 22 September was presumably caused by a very rough ice surface scattering the radar pulse in combination with several internal ice layers in the snow pack (see chapter 4.5). Figure 4.20 shows a typical radar result after several processing steps. The main processing challenge is to clean the data from the direct wave, travelling inside the antenna from transmitter (Tx) to receiver (Rx) dipole. As the Rx-Tx distance is 15 cm in the used antenna, the direct wave interferes with the snow/ice reflection, arriving at similar times as the direct wave. Once the direct wave is successfully removed, the radar section shows one dominant reflection along with several multiples (Fig. 4.20). For snow thickness smaller than ~ 15 cm the reflection is not as clear or totally lacking due to the mentioned interference of direct wave and snow/ice reflection. Thus radar snow thickness profiles are biased towards thicker snow, if thin snow layers are present. Figure 4.21 underlines this constraint. On 8 September, 2 and 4 October, a significant part of the snow stick profile contained a very thin snow layer, resulting in a residual between snow stick- and radar- derived mean snow thickness. The shift between mean thicknesses on 30 September arises from not coinciding radar- and snow-stick profiles on that day. The radar profile on this day covers a much larger area (~ 400 m) than the 170 m long tape measure profile.

4.3 Snow thickness distribution

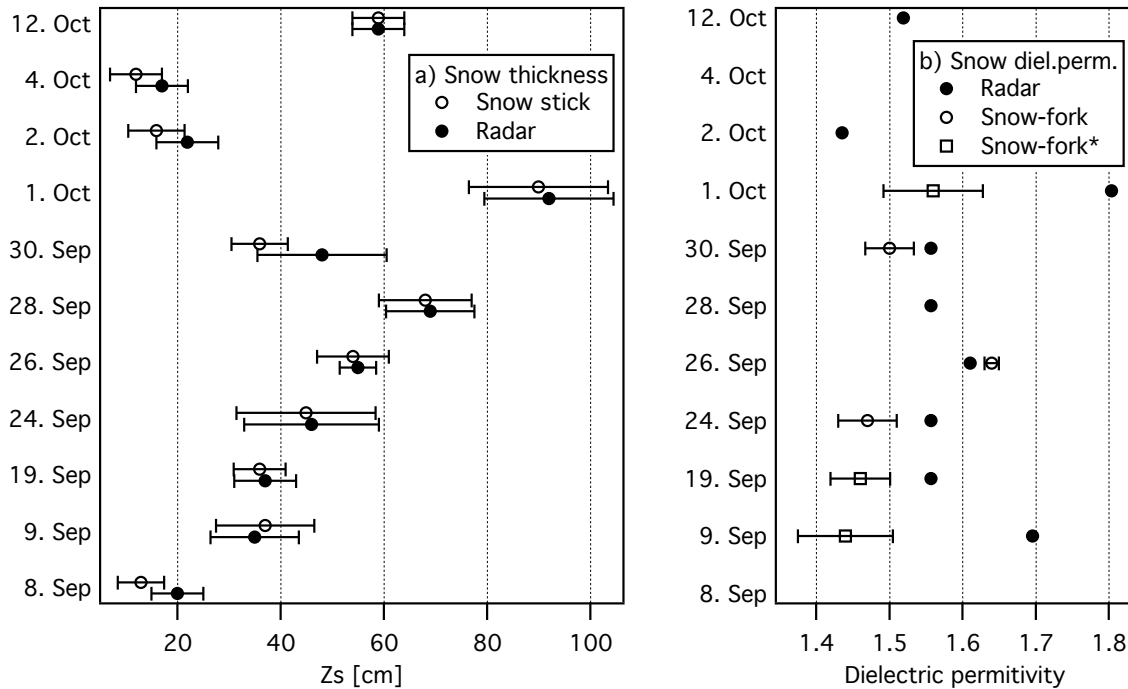


Fig. 4.21: Comparison of a) Radar and snow stick snow thickness statistics as well as b) Radar-velocity-derived dielectric permittivity and permittivity measured with the “Snow fork”. Error bars show the respective standard deviation for lateral snow thickness profiles (a) and vertical snow fork permittivity sections (b). Snow-fork* in b) delineates snow pits on the same floe as the radar sounding, whereas otherwise the radar antenna was placed exactly over the snow pit.

To compute snow thickness from radar wave travel times, the speed of light in snow (radar wave velocity, determined by the dielectric permittivity) must be known. The dielectric permittivity of snow is governed by its density and wetness parameters that are measured by the “snow-fork” discussed in chapter 4.5. Thus one method to derive the permittivity of the snow pack is to run an average over the 5 to 10 cm snow-pit sections described in chapter 4.5. Resulting snow-fork permittivities are shown in figure 4.21b. Additionally, radar soundings over known snow thickness (e.g. over the snow pit) allow determining the radar velocity and thus the dielectric permittivity of the underlying snow. Figure 4.21b provides a comparison of permittivities, either from coinciding radar measurements and snow pits (24.9., 26.9. & 30.9.) or days when snow pit and radar calibration site were in proximity (Snow-fork*). The variability within the snow pack (standard deviations in Fig. 4.21b) has a similar magnitude as the deviations between radar and snow-fork permittivity. Generally dielectric permittivities of snow on sea ice are consistent around 1.55 ± 0.1 . The resulting radar velocities vary from 23 to 25 cm/ns, corresponding to a precision of ± 3 cm for 80 cm thick snow. This means that also without a prior knowledge of the floe’s snow properties, GPR is able to retrieve accurate snow thickness estimates, assuming a wave speed of ~ 24 cm/ns.

4.4 Ice types and properties derived from ice coring

During ANT-XXIII/7, 22 ship- and 6 helicopter-ice stations were performed. For the ship stations the floe was accessed over a port-side gangway. These stations included a common sea ice drilling site, on which among others a TEX-core was drilled to analyse texture and measure salinity, temperature, density and $\delta^{18}\text{O}$. Additionally, 6 helicopter stations were performed in a range of 5 to 60 miles from the ship. Duration of the ice-physics field work at the ice station was between one and four hours.

Sea ice temperature was measured immediately after coring by drilling sideways into the core and inserting a hand held Pt1000 thermometer. Vertical resolution was 10 cm except at the top and bottom of the core (5 cm). After these measurements the core was brought into a freezing lab (-15 °C) on board to prepare thick sections (~0.5 cm thick) for texture analyses. From 48 samples of major interest thin sections were created and photographed under plain light and crossed polarisors. After texture analyses the core was cut and melted for salinity, density, and $\delta^{18}\text{O}$ measurements, according to stratigraphic units into samples of 2 to 10 cm thickness.

To adjust the results to water level, ice thickness, freeboard and snow thickness of each borehole were measured. Beside these TEX-cores also an archive core (ARC) was drilled and immediately stored at -30°C.

4.4.1 Bulk ice properties

In total 27 ice cores and 3 additional surface cores, snow plus the uppermost 50 cm of sea ice, were drilled and analyzed. Mean salinity and age (FYI or SYI) are presented in table 4.1.

As shown in table 4.3, columnar ice was predominant over all ice cores along the cruise track. Only 28.7 % of the ice was granular ice, and those sections were mainly found in the top parts of cores. Furthermore, 14.4 % of the ice was mixed and some platelet ice (1.0 %) was found in the core from 19 September.

On two of the four SYI floes layers of superimposed ice were found underneath thick and cold snow (Fig. 4.3). These layers indicate the former summer sea ice surface, where this fresh water ice has formed due to snow melt and high snow wetness. Additionally 2 cm of superimposed ice were found on top of an ice core from the marginal ice zone (17 October). Here, the passage of low pressure systems transports warm and moist air into the marginal sea ice zone and causes snow melt even during September and October (see Fig. 4.5 and Section 4.5). Furthermore, one *Föhn*-event was observed during the cruise. Both might have contributed to superimposed ice formation, or at least ice layer formation within the snow, which might later during the year contribute to superimposed ice.

4.4 Ice types and properties derived from ice coring

Tab. 4.3: Fraction of different sea ice textures of all ice cores, derived from thick-section analyses

Columnar:	55.2 %
Granular:	28.7 %
Mixed:	14.4 %
Platelet:	1.0 %
Polygonal:	0.7 %

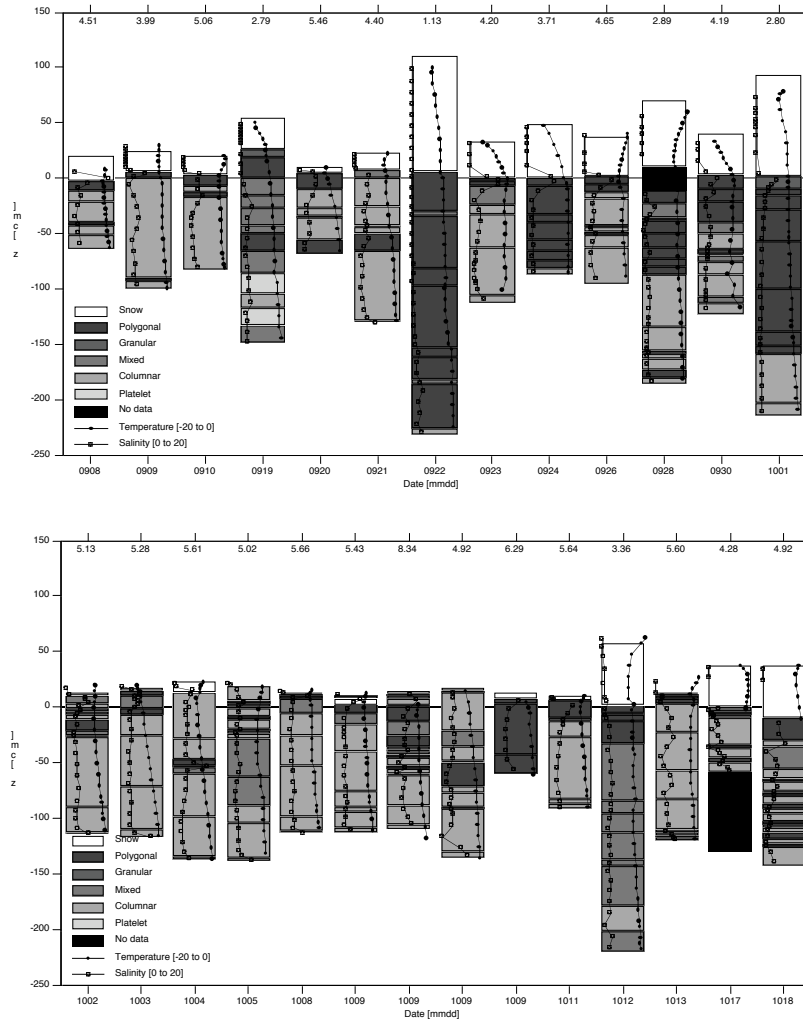


Fig. 4.22: Sea ice texture, temperature and salinity of all (TEX) ice cores. Temperature and salinity are scaled within each single core texture, such that: Temperature ranges from -20 °C (left) to 0 °C (right) and salinity from 0 (left) to 20 (right). Horizontal lines indicate stratigraphic units as texture changes or interfaces as they result from distinct growth stages or rafting. Additionally, snow thickness, temperature and salinity are shown. Deviations of snow thickness and snow property measurement positions result from local variations, since the snow pit was measured close by, but not at, the drilling site. z=0 refers to water level to compare ice cores with respect to freeboard. Numbers on top give mean salinity of the entire core. The four ice cores from 9 October were taken (from left to right) at the ship and at L1, L2, L3 (see map in Fig. 4.1).

4. Regional variability of sea ice properties and thickness in the northwestern Weddell Sea obtained by in-situ and satellite measurements

As may be seen from figure 4.22, SYI floes might be identified by a mean salinity of <3 , while all FYI cores had salinities above 3 and ranging up to 8.34 close to the Larsen-A polynya on October 09. Ice core temperatures were mainly linear profiles from salt water freezing point ($-1.8\text{ }^{\circ}\text{C}$) to sea ice surface temperatures between $-2.3\text{ }^{\circ}\text{C}$ and $-10.9\text{ }^{\circ}\text{C}$ with a mean of $-5.9\text{ }^{\circ}\text{C}$.

The ice stations might be classified into three groups from ice texture, as shown in figure 4.23:

I) Marginal sea ice zone: difference between early September and mid October are formation of superimposed ice which is probably due to the passage of low pressure systems, which transport warm and moist air into the marginal sea ice zone. Sea ice is predominantly composed of columnar sea ice with snow cover between 0.13 and 0.56 cm.

II) Deformed FYI and SYI (all SYI) with generally thick snow and high proportions of granular ice, superimposed ice is found.

III) FYI from Larsen polynyas comparably homogenous ice.

Only 2 coring sites (0908, 1018) had negative freeboard (7 %), both in the marginal ice zone. In contrast, 27 % of all thickness drill-holes had negative freeboard.

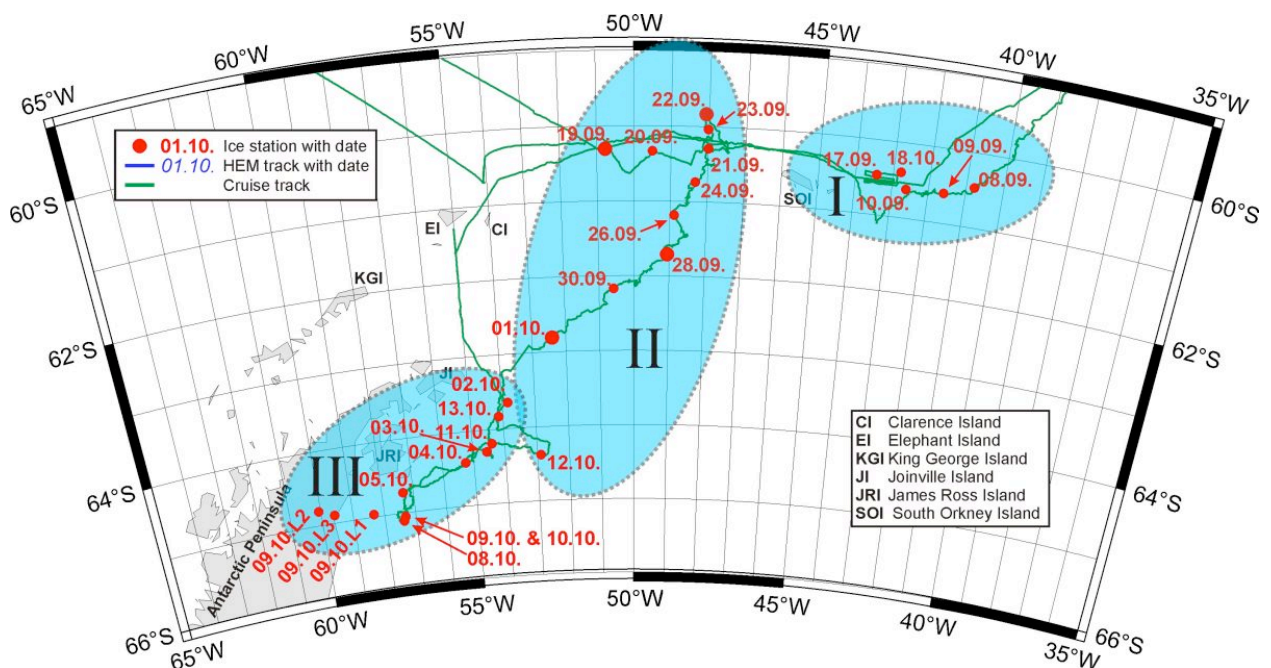


Fig. 4.23: Classification of the ice stations based on sea ice texture and snow properties: I) Marginal ice zone of FYI, II) SYI and deformed FYI with thick snow cover and III) sea ice from Larsen-A and B polynyas

Polynya ice formation

Intensive studies of sea ice properties, thickness and evolution were performed at the Larsen-A polynya. The ice texture in this region was dominated by columnar sea ice, which is quite different from the expected granular / frazil ice of polynya origin. This shows, that after initial ice formation in the polynya thermodynamic ice growth is dominating sea ice formation.

Nevertheless one ice core (1009L3) was composed of granular ice only and had a 50 cm thick unconsolidated frazil ice mass underneath and a very high mean salinity of 6.29. The unconsolidated part could not be sampled for texture, temperature or other analyses, but temperature has to be assumed to be at the freezing point (-1.8 °C).

4.4.2 Thin section analyses

The thin section analyses in ANT-XXIII/7 have three purposes. First we look for the evidences of snow contribution on sea ice thickness, second we look for the ice growth rate variations in ice thermal growth process, third we look for ice thickness increasing from dynamic processes.

In each ice station, one ice core was taken for ice texture analyses. While the ice core was moved into the cold container in *Polarstern*, thick section was cut first and ice stratigraphy descriptions were finished under polarized light. Based on these stratigraphy descriptions, the ice core was cut into ice blocks for their salinity and density measurements. Also, the thin sections were decided to cut for the three purposes mentioned above. Therefore, piece(s) about 10 cm in length were cut from the thick section fragments. These pieces covered the parts interested in an ice core or whole ice core. Then each piece of the cut thick section was frozen on a glass of 12 cm × 12 cm by cold fresh water. Later the piece of thick section with the glass was frozen on microtome and was cut it into thin sections with less than 1 mm in thickness. The thin section was observed in the cold container and taken photos under plain light and polarized light. Totally, 48 thin sections from 15 ice cores were cut and 46 thin sections were successful (see Table 4.4).

Tab. 4.4: Statistics of thin sections distribution

Ice core	Thin section	Position (cm)
060910 Tex	9 vertical	0-10, 10-20, 20-30, 30-35, 35-45, 45-55, 55-65, 65-75, 75-85
060919 Tex	4 vertical	0-10, 42-52, 113-123, 143-153
060919 Surf	1 vertical	0-10
060924 Tex	1 vertical	50-60
061001 Tex	3 vertical	0-10, 10-18, 190-200
061001 Surf	1 vertical	0-10
061002 Tex	1 vertical	0-10

4. Regional variability of sea ice properties and thickness in the northwestern Weddell Sea obtained by in-situ and satellite measurements

Ice core	Thin section	Position (cm)
061003 Tex	2 vertical	0-10, 10-20
061005 Tex	16 vertical	0-10, 10-20, 22-30, 30-42, 42-52, 52-62, 62-72, 72-82, 82-92, 92-104, 104-113, 113-122, 122-131, 131-140, 140-149, 149-157
061009 Tex	1 vertical	0-10
061013 Tex	1 vertical	122-132
061017 Tex	1 vertical	0-10
061018 Tex	1 vertical	0-10
061018 Sample1	1 vertical 2 horizontal	0-10 (vertical), 0-2, 2-4 (horizontal)
061019 Surf	1 vertical	10-20

From these thin sections, there is not any new finding. But the ice growth rate, ice rafting and snow contribution on ice thickness can be confirmed by these thin sections. As examples, figure 4.24 shows superimposed ice crystals. Figure 4.25 and figure 4.26 give the stratigraphy descriptions and thin section photos of the ice cores of 060905 Tex and 060905 Tex respectively.

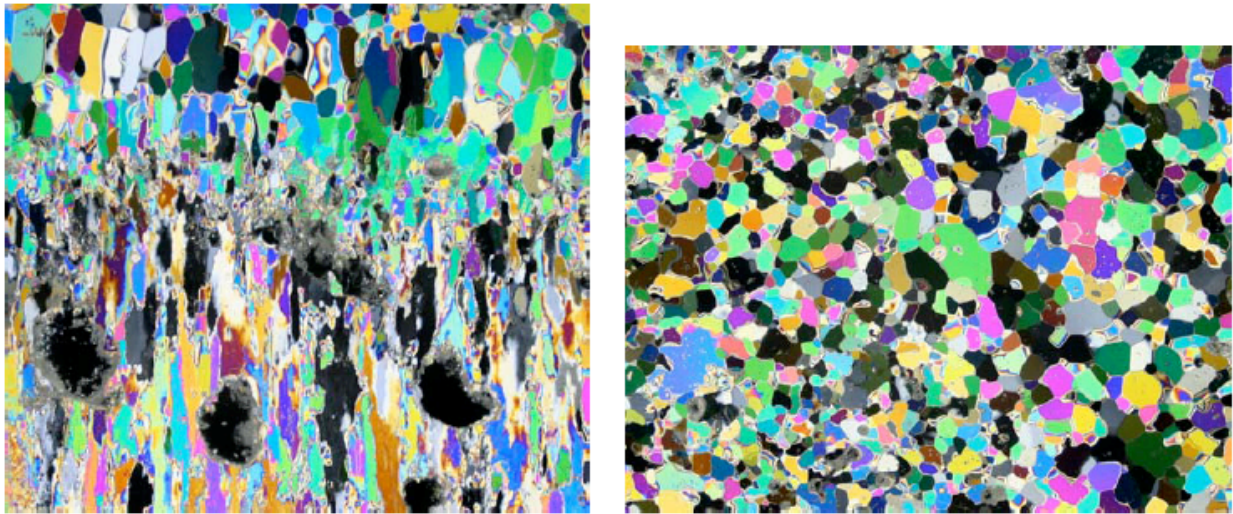


Fig. 4.24: Typical texture of superimposed ice samples

4.4 Ice types and properties derived from ice coring

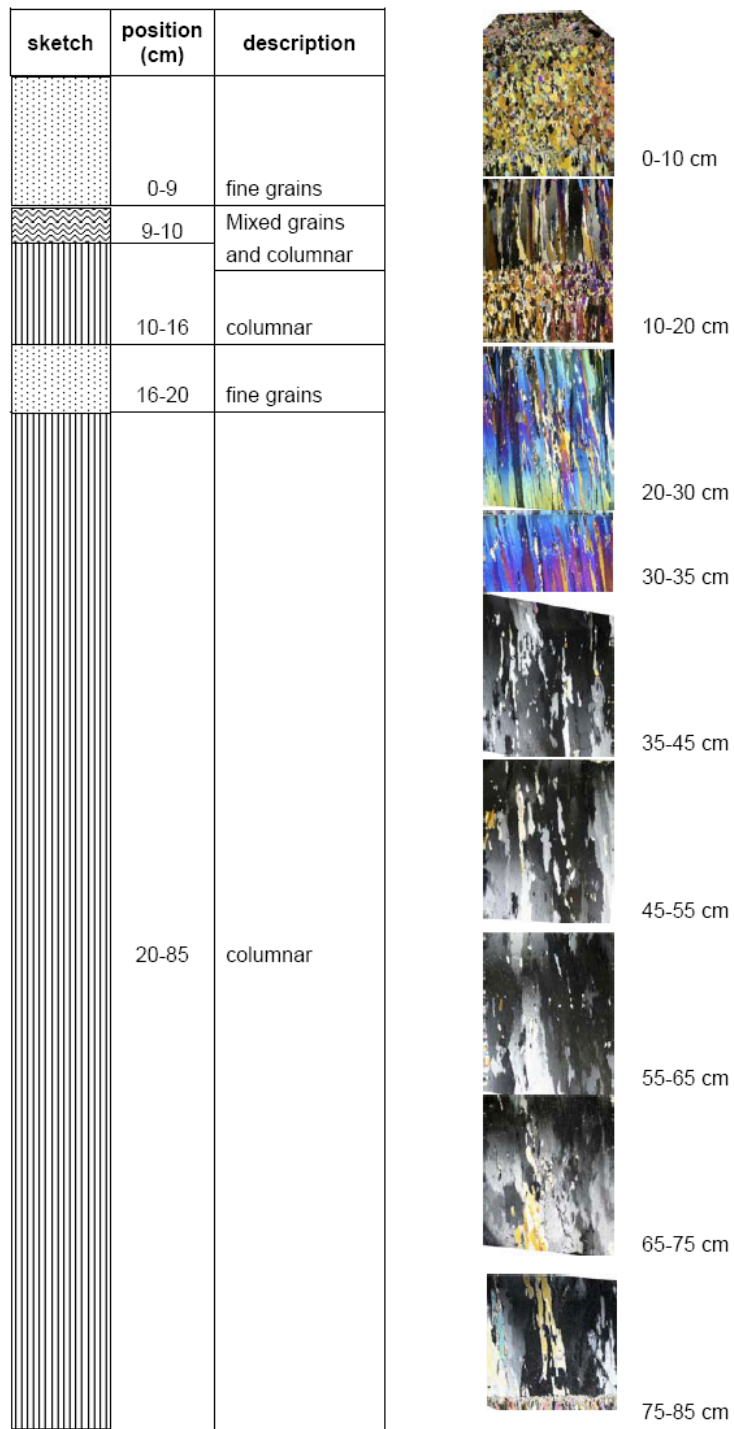


Fig. 4.25: Stratigraphy of ice core 060910 Tex

4. Regional variability of sea ice properties and thickness in the northwestern Weddell Sea obtained by in-situ and satellite measurements

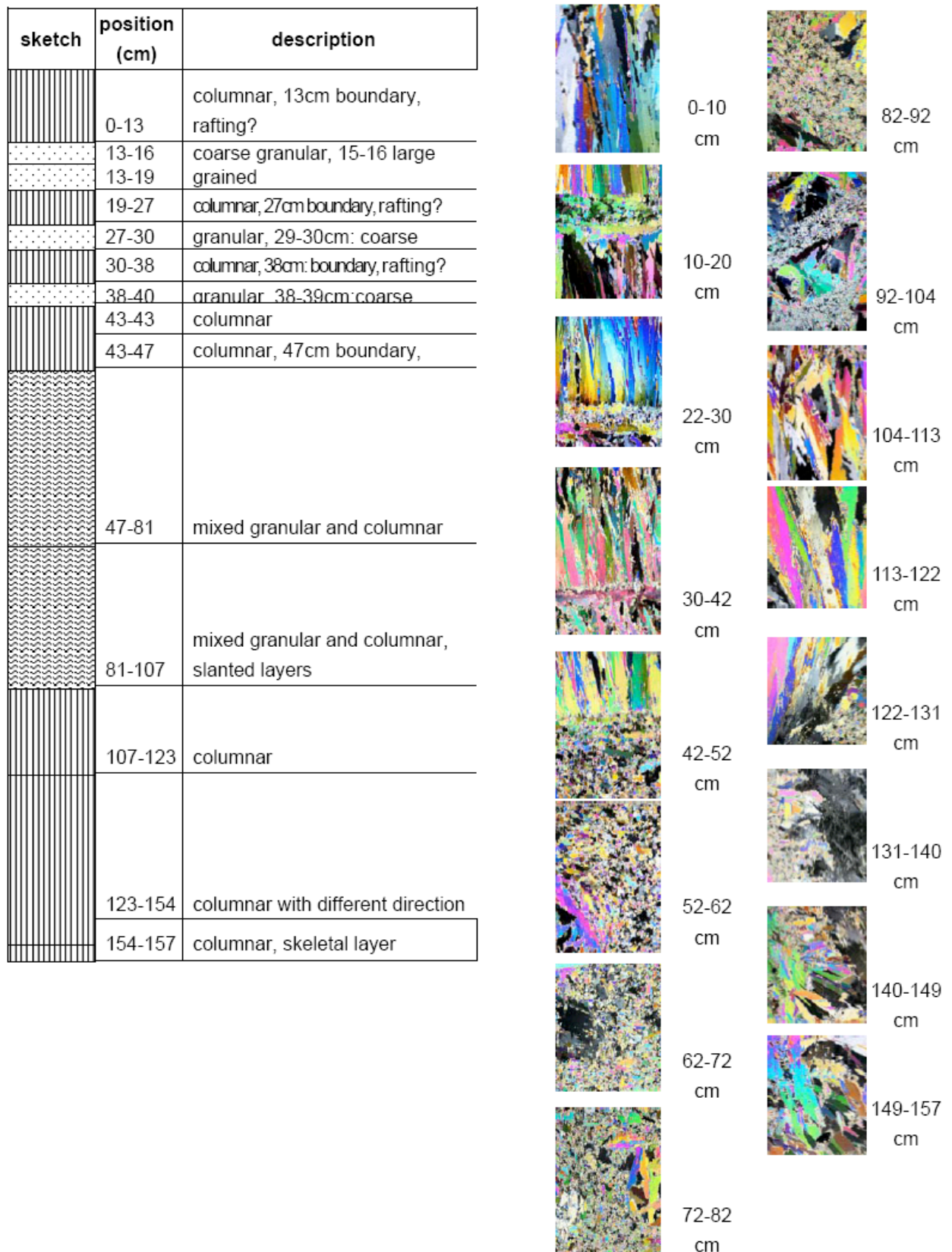


Fig. 4.26: Stratigraphy of ice core 061005 Tex

4.5 Snow properties

The snow cover on Antarctic sea ice undergoes significant and irreversible metamorphism and mass loss due to melt and evaporation during summer. But in most regions of the Weddell Sea, at least part of the snow cover survives the melting season and might be studied as part of the actual snow pack also during the following winter. During ANT-XXIII/7, we have focused in particular on the properties of metamorphous snow, internal ice layers and superimposed ice. Our findings can be related to results of spring and summer observations, as they were made during ISPOL.

Physical snow properties were measured on 23 ice station floes close (<5 m) to the ice coring site in snow pits. Vertical profiles of snow temperature, wetness, density and $\delta^{18}\text{O}$ were measured in snow pits from the snow to the sea ice surface in intervals of 0.03 to 0.10 m, depending on total snow thickness and stratigraphy. Snow temperature was determined with a hand-held Pt1000 thermometer. Snow wetness and density were measured with the TOKKIA Snow Fork, a dielectric resonator. Density measurements were additionally performed by weighting a defined volume (0.1 to 0.5 l) of snow. These density samples were also melted for salinity measurements as well as sealed and shipped for $\delta^{18}\text{O}$ analyses. Snow stratigraphy was obtained from every snow pit, except one during night hours.

The snow during ANT-XXIII/7 mainly consisted of granular snow and depth hoar. Very often, both types co-existed in the same stratigraphic unit. Therefore, the classification in figure 4.27 only considers the dominant snow type. Overall they were found in nearly all snow pits, which is especially remarkable regarding depth hoar, which is a typical snow type for transition seasons, when vertical temperature and moisture gradients in the snow are most pronounced.

Only 1.4 % of the snow were composed of new snow layers (4.5), which is consistent with very low precipitation during the cruise and generally thin snow in the observation area. Furthermore it is remarkable, that only 2.3 % of the snow were slush, which correlates to mainly positive freeboard on the station floes (Fig 4.22).

Tab. 4.5: Fraction of different snow types on the station floes, derived from snow pit stratigraphy

ice layers	7.2 %
slush	2.3 %
depth hoar	24.5 %
granular snow	32.9 %
compact snow	31.7 %
new snow	1.4 %

Snow temperatures and salinities are shown in figure 4.22. These temperatures represent a gradient from sea ice surface temperatures to air temperature, which was usually strongly negative. Anyhow, a drastic change in snow temperatures could be

4. Regional variability of sea ice properties and thickness in the northwestern Weddell Sea obtained by in-situ and satellite measurements

observed between September 24 and 26, when strongly negative temperature gradients and snow surface temperatures below -10°C turned into positive gradients and melting point temperatures only two days and a few miles further south (26 and 28). This change is induced by the above described warm and moist air advection from a passing low pressure system. The subsequent cooling of the snow (30 September) caused refreezing of liquid water contents. A second remarkable event of warm snow occurred at the end of the observation period from 9 October onwards and was most expressed in the marginal sea ice zone, where even formation of superimposed ice was detected.

Snow salinity was generally low except just above the snow-ice interface, where snow is subject to infiltration of seawater and brine. Extensive flooding was only observed on two stations.

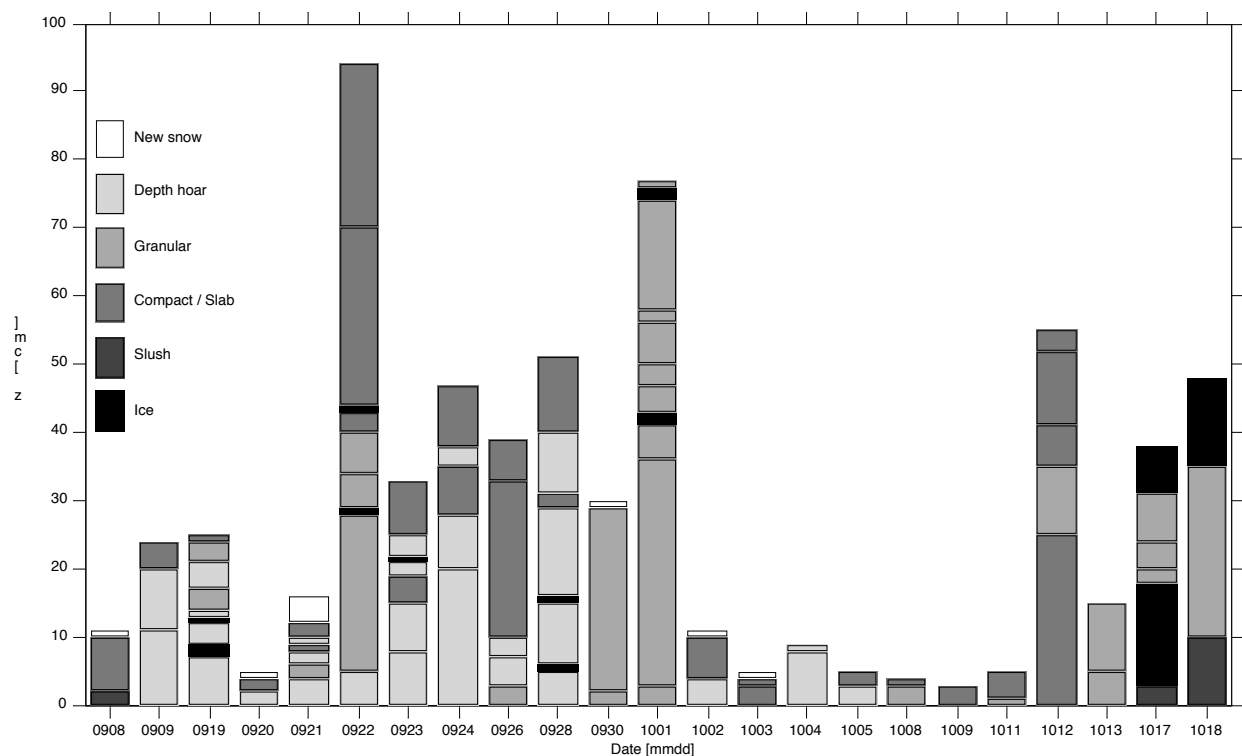


Fig. 4.27: Stratigraphy of all snow pits

In general, snow properties confirm the different regions of sea ice classes (Fig. 4.23).

All SYI (19.09., 22.09., 28.09., 01.10.) snow covers contained ice layers, which were formed through metamorphism and snow melt during the last summer (Fig 4.27). All other floes, on which ice layers were part of the snow cover were sampled at the northern most ice edge (23.09., 17.10. and 18.10.). Here passing low pressure systems caused melt-freeze cycles with enhanced metamorphism and even melt events. Especially on October 17 thick ice layers with thickness up to 15 cm. These layers will later during spring and summer contribute to superimposed ice formation on top the sea ice.

4.6 Floe size distribution

Snow density and wetness data do not show any significant trend (Fig. 4.28). Mean densities were 317 kg m^{-3} (weighted samples) and 251 kg m^{-3} (Snowfork), but these values are difficult to compare, since they do not comprise the same amount of stations. But even considering the same floes, density values of snow samples are 70 kg m^{-3} higher than those of the snow fork.

Snow wetness was generally low ($< 4 \text{ \%}_{\text{liquid water}}$), but the scatter within each profile is high. These data need to be verified and analysed later on and will be discussed, including meteorological conditions and observations.

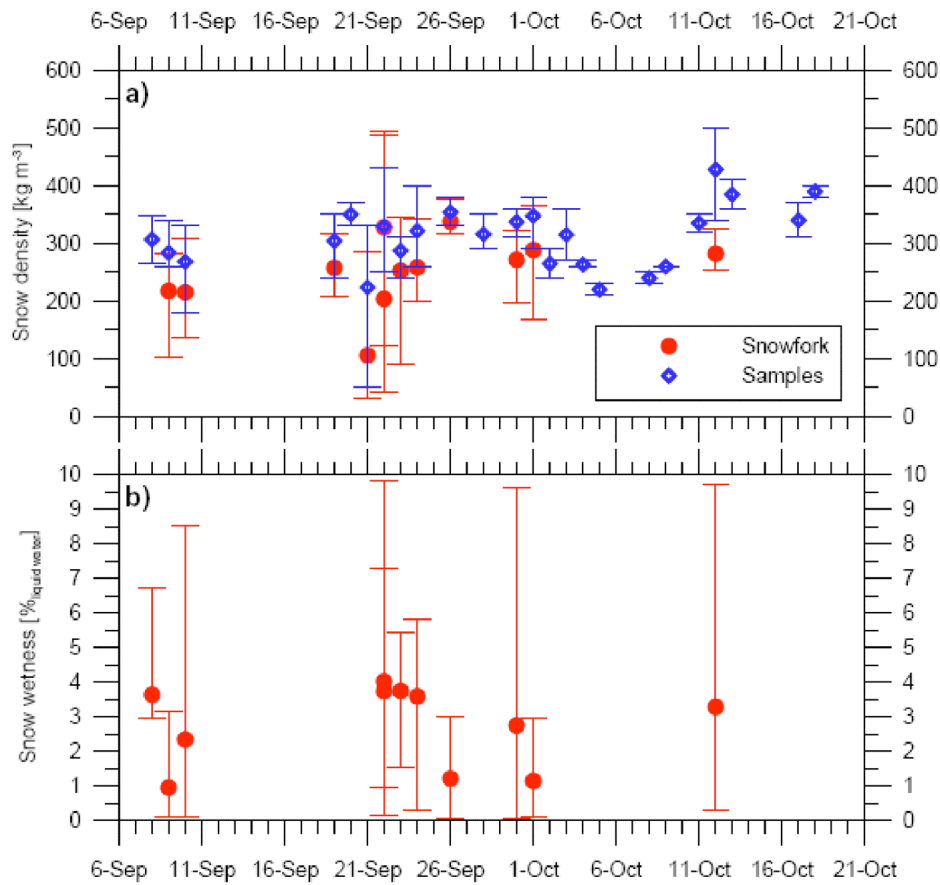


Fig. 4.28: (a) Snow density and (b) snow wetness of all snow pits. Symbols indicate mean values of vertical snow profiles, consisting of 1 to 18 measurements, depending on snow thickness. Error bars give minimum and maximum values of the according profiles, not standard deviation. Snowfork measurements were only performed for snow thicknesses $> 0.10 \text{ m}$.

4.6 Floe size distribution

In the seasonal sea ice zone, various types of ice floes are present, and their sizes range from about one meter to kilometres. Commonly, the present numerical sea ice models treat two variables, ice concentration and thickness, to represent these ice

states. In addition to these variables, ice floe size distribution can also be an important parameter because in the melting season lateral melting is essential to the reduction of sea ice area and the total perimeter of ice floes depends much on ice floe size. According to Steele [1992], the dependence on floe size becomes particularly significant for floe sizes smaller than about 30 m. Therefore, it is important to clarify the floe size distribution for small ice floes. However, the analysis of ice floe size distribution has been limited mainly to floe sizes larger than about 100 m so far, and little is known for small ice floes. Toyota et al. [2006] showed from the analysis of the Okhotsk sea ice that the regime of floe size distribution changes for ice floe sizes smaller than about 40 m, probably due to ocean-ice interaction. The purpose of this observation is to extend their analysis to the Antarctic Seas.

On 19 September (a test flight was performed on September 9), October 17 and 18, the observation was conducted with a helicopter in the marginal ice zone, where relatively small ice floes were dominant (Fig. 4.29 and 4.31). We mounted a downward-looking video camera at the step of the helicopter (Fig. 4.30), and recorded the ice conditions right below the helicopter at two altitudes: the lower altitude is for smaller ice, while the higher one is for larger ice. The position and flight altitude were recorded with GPS every 10 sec. The flight courses were selected nearly from ice edge to inner area. The horizontal distances are about 40 km during each flight. To determine the scale of floes, the ship was included into the video images at each altitude. The observation was almost successfully done except for the test flight on September 9. The tracks and altitudes of the helicopter are shown in figure 4.31 and table 4.6, respectively. The representative ice conditions are shown in figure 4.32.

Tab. 4.6: Flight altitudes of video flights. Parenthesized values are the width of the images

Flight date	Low [m]	High [m]	Middle [m]
Sep. 19	120 (75)	500 (320)	-
Oct. 17	100 (63)	800 (510)	160 (100)
Oct. 18	180 (115)	1150 (700)	-

In analysis, we will focus on the self-similar properties of ice floes, following the past researches. The procedure will be as follows: firstly, to provide for efficient floe analysis, consecutive video images taken every 1/30 second will be integrated into a composite picture by merging the images at the best fitted point. Then each ice floe will be extracted by means of image processing, and its area and perimeter will be measured. The self-similar properties will be tested by checking that the cumulative number distribution $N(d)$, the number of floes with diameters no smaller than d , follows the power law. The result will be compared with that of the Okhotsk ice and the hypothesis of two regimes by Toyota et al.[2006] will be examined. This analysis

4.6 Floe size distribution

is expected to contribute to the understanding of the growth and decay processes of ice floes.

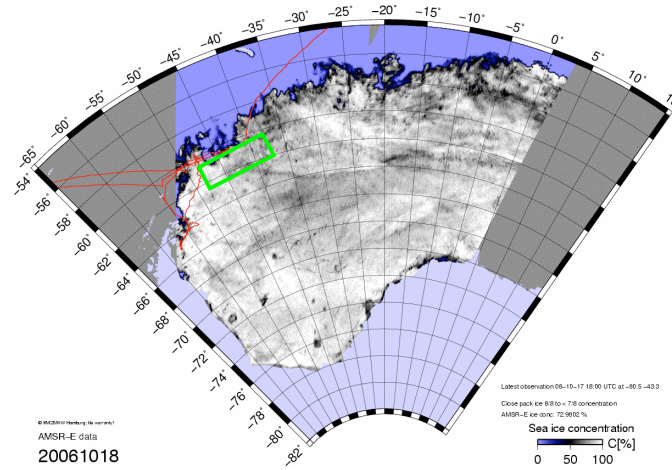


Fig. 4.29: Observation area (green lines) with sea ice chart, as of October 18 in 2006

Fig. 4.30: Mounting a video camera on the helicopter



4. Regional variability of sea ice properties and thickness in the northwestern Weddell Sea obtained by in-situ and satellite measurements

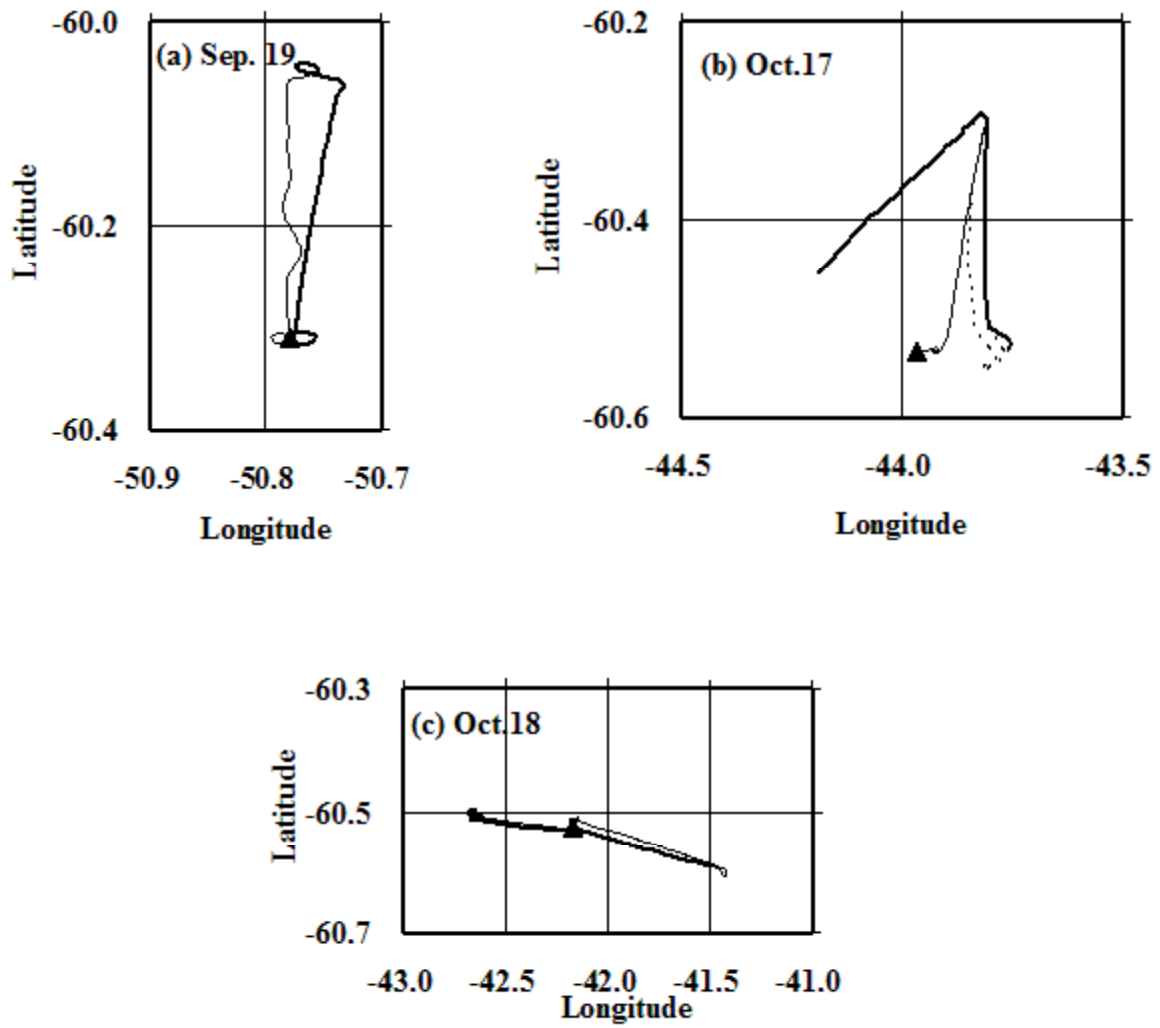


Fig. 4.31 Helicopter tracks for each case thick, thin, and broken lines are for high, low, and middle altitudes, respectively. The altitudes are shown in table 4.6.

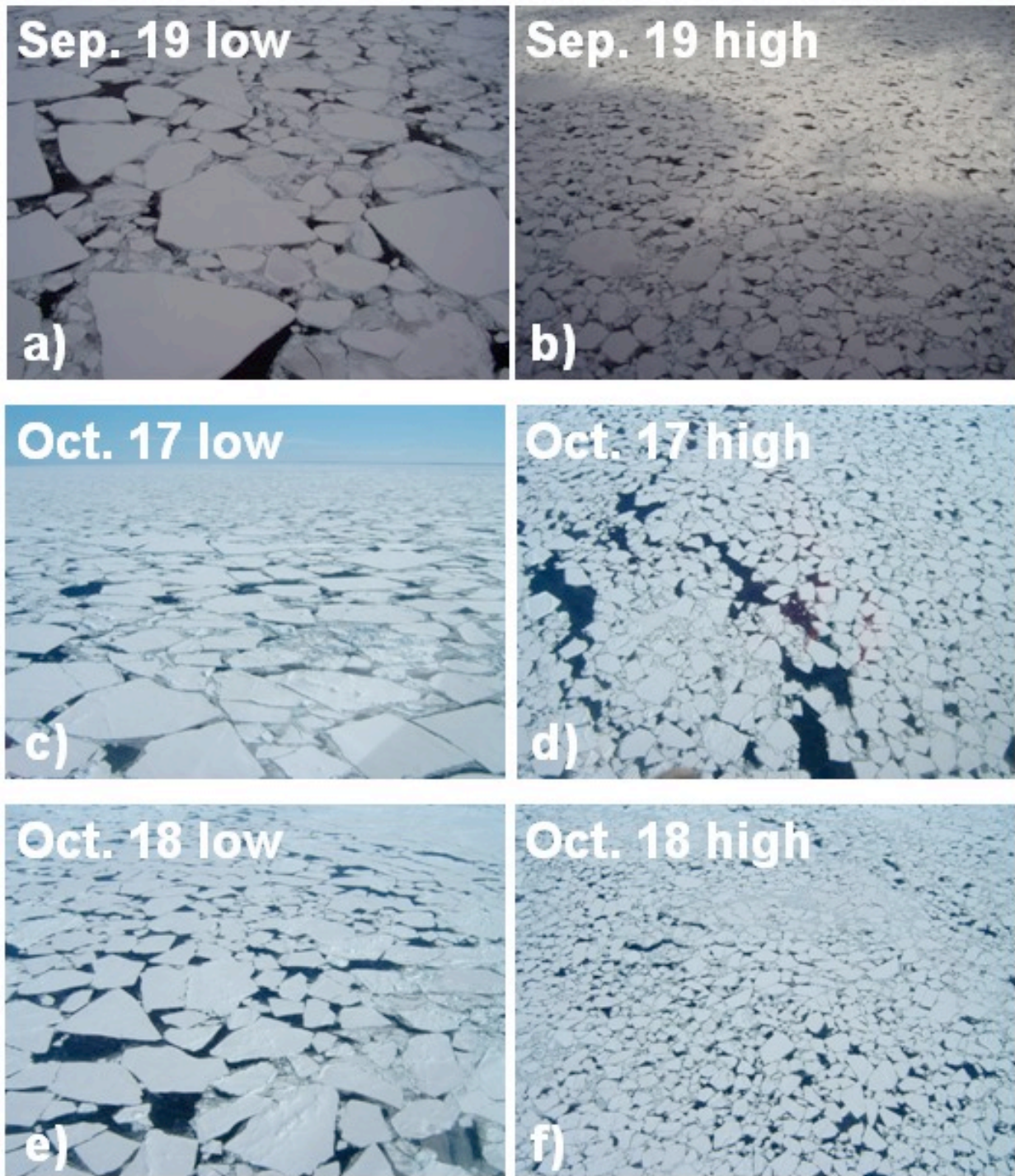


Fig. 4.32: Photographs of ice floe distribution taken from the helicopter at the low (left) and high (right) levels

Reference

- Steele, M. (1992), Sea ice melting and floe geometry in a simple ice-ocean model, *J.Geophys.Res.*, 97(C11), 17729-17738.
- Toyota, T., S. Takatsuji, and M. Nakayama (2006), Characteristics of sea ice floe size distribution in the seasonal ice zone, *Geophys.Res.Lett.*, 33, L02616, doi:10.1029/2005GL024556.

5. WEDDELL SEA AIR-ICE CHEMISTRY INTERACTION STUDY

Hans-Werner Jacobi¹⁾, Katrine Aspmo²⁾, Henning Kirk³⁾

¹⁾Alfred-Wegener-Institut

²⁾GKSS-Forschungszentrum Geesthacht

³⁾Institut für Umweltphysik, Bremen

Objectives

The occurrence of episodes during which the concentrations of atmospheric ozone (O_3) and mercury in the atmospheric boundary layer decrease to very low or even negligible values is now a well-known and -observed feature of the springtime troposphere in both polar regions. Moreover, satellite measurements show simultaneous episodes of high amounts of bromine oxide (BrO) over large areas of the sea ice-covered oceans, which are often as twice as high as the stratospheric BrO background. As BrO is a highly reactive radical, it plays a major role in the local atmospheric chemistry during these ozone and atmospheric mercury depletion events (ODE and AMDE). The strong correlation between an exponential increase of the BrO concentration and the loss of O_3 and mercury can be described by a photochemical model, including chemical reactions, which as an autocatalytic cycle. One of the crucial reactions is the release of molecular bromine (Br_2) from sea salt. The Br_2 quickly dissociates under the influence of UV and visible radiation and subsequently destroys O_3 leading to the formation of O_2 and BrO. In the following step the BrO can either oxidise mercury or trigger an additional Br_2 release. The additional formation of reactive bromine compounds is called bromine explosion mechanism since it can lead to an exponential growth of the concentrations of reactive bromine species in the atmosphere.

Mercury in the atmosphere results from numerous anthropogenic and natural processes. The atmosphere is an important medium for the transport of mercury from a local to a global scale, which leads it to be found in remote areas including polar regions. Under normal atmospheric conditions, gaseous elemental mercury (GEM) is the most dominant specie, with a southern hemispheric background concentration of 1.3 ng m^{-3} . Under these same normal conditions, the so-called reactive mercury species, such as the operationally defined reactive gaseous mercury (RGM) and mercury associated to airborne particulate matter (Hg-P), are found in much lower concentrations, which are often not more than 1-5 % of the total atmospheric mercury composition. During AMDEs GEM is transformed through a chain of photo-chemically driven oxidative reactions to inorganic species either as RGM or Hg-P. Due to the physical properties of RGM and Hg-P, their lifetimes in the atmosphere are relatively short, on the scale of days. This, in turn, leads to a fast deposition of these mercury species onto snow and ice surfaces, and can potentially cause the contamination of

terrestrial and aquatic systems upon snowmelt, that further can result in an increased input and accumulation of mercury in polar ecosystems.

Many indications exist that the described heterogeneous chemical processes responsible for the ODEs and AMDEs are induced by the specific surface properties of newly formed sea ice. It has been hypothesized that frost flowers – fragile, but salty crystals which can form under certain conditions on sea ice – are responsible for these chemical reactions. Therefore, the major goals of the Weddell Sea – Air Ice Chemistry Interaction study were (i) the investigation of chemical processes at the sea ice surface influencing the composition of the atmosphere with respect to reactive trace gases and aerosols, (ii) the investigation of the surface properties of newly formed sea ice with a focus on the formation, growth, lifetime, and chemical properties of frost flowers, and (iii) the validation of satellite data regarding the distribution of reactive trace gases and the occurrence of frost flowers in the southern polar region.

Work at Sea

During the cruise we performed a range of observations. Most of the measurements were performed on the upper most deck of the ship (the so-called ‘Peildeck’) using a heated air measurement container. The measurements included continuous measurements of atmospheric trace gases like O₃, carbon monoxide, and formaldehyde. The mercury components GEM, RGM, and Hg-P were semi-continuously measured throughout the expedition, by use of a fully automated speciation unit that was installed in front of the air measurement container. This unit allows for simultaneous collection of GEM, RGM and Hg-P (Tekran Inc, Toronto, Canada), and consists of a combined heated denuder module for collection of RGM and a re-usable particulate quartz filter module for collection of Hg-P coupled to a mercury vapor analyzer. While RGM and Hg-P are collected by the denuder module and the particulate module, respectively, GEM passes through and is measured in pre-defined intervals. After collection of RGM and Hg-P, these components are sequentially thermally desorbed during the analysis phase and determined as elemental mercury by the mercury vapor analyzer. During this time, measurements of GEM were interrupted.

Many trace gases, which are important in atmospheric chemistry, are strong absorbers in the UV and visible range of the solar irradiation spectrum. Among these absorbing compounds are also the halogen oxides like BrO and chlorine oxide (ClO). Therefore, the differential optical absorption spectroscopy (DOAS) is a suitable method for the detection of these species. From 27 August until 25 October continuous measurements were performed with a ship-borne 2-channel multi-axis DOAS instrument also installed in the air measurement container. The collected spectra of the UV-channel allow the simultaneous detection of BrO, O₃, nitrogen dioxide (NO₂), oxygen dimer (O₄), and chlorine dioxide (ClO). The channel working in the visible part of the solar spectrum can be used for the determination of O₃, NO₂, water vapour, and iodine oxide (IO). Additionally, a second mobile DOAS unit with the

UV-channel was operated at various measurement sites with different viewing directions to investigate local variations in the BrO amounts in comparison to the ship-borne measurements.

Aerosols were collected on filters using an autonomous high-volume sampler, which was installed on the front rail of the 'Peildeck'. Further ship-borne observations included continuous wavelength-resolved measurements of the incoming UV-A and UV-B radiation and regular total atmospheric ozone columns.

In addition to the ship-borne measurements in the atmospheric boundary layer, we performed helicopter measurements to obtain vertical profiles of GEM and O₃. An insulated box, containing separate GEM and O₃ analyzers, was installed in a helicopter. Sample inlets were located as far to the front of the helicopter as possible to avoid helicopter exhaust and downwash coming into the sample inlets. Confined layers of the atmosphere were sampled by flying in triangles at specific altitudes. The flying altitudes were chosen after investigating daily radio soundings launched from the ship. Typically, 5 elevations were chosen, up to a maximum height of 2,500 m, according to the location of the inversion layers. Each elevation was sampled approximately 10 – 15 minutes. O₃ was measured continuously along the entire flight track with a time resolution of 1 min and 1 or 2 GEM measurements were made at each elevation. During the same flights, DOAS measurements were performed using the mobile instrument in combination with a newly designed and simplified telescope, which was built on board.

To investigate the properties of new sea ice, we collected samples from areas where new sea ice recently formed. In total 359 samples were collected at 32 different sites. These field sites were accessed by helicopter transfer (13 sites), during regular ice stations (9 sites), with the mummy chair (8 sites), or with the boat (2 sites). Furthermore, we collected 179 snow samples at 20 different sites either during regular ice stations (14 sites) or by helicopter transfer (6 sites). All these samples were stored at -20 °C and shipped back to the home institutes for further chemical analysis regarding major and minor sea salt ions or mercury species.

Preliminary results

The obtained O₃ time series is shown in figure 5.1. The values of the 5-min averages range from 4.3 to 33 ppbV in the depicted measuring period. A seasonal trend is clearly visible as indicated by the drop of the 10-day averages, which decreased from around 30 ppbV in late winter at the beginning of the cruise to around 16 ppbV in spring at the end of the cruise. A similar behaviour is typical for O₃ on coastal stations in Antarctica like at Neumayer Station. However, our observations indicate that this seasonal cycle is not restricted to the Antarctic continent or the sea ice covered Weddell Sea. For example, between 13 and 19 September we crossed the Drake Passage. Although we operated here in the open water, the measurements still fit into the overall measured trend. Therefore, the observed trend may be typical also for larger areas of the South Atlantic.

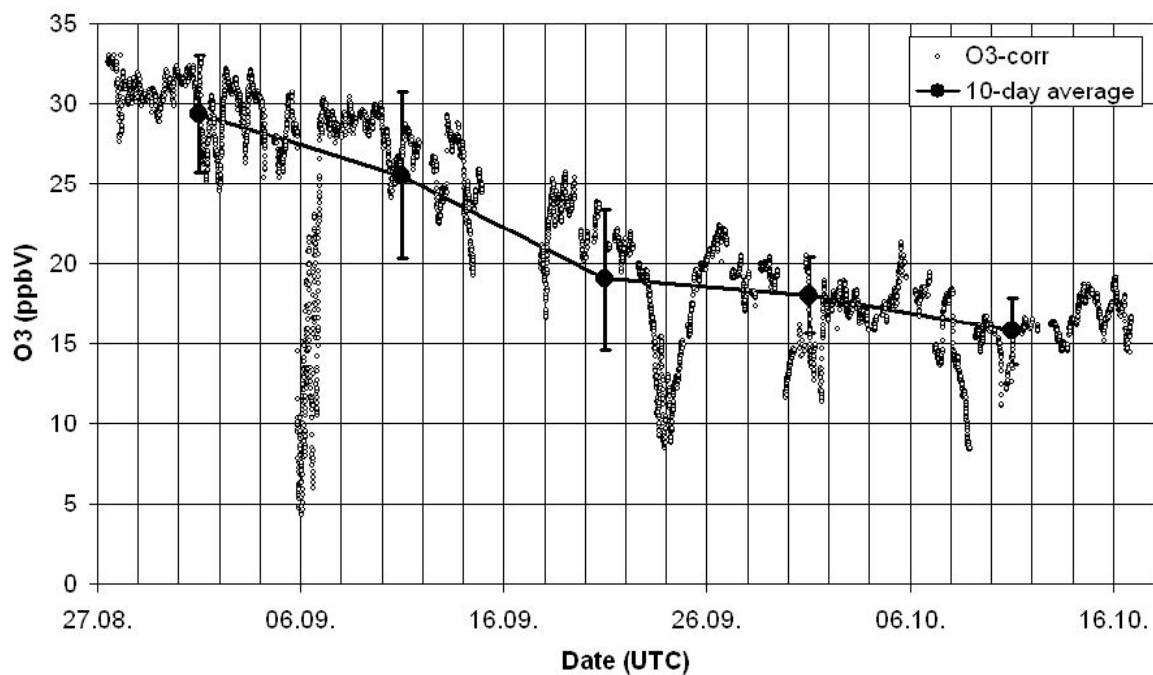


Fig. 5.1: Times series of measured O_3 concentrations on board. Open circles represent 5-min averages, filled dots indicate 10-day averages.

GEM concentrations measured during the entire cruise ranged from less than 0.1 to 1.9 ng m^{-3} (Fig. 5.2). The mean concentration values of GEM measured were $(1.1 \pm 0.3) \text{ ng m}^{-3}$, which is lower compared to the southern hemispheric average of 1.3 ng m^{-3} .

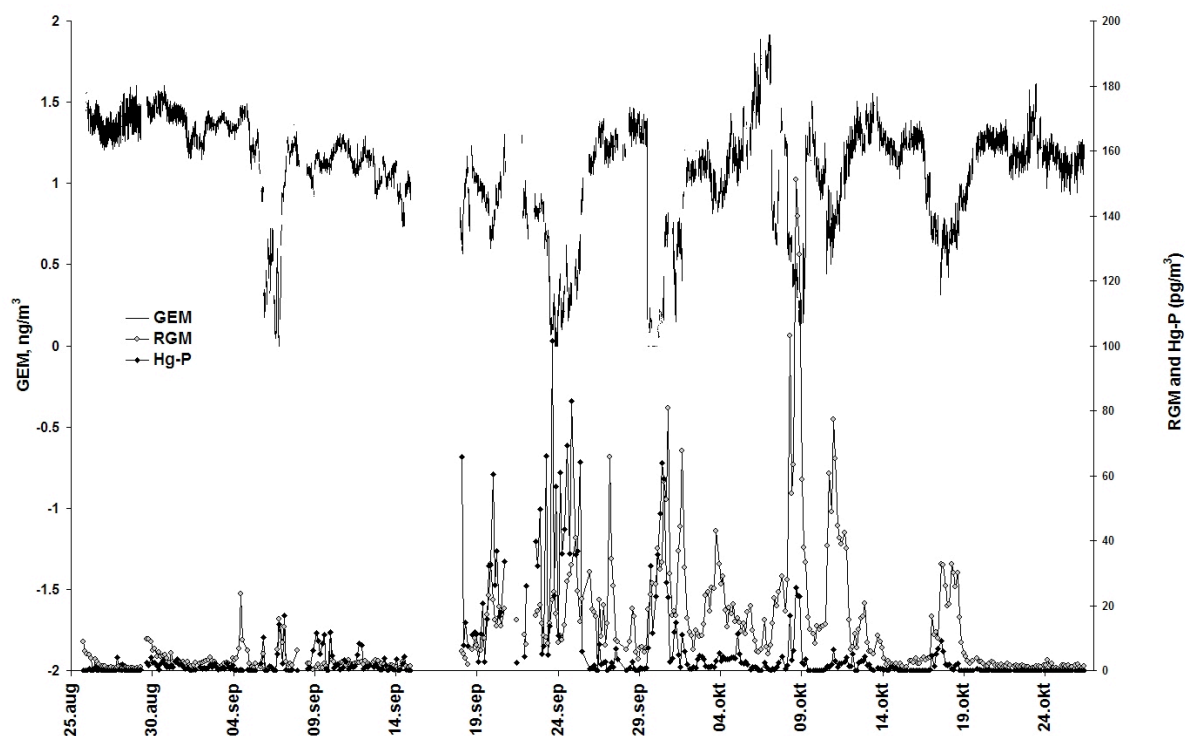


Fig. 5.2: Times series of measured GEM (left axis), RGM and Hg-P concentrations (right axis) on board. The symbols represent 5-min averages for GEM and 3-h averages for RGM and Hg-P.

Comparable to O_3 , GEM also showed a decreasing concentration trend with increasing latitude as long as measurements were made over open water. However, in sea ice covered areas, GEM, in contrast to O_3 , recovered to its “normal” background concentrations. The ocean plays an important role in the global mercury cycle and serves as both a source and a sink for atmospheric mercury through air-sea exchange. Deposition of atmospheric mercury is the most important input of mercury to remote water bodies. Our data indicate that in the South Atlantic and the open water part of the Weddell Sea, the ocean serves more as a sink than a source of mercury. Snow- and ice-covered surfaces seem to be less prone to mercury uptake than water.

The oxidized mercury species, RGM and Hg-P, ranged from less than 2 and up to 160 pg m^{-3} and less than 2 to 100 pg m^{-3} , respectively (Fig. 5.2). The mean concentration values of RGM and Hg-P measured were 12 and 6 pg m^{-3} , respectively. During background conditions, concentration values of RGM and Hg-P were close to or below the detection limit of the methods ($\text{MDL} = 2.0 \text{ pg m}^{-3}$ for both RGM and Hg-P), whereas during depletion events, increasing concentrations of RGM and Hg-P were observed in concert with decreasing concentrations of GEM and ozone.

Satellite pictures of former years showed that the Weddell Sea is quite frequently covered with a significant cloud of elevated BrO concentrations. However, from the satellite data it was not clear, if the BrO formation takes place over wide areas with the necessary initial conditions or if the satellite instrument delivers an average of lots

of smaller and local events, which would only be distinguishable by ground-based spot measurements. Since the measurements deliver total vertical columns of BrO their sensitivity in the troposphere is limited by the high values from the stratospheric background. Only if the tropospheric values reach comparable or even higher values than the stratospheric contribution clear BrO signals can be expected. These clear signals were limited to only a few days of the entire cruise. Taking into account the O₃, GEM, and meteorological data sets, most of these events can clearly be identified as transport phenomena, where processed air already enriched in BrO was advected to the measurement locations.

In total, 6 AMDEs were recorded throughout the cruise, where concentrations of GEM suddenly decreased to between < 0.1 and 0.5 ng m^{-3} . The depletion events recorded were observed on 5 – 6 September, 23 – 25 September, 30 September – 1 October, 8 – 9 October, 10 – 11 October, and 16 – 19 October (Fig. 5.2). Most of the AMDEs were accompanied also by a drop of O₃ concentrations. However, as shown in figure 5.1 these drops were in most cases not as pronounced as for GEM. Only during one event (5 – 6 September) the O₃ concentrations decreased to values below 5 ppbV and during two further events the concentrations were below 10 ppbV (23 – 25 September and 8 – 9 October). For AMDEs it has become an established practice to refer to the events as locally occurring or if they happened elsewhere and were further advected to the measurement site. In the interpretation whether an observed event is locally occurring or a result of transport, meteorological data and BrO maps retrieved from satellite measurements, in addition to back trajectories and the relative distribution between RGM and Hg-P are often used as indicators. Since RGM may attach to Hg-P due to RGM's "sticky" characteristics, concentrations of RGM higher than Hg-P can be an indication of a locally occurring event, and conversely concentrations of Hg-P higher than RGM makes it likely that the depletion happened elsewhere and the depleted air was transported to the measurement site. Further, when no increase in both RGM and Hg-P is observed during an AMDE, the air mass measured has likely been transported long distances.

For example, during the depletion event observed on 5 – 6 September, GEM concentrations decreased to $< 0.1 \text{ ng m}^{-3}$, although no significant increase in RGM and Hg-P concentrations was observed. These observations, in combination with BrO maps, indicate that this depletion event was a result of the long-range transport of already depleted air. Further, during the depletion observed on 23 – 25 September, concentrations of GEM again decreased to $< 0.1 \text{ ng m}^{-3}$, and concentrations of RGM and Hg-P increased to 40 and 100 pg m^{-3} , respectively. These observations, again in combination with BrO maps indicate that this depletion event also was a result of long-range transport, however not transported as far as the depletion event observed on 5 – 6 September.

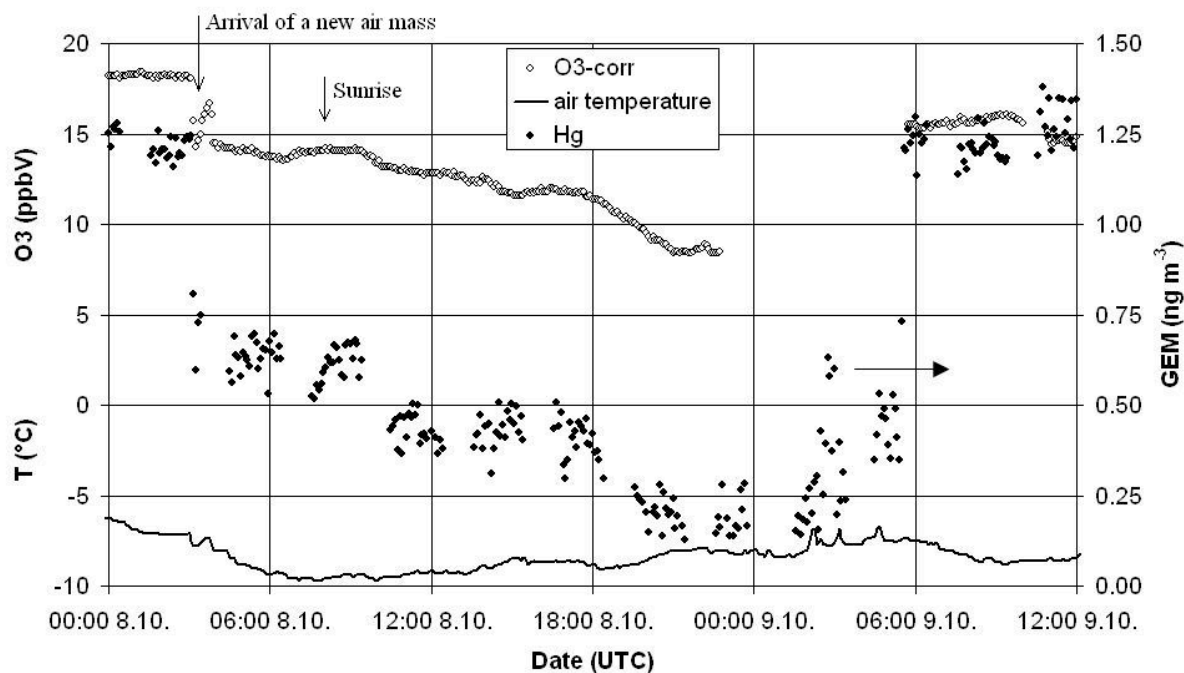


Fig. 5.3: Depletion event for O_3 and GEM observed on 8 – 9 October. Also shown is the time series of the air temperature.

The overall situation was different during the depletion event observed on 8 – 9 October (Fig. 5.3). During the night O_3 as well as GEM concentrations dropped within 10 min to significantly lower values. These quick drops are connected to a change in air masses at the measurement location. During the night a catabatic flow down slope of the shelf ice developed. Therefore, the new air mass led to simultaneous drop in the air temperature. During the rest of the night, O_3 and GEM concentrations remained stable. Only after sunrise the concentrations of both compounds decreased further. The concentrations of GEM decreased to 0.2 ng m^{-3} , and RGM and Hg-P increased to 160 and 25 pg m^{-3} , respectively (Fig. 5.2). The O_3 concentrations declined to values below 10 ppbV. The depletion of O_3 and GEM seem to proceed with accelerating destruction rates as would be expected according to the bromine explosion mechanism (Fig. 5.3).

Figure 5.4 shows the preliminary results of the DOAS measurements for 8 October. To interpret the figure some remarks to the DOAS technique may be helpful. The instrument is collecting scattered light from several, well defined directions with viewing angles between 0 and 90° . Here, 90° corresponds to zenith viewing direction. Depending on the viewing direction and the elevation angle of the sun, the length of the true path of the light reaching the telescope across the atmosphere will change. Slight changes of the viewing angle close to the horizontal direction introduce a particularly large elongation of the pathlength through the troposphere. At the same time the path length through the stratosphere changes only slightly. If the light passes through an absorbing layer in the lower troposphere, the signal increases compared to the zenith sky observation due to the growth of the integrated absorption cross

section. The absorption simply follows the Lambert-Beer law. The amount of molecules causing the total absorption along the true light path is called slant column and is shown in figure 5.4 for 8 October as a function of time. To obtain final results these data must be corrected with a model run, which calculates the true light path by transforming the slant columns to vertical columns. Final calculations of the concentrations of all measured absorbers can be performed only after the motion of the ship is included in the corrections.

Figure 5.4 shows the time series of the slant columns calculated for the zenith viewing direction, a viewing direction of 30° , and the regular scans for viewing directions between 0 and 15° . Under clear sky conditions the slant columns for the zenith viewing direction should exhibit a smooth curve with maxima at sunrise and sunset and a minimum around local noon. However, the observed slant columns show rather large minima and maxima during the day probably due to cloud effects. Nevertheless, between approximately 15:00 and 20:00 a steady increase of the slant column can be identified. Moreover, during this period the slant columns calculated for lower viewing angles always show higher values. The deviations between lower viewing angles and the zenith viewing direction increase with decreasing viewing angles. For example, the regular peaks in the slant columns for the scans correspond to the lowest viewing angle of 1° . This clearly indicates higher amounts of BrO during the indicated period in the lowest atmospheric layer. These observations demonstrate that this depletion event was possibly a result of locally occurring chemical processes.

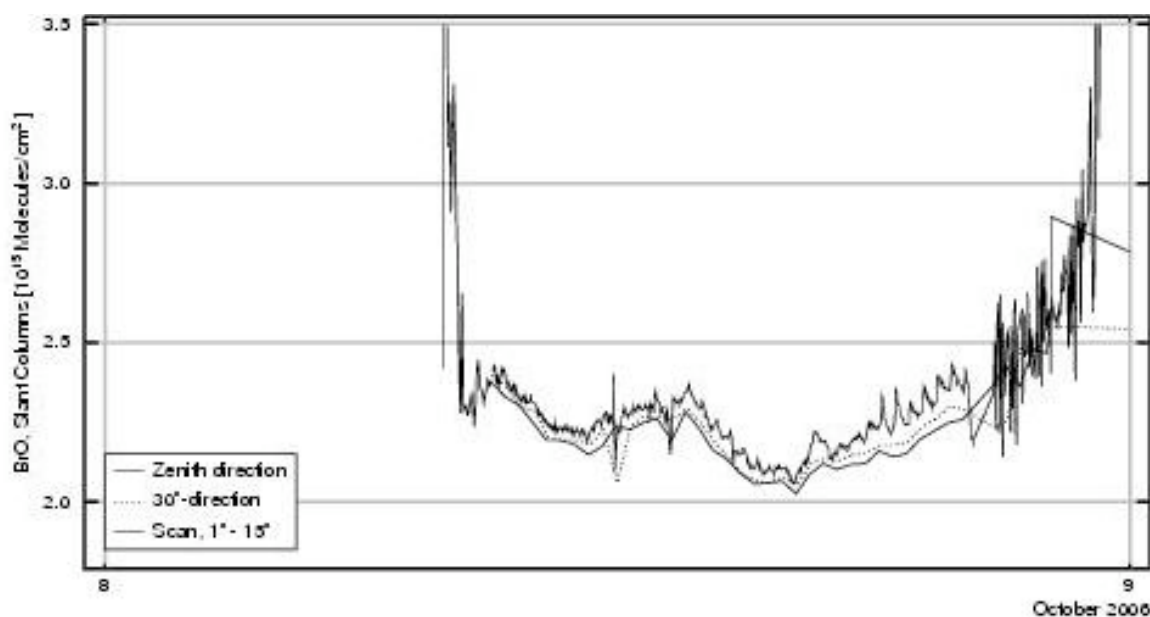


Fig. 5.4: Calculated slant columns of BrO for 8 October. The lines represent values for the zenith viewing direction (bottom solid line) for a viewing direction of 30° , and for scans of viewing direction between 1° and 15° . A full scan between 1° and 90° is completed within 20 minutes.

On the afternoon of 8 October the occurrence and formation of frost flowers were observed in the vicinity of the ship. An ice station lasted from 13:22 to 20:08. A field

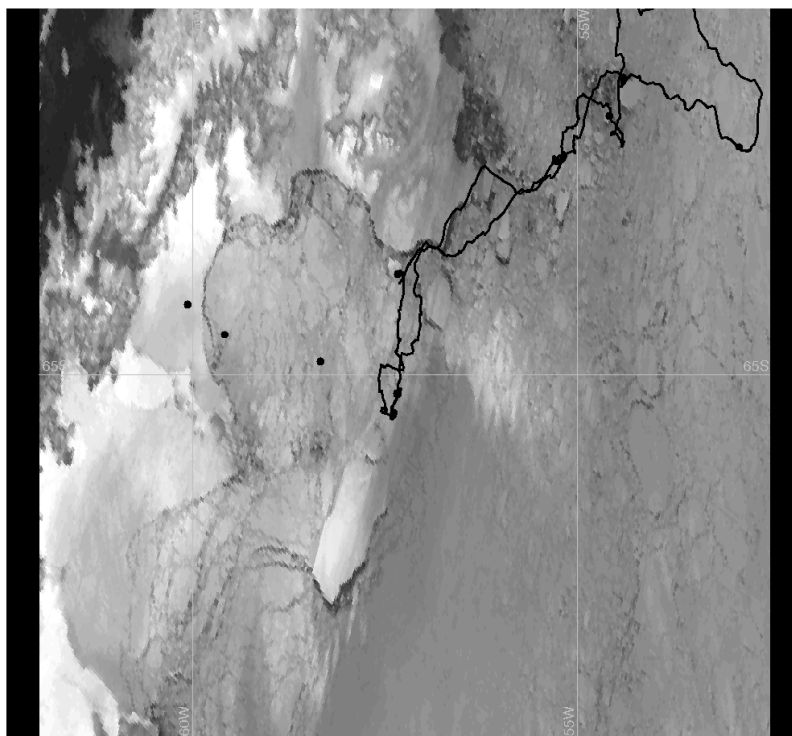
of new and grey ice was located at the edge of the selected ice floe. On this grey ice some frost flowers with needle-like shapes developed during the course of the afternoon (Fig. 5.5).



Fig. 5.5: Field of frost flowers on an area of new ice observed and sampled during the ice station on 8 October (left). Example of a needle-shaped frost flower crystal sampled on the new ice area (right).

On the following day (9 October) two helicopter flights in the direction of the Larsen Ice Shelf were performed. During these flights three different locations with increasing distances from the ship's location were visited (Fig. 5.6). The station closest to the Antarctic Peninsula was located on fast ice. Here, no new ice areas were found. However, the other two stations were located in areas where new ice was encountered. At the edge of the visited floe, frost flowers were present. Samples of both fields were taken and will be analyzed for sea salt components. These samples will be used to characterize the chemical properties of the frost flowers and the new ice area upwind of the ship's position.

Fig. 5.6: AVHRR satellite image from 10 October covering the western Weddell Sea and the northern part of the Antarctic Peninsula. The black line indicates the cruise track, the black dots on the left of the cruise track represent the locations visited during two helicopter flights on 9 October (see text).



In total, 9 vertical profiles were conducted during helicopter flights. Preliminary results from two of these flights are shown in figure 5.7, panel A and B. Typically, results from all flights indicate that although O_3 and GEM show similar concentration patterns on the ground, this is perhaps not the case for higher altitudes and the free troposphere. Considering the vertical profile from 3 October, O_3 was depleted above the ground inversion layer (up to ~ 300 m) and throughout the measured vertical column, whereas GEM concentrations rather tended to increase with altitude. Considering the vertical profile obtained on 11 October, O_3 was depleted above the inversion layer at 1,800 – 2,000 m, whereas concentrations of GEM stayed constant throughout the vertical column. Combining back trajectories at different elevations (Fig. 5.7, panel C – F) and BrO maps (Fig. 5.7, panel G and H), it can be seen that what the depleted ozone air masses have in common, is that they have been close to the surface at a time and location where the air was enriched in BrO. Further, the O_3 depleted air was uplifted and transported to the measurement location and elevation. However, why O_3 and mercury deviate at higher altitudes needs more investigation.

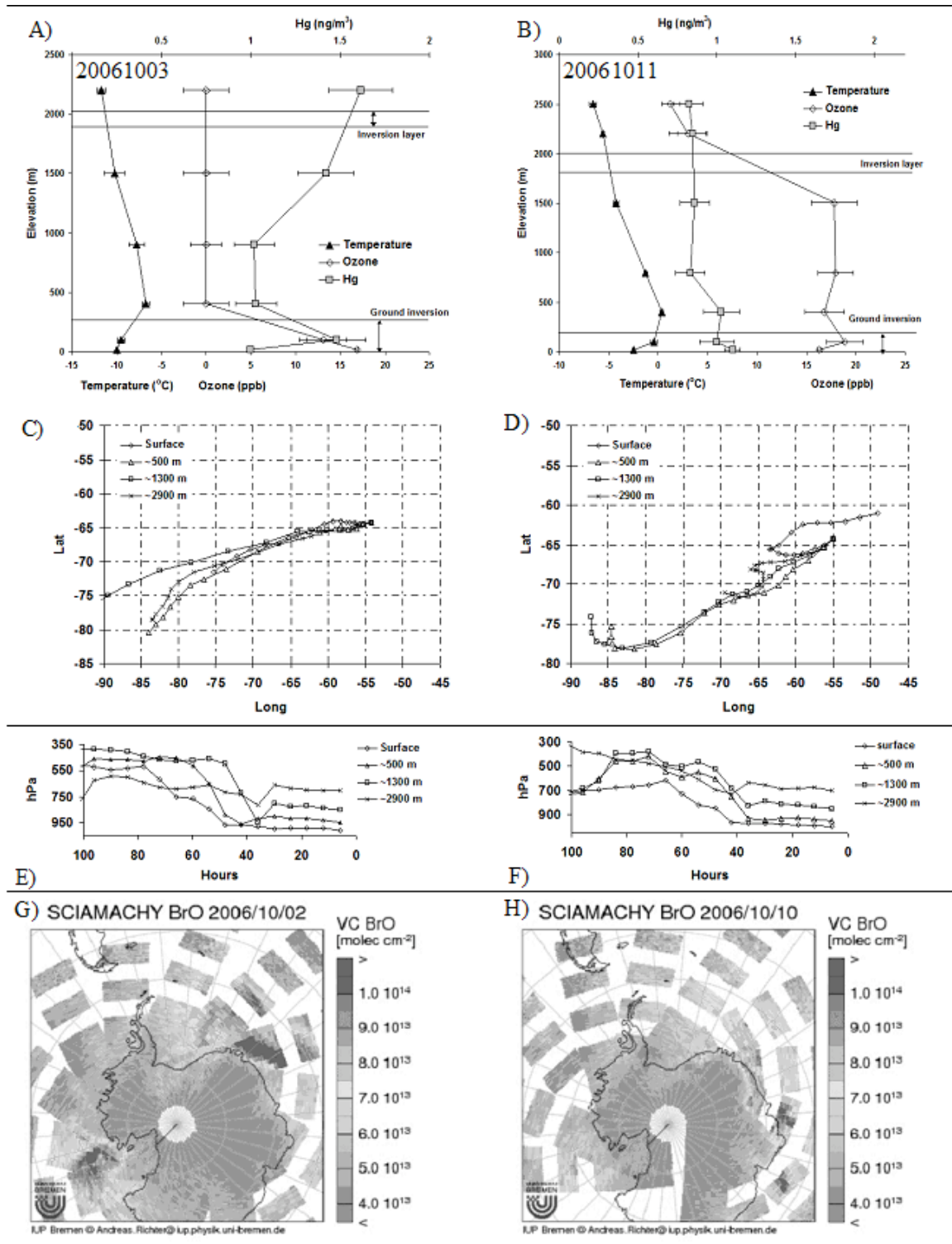


Fig. 5.7: Vertical profiles showing concentrations of O₃ and GEM with increasing altitude, from 3 and 11 October (Panel A and B). Back trajectories ending at the surface, 500 m, 1,300 m, and 2,900 m plotted with location (Panel C and D). Back trajectories showing elevation plotted with backward travel time (Panel E and F). Satellite retrieved BrO maps from 2 and 10 October (Panel G and H).

6. BIOLOGY

6.1 Sea ice biogeochemistry and biodiversity in winter and early spring

Erika Allhusen¹, Dai Fangfang², Gerhard Dieckmann¹, Klaus Meiners³, Louiza Norman⁴, Stathis Papadimitriou⁴, David Thomas⁴, Christiane Uhlig², Wang Zipan²

¹Alfred-Wegener-Institut
²College of Life & Environment, Ningbo, China
³Antarctic Climate & Ecosystems, Hobart, Australia
⁴School of Ocean Sciences, Angelsey, United Kingdom

Objectives

Sea ice is a structuring component of the Southern Ocean and plays a pivotal role in the biogeochemical cycles of Antarctic marine ecosystems. The sea-ice cover greatly affects energy and material fluxes between the ocean and the atmosphere, and provides a habitat for diverse microbial assemblages which, in terms of biomass, are generally dominated by algae. Sea-ice primary production significantly contributes to overall ecosystem primary production and provides an important food source for pelagic herbivores during winter and early spring, when food supply in the water column is low.

The development of algal biomass and primary production in sea ice are key parameters in our understanding of the sea ice ecosystem. Our current understanding of the onset of algal growth and production in winter is still rudimentary. The measurement of chlorophyll in conjunction with other complementary biogeochemical investigations should provide new insight into the time period in which growth and development of the sea ice community begins. In order to determine temporal changes of the sea-ice habitat during the transition between winter and spring, chemical, physical and biological properties were investigated in sea ice floes of different origin (also see chapter 4. by Haas et al.).

The biogeochemistry of sea ice in the transition from austral winter to spring has been poorly documented to date. Our aim has been to obtain information on biogeochemical processes in sea ice during this seasonal transition. Our specific objectives are: *i*) to make an extensive characterization of the physical-chemical environment experienced by sea ice communities, *ii*) to investigate biological processes in relation with the physical-chemical environment, *iii*) to investigate the chlorophyll a distribution in sea ice as well as the photosynthetic parameters of sea-ice algae and optical properties of sea ice, *iv*) to investigate the influence of major grazers on biogeochemical processes in sea ice, *v*) to examine the distribution of viruses within sea ice, *vi*) to investigate the occurrence and abundance of cryogenic carbonate minerals (CaCO₃) in sea ice as part of its internal carbon cycle, and *vii*) to

investigate the habitat range of the foraminifera *Neogloboquadrina pachyderma*, using stable carbon and oxygen isotopes in its shell for environmental reconstruction and finally viii) to obtain samples for sea ice molecular biological studies.

Carbonate mineral precipitation and degassing of dissolved carbon dioxide can be closely coupled and have been well-documented in ice derived from low ionic strength water (e.g Killawee et al., 1998). Carbonate precipitates that form at near-zero and subzero temperatures have been identified as cryogenic calcite and aragonite (op. cit.), while rare occurrences of the metastable forms vaterite (CaCO_3) and ikaite ($\text{CaCO}_3 \cdot 6\text{H}_2\text{O}$) have been reported around spring discharges in supraglacial and permafrost environments (Omelson et al., 2001; Grasby, 2003), as well as in low temperature saline lake waters (Bischoff et al., 1993 a, b). Mineral precipitation and degassing would appear to be typical, emergent features of sea ice formation and growth, particularly evident in the sea ice dynamics of the dissolved inorganic carbon pool. However, with the exception of the experimental work by Gitterman (1937), observations from natural and artificial sea ice have failed to detect chemical changes commensurate with such processes, and direct observations of carbonate or other minerals in natural sea ice are scarce (Anderson and Jones, 1985; Gleitz et al., 1995). A key feature of our activities was to look for direct evidence of calcium carbonate precipitation in late winter sea ice.

Work at sea

Extensive sampling took place in a series of ice stations between 8 September 2006 and 13 October 2006 along an east to west transect between 60° and 61° S and 40 to 52° W around the South Orkney Islands, as well as along a northeast to southwest transect between 60° S and 65° S from the South Orkney Islands to the Larsen-A Ice Shelf. Samples were taken from: *i*) 11 sectioned ice cores in collaboration with Haas et al. for bulk ice measurements, *ii*) sackholes drilled in sea ice at 22 ice stations along the transects, and *iii*) depth profiles of seawater from CTD stations in collaboration with Schiel et al. and Zemmeling et al. Further samples were generated by a number of experiments designed to investigate the contribution of major sea ice grazers, i.e., sea ice dwelling and pelagic copepod species (laboratory-controlled incubations) in collaboration with Schiel et al.

The collected samples provided measurements of salinity, temperature, dissolved ammonium by fluorescence spectroscopy, dissolved oxygen by Winkler titration with photometric end point detection, pH and total alkalinity using a standard glass electrodes calibrated with NBS standards and Gran titration, chlorophyll, and coloured dissolved organic matter (C-DOM) spectra in the visible and UV light ranges (200 – 750 nm). The determination of the following parameters will be conducted in the home laboratories: major dissolved inorganic nutrients, nitrate plus nitrite ($[\text{NO}_x]$), phosphate ($[\text{P}]$), and silicate ($[\text{Si}]$), dissolved organic nitrogen ($[\text{DON}]$), dissolved organic carbon (DOC), urea, dissolved inorganic carbon (DIC) and its stable isotopic composition ($\delta^{13}\text{C}$ -DIC), elemental and stable isotopic composition of particulate organic carbon and nitrogen (POC, PON, $\delta^{13}\text{C}$ -POC, $\delta^{15}\text{N}$ -PON) isolated from bulk

ice and sackhole brine by gentle vacuum filtration, the stable isotopic composition of oxygen ($\delta^{18}\text{O}$) in sackhole brines, seawater, and foraminiferan shells, and the stable isotopic composition of carbon and nitrogen in foraminiferan cytoplasm and copepods. Further characterization of the fluorescence of sea ice C-DOM will be conducted in collaboration with C. Stedmon in Denmark. Characterization of sea ice DOM on the molecular level will also be conducted in collaboration with G. Underwood at the University of Essex, UK. The characterization of viruses in sea ice will be conducted in collaboration with the University of Aberystwyth, UK.

Ice cores were collected in conjunction with other sea ice studies (see chapter 4. by Haas et al.). Cores were sectioned as already described above and returned to the laboratory where they were allowed to melt at +4 °C. For the determination of chlorophyll *a*, the melted ice samples were filtered onto Whatman GF/F filters, extracted in 90 % acetone, homogenized and analyzed fluorometrically with a Turner Designs 10-AU digital fluorometer. Detection limit of this method is 0.1 $\mu\text{g chl}a \text{ l}^{-1}$. Sub-samples of the melted core sections were collected for species enumeration and fixed for later analyses with buffered formaldehyde (1 % final concentration).

Sea ice cores were collected for analyses of calcium carbonate at all sea ice stations. One core was cut into sections as described for other parameters. In addition on most stations we collected 3 cores from the top 40 cm of the sea ice from which we collected bulk samples. The sections were returned to the ships laboratory and allowed to melt at +4 °C. Calcium carbonate crystals were obtained by swirling the melted samples and subsequently collecting the crystals under a binocular microscope. The crystals from each section of the first core were filtered through a pre-weighed GFC (Whatmann) filter, rinsed with 50 % ethanol and stored on a filter plate at -30 °C. The bulk samples were filtered through a polycarbonate filter and stored in Falcon tubes in 50 % ethanol at -30 °C for further analyses in the home laboratory. Crystals were also photographed through a binocular microscope to record various shapes. Subsequent work at the home laboratory will include the quantification of CaCO_3 precipitation as well as analyses of crystals to establish the form of calcium carbonate.

At 21 stations the under-ice hyperspectral irradiance was measured with a TriOS Ramses ACC radiometer. The radiometer was deployed under the ice using an unfolding telescopic arm which allowed to measure under-ice irradiance at totally undisturbed sites of the ice floes and away from any access holes. After irradiance measurements were completed, ice and snow thickness as well as the freeboard of the ice floes were measured and an ice core was collected from the radiometer site. The ice core was cut into sections which were melted at 4 °C in the dark in the ships laboratories. Melted ice core samples were analysed for pigment content (chlorophyll *a* and pheopigments) according to Arar and Collins (1997). Additional subsamples were filtered onto Whatman GF/F filters which will be used for the determination of the absorbance of sea ice particles following the protocol of Tassan and Ferrari (1995). This work will be performed in the home laboratories.

In addition on each station sea-ice brine was collected from sackholes and the lower-most centimetres of the sea ice floe were sampled by means of ice coring. These samples were used for the determination of photosynthetic parameters (effective quantum yield, maximum quantum yield and electron transfer rate of Photosystem II) of ice algae communities colonising the interior and the bottom of the ice floes. Analyses were performed with a Waltz Water-PAM fluorometer using a rapid light curve protocol. The collected data will give information on the spatial distribution of physical and biological sea-ice parameters and the influence of physico-chemical parameters on sea ice primary production.

Preliminary results

6.1.1 Bulk ice

Salinity, chlorophyll & nutrients

The bulk ice salinity measurements from sectioned cores ranged from 0.4 to 14 (Fig. 6.3). The depth profiles of this property were C- or L-shaped, with top and bottom maxima or a bottom maximum, respectively. A number of salinity profiles had a sigmoid shape, with top, middle and bottom salinity maxima.

The total of 20 cores collected for biomass studies, revealed different distribution patterns of chl_a. Most had a pronounced bottom assemblage with mean chl_a concentrations being one order of magnitude higher at the bottom decimetre than in any other segment of the core (Fig. 6.1). The highest concentration was measured in the bottom 7 cm of the ice core taken on 5 October. The depth profiles of chlorophyll were mostly L-shaped, with maximum concentrations in the bottom 5 to 10 cm of the ice core, indicative of the location of maximum biomass of the internal autotrophic community. On two occasions (24 September and 30 September), the chlorophyll maximum (14 and 20 $\mu\text{g L}^{-1}$, respectively) was measured in the topmost 10 cm of the core, while on one occasion (26 September), a broad chlorophyll peak, with a maximum of 87 $\mu\text{g L}^{-1}$, was observed in the middle part of the core, between 20 and 60 cm depth. Integrated chlorophyll *a* values for the 20 different ice floes ranged between 1,36 to 79,4 mgm^{-2} with a mean of 17.0. First comparisons of the chl_a with salinity and stratigraphy within and between cores indicate both temporal and geographical differences. See chapter 4. by Haas et al. for stratigraphy data. Species enumeration studies to be carried out at the home laboratory will provide a more comprehensive view on the origin and history of the different ice floes.

Fig. 6.1: Plot of chlorophyll a and salinity versus ice core depth and related to sea ice stratigraphy for Core 061005

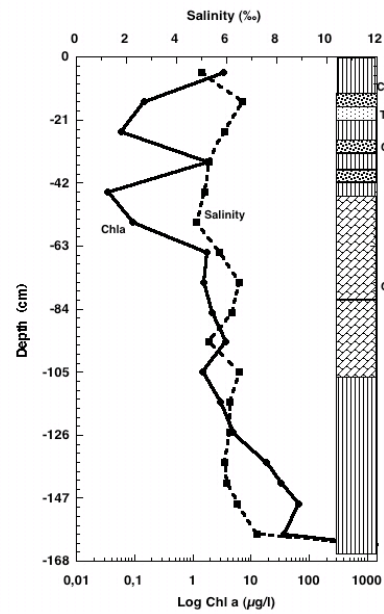
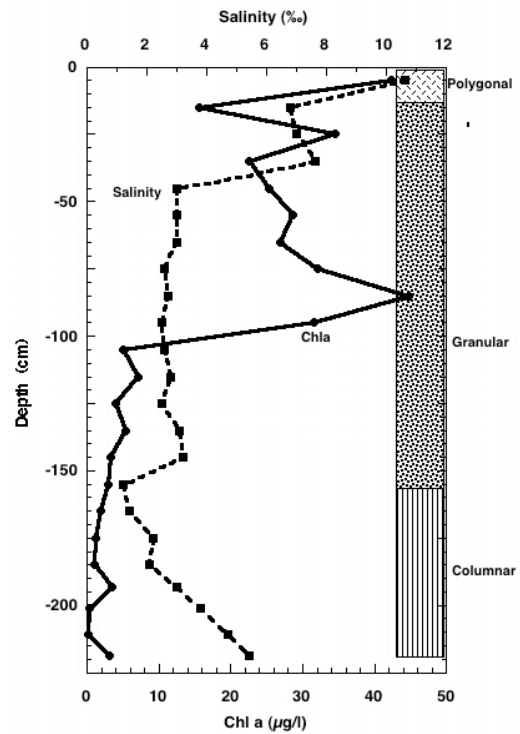


Fig. 6.2: Plot of chlorophyll a and salinity versus ice core depth and related to sea ice stratigraphy for core 061001



The concentration of dissolved ammonium bulk ice ranged from < 0.1 to $3.5 \mu\text{M}$ (Fig. 6.3a), with depth profiles similar to those of salinity. By comparison with the dissolved ammonium concentration in regional oceanic waters of mostly less than $0.1 \mu\text{M}$, the bulk ice was considerably enriched in this solute.

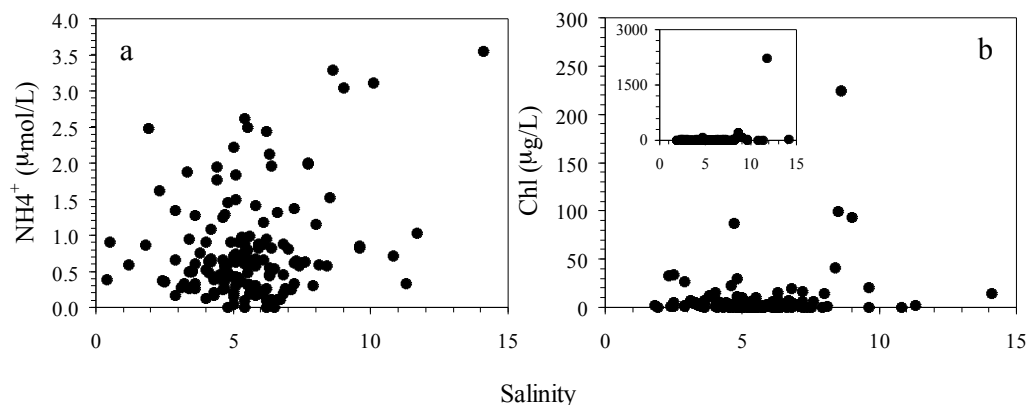


Fig. 6.3: a) dissolved ammonium, and b) chlorophyll as a function of salinity in bulk ice

CDOM in bulk sea ice

The samples from the under-ice water column exhibited S values of between 0.018 and 0.024 nm^{-1} and low absorbance values of $0.1 - 0.5 \text{ m}^{-1}$, which are consistent with those found in oligotrophic ocean waters. Analysis of the ice core and brine data indicate that unlike open water samples the absorption curve of these two types of sample is not smooth but often exhibits peaks at 350 nm and 270 nm . Examples of typical absorbance spectra of water column, bulk ice and brine samples are shown in Fig. 6.4a.

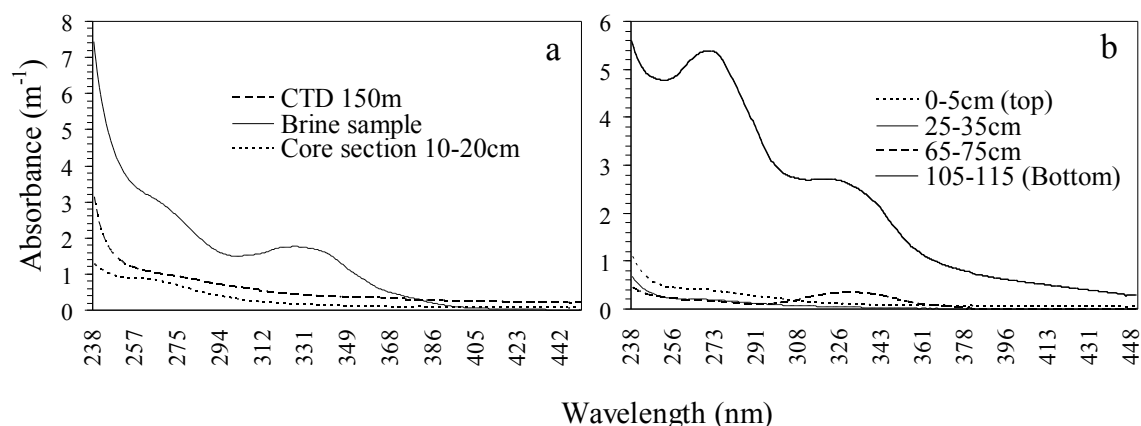


Fig. 6.4: a) Typical spectral shapes exhibited by surface seawater, bulk ice, and brine samples, and b) variation in absorbance values between 240 nm and 440 nm with depth in a 115 cm ice core collected from station 578 on 08/10/06

Complete bulk ice C-DOM depth profiles were generated from measurements taken from cores sectioned into 10 cm segments. Absorbance values were generally low, ranging from 0.2 m^{-1} to 2 m^{-1} . However, in chlorophyll-rich sections, values greater than 4 m^{-1} and up to 15 m^{-1} (at 280 nm) were observed. A shoulder was observed in all core sections at between 260 nm and 290 nm (Fig. 6.4), which becomes more pronounced and develops into a peak in chlorophyll-rich segment. This is often accompanied by a second peak at $\sim 350 \text{ nm}$ (Fig. 6.4). The compound(s) that may be responsible for these anomalies is unknown as no correlation was seen between absorbance values at 240, 280, 300, 330, 350, and 440 nm and either chlorophyll or dissolved ammonium. The location of raised absorbance values is not uniform between cores but appears to be dependent on the location (i.e., top, middle, or bottom of the core) of the chlorophyll (i.e., autotrophic biomass) maximum.

6.1.2 Photosynthetic parameters of sea-ice algae and optical properties of sea ice

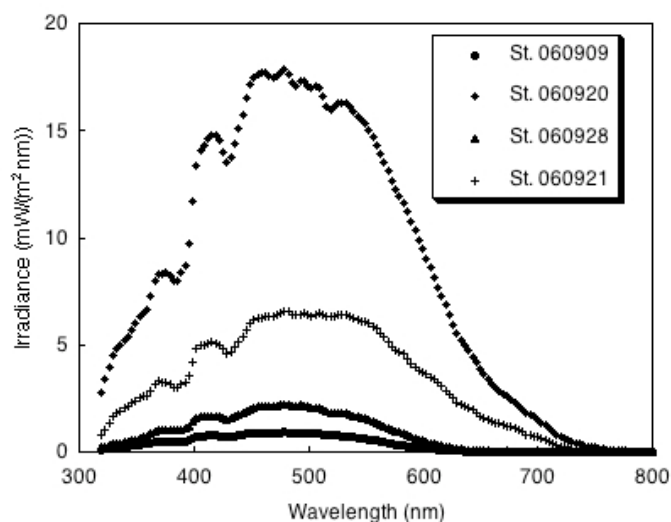
Only recently modern techniques like pulse amplitude modulated (PAM) fluorometry have been introduced to sea ice ecological research. These studies primarily focused on small scales and were mainly carried out on land-fast-ice. Information on the large-scale distribution of pack ice algae and their photosynthetic parameters as well as on the influence of physico-chemical factors on these parameters is still scarce.

Therefore the first aim of this part of the work was to measure bio-optical properties of sea ice and to determine the influence of sea-ice algae on the spectral composition of the irradiance transmitted through Antarctic pack ice. These measurements will be used to explore the potential to use light spectra to estimate sea-ice algae distribution with non-invasive optical sensors from beneath the sea ice.

The second aim of this part of the work was to determine of photosynthetic parameters of pack-ice algae using PAM fluorometry. These measurements will be related to an extensive set of physical and biogeochemical parameters to understand the influence and forcing of abiotic factors on sea ice primary production.

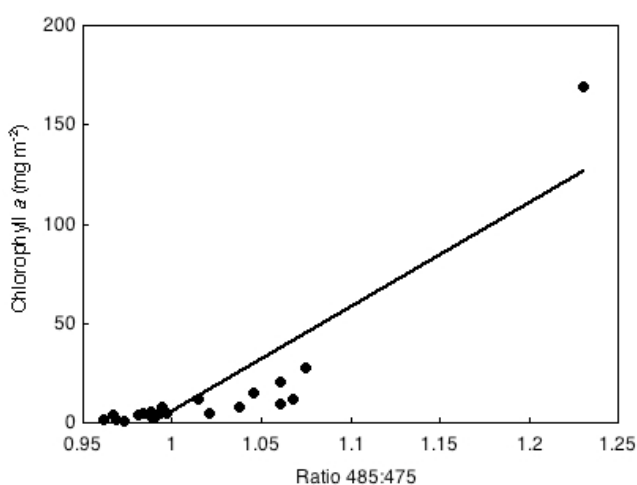
Under-ice light spectra were strongly affected by surface irradiance as well as by ice and snow thickness and the chlorophyll *a* content of the ice. Ice thickness at radiometer sites ranged from 62 cm to 142 cm; snow thickness varied between 1 cm and 52 cm. The integrated chlorophyll *a* concentrations of the sampled sea ice varied between 0.7 mg m^{-2} and 169.0 mg m^{-2} with an average of 15.5 mg m^{-2} . Figure 6.5 shows examples of light spectra from four different stations with ice and snow thicknesses of 116 cm and 32 cm (St. 060909), 81 cm and 5 cm (St. 060920), 87 cm and 9 cm (St. 060928) and 136 cm and 27 cm, respectively.

Fig. 6.5: Under-ice light spectra from four different stations measured at different times of the day. For details see text.



The ACE CRC sea ice group will adopt different methods for the spectral data analysis including the classical Single Band Ratio technique, the Normalised Ratio technique (Clark and Roush 1984) and the Scaled Band Area technique (Nolin and Dozier 2000) to derive algorithms for the estimation of ice algal biomass from under-ice hyperspectral light measurements. In a pioneer study Mundy et al. (in press) used the Single Band Ratio technique successfully to estimate sea ice algal biomass in Arctic fast ice. They showed that snow has only little effects on the distribution of the transmitted spectral irradiance at wavelengths between 400 and 500 nm. In their study the ratio 485nm:475nm explained up to 89 % of the integrated chlorophyll *a* content in coastal fast-ice in Resolute Bay (Mundy et al. in press). Figure 6.6 shows the correlation between this ratio and the integrated chlorophyll *a* content of overlying sea ice for Antarctic pack ice studied during the ANT-XXIII/7 cruise. The good correlation indicates that under-ice light spectra can be used to estimate ice algal biomass/chlorophyll *a* content of Antarctic pack ice.

Fig. 6.6: Under-ice spectral transmitted irradiance ratio (485nm:475nm) versus integrated chlorophyll *a* content of overlying sea ice ($n=21$, $R=0.88$)



Chla fluorescence techniques have been increasingly applied to study ice algal photophysiology and sea-ice ecology. The techniques involve the measurement of light energy emitted from the light harvesting pigments associated with the process of photosynthesis. Figure 6.7 shows rapid light curves for ice algae living in the interior of an ice floe (brine) and at the bottom of an ice floe. The electron transfer rate, a measure of the photosynthetic rate, is plotted as a function of the photosynthetic active radiation (PAR). The algae of the brine sample have a much higher photosynthetic rate (initial slope of the rapid light curve) and are adapted to higher PAR levels compared to the shade-adapted bottom-ice community. Using non-linear regression analysis the rapid light curves will be used to derive various photosynthetic parameters of the different ice algae communities, which allows to understand how the algae cope with the harsh environmental conditions in winter sea ice. Different photosynthetic parameters including the effective quantum yield, maximum quantum yield and electron transfer rate of Photosystem II will be related to other biogeochemical parameters measured by this group.

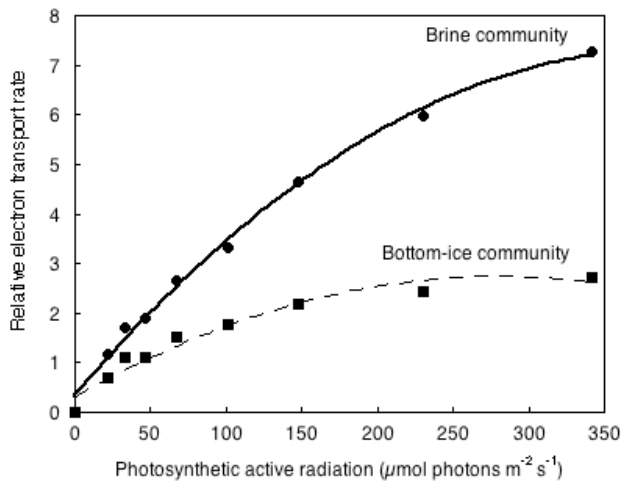


Fig.6.7: Rapid light curves for a sea-ice surface/interior community (brine community) and a bottom-ice community at St. 060919

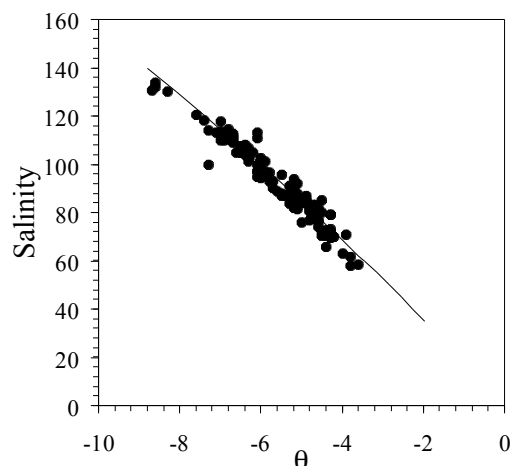
6.1.3 Sea ice brine from sackholes

Temperature and salinity of sea ice brines

The temperature of the sackhole brines ranged from -8.7 to -3.6°C, while their salinity ranged from 58 to 134 (Fig. 6.8). Salinity being a function of temperature in sea ice, the observations followed closely their reported functional relationship

$$S = \frac{\theta}{\theta - 54.11} \text{ (Fig. 6.8).}$$

Fig. 6.8: Salinity as a function of temperature in sackhole brine



Dissolved oxygen, pH, total alkalinity, calcium carbonate and total dissolved inorganic carbon in sea ice brines

The brines exhibited a large concentration range of dissolved oxygen (O_2), from 93 to 462 $\mu\text{mol kg}^{-1}$ (Fig. 6.9a). By comparison with the theoretical concentration of oxygen in hypersaline solutions in equilibrium with air at sub-zero temperatures, the measured concentration span represents conditions that range from strongly undersaturated (40 %) to highly supersaturated (170 %).

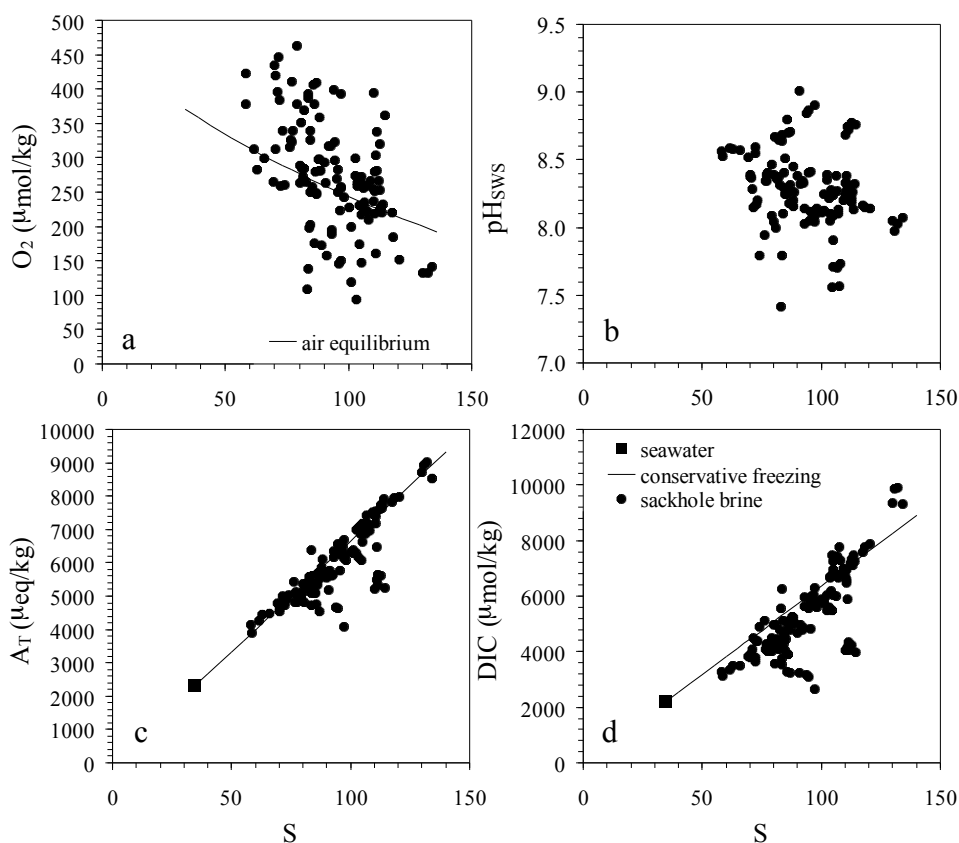


Fig. 6.9: a) The concentration of dissolved oxygen (O_2), b) in-situ pH on the seawater scale (pH_{sws}), c) total alkalinity (A_T), and d) the concentration of total dissolved inorganic carbon (DIC) vs. salinity in sackhole brines

An estimate of the *in-situ* pH (seawater scale) was obtained from the measured A_T and pH_{NBS} at 20 °C. The estimated pH_{SWS} ranged from 7.4 to 9.0 (Fig. 6.9b). The measured A_T ranged from 3887 to 9025 $\mu\text{eq kg}^{-1}$. Although A_T varied directly with salinity, it exhibited variable extent of deviation from conservation during the freezing of surface seawater on many occasions (Fig. 6.9c). The most pronounced deviation from the expected conservative value was associated with a substantial reduction in A_T .

The concentration of DIC, which was estimated from the measured pH_{NBS} and A_T at 20 °C, ranged from 2646 to 9888 $\mu\text{mol kg}^{-1}$. The functional relationship of the DIC concentration with salinity was less prominent than that of A_T because DIC generally deviated from conservation during freezing of surface seawater, with a pronounced decrease on most occasions, as well as a moderate increase in several samples (Fig. 6.9d).

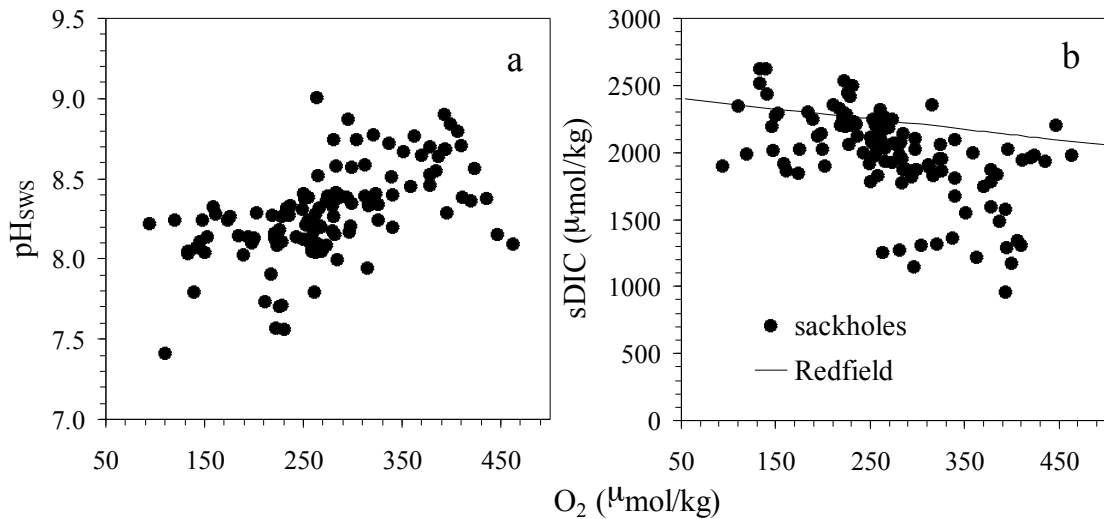


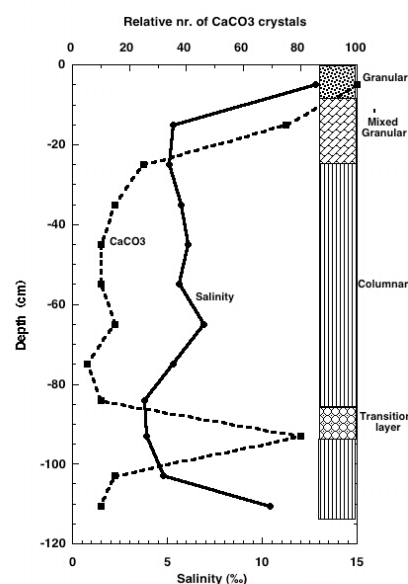
Fig. 6.10: a) pH_{SWS} , and b) salinity-normalized DIC (sDIC; $S = 35$) as a function of O_2 in sackhole brine

The pH_{SWS} varied directly with the measured O_2 in the brine, while the sDIC (sDIC = measured DIC normalized to a standard seawater salinity of 35 to remove the cryogenic concentration, or dilution, effect) varied inversely with the measured O_2 concentration (Fig. 6.10). The biological processes of primary (autotrophic) and secondary (heterotrophic) production modify the pH of the medium, as well as the concentrations of DIC and O_2 . The observed co-variances reflect the effect of biological activity on the chemical composition of the brine. However, the linear trend seen between sDIC and O_2 deviated from the stoichiometric trend predicted for the Redfield molar C: O_2 ratio (-106:138) (Fig. 6.10b). Additional effects on DIC and O_2 that can give rise to the observed deviation include those due to the abiotic processes of brine degassing and cryogenic $CaCO_3$ formation.

These findings were supported by the first direct evidence of $CaCO_3$ precipitation in sea ice. However, the occurrence and distribution of $CaCO_3$ was inconsistent. The

highest number of crystals was usually recorded in the top portion of the ice cores, with the exception of some cores where large numbers were recorded further down in the core (Fig. 6.11). The shapes and sizes of the crystals of the also varied considerably (see Fig 6.12 for examples). Preliminary comparisons of CaCO_3 distribution with other parameters such a salinity did not reveal any consistency, with the exception of two cores where large numbers of crystals were associated with particular ice stratigraphy (Fig 6.11). In this core the highest number of crystals was associated with granular or a typical transition layer. See chapter 4 by Haas et al. for more details on ice stratigraphy.

Fig. 6.11: Plot of relative number of CaCO_3 crystals in Core 060923 in relation to salinity and core stratigraphy



The size of the crystals ranged from less than 0,1 mm to a maximum of 2 mm. The reason for the different crystal shapes is not yet known but may result from the confinement of the crystals in brine pockets or channels as can be seen in the crystal on the top left in figure 6.12. Further research on the CaCO_3 will deal with the fate of the crystals in the sea ice. The question is whether, when and under which conditions the crystal dissolve and whether they may in fact be released into the water column when the sea ice melts.

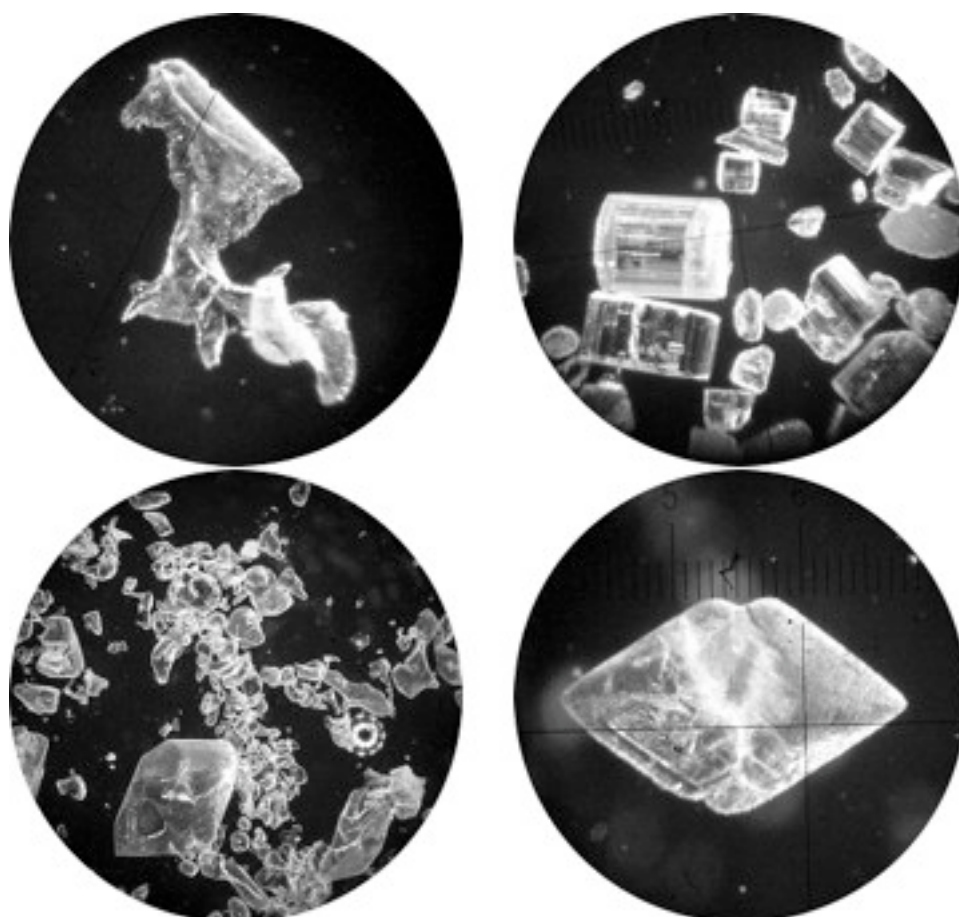


Fig. 6.12: Photographs of various CaCO₃ crystal shapes found in sea ice cores. Scales vary for each picture.

Dissolved ammonium, and chlorophyll in sea ice brines

The measured concentration of dissolved ammonium in brine ranged from < 0.1 to $35.3 \mu\text{mol kg}^{-1}$. The salinity-normalized ($S = 35$) concentration of dissolved ammonium (range: <0.1 to $11.5 \mu\text{mol kg}^{-1}$) indicated that the brine was enriched relative to surface seawater ($< 0.1 \mu\text{mol kg}^{-1}$) by one to two orders of magnitude on several occasions (Fig. 6.13a). The chlorophyll concentration ranged from 0.1 to $16.1 \mu\text{g L}^{-1}$ (Fig. 6.13b).

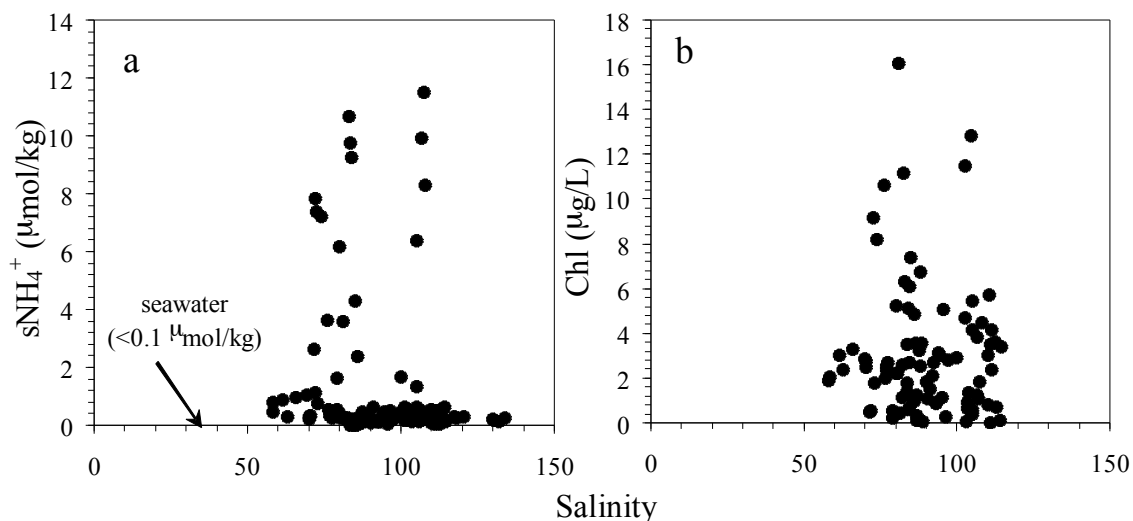


Fig. 6.13: a) Salinity-normalized dissolved ammonium, ($S = 35$) and b) measured concentration of chlorophyll as a function of salinity in sackhole brine

C-DOM in sea ice brines

Generally, the absorbance values observed in brine samples were considerably higher than those in either the bulk ice or seawater samples. This is particularly apparent at 240 nm where values between 6 m^{-1} and 9 m^{-1} were common as opposed to values between 1 m^{-1} and 3 m^{-1} seen in bulk ice. There is often a shoulder at between 260 nm and 290 nm but unlike bulk ice samples there is also an additional shoulder between 300 nm and 350 nm (Fig. 6.14). As also observed in bulk ice, these shoulders often become peaks in chlorophyll-rich brines.

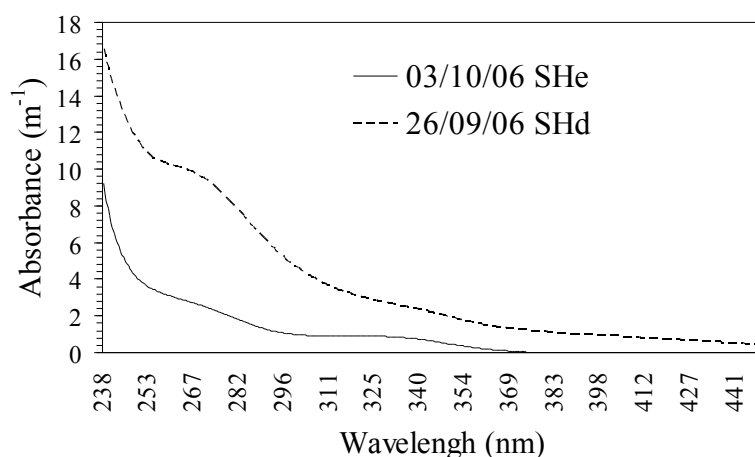


Fig. 6.14: Absorbance spectra between 240 nm and 440 nm of brine samples collected from stations 564 and 574 on 26/09/06 and 03/10/06, respectively

No correlation existed between absorbance and the concentration of chlorophyll, dissolved ammonium, or salinity, which makes the source of this feature difficult to identify at present. However, analysis of data collected from a single ice floe in the western Weddell Sea during the ISPOL cruise between 1 December 2004 and 31 December 2004 yielded a good correlation with DOC at 280 nm (Pearson correlation, $r = 0.776$, $p \leq 0.001$) and DON at 330 nm and 350 nm (Pearson correlation, $r = 0.784$, $p \leq 0.001$) (Fig. 6.15). It is anticipated that once DOC and DON measurements become available a similar trend may be observed in the current data set.

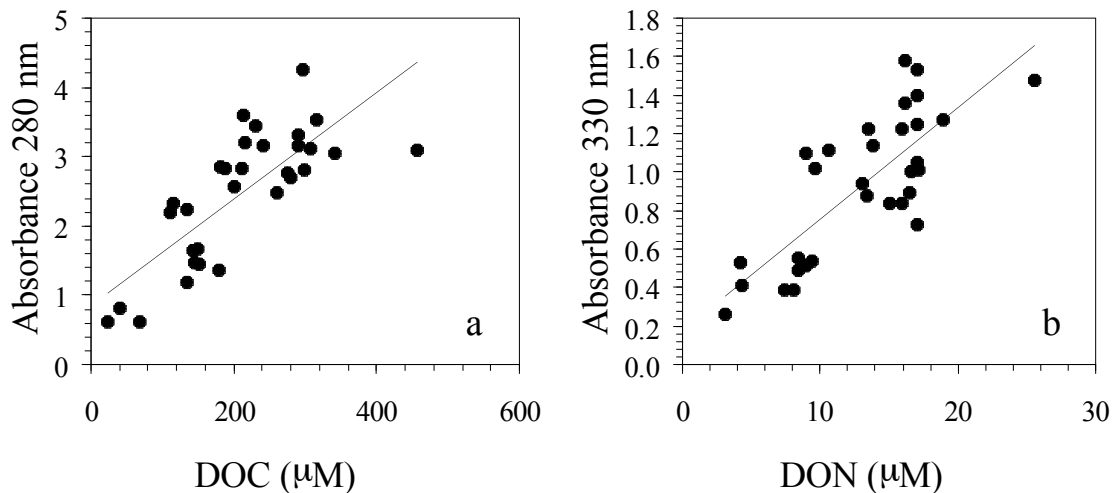


Fig. 6.15: a) Correlation between absorbance at 280 nm and DOC (μM), and b) correlation between absorbance at 330 nm and DON (μM) in sackhole brine samples collected during ISPOL (1/12/04 – 31/12/04)

6.1.4 Sea Ice Molecular Biology (SIMEC)

The aim of this project is to determine the eukaryotic biodiversity and transcriptional activity in Antarctic sea ice samples and link both using phylogenetics. Sea ice is a seemingly hostile habitat with regard to its abiotic constraints. Despite harsh conditions it is heavily populated by micro-organisms thus constituting an ecosystem of global significance. Knowledge on the diversity of organisms inhabiting sea ice is presently mainly restricted to microscopic investigations. Their gene expression activity is virtually unknown. We will describe the molecular biodiversity of selected sea ice communities by applying environmental 18s rDNA libraries, so as to unravel the identity of unknown or unculturable species, „hidden biodiversity“. We also aim to determine the transcriptional input of eukaryotic sea ice organisms to ecosystem functioning by randomly sequencing environmental cDNA libraries (“ESTs”). Using phylogenetic tools we will determine function and phylogenetic affiliation of ESTs and so link sea ice biodiversity with transcriptional activity of major groups. Finally we intend to correlate biodiversity and transcriptional activity with *in-situ* physical and biochemical parameters measured during sampling.

Sea ice samples were taken from 16 stations in the western Weddell Sea by drilling ice cores and collecting biomass rich pieces of sea ice. The latter originated from samples collected from sea ice recently broken by the ship. For further processing only the biomass rich sections of the cores, mostly the bottom 2 to 10 centimeters, were used. The eukaryotic organisms were brought onto polycarbonate filters and preserved in liquid nitrogen. From several samples of each station DNA and RNA extraction were already done on board, three replicates were stored at -80°C and taken home as back-up. Considering the concentration and purity 8 stations are promising for the use of the establishment of the rDNA and cDNA libraries. Further analysis of the quality of DNA and RNA will be done in Bremerhaven followed by establishment of the libraries and sequencing.

References

- Anderson L. G. and Jones E. P. (1985) Measurements of total alkalinity, calcium and sulphate in natural sea ice. *J. Geophys. Res.* 90, 9194–9198.
- Arar EJ and Collins GB (1997) Method 445.0: *In vitro* determination of chlorophyll *a* and pheophytin *a* in marine and freshwater algae by fluorescence. U.S. Environmental Protection Agency Publ 445: 1-17.
- Bischoff J. L., Stine S., Rosenbauer R. J., Fitzpatrick J. A., and Stafford T. W., Jr. (1993a) Ikaite precipitation by mixing of shoreline springs and lake water, Mono Lake, California, USA. *Geochim. Cosmochim. Acta* 57, 3855–3865.
- Bischoff J. L., Fitzpatrick J. A., and Rosenbauer R. J. (1993b) The solubility and stabilization of ikaite ($\text{CaCO}_3 \cdot 6\text{H}_2\text{O}$) from 0° to 25°C : Environmental and paleoclimatic implications for thinolite tufa. *J. Geol.* 101, 21–33.
- Clark RN and Roush T (1984) Reflectance spectroscopy: quantitative analysis techniques for remote sensing applications. *J Geophys Res* 89: 6329-6340.
- Gleitz M., Rutgers v. d. Loeff M, Thomas DN, Dieckmann GS and Millero FJ. (1995) Comparison of summer and winter inorganic carbon and nutrient concentrations in Antarctic sea ice brine. *Mar. Chem.* 51, 81–91.
- Grasby S. E. (2003) Naturally precipitating vaterite ($-\text{CaCO}_3$) spheres: Unusual carbonates formed in an extreme environment. *Geochim. Cosmochim. Acta* 67, 1659–1666.
- Killawee J. A., Fairchild I. J., Tison J.-L., Janssens L., and Lorrain R. (1998) Segregation of solutes and gases in experimental freezing of dilute solutions: Implications for natural glacial systems. *Geochim. Cosmochim. Acta* 62, 3637–3655.
- Mundy CJ, Ehn J, Barber DG and Michel C (in press). Transmitted spectral irradiance ratios for non-invasive estimates of microalgal biomass in landfast first-year sea ice. *Limnol & Oceanogr* .
- Nolin AW, Dozier J (2000) A hyperspectral method for remotely sensing the grain size of snow. *Remote Sens Environ* 74: 207-216.
- Omelson C. R., Pollard W. H., and Marion G. M. (2001) Seasonal formation of ikaite ($\text{CaCO}_3 \cdot 6\text{H}_2\text{O}$) in saline spring discharge at Expedition Fiord, Canadian High Arctic: Assessing conditional constraints for natural crystal growth. *Geochim. Cosmochim. Acta* 65, 1429–1437.
- Tassan S and Ferrari GM (1995) An alternative approach to absorption measurements of aquatic particles retained on filters. *Limnol & Oceanogr* 40(8): 1358-1368.

6.2 Life cycle strategy of pelagic and sympagic zooplankton

Astrid Cornils¹⁾, Rainer Kiko²⁾, Maike Kramer³⁾, Kerstin Nachtigal⁴⁾, Louiza Norman⁵⁾, Stathys Papadimitriou⁵⁾, Franz Josef Sartoris¹⁾, Sigrid Schiel¹⁾, Jacqueline Stefels⁶⁾, David Thomas⁵⁾

¹⁾Alfred-Wegener-Institut

²⁾Institut für Polarökologie, Kiel

³⁾Universität Oldenburg

⁴⁾Leibniz-Institut für

Meereswissenschaften, IFM-GEOMAR Kiel

⁵⁾School of Ocean Sciences, Anglesey

⁶⁾Rijksuniversiteit Groningen

Objectives

The Antarctic pelagic ecosystem is governed by a distinct seasonality in light, ice cover and hence, primary production. Herbivorous animals, which include many important species, are strongly affected by this production cycle. It has been shown that the dominant copepods have developed specific adaptations to utilise short-term food pulses and to endure periods of food scarcity in the pelagial. The life cycles are all well-timed to the annual periodicity, although the different species exhibit varying strategies: Ontogenetic migration coupled with a diapause at greater depth is a feature of high latitude copepod species but also of upwelling species, hence, of species living in regions with a pronounced seasonality in food availability. However, in contrast to the Arctic Ocean, only one calanoid copepod in the Southern Ocean, *Calanoides acutus*, has adopted this strategy for sure and seems to be the only true diapause species. Most Antarctic copepods apparently do not have a resting stage. They remain active during winter and adjust their feeding behaviour. Hence, when phytoplankton are scarce in the water column each species has developed its own specific strategy to avoid competition with other species.

A further overwintering strategy is to use the sea ice as habitat. Apart from harbouring a diverse group of autotrophs and protozoans, sea ice has been found to be a refuge for a number of metazoans which have adapted to live within the sea ice or at the ice/water interface, some of them permanently, some only temporarily. Hence, the sea ice itself and the ice/water interface serve as an important feeding ground for metazoans providing abundant food resources. But compared to the species richness in the water column, the number of ice-inhabiting species is low suggesting a highly specialized fauna. However, results obtained in spring 2004 to 2005 in the western Weddell Sea showed that more species than previously known live in close association to the sea ice. Acoel trubellarians, harpacticoid and calanoid copepods are the dominant metazoans occurring in the Antarctic sympagic (ice-associated) meiofauna. Their survival strategies greatly depend on ice formation and persistence.

All organisms inhabiting the sea ice have adapted to the highly variable environmental conditions of the ice habitat and must cope physiologically with both low temperatures and extremely high salinities.

In contrast to intensive work on distribution patterns in the water column and within the sea ice, our knowledge of physiological and biochemical adaptation of pelagic and sympagic organisms to the sea ice micro-environments is scarce.

The questions addressed during this study were:

- How do resting and non-resting species differ in their biochemical and physiological status?
- Which are the biotic and abiotic factors controlling the survival and development of sympagic organisms?
- Which mechanisms are responsible for the limits of tolerance to temperature and salinity?

Work at sea and preliminary results

6.2.1 Quantitative studies

Water column

The major gear employed for the quantitative sampling of mesozooplankton was the multiple opening and closing net equipped with five nets of 100 and /or 55 μm each. Stratified vertical hauls were carried out in order to study differences in the vertical and regional distribution of copepod species in relation to hydrographic regimes. On the shelf and slope stations the hauls covered the entire water column between the surface and maximal 1,000 m, while at oceanic stations, the net was deployed down to 2,000 m. The depth ranges were defined according to the temperature profiles at the respective station. In addition, a "maxi type" multiple opening-closing net with an opening of 0.5 m² equipped with nine nets of 100 μm mesh size and with a digital flowmeter was deployed twice. Nine successive depth layers were sampled between near the sea floor and the surface. The net samples were preserved in 4 % buffered formalin and at one station in 100 % ethanol for molecular genetic purposes.

For each of the plankton stations, water from a CTD was filtered for subsequent analyses of chlorophyll *a*, POC and PON concentrations.

Species composition, abundance, biomass, population structure and vertical distribution, maturity of gonads and gut contents will be analysed from these samples.

In general, we encountered a winter situation at the beginning of the cruise in the Scotia Sea and in the Scotia Weddell Confluence. The zooplankton abundance at greater depths were high and the communities were dominated by the large calanoid copepods *Calanoides acutus* and by numerous small cyclopoid and calanoid copepod species. In contrast, the abundances were low in the upper water layers. Six weeks later, we visited again our first station in the Scotia Sea on our route back to Cape Town. At this time, a spring bloom had developed and the phytoplankton biomass had increased approximately twelve-fold. The zooplankton had left their winter quarters at greater depth and had returned to the highly productive surface layers.

The net samples on the Larsen shelf revealed a very different picture. The water column seemed to be completely mixed and sediment particles were found up to the surface layers. The pteropod *Limacina* sp. and small cyclopoid copepods clearly dominated the zooplankton communities and the overall abundance of all other species was very low.

A thorough investigation of the samples will elucidate the regional and vertical distribution of the zooplankton community, and the data will be discussed with respect to the life strategies of the dominant species and relationships to hydrography and phytoplankton.

Under-ice water layer

Temperature and salinity profiles in the sub-ice water layer (0 – 6 m below the ice underside) were measured *in-situ* with a conductivity meter lowered through a core hole. Discrete water samples for analysis of algal pigments were collected from 0 and 5 m depth below the ice with a polyethylene tube with a valve at one end. The unequipped end of the tube was lowered into the water through a core hole with the valve closed. At the sampling depth, the valve was opened and closed again and the tube with the enclosed water sample was hoisted to the surface. For determination of Chl a concentration, samples were filtered through Whatman GF/F filters, extracted in 90 % acetone, homogenized and analyzed fluorometrically.

Organisms from the under-ice water (0 and 5 m depth below the ice) were quantitatively sampled with an under-ice pumping system equipped with a standardized water meter (accuracy 0.1 l) and inserts of plankton gauze (mesh size 50 μm) to concentrate the organisms. Samples were fixed in borax buffered formalin in seawater (4 %). Enumeration of species and stages from the sub-ice layer will be done in the home laboratory.

Sea ice

At most stations seven ice cores were drilled with a motor-powered KOVACS ice corer (internal diameter: 9 cm) in areas of non-deformed ice. At stations with an ice thickness of more than 2 m, only three ice cores were drilled. Generally, the uppermost parts of one core were cut into 10-cm segments, only the lowermost part was cut into a 5-cm segment. All segments were melted in the dark at 4 °C in a surplus of 0.2- μm -filtered seawater to avoid osmotic stress. Once melted, the samples were concentrated on a 20- μm mesh sized gauze and fixed in borax buffered formalin (4 % final concentration). In order to analyze the composition and abundances of sympagic meiofaunal organisms the specimens will be sorted into taxa under a stereo-microscope in the home laboratory.

From the other six (two) cores only the lowermost 5 cm were taken. Three (one) of these cores were melted in a surplus of 0.2- μm -filtered seawater, concentrated over a 20- μm gauze and then analysed unfixed. The other three (one) bottom sections were placed into a box with 50 ml filtered seawater immediately after coring, and shaken gently for about one minute. Then the water was filtered using gauze of 50 μm mesh size, and the filters with the animals were conserved in PAF (picric acid

formaldehyde). At the home laboratory, the animals will be cut, and the gut content will be analysed using raster electron microscopy (REM).

Other groups took cores for the determination of temperature, salinity, texture, nutrients, DMS/DMSP content and abundance of CaCO₃-Crystals at the same location (within 2 m²).

Live counts of sea ice meiofauna from ice-core bottom sections (0 – 5 cm) revealed higher abundances than it had been expected on the basis of earlier studies of sea ice organisms during winter time. Live counts and non-quantitative analyses also revealed a surprisingly high metazoan diversity. In accordance with earlier studies conducted during austral winter, white turbellarians, harpacticoid copepods and copepod nauplii were again found to dominate the metazoan community. However also organisms of other taxa were found, including the calanoid copepods *Stephos longipes* and *Paralabidocera antarctica* as well as some species, which have not been described for sea ice so far. Small individuals of the ctenophore *Calianira antarctica*, juveniles and adults of the nudibranch *Tergipes antarcticus*, eggs and larvae of gastropods (assumably of *Tergipes antarcticus*). Furthermore big, red turbellarians of an undetermined species were found in the ice at several stations and partly with considerably high abundances. At one station, very delicate, worm-shaped organisms of bright red colour were found.

Detailed taxonomic analyses, based on morphological studies and DNA analyses, and further countings will be conducted at the home laboratory. They shall provide further information on the community structure of sympagic meiofauna, on vertical distribution within the ice and on possible regional trends.

6.2.2 Experimental studies

Feeding and Reproduction

The feeding activities of female and copepodite stage V of *Calanoides acutus* and females *Calanus propinquus* were observed in incubation experiments. The animals were sampled from different depth layers with the multinet. The incubation experiments were conducted for 24 hours with natural phytoplankton suspension from the rosette in 20 m depth as food source.

Additional incubation experiments were conducted with *Stephos longipes*, obtained by Bongo net hauls. Females were incubated in filtered sea water mixed with different concentrations of ice algae (3.1 and 1.5 $\mu\text{g Chl } a \text{ L}^{-1}$). Additionally subsamples for microscopic counting were taken to obtain information on preferential feeding on different size classes.

Copepods were removed after the experiment, screened for mortality and transferred to pre-weighed tin caps for CN-measurements. The chlorophyll *a* concentration as equivalent for phytoplankton, was determined at the start and the end of the experiments. The total volume of each experimental bottle were filtered onto Whatman GF/F filters and analysed for chlorophyll *a*.

For each experiment, the growth rate of phytoplankton, the grazing coefficient, the mean cell concentration, the filtration rate and the ingestion rate were calculated.

In-situ egg production experiments have been conducted with *C. acutus*, *C. propinquus* and *S. longipes*. Females were incubated individually for several days, half of them fed with diatoms and half unfed. Every 24 hours the number of eggs was counted. Except for the last experiments, the females were preserved in 4 % formalin afterwards for gonad development analysis.

In order to gain information on the sympagic food web, feeding experiments were conducted with big white sympagic turbellarians and with the sympagic ctenophore *Calianira antarctica* as predators. Ciliates and small turbellarians were used as prey for both ctenophores and turbellarians; harpacticoid copepods, copepodites of the calanoid copepod *Stephos longipes* and copepod nauplii were used as prey for the ctenophores only. Experiments were conducted in cell wells filled with filtered seawater and kept in the dark at 0 °C. In each experiment, one to four predators were used, and ten or twenty prey individuals were added per predator individual. The state of predators was checked and prey individuals were counted regularly (usually every second day); dead predator individuals and eaten prey individuals were replaced in order to keep the predator-prey-ratio constant. Most experiments were run for a period of one to four weeks, some for a shorter period (one to four days). Predation rates (expressed as prey individuals per predator individuals and day) were estimated for each experiment by linear regression based on the assumption, that predation rates remained constant over the time of the experiments: thus the

cumulative number of prey individuals eaten at any moment would be proportional to the time from the beginning of the experiment.

In addition to the experimental work, individuals of all sea ice copepods, ctenophore *Calianira antarctica* and of red and white sympagic turbellarians were conserved for analyses of fatty acids and stable isotopes ($\delta^{13}\text{C}$, $\delta^{15}\text{N}$). The animals were starved and then frozen at $-80\text{ }^{\circ}\text{C}$, partly after rinsing them with distilled water.

The first experiments with *C. acutus* showed no or very low ingestion rates with a range of 0 to 5 ng chlorophyll *a* individual⁻¹ day⁻¹ (average: 1.6 ± 0.4 SE), while *C. propinquus* was clearly feeding (13.7 ± 1.4 SE). These results coincided with the observations of the egg production of the fed individual incubations. Eggs were produced by *C. acutus* only once by one female (clutch size: 44 eggs), however, this species did not produce faecal pellets and hence, is unlikely to feed. In contrast, the fed females of *C. propinquus* always produced faecal pellets and the production of eggs was observed by two females (clutch size: fed 38/ unfed 28 eggs).

However, the last feeding experiment conducted on 19 October revealed, for the first time during this cruise, high ingestion rates for *Calanoides acutus* of 242, 2 (± 31.8 SE) ng chlorophyll *a* individual⁻¹ day⁻¹. 18 feeding females have been afterwards incubated in filtered seawater for 18 hours and 6 of them produced eggs during that time (average clutch size: 47.8 eggs, range: 9 – 95 eggs), the other females showed mature brownish oocytes in their diverticula.

The experiments conducted with *Stephos longipes* revealed that the ingestion rates were higher at the lower ice algae concentration. At a chlorophyll *a* concentration of $3.1\text{ }\mu\text{g L}^{-1}$ the ingestion rate was $30.9 (\pm 6.9\text{ SE})$ ng chlorophyll *a* individual⁻¹ day⁻¹, while at $1.5\text{ }\mu\text{g L}^{-1}$ $117.5 (\pm 2.9\text{ SE})$. Females of *S. longipes* did not reproduce over the entire studied period.

The feeding experiments with sympagic turbellarians and ctenophores revealed that both feed on ciliates as well as on small turbellarians, furthermore ctenophores also feed on calanoid and harpacticoid copepods and on copepod nauplii. When using ciliates as prey, predation rates of ctenophores were higher than those of turbellarians (about one order of magnitude). Predation rates of ctenophores were also considerably higher when feeding on copepods or nauplii than when feeding on ciliates or turbellarians (about one order of magnitude).

Up to date it has been assumed that metazoans living in sea ice feed exclusively on algae and protozoans, and that they are preyed upon only by predators living under the ice. However, the feeding experiments conducted on this cruise clearly demonstrated predatory activity of sympagic turbellarians and ctenophores and showed that predation rates of ctenophores feeding on sympagic copepods or nauplii may be high. As the abundances of turbellarians in sea ice are often high, and also ctenophores are frequently found within the ice, their predation activity may considerably influence the structure of the sympagic community.

Analyses of fatty acids and stable isotopes as well as gut content analyses of sympagic species will provide further information about the structure of the sympagic food web.

Excretion and respiration

For the experimental work, live pelagic specimens were caught with a Bongo net and a multinet from different depth layers to study the metabolic activities in animals living in upper and deeper water depths. Ice-associated copepods were obtained from slush ice and also from the Bongo samples. All experiments on the physiological rates response to stress were carried out in a wide range of temperatures and salinities in the dark for 1 to 3 days in cooled containers.

Respiration was studied in incubations using oxygen concentrations measured by the Winkler method. Excretion was measured on board by ammonium production and samples were taken for the later determination of urea, DON, nitrate and phosphate. The respiration and excretion rates were calculated as the difference between dissolved oxygen and ammonium in the control and experimental bottles before and after the experiment.

The respiration rates of female *Calanoides acutus* varied greatly with time and sampling depth (Fig. 6.16). The respiration rates were low at the beginning of our studies probably indicating overwintering conditions and increased with time. An increase was also found for the respiration rates with decreasing sampling depth with low rates at greater depths compared to mid-water layers.

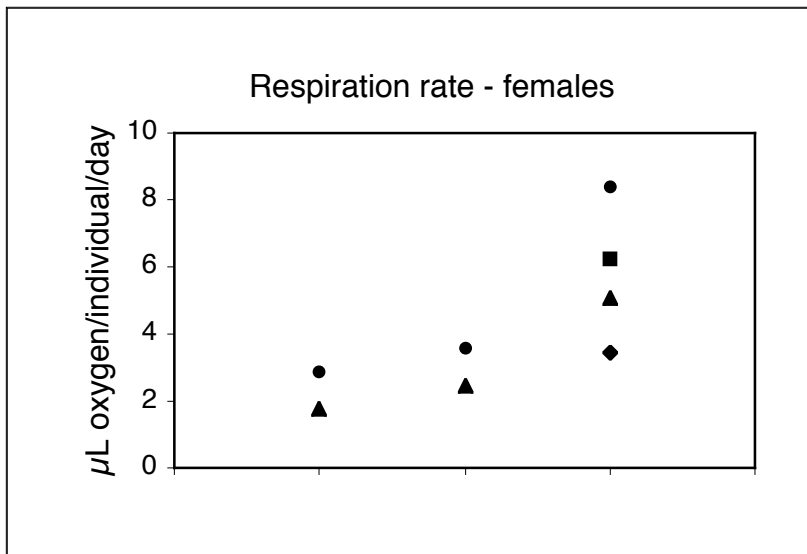
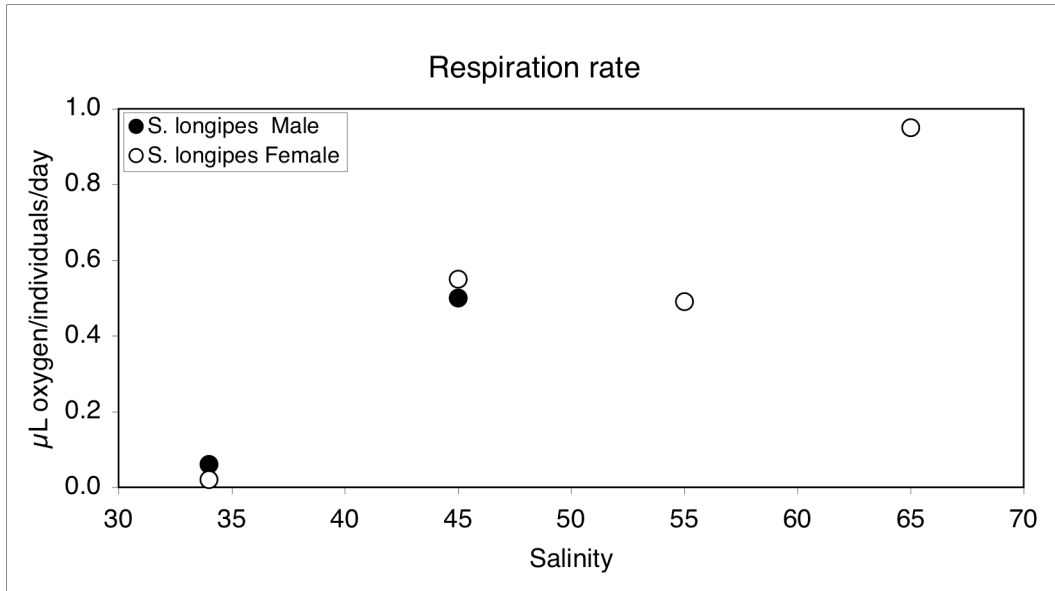


Fig. 6.16: Respiration rates of *Calanoides acutus* females from different water depth at different times

The oxygen consumption values determined in this study fit well into the range of previous data. The extremely low oxygen consumption rates at the beginning were probably due to overwintering conditions (diapause) of the specimens.

The small ice-associated calanoid copepod *Stephos longipes* oxygen consumption rates were low at a salinity of 35 and increased with increasing salinities (Fig. 6.17a) probably indicating stress situations at higher salinities, which this species easily encounters in the brine channels of the sea ice.

a)



b)

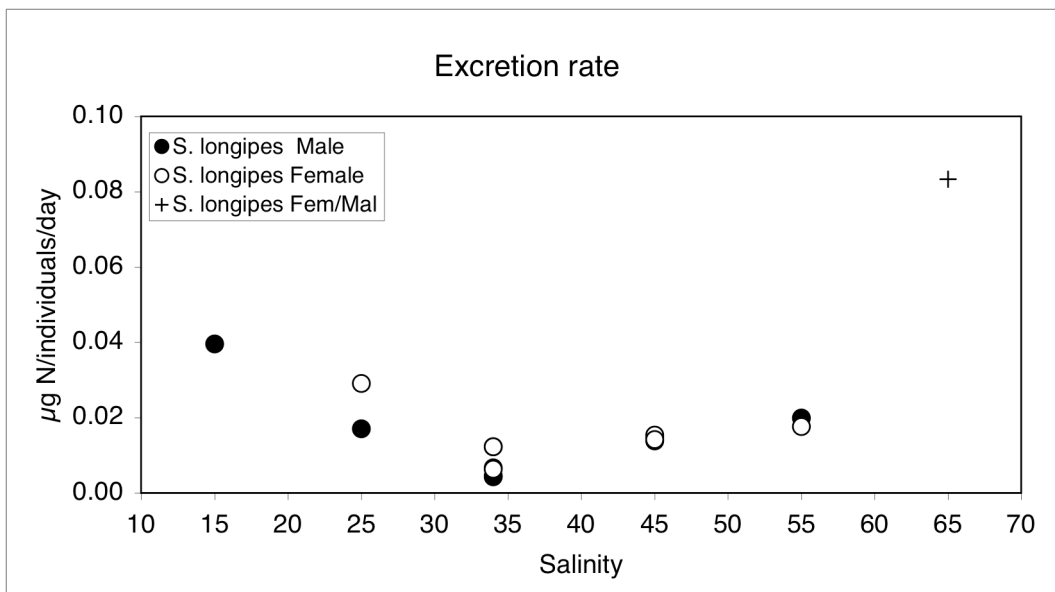


Fig. 6.17: Respiration rate (a) and excretion rate (b) of *Stephos longipes* at different salinity and temperature regimes

Our experiments on excretion rates of adults of the small ice copepod *Stephos longipes* in relation to different salinity/temperature regimes show clearly an increase at high salinity (S=65) as well as at low salinities (Fig. 6.18), which coincides clearly with a high mortality rate of individuals at these extreme salinities. This means that adults are well adapted to a salinity range between about 35 and 55 and they seem to be stressed at lower and higher values.

In-situ survival of sympagic organisms

Sympagic animals live inside a brine channel system, which forms, when seawater freezes. During this process, the contained salt is not included into the ice crystals, but collects in interstices, which finally form the brine channels. Salinities in these brine channels can vary between S = 2 and 200 and temperatures between 0° and -20°C. Sympagic animals therefore have to cope with varying and sometimes extreme temperatures and salinities. Also the brine volume is reduced, when temperatures inside the ice drop. Until now, our knowledge about temperature thresholds for different sympagic species is still scarce. Especially *in-situ* conditions are difficult to simulate in the laboratory.

In order to study the survival limits of different sympagic species under *in-situ* conditions, we took the lowermost 5 cm from 25 ice cores in an 2 m² area of level ice (ice thickness on average 1 m) and incubated them at different temperatures (five cores each at -2.5 °C, -4 °C, -5 °C, -6 °C and -7 °C) for two days. Thereafter the cores were thawed in a surplus of filtered seawater at 4 °C and enriched over a 20 µm gauze live and dead specimens determined, isolated from the sample and fixed with borax buffered formalin (4 % final conc.) separately.

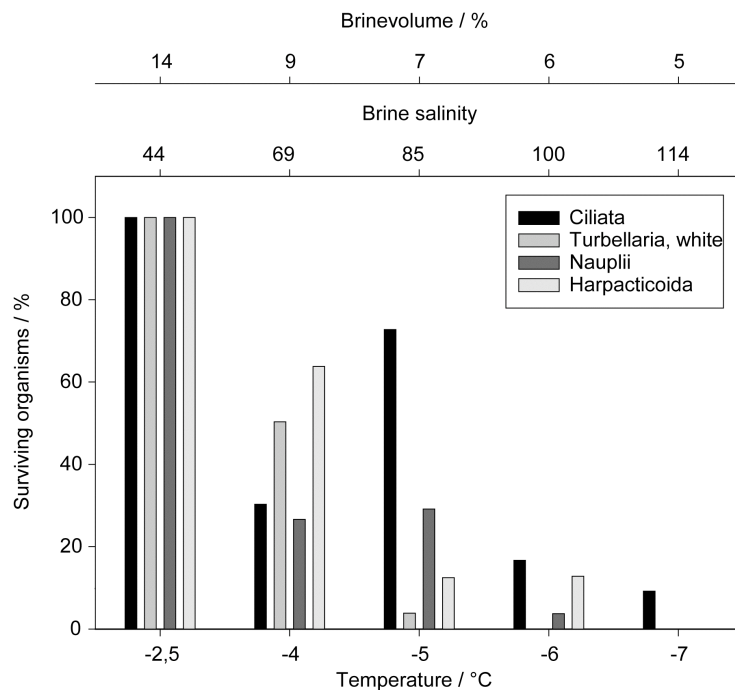


Fig. 6.18: Survival of different meiofauna taxa in 5 cm bottom sections incubated for two days at the indicated temperatures

By incubating 5 cm bottom sections at different subzero temperatures we were able to determine the survival limits of Harpacticoids (-6.0 °C), white Turbellarians (-5.0 °C) and Ciliates (below -7 °C) in the brine system itself. Furthermore our data show, that *Stephos longipes* survives at least -4.0 °C and the red Turbellarians -6.0 °C within the ice. These limits are probably determined by temperature and salinity, but also through the reduction of brine channel size and the different capabilities of the sympagic animals, to cope with these changes. Further analysis, first of all the identification of the harpacticoids to species level in the home laboratory will lead to a better understanding of survival limits for these animals.

6.2.3 Ion regulation

Objectives

The biogeography of marine crustaceans in cold oceans is related to the combined effects of extracellular Mg^{2+} levels $[Mg^{2+}]_e$ and low temperature, which act synergistically to slow muscular activity in the cold. In conclusion, crustaceans with well developed magnesium extrusion mechanisms are likely to be favoured in the cold compared to their counterparts with less effective mechanisms. To our knowledge no information is available about extracellular ion regulation in copepod crustaceans.

Work at sea

To test our hypothesis that physiological performance at low temperatures depends on $[Mg^{2+}]_e$ regulation pelagic and sympagic copepod species have been collected and the capability to regulate $[Mg^{2+}]_e$ has been investigated.

Preliminary results

All of the copepod species investigated (pelagic as well as sympagic) do regulate extracellular magnesium levels below sea water levels confirming the relationship between $[Mg^{2+}]_e$ and the activity level of animals at subzero temperatures.

In *Calanoides acutus*, which undergoes vertical ontogenetic migrations including diapausing in greater depth, large amounts of ammonium (NH_4^+) have been detected in the haemolymph. However, these high ammonium values could also be detected in *Rhincalanus gigas* and suggest that this species also overwinters at depth in a resting stage. In some of these copepods NH_4^+ replaces nearly 90 % of the Na^+ . Most likely this acts as a buoyancy mechanism. The reduction of fluid density by ion replacement, the 'lighter' ions i.e. NH_4^+ replacing 'heavier' ions i.e. Na^+ , to achieve neutral or positive buoyancy is well known from a group of pelagic cephalopod, the cranchiid squids and from a deep sea shrimp *Nostostomus gibbosus*. Compared to other buoyancy mechanisms, ammoniacal buoyancy offers an advantage in that it maintains function at high ambient pressure and results from storage of a waste product of energy metabolism. This is the first report of copepod species using ion replacement to reduce fluid density.

6.2.4 Osmoregulation and thermal hysteresis

Objectives

Intracellular ice formation is hazardous for any organism. Therefore, sympagic organisms need to protect themselves against it. One option to avoid ice formation is, to keep the body fluid at the ambient osmolarity. Another option is the synthesis of antifreeze proteins, which hamper ice formation through attachment to the ice surface. This results in a reduction of the freezing point of the liquid. The melting point of the crystal is not influenced. Therefore a thermal hysteresis can be measured.

Work at sea

We determined the osmolarity of the hemolymph for two species, *Paralabidocera antarctica* and *Calanus acutus* and searched for thermal hysteresis in four Species, *Paralabidocera antarctica*, *Calanus acutus*, *Stephos longipes* and *Drescheriella spec.*

Preliminary results

Paralabidocera antarctica and *Calanus acutus* are isosmolar to seawater, furthermore *P. antarctica* is isosmolar to media with a salinity of 25 and 55. Therefore the sympagic species *P. antarctica* is protected from internal crystal growth in a range from -3.1 °C to -1.4 °C. From the four tested species, only *S. longipes* hemolymph showed a clear thermal hysteresis of approx. 2 °C. Therefore this sympagic species is probably protected from internal ice growth by antifreeze proteins. This is also supported by our molecular-biological studies, which revealed the presence of a mRNA coding for an antifreeze protein in *S. longipes*. We will analyse the osmolarity of the hemolymph of *S. longipes* and *Drescheriella glacialis* at different incubation salinities and temperatures in the home laboratory. For this and for molecular-biological, as well as other physiological experiments we established laboratory cultures of these copepods.

6.3 Dynamics of organic sulphur compounds in sea ice

Objectives

Organic sulphur compounds have received much attention due to their potential role in climate control. Sea ice constitutes an important pool of organic sulphur compounds. The most important sulphur compounds are: dimethylsulphoniopropionate (DMSP), dimethylsulphide (DMS) and dimethylsulphoxide (DMSO). DMSP is produced by algae; DMS is one of the cleavage products of DMSP and DMSO is an (photo-)oxidation product of DMS. DMS is a semi-volatile compound that is studied intensively because its atmospheric oxidation products are involved in the formation of condensation nuclei and clouds. Model studies indicate that, especially over large areas of the Southern Hemisphere, DMS may affect climate. Estimations on Antarctic DMS production are based on a very limited number of data. The marginal ice zone has been depicted as the main source area for high DMS emissions during the period of ice melt. There is, however, very limited data available on the distribution, pool sizes and dynamics of DMS and related compounds in sea ice.

The data set collected during ANT-XXIII/7 will add to data collected during the ISPOL cruise (ANT-XXII/2) in the summer season of 2004/2005. Given the potential physiological roles of DMS, DMSP and DMSO (cryoprotectant, osmoticum, oxygen-radical scavengers), it is hypothesised that organisms trapped in brine pockets, need these compounds to survive the extreme conditions in winter sea ice. Therefore, our main aim was to study the dynamics of these sulphur compounds during the transition of winter to spring. More specific, the first objective was to study the spatial heterogeneity of S-compounds in sea ice and to couple these data to algal pigment fingerprints and biomass parameters. This work is done at the 'main coring site' and can therefore be linked to a suite of physico-chemical parameters measured by others (Dieckmann et al, Haas et al; Thomas et al.). A second objective was to study conversion processes of S-compounds in bottom ice communities and during ice melt in incubation experiments.

Work at Sea

Due to the instable nature of DMS and DMSP, a detailed study of the dynamics of these compounds is yet impossible without direct analyses. We therefore performed all sulphur analyses on board, using a Proton Transfer Reaction Mass Spectrometer (PTR-MS). This also allowed us to make use of stable isotopes of DMS and DMSP added to ice samples, in order to follow conversion processes during ice melt. DMS can be analysed directly by PTR-MS from a carrier-gas stream that purges a liquid sample. DMSP is analysed as DMS after hydrolysis of a sample with NaOH for at least 24 hours. DMSO is analysed as DMS after reduction with TiCl₃ for at least 3 days. Dissolved DMSP was separated from particulate DMSP by gravity filtration over a Whatman GF/F filter. Since there was no indication of a particulate DMSO fraction, DMSO was analysed only in filtered samples. In all fractions, natural and artificially added stable isotopes were analysed simultaneously.

Extensive sampling of ice cores and sackholes was done in close collaboration with Dieckmann, Haas, Thomas and co-workers. Spatial variability of DMS, DMSP and DMSO was investigated in 14 ice cores: 11 were taken at the 'main coring site' at regular intervals along the cruise track; 3 cores were taken by helicopter from the Larsen-A shelf area. Cores were sectioned in 5 to 10 cm intervals and thawed at +4 °C in hypersaline water. To all cores, except those from the Larsen-A area, stable DMS and DMSP-isotopes were added before melting took place. After melting, DMS, DMSO and DMSP in filtered and unfiltered fractions were determined. From the same melted samples, subsamples were taken for algal-pigment analyses, which can give us an indication of the abundance and biomass of different phytoplankton groups in the samples. Pigment samples were stored at -80 °C and will be analysed at home by HPLC. In addition, DMS, dissolved and particulate DMSP and DMSO were investigated in brine samples from sackholes at 22 locations. This was a collaborative action with D. Thomas and co-workers.

During 7 occasions, on-board incubation experiments were performed with ice algal communities. In these experiments, the effects of light and salinity on various conversion processes were studied. Samples were taken for DMS, dissolved and particulate DMSP and DMSO, for HPLC-pigments, phytoplankton composition (G. Dieckmann et al.) and for photosynthetic parameters using PAM fluorometry (K. Meiners). Finally, in collaboration with R. Kiko and S. Schiel, zooplankton samples were analysed for their DMSP content, thereby adding to the dataset from ISPOL, in which the omnipresence of DMSP in many zooplankton species was shown.

Although all sulphur compounds were analysed on board, data calculation will be done later. Therefore, only qualitative statements can be given here.

Preliminary and expected results

6.3.1 Ice cores

Bulk concentrations of S-compounds in sea-ice cores showed a high variability. A rough qualification showed that DMS varied between 1 and 5,000 nM, dissolved DMSP between 1 and 1,000 nM, particulate DMSP between 1 and 2,000 nM and DMSO between 1 and 800 nM. As a general rule, high internal concentrations were more developed in ice cores of the northern part of the cruise track, whereas bottom communities with high S-concentrations were better developed in ice along the Antarctic Peninsula. Conversion of DMS and DMSP during the melting process seems to correlate with high algal biomass. Interestingly, the added isotopes seem to reveal that DMSP conversion into DMS, DMSP uptake into particulate material and DMS oxidation into DMSO are common processes in sea-ice communities.

6.3.2 Sackholes

Concentrations of S-compounds in brine samples also were highly variable. Roughly, DMS varied between <1 and 5,000 nM, DMSP between 10 and 3,000 nM and DMSO between 10 and 10,000 nM. DMSO levels were usually in the same order of

magnitude as total DMSP levels. We expect to find high variability in healthiness of the sampled communities, as can be revealed from the fraction of dissolved DMSP to total DMSP. This information will later be compared with photosynthetic parameters (K. Meiners) and other biochemical parameters (Thomas et al.).

6.3.3 Experiments

In an on-board climate chamber, 4 experiments were done with bottom-ice communities diluted in filtered surface water. DMSP to DMS conversion could always be detected. DMSP incorporation and DMS oxidation differed between experiments. Samples taken for community structure and biomass may reveal the nature of these differences. In 3 experiments with ice sections of the bottom 25 cm of ice cores a comparison can be made with dark incubations of comparable ice sections. This may give an indication of the light and biomass dependency of the conversion processes studied. As an example, one experiment with 3 ice core sections incubated in the light is presented here. The fate of added stable isotopes revealed that 25 to 33 % of DMSP was taken up by particles and 8 % was converted into DMS (Fig. 6.20 a). A fraction of 35 to 50 % could not be found back in the form of DMS, DMSP or DMSO. A possible explanation is that that part has been demethylated. DMS was more stable with 50 to 75 % of the added isotope still present as DMS after the 48h incubation; 3 to 12 % had been oxidised into DMSO (Fig. 6.20 b). The remaining 23 to 41 % possibly has been assimilated by bacteria.

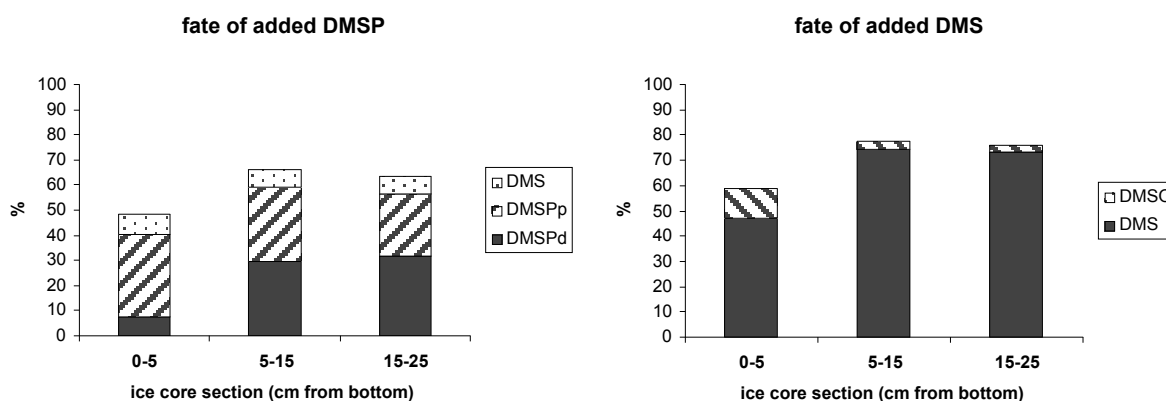


Fig. 6.20: Fate of stable isotopes added to ice core sections that were left to melt in hypersaline water over a period of 48h

6.3.4 Zooplankton

Several zooplankton species were analysed for their DMSP content. In salinity experiments with the copepod *Stephos longipes*, highest DMSP contents were observed in animals from ambient salinities. The release of DMSP, both at low (15) and high (>55) salinities, may be an indication of a poor physiological condition. Previous starvation experiments during ISPOL had shown that *S. longipes* is not able to retain DMSP in its body tissue. If *S. longipes* uses DMSP to balance its water

potential under cold conditions, both experiments suggest that this copepod is not very well equipped to stay in sea ice during winter conditions with low temperatures and high salinities. In contrast, Turbularians seem to be able to retain DMSP in their body, even after a prolonged period of starvation. In general, zooplankton species that live in ice for a substantial part of their life cycle, contain larger amounts of DMSP than their pelagic counterparts.

With our data we expect to provide essential and basic information on the heterogeneity and dynamics of sulphur compounds in multi- and first-year sea ice of the Weddell Sea. With this insight we hope to be able to quantify the influence of biological processes on DMS emission to the atmosphere around Antarctica and improve scenarios of climate forcing by ice-ocean-atmosphere interactions and the significance of sea ice. It is also expected to provide fundamental information on the role of organic S-compounds in the physiology of sea-ice organisms to survive extreme sea-ice habitats during winter and to cope with sudden shifts in light, temperature and salinity when ice melts.

7. BATHYMETRY

7.1 Sea floor morphology and topography of the northern Weddell Sea

Evgeney P. Dubinin¹⁾, Anja Rieck²⁾, Jana Schneider²⁾ ¹⁾Vernadsky Institute of Geochemistry and Analytical Chemistry, Moscow, Russia
²⁾Alfred-Wegener-Institut

Introduction

Precise depth measurements are necessary to provide seafloor morphology and structure as basic information for geosciences as well as for physical and life sciences. During the ANT-XXIII/7 the bathymetric group played an important role for oceanographic studies. The knowledge about the precise sea floor topography is essential for the site selection of oceanographic CTD-stations and other sample locations in areas of the Weddell Sea Deep Water passages (WSDW).

Objectives

The paramount task and focus of the bathymetric work programme was to supervise the continuous and proper operation of the Hydrosweep multibeam system in technical and scientific terms and to organize the recording, processing and archiving of swath sonar data. Secondly, the refraction correction and the physical calibration of multibeam data were conducted by the use of CTD- and Hydrosweep Cross-calibration measurements. Finally the depths data was modelled and visualized as bathymetric map or 3D-view. A further objective of the bathymetry group was the collection of echo sounding for global bathymetric databases of international organisations like the IHO or GEBCO.

A special area of research interests was the vicinities of the Orkney and the Philip Passages east and west of the South Orkney Plateau, as well as the slopes of the Powell Basin and the slope regions off the Larsen Shelf. Furthermore, a systematic survey was planned north of the South Orkney Plateau, where an earthquake of a magnitude of 7.5 took place on 4 August 2003 (epicentre 60°30'S, 43°24'W) in order to study eventual slumpings or other changes of the sea floor topography in the earthquake area.

Work at sea

During the entire cruise, the Hydrosweep system was operated at 90° aperture subdivided into 59 physical preformed beams (PFBs). The refraction correction was realized on the base of sound velocity profiles derived from 22 (out of 58) CTD-

stations in the operations area sampled and consigned by the oceanographic working group. During transits without any CTD stations Hydrosweep's cross fan calibration data was used.

On the Hydrosweep operator and control monitor (Hydromap Online) all relevant sensor data are displayed for supervising the correct operation of the system and for evaluating and controlling the recorded data.

The recorded data were exported into the international raw data format SURF in blocs of 8 hours. Visual analyses of the navigation data was performed to detect outliers, gaps and errors in ship's position using the Hydrosweep Software 'Hydromap Offline'.

For the post-processing the bathymetric data was imported into CARIS HIPS & SIPS software to manually flag unplausible depths, and to determine digital terrain models (DTM). Depending on water depth, ship speed, ice situation and data quality, the cell size for the DTM modelling was chosen between 50 to 100 m. The DTM were also used for a specific quality assessment of the depth data and to localize the PIES-stations.

The final processing step includes the depths data export into ASCII-xyz (longitude, latitude, depth) files, which is a convenient input format for the map generation software GMT (Generic Mapping Tool). All multibeam data and the ship's navigation data were processed and visualized during the cruise.

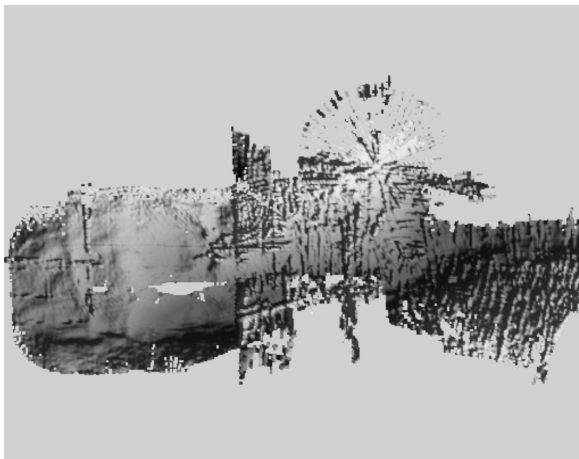


Fig. 7.1: Boundary between open water and ice

Figure 7.1 exhibits distinctly the quality difference between measurements in open waters (westerly part) and in ice covered waters (easterly part). Wrong depth values are flagged using CARIS HIPS software, and are excluded from export, further calculations and mapping. As a consequence, the number of depth measurements decreases and size of gaps increases in sea-ice covered regions.

Statistics

Measured track length: 8,878 nm / 16,442 km

Depth accuracy: ~ 0.5 – 1 % of water depth

Min. water depth: 170 meter

Max. water depth: 8,010 meter.

Preliminary results

During the cruise multibeam and navigational data were continuously recorded, processed and archived. Small scale bathymetric maps were produced using GMT in order to support specific studies in research areas like the Orkney Passage, Philip Passage, Bransfield Strait and along the Larsen continental shelf, and for the interpretation of oceanographic CTD-stations.

The routes of the WSDW in the east (Orkney Passage) and the west (Philip Passage) of the South Orkney Plateau were well mapped with the multibeam system. In combination with existing data new bathymetric working charts were produced on board (Fig. 7.2) The oceanographic programme was further supported by surveys along the CTD station profile.

7.2 Regional bathymetric studies

7.2.1 Philip Passage

Figure 7.2 visualizes the bathymetry of the South Scotia Ridge north of the Powell Basin. The deepest parts of the Philip Passage are covered by multibeam data which were combined with the results from previous *Polarstern* expeditions and plotted over ETOPO2 contour lines.

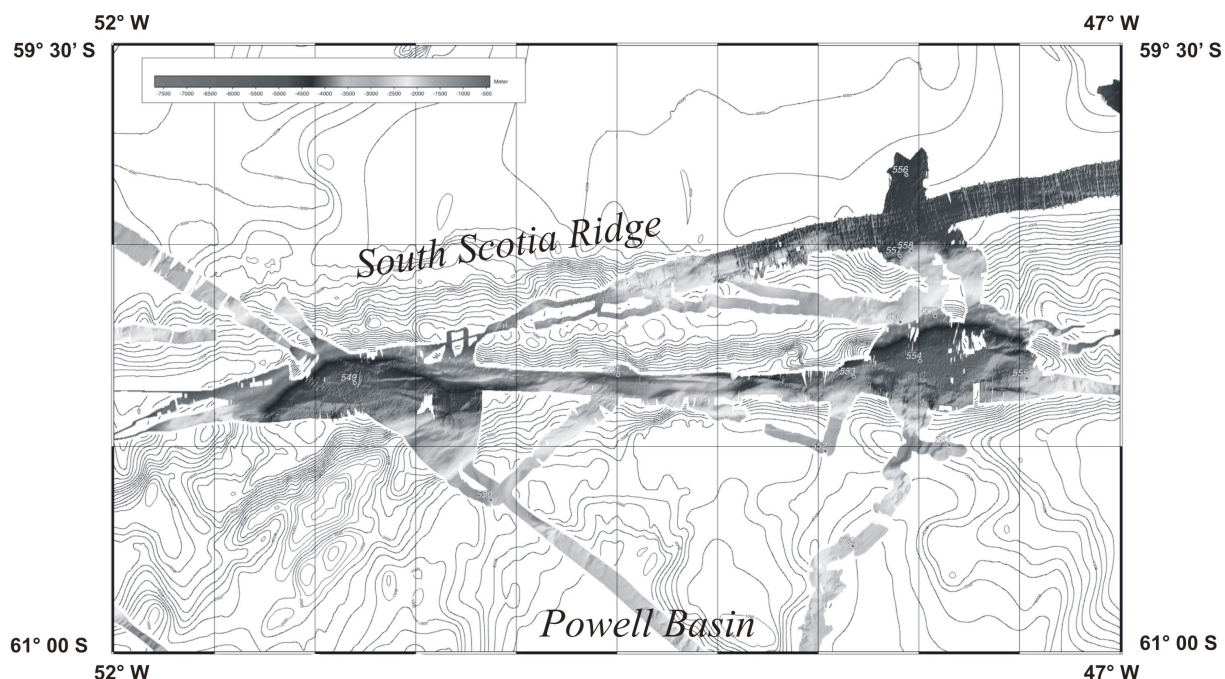


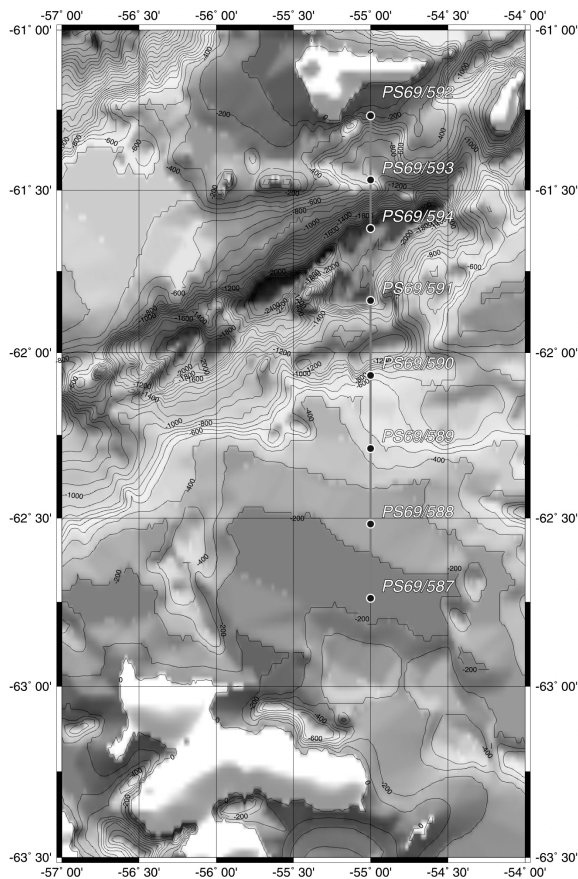
Fig. 7.2: Multibeam tracklines at the Philip Passage over ETOPO2 contours

In order to study the influence of the topographic relief on the transport routes and mechanisms of the WSDW a large number of CTD were taken in the passage area. Since no detailed bathymetric data were available a priori the selection of the stations was based on GEBCO or ETOPO2 data.

In regions of pronounced topographic relief (e.g. a western slope along a basin or the deepest point of a trough), CTD stations were determined and selected *in-situ* by studying the online multibeam contours. During these operations and particularly at stations 559 and 560 strong discrepancies between the actual sea floor topography and the GEBCO and ETOPO2 charts amounted up to several hundreds of meters in depth, and kilometers in position.

Similar bathymetric studies were performed also in the Orkney Passage.

7.2.2 Bransfield Strait



The bathymetric map (Fig. 7.3) visualizes the CTD stations along the meridian 55°W in relation to the ambient seafloor topography. This CTD transect was measured in the frame of a Brazilian oceanographic project repeatedly over several campaigns. As a result of new multibeam measurements, substantial discrepancies to the used GEBCO depths were found, resulting in a reasonable re-location of stations to the greatest adjacent depth.

Fig. 7.3: Bathymetric map for the Bransfield Strait CTD-stations

7.2.3 Bathymetry of the Earthquake Epicentre

On 4 August, 2003 an Earthquake (7.5 Mag.) occurred north of the South Orkney Plateau. The epicenter was located on 64°31.94' S and 43°24.72' W at the southern slope of the South Scotia Trough. In order to study possible slumpings or other deformations of the seafloor topography, it was planned to perform in addition to multibeam data measured in this region during ANT-XXII/4 additional swathes

covering directly the epicenter and its vicinity. Due to time shortage five lines parallel to the slope were surveyed. Heavy ice coverage in the survey area produced noisy data resulting in outliers and data gaps. A reduction of data quality and quantity was noticed after the post-processing.

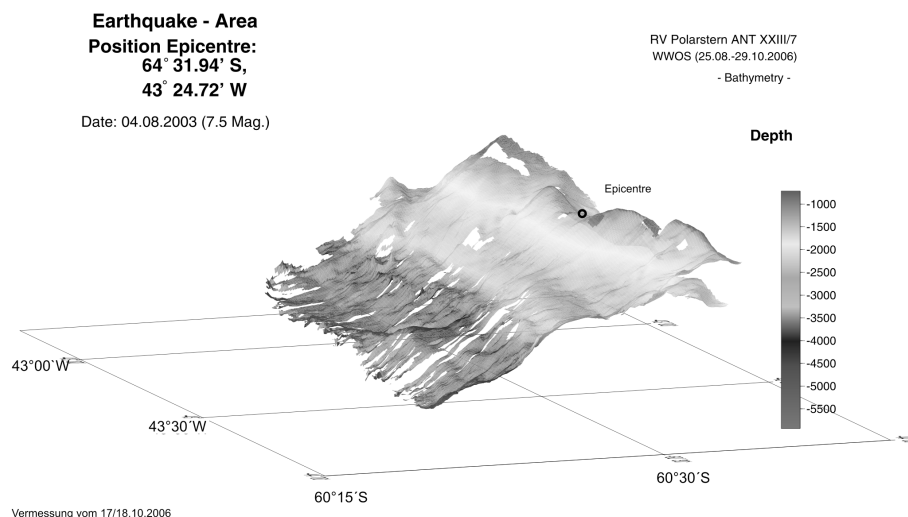


Fig. 7.4.: GMT- 3D-map at the surveyed region north of the South Orkney Islands

Figure 7.4 is a perspective view from northwest of the topography around the earthquake epicentre. The earthquake area was covered during a 24 hours survey with 5 profiles with average swath width of 3 nm. The area extends from 42°50'W to 43°45'W and 60°20'S to 60°35'S (50.5 km x 27.9 km). The shaded perspective view in figure 7.4 represents the northern slope of the South Orkney Plateau to the South Orkney Trough, from less than 1,000 m to 6,000 m water depth. The seismically detected epicenter is located between small hills at the upper edge of the shelf. Nevertheless, from this product there are no obvious marks, like slumpings as possible consequences of the earthquake visible in the topography. Furthermore, additional data and investigations are needed for further interpretation.

7.2.4 Transit

During the transits to and between the main research areas several submarine features of geologic interest were crossed. A cross section of the South Sandwich Trench with its deepest part of more than 8,010 m is shown in Fig. 7.5, and another cross section in Fig. 7.6 represents the Discovery Rise in SW-NE direction.

Actual collected and processed bathymetric data will close some gaps in existing data, sets for regional mapping projects like the International Bathymetric Chart of the Southern Ocean (IOC/IHO/SCAR project IBCSO) and improve the data bases for Nautical Charts in Antarctic waters (IHO HCA). The data will be submitted to the international IHO Data Centre for Digital Bathymetry (DCDB).

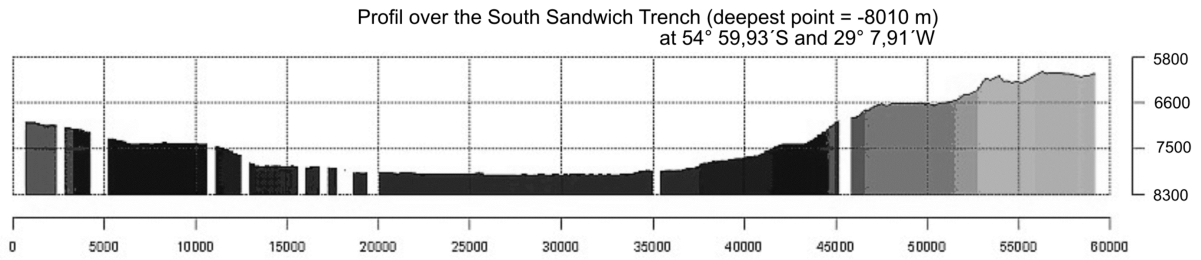


Fig. 7.5: Profile over the South Sandwich Trench (deepest point = -8010 m)

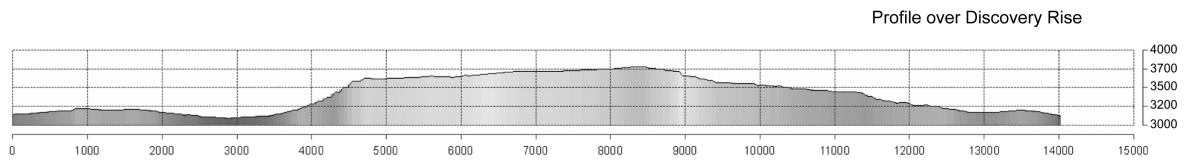


Fig. 7.6: Profile over Discovery Rise

APPENDIX

A.1 PARTICIPATING INSTITUTIONS

A.2 CRUISE PARTICIPANTS

A.3 SHIP'S CREW

A.4 STATION LIST

A.1 BETEILIGTE INSTITUTE / PARTICIPATING INSTITUTIONS

	Address / Adresse
ACE	Antarctic Climate & Ecosystems Cooperative Research Centre (ACE CRC) Private Bag 80 Hobart, Tas 7001 /Australia
AWI	Alfred-Wegener-Institut für Polar- und Meeresforschung in der Helmholtz-Gemeinschaft Postfach 120161 27515 Bremerhaven
CLE	College of Life & Environment Zhejiang Wanli University Ningbo, 315100 / China
DWD	Deutscher Wetterdienst Geschäftsfeld Seeschifffahrt Bernhard-Nocht-Str. 76 20359 Hamburg
FSU	Department of Oceanography Florida State University 0102 OSB, West Call Street Tallahassee, Florida 32306-4320 / USA
FURG	Fundação Universidade Federal do Rio Grande Rua Eng. Alfredo Huch, 475 - Centro CEP: 96201-900 - Rio Grande/RS / Brasil
GEOKHI	Vernadsky Institute of Geochemistry and Analytical Chemistry Russian Academy of Sciences 19, Kosygin Street Moscow / 119991 Russia

	Address / Adresse
GKSS	GKSS-Forschungszentrum Geesthacht GmbH Max-Planck-Straße 1 21502 Geesthacht
HeliService	Heli Service International GmbH Am Luneort 15 27572 Bremerhaven
IFM-GEOMAR	Leibniz-Institut für Meereswissenschaften IFM-GEOMAR Düsternbrooker Weg 20 24105 Kiel
ILTS	Institute of Low Temperature Science Hokkaido University Nishi-8, Kita-19 Sapporo 060-0819 / Japan
IPÖ	Institut für Polarökologie Universität Kiel Wischhofstr. 1-3, Geb. 12 24148 Kiel
IUP	Institut für Umweltphysik Universität Bremen Otto-Hahn-Allee 1 28359 Bremen
LCOE	State Key Laboratory of Coastal and Offshore Engineering Dalian University of Technology 116024 Dalian / China
NIOZ	Royal Netherlands Institute for Sea Research P.O.Box 59 NL-1790 AB Den Burg (Texel) The Netherlands

Address / Adresse

PG	Pfaffling Geophysics Eilbeker Weg 36 22089 Hamburg
RUG	Rijksuniversiteit Groningen Oude Boteringestraat 44 9712 GL Groningen The Netherlands
UEA	University of East Anglia Norwich NRW 7TJ United Kingdom
UWB	School of Ocean Sciences University of Wales, Bangor Menai Bridge Anglesey, LL59 5AB United Kingdom

A.2 FAHRTTEILNEHMER / CRUISE PARTICIPANTS

Name	Vorname/ Name	First	Institut/ Institute	Beruf / Profession
Allhusen	Erika		AWI	Technician
Aspmo	Katrine		GKSS	Chemist
Büchner	Jürgen		Heli Service	Pilot
Cornils	Astrid		AWI	Biologist
Da Silva Duarte	Vagner		FURG	Oceanographer
Dai	Fangfang		CLE	Biologist
Dieckmann	Gerhard		AWI	Biologist
Dubinin	Evgeny P.		GEOKHI	Geophysicist
Feldt	Oliver		Heli Service	Technician
Franz	Karl		Heli Service	Pilot
Friedrich	Anica		Uni Trier	Student, Life sciences
Friedrich	Ana Claudia		FSU	Chemist
Haas	Christian		AWI	Geophysicist
Hartig	Rüdiger		DWD	Meteorologist
Heckmann	Markus		Heli Service	Technician
Hellmer	Hartmut		AWI	Oceanographer
Heuven	Steven van		NIOZ	Oceanographer
Os	Desiree den		RUG	Biologist
Jacobi	Hans-Werner		AWI	Chemist
Kerr Duarte Perreira	Rodrigo		FURG	Oceanographer
Kiko	Rainer		IPÖ	Biologist
Kirk	Henning		IUP	Physicist
Kramer	Maike		UO	Student, Marine sc.
Lemke	Peter		AWI	Physicist, Chief Scientist
Li	Zijun		LCOE	Oceanographer
Macrander	Andreas		AWI	Oceanographer
Mata	Mauricio		FURG	Oceanographer

Name	Vorname/ Name	First	Institut/ Institute	Beruf / Profession
Meiners	Klaus		ACE	Biologist
Nachtigall	Kerstin		IFM-GEOMAR	Technician
Nicolaus	Marcel		AWI	Geophysicist
Norman	Louiza		UWB	Biologist/Chemist
Nunez	Nuno		UEA	Student, Cartography
Olbers	Dirk		AWI	Physicist
Papadimitriou	Stathys		UWB	Chemist
Pfaffling	Andreas		PG	Geophysicist
Rieck	Anja		AWI	Student, geodesy
Rücker van Caspel	Mathias		FURG	Oceanographer
Sartoris	Franz-Josef		AWI	Biologist
Schiel	Sigrid		AWI	Biologist
Schneider	Jana		AWI	Student, cartography
Sellmann	Lutz		AWI	Physicist
Sonnabend	Hartmut		DWD	Technician
Stefels	Jacqueline		RUG	Biologist
Thomas	David		UWB	Biologist
Toyota	Takenobu		ILTS	Geophysicist
Uhlig	Christiane		AWI	Student, biology
Vogel	Ines		AWI	Technician
Wang	Zipan		CLE	Biologist
Wassmuth	Jürgen			Photographer

A.3 SCHIFFSBESATZUNG / SHIP'S CREW

No.	Name	Rank
01.	Pahl, Uwe	Master
02.	Grundmann, Uwe	1.Offc.
03.	Farysch, Bernd	Ch. Eng.
04.	Fallei, Holger	2.Offc..
05.	Niehusen, Frank	2.Offc.
06.	Peine, Lutz G.	2.Offc.
07.	Ignatzy, Klaus	Doctor
08.	Hecht, Andreas	R.Offc.
09.	Minzlaff, Hans-Ulrich	1.Eng.
10.	Sümnicht, Stefan	3.Eng.
11.	Wanke, Steffen	3.Eng.
12.	Scholz, Manfred	Elec Eng.
13.	Himmel, Frank	ELO
14.	Muhle, Helmut	ELO
15.	Nasis, Ilias	ELO
16.	Verhoeven, Roger	ELO
17.	Loidl, Reiner	Boatsw.
18.	Reise, Lutz	Carpenter
19.	Bäcker, Andreas	A.B.
20.	Behm, Dietmar	A.B.
21.	Hagemann, Manfred	A.B.
22.	Lamm, Gerd	A.B.
23.	Schmidt, Uwe	A.B.
24.	Schubert, Holger	A.B.
25.	Wende, Uwe	A.B.
26.	Winkler, Michael	A.B.
27.	Preußner, Jörg	Storek.
28.	Elsner, Klaus	Mot-man
29.	Hartmann, Ernst-Uwe	Mot-man
30.	Ipsen, Michael	Mot-man
31.	Pinske, Lutz	Mot-man
32.	Voy, Bernd	Mot-man
33.	Müller-Homburg, R.-D.	Cook
34.	Martens, Michael	Cooksmate
35.	Möller, Wolfgang	Cooksmate
36.	Jürgens, Monika	1.Stwdess
37.	Wöckener, Martina	Stwdss/Kr
38.	Czyborra, Bärbel	2.Stwdess
39.	Gaude, Hans-Jürgen	2.Steward
40.	Hu, Guo Yong	2.Steward
41.	Huang, Wu-Mei	2.Steward
42.	Wartenberg, Irina	2.Stwdess
43.	Wartenberg, Irina	2.Stwdess.
44.	Yu, Kwok Yuen	Laundrym.

A.4 STATION LIST

A.4 STATION LIST PS 69

Station	Date	Time	Position Lat	Position Lon	Depth [m]	Gear Abbreviat.	Action	Remarks
PS69/536-1	26.08.06	15:11	37° 5,96' S	12° 45,48' E	4884,7	PIES	Beginn Auslegung	1 Benthos 50m leine
PS69/536-1	26.08.06	15:13	37° 5,98' S	12° 45,57' E	4848,4	PIES	Ende Auslegung	geslipt
PS69/536-1	26.08.06	15:15	37° 6,01' S	12° 45,66' E	0,0	PIES	Information	per Posidonia verfolgt
PS69/536-2	26.08.06	15:27	37° 6,11' S	12° 46,17' E	4777,7	CTD/RO	zu Wasser	
PS69/536-1	26.08.06	16:58	37° 5,65' S	12° 47,83' E	4860,9	PIES	Information	am Grund bei B=37°05,56 S L = 012° 46,16 E bei 4800 m
PS69/536-2	26.08.06	17:10	37° 5,55' S	12° 48,01' E	4873,4	CTD/RO	auf Tiefe	Winde EL 31 4914 m
PS69/536-2	26.08.06	18:44	37° 5,23' S	12° 49,68' E	4962,4	CTD/RO	an Deck	
PS69/537-1	29.08.06	07:47	41° 10,85' S	4° 15,53' E	4862,0	PIES	Information	UKW 156,875 MHz & Ch 77 erfolgreich
PS69/537-1	29.08.06	08:20	41° 10,95' S	4° 15,56' E	4865,0	PIES	Beginn Auslegung	2 Schwimmkörper
PS69/537-1	29.08.06	08:24	41° 10,93' S	4° 15,60' E	4866,0	PIES	Information	PIES mit Gewicht
PS69/537-1	29.08.06	08:24	41° 10,93' S	4° 15,60' E	4866,0	PIES	Information	Geslipt
PS69/537-2	29.08.06	08:48	41° 11,34' S	4° 15,86' E	4856,0	CTD/RO	zu Wasser	
PS69/537-1	29.08.06	09:51	41° 11,59' S	4° 16,96' E	4851,0	PIES	Ende Auslegung	Gerät am Boden
PS69/537-2	29.08.06	10:29	41° 11,89' S	4° 17,26' E	4855,0	CTD/RO	auf Tiefe	EL31 4914meter
PS69/537-2	29.08.06	11:42	41° 12,32' S	4° 17,91' E	4846,0	CTD/RO	an Deck	
PS69/538-1	30.08.06	10:13	42° 59,31' S	0° 0,52' E	4356,0	PIES	Beginn Auslegung	Transponder und Schwimmkörper zu Wasser
PS69/538-1	30.08.06	10:15	42° 59,39' S	0° 0,59' E	4360,0	PIES	Information	PIES mit Gewicht im Wasser und geslipt
PS69/538-1	30.08.06	10:16	42° 59,43' S	0° 0,62' E	4361,0	PIES	Ende Auslegung	
PS69/539-1	01.09.06	07:05	46° 13,25' S	8° 30,16' W	3668,0	PIES	Beginn Auslegung	
PS69/539-1	01.09.06	07:09	46° 13,22' S	8° 30,09' W	3666,0	PIES	auslösen	
PS69/539-2	01.09.06	07:26	46° 12,78' S	8° 29,14' W	3671,0	CTD/RO	zu Wasser	
PS69/539-1	01.09.06	08:14	46° 12,97' S	8° 28,94' W	3670,0	PIES	Information	am Grund B= 46°13,22 S & L=008° 30,6 W ca 3600m
PS69/539-2	01.09.06	08:40	46° 13,07' S	8° 28,80' W	3669,0	CTD/RO	auf Tiefe	3601 m
PS69/539-2	01.09.06	09:39	46° 13,28' S	8° 28,41' W	3664,0	CTD/RO	an Deck	
PS69/540-1	06.09.06	22:40	58° 0,06' S	37° 30,42' W	3428,0	CTD/RO	zu Wasser	
PS69/540-1	06.09.06	23:45	57° 59,08' S	37° 28,73' W	3462,0	CTD/RO	auf Tiefe	EL31 3407meter
PS69/540-1	07.09.06	00:55	57° 58,19' S	37° 27,17' W	3405,0	CTD/RO	an Deck	
PS69/540-2	07.09.06	01:54	57° 57,54' S	37° 25,78' W	3483,0	MN	zu Wasser	
PS69/540-2	07.09.06	02:14	57° 57,36' S	37° 25,20' W	3485,0	MN	auf Tiefe	EL30, Tiefe nach Drucksensor 500meter
PS69/540-2	07.09.06	02:15	57° 57,35' S	37° 25,17' W	3486,0	MN	Hieven	
PS69/540-2	07.09.06	02:41	57° 57,09' S	37° 24,31' W	3454,0	MN	an Deck	
PS69/540-3	07.09.06	02:47	57° 57,04' S	37° 24,10' W	3457,0	MN	zu Wasser	
PS69/540-3	07.09.06	04:07	57° 56,38' S	37° 21,04' W	3587,0	MN	auf Tiefe	2.280m
PS69/540-3	07.09.06	04:08	57° 56,38' S	37° 20,99' W	3589,0	MN	Hieven	
PS69/540-3	07.09.06	05:30	57° 55,56' S	37° 18,14' W	3523,0	MN	an Deck	
PS69/541-1	07.09.06	19:46	59° 19,16' S	39° 14,44' W	2265,0	EF	Beginn	
PS69/541-1	07.09.06	20:04	59° 19,16' S	39° 14,28' W	2305,0	EF	Ende	
PS69/542-1	08.09.06	18:52	60° 27,96' S	40° 48,98' W	759,0	ICE	Anlegen an Scholle	

A.4 STATION LIST PS 69

Station	Date	Time	Position Lat	Position Lon	Depth [m]	Gear Abbreviat.	Action	Remarks
PS69/542-1	08.09.06	19:07	60° 27,88' S	40° 48,68' W	719,0	ICE	Eisgangway ausgebracht	
PS69/542-1	08.09.06	19:11	60° 27,86' S	40° 48,61' W	711,9	ICE	Forscher auf dem Eis	
PS69/542-2	08.09.06	19:21	60° 27,78' S	40° 48,45' W	694,4	CTD/RO	zu Wasser	
PS69/542-2	08.09.06	19:39	60° 27,63' S	40° 48,17' W	692,7	CTD/RO	auf Tiefe	674 m
PS69/542-2	08.09.06	20:01	60° 27,43' S	40° 47,89' W	703,6	CTD/RO	an Deck	
PS69/542-3	08.09.06	20:20	60° 27,27' S	40° 47,68' W	713,9	MN	zu Wasser	
PS69/542-3	08.09.06	20:41	60° 27,08' S	40° 47,47' W	732,6	MN	auf Tiefe	nach Sensor 500 m , Draht 541 m
PS69/542-3	08.09.06	21:02	60° 26,91' S	40° 47,27' W	733,4	MN	an Deck	
PS69/542-1	08.09.06	21:25	60° 26,73' S	40° 47,09' W	737,3	ICE	Verlassen die Scholle	
PS69/543-1	09.09.06	13:30	60° 36,03' S	41° 38,55' W	2611,0	ICE	Anlegen an Scholle	
PS69/543-1	09.09.06	13:45	60° 35,93' S	41° 38,46' W	2588,0	ICE	Eisgangway ausgebracht	
PS69/543-1	09.09.06	13:50	60° 35,92' S	41° 38,38' W	2584,0	ICE	Forscher auf dem Eis	
PS69/543-2	09.09.06	14:04	60° 35,88' S	41° 38,17' W	2565,0	CTD/RO	zu Wasser	
PS69/543-2	09.09.06	14:51	60° 35,79' S	41° 37,33' W	2494,0	CTD/RO	auf Tiefe	EL31 2446meter
PS69/543-2	09.09.06	15:45	60° 35,73' S	41° 36,35' W	2443,0	CTD/RO	an Deck	
PS69/543-3	09.09.06	15:57	60° 35,73' S	41° 36,14' W	2436,0	MN	zu Wasser	
PS69/543-3	09.09.06	16:16	60° 35,73' S	41° 35,81' W	2424,0	MN	auf Tiefe	500m
PS69/543-3	09.09.06	16:39	60° 35,74' S	41° 35,41' W	2421,0	MN	an Deck	
PS69/543-4	09.09.06	16:44	60° 35,75' S	41° 35,31' W	2420,0	MN	zu Wasser	
PS69/543-4	09.09.06	18:12	60° 35,85' S	41° 33,49' W	2393,0	MN	auf Tiefe	2.133m
PS69/543-4	09.09.06	19:11	60° 35,89' S	41° 32,12' W	2343,0	MN	an Deck	
PS69/543-5	09.09.06	19:23	60° 35,90' S	41° 31,84' W	2332,0	CTD/RO	zu Wasser	
PS69/543-5	09.09.06	20:08	60° 35,93' S	41° 30,75' W	2311,0	CTD/RO	auf Tiefe	2263 m
PS69/543-5	09.09.06	20:43	60° 35,93' S	41° 29,98' W	2302,0	CTD/RO	an Deck	
PS69/543-1	09.09.06	20:48	60° 35,93' S	41° 29,88' W	2298,0	ICE	Verlassen die Scholle	
PS69/543-6	09.09.06	21:00	60° 35,90' S	41° 29,65' W	2282,0	MN	zu Wasser	
PS69/543-6	09.09.06	21:37	60° 35,76' S	41° 29,03' W	2211,0	MN	auf Tiefe	1066 m
PS69/543-6	09.09.06	22:16	60° 35,71' S	41° 28,32' W	2194,0	MN	an Deck	
PS69/544-1	10.09.06	04:44	60° 37,43' S	42° 1,94' W	3565,0	CTD/RO	zu Wasser	
PS69/544-1	10.09.06	05:54	60° 38,08' S	42° 0,78' W	3689,0	CTD/RO	auf Tiefe	3,602m
PS69/544-1	10.09.06	06:54	60° 38,73' S	41° 59,63' W	4015,0	CTD/RO	an Deck	
PS69/544-2	10.09.06	07:06	60° 38,90' S	41° 59,32' W	4043,0	AFLOAT	zu Wasser	
PS69/545-1	10.09.06	12:41	60° 40,70' S	42° 10,68' W	1948,0	CTD/RO	zu Wasser	
PS69/545-1	10.09.06	13:21	60° 40,64' S	42° 10,00' W	2192,0	CTD/RO	auf Tiefe	EL31 2004meter
PS69/545-1	10.09.06	14:00	60° 40,56' S	42° 9,26' W	2506,0	CTD/RO	an Deck	
PS69/545-2	10.09.06	14:15	60° 40,37' S	42° 9,36' W	2518,0	EF	Beginn	
PS69/545-2	10.09.06	14:31	60° 40,35' S	42° 9,04' W	2630,0	EF	Ende	
PS69/546-1	10.09.06	23:01	60° 37,87' S	42° 36,54' W	600,5	ICE	Anlegen an Scholle	
PS69/546-1	10.09.06	23:15	60° 37,84' S	42° 36,41' W	577,1	ICE	Eisgangway ausgebracht	
PS69/546-1	10.09.06	23:17	60° 37,83' S	42° 36,38' W	569,7	ICE	Forscher auf dem Eis	

A.4 STATION LIST PS 69

Station	Date	Time	Position Lat	Position Lon	Depth [m]	Gear Abbreviat.	Action	Remarks
PS69/546-1	11.09.06	00:43	60° 37,53' S	42° 35,19' W	424,6	ICE	Forscher an Bord	
PS69/546-1	11.09.06	01:02	60° 37,45' S	42° 34,98' W	421,9	ICE	Eisgangway an Bord	
PS69/546-1	11.09.06	01:04	60° 37,44' S	42° 34,96' W	421,1	ICE	Verlassen die Scholle	
PS69/547-1	11.09.06	05:19	60° 42,57' S	42° 35,44' W	1184,0	CTD/RO	zu Wasser	
PS69/547-1	11.09.06	05:44	60° 42,55' S	42° 35,51' W	1186,0	CTD/RO	auf Tiefe	1.117m
PS69/547-1	11.09.06	06:10	60° 42,64' S	42° 35,79' W	1219,0	CTD/RO	an Deck	
PS69/548-1	11.09.06	08:34	60° 52,06' S	42° 59,83' W	359,4	CTD/RO	zu Wasser	
PS69/548-1	11.09.06	08:46	60° 52,05' S	42° 59,75' W	360,2	CTD/RO	auf Tiefe	336 m
PS69/548-1	11.09.06	08:58	60° 52,04' S	42° 59,69' W	359,1	CTD/RO	an Deck	
PS69/548-2	11.09.06	09:05	60° 52,04' S	42° 59,66' W	358,9	MN	zu Wasser	
PS69/548-2	11.09.06	09:27	60° 52,00' S	42° 59,59' W	360,1	MN	auf Tiefe	200 m
PS69/548-2	11.09.06	09:35	60° 51,98' S	42° 59,57' W	360,3	MN	an Deck	
PS69/548-3	11.09.06	09:45	60° 51,97' S	42° 59,56' W	359,9	MN	zu Wasser	
PS69/548-3	11.09.06	09:58	60° 51,95' S	42° 59,57' W	358,8	MN	auf Tiefe	316 m
PS69/548-3	11.09.06	10:12	60° 51,92' S	42° 59,55' W	358,1	MN	an Deck	
PS69/549-1	19.09.06	08:27	60° 21,02' S	50° 49,31' W	5374,0	CTD/RO	zu Wasser	
PS69/549-1	19.09.06	10:14	60° 20,61' S	50° 48,15' W	5384,0	CTD/RO	auf Tiefe	5307 m
PS69/549-1	19.09.06	11:39	60° 19,99' S	50° 47,51' W	5371,0	CTD/RO	an Deck	
PS69/549-2	19.09.06	12:29	60° 19,77' S	50° 47,91' W	5375,0	ICE	Anlegen an Scholle	
PS69/549-2	19.09.06	12:35	60° 19,73' S	50° 47,92' W	5374,0	ICE	Eisgangway ausgebracht	
PS69/549-2	19.09.06	12:37	60° 19,71' S	50° 47,91' W	5369,0	ICE	Forscher auf dem Eis	
PS69/549-3	19.09.06	13:24	60° 19,39' S	50° 47,76' W	5366,0	MN	zu Wasser	
PS69/549-4	19.09.06	14:09	60° 19,15' S	50° 47,66' W	5319,0	CTD/RO	zu Wasser	
PS69/549-4	19.09.06	14:21	60° 19,09' S	50° 47,62' W	5298,0	CTD/RO	auf Tiefe	EL31 496 meter
PS69/549-4	19.09.06	14:34	60° 19,02' S	50° 47,58' W	5273,0	CTD/RO	an Deck	
PS69/549-3	19.09.06	14:49	60° 18,95' S	50° 47,52' W	5227,0	MN	Funktionsstörung - Neubeginn	
PS69/549-3	19.09.06	15:09	60° 18,86' S	50° 47,42' W	5169,0	MN	auf Tiefe	530m
PS69/549-3	19.09.06	15:09	60° 18,86' S	50° 47,42' W	5169,0	MN	Hieven	
PS69/549-3	19.09.06	15:30	60° 18,78' S	50° 47,29' W	5129,0	MN	an Deck	
PS69/549-5	19.09.06	15:43	60° 18,73' S	50° 47,21' W	5092,0	MN	zu Wasser	
PS69/549-5	19.09.06	15:48	60° 18,71' S	50° 47,18' W	5086,0	MN	auf Tiefe	
PS69/549-5	19.09.06	15:48	60° 18,71' S	50° 47,18' W	5086,0	MN	Hieven	
PS69/549-5	19.09.06	15:54	60° 18,69' S	50° 47,13' W	5075,0	MN	an Deck	
PS69/549-6	19.09.06	16:31	60° 18,57' S	50° 46,85' W	5035,0	MN	zu Wasser	
PS69/549-6	19.09.06	17:44	60° 18,29' S	50° 46,17' W	4954,0	MN	auf Tiefe	2.097m
PS69/549-6	19.09.06	17:44	60° 18,29' S	50° 46,17' W	4954,0	MN	Hieven	
PS69/549-6	19.09.06	18:57	60° 17,98' S	50° 45,29' W	4815,0	MN	an Deck	
PS69/549-7	19.09.06	19:13	60° 17,91' S	50° 45,09' W	4757,0	CTD/RO	zu Wasser	Test
PS69/549-2	19.09.06	19:13	60° 17,91' S	50° 45,09' W	4757,0	ICE	Eisgangway an Bord	
PS69/549-7	19.09.06	19:19	60° 17,88' S	50° 45,02' W	4728,0	CTD/RO	auf Tiefe	100 m
PS69/549-7	19.09.06	19:20	60° 17,88' S	50° 45,00' W	4723,0	CTD/RO	an Deck	
PS69/549-8	19.09.06	19:30	60° 17,89' S	50° 45,30' W	4696,0	EF	Beginn	
PS69/549-8	19.09.06	19:49	60° 17,83' S	50° 45,12' W	4628,0	EF	Ende	
PS69/550-1	20.09.06	02:36	60° 37,96' S	50° 7,44' W	1842,1	CTD/RO	zu Wasser	
PS69/550-1	20.09.06	03:11	60° 37,84' S	50° 7,62' W	1834,0	CTD/RO	auf Tiefe	1.774m
PS69/550-1	20.09.06	03:44	60° 37,75' S	50° 7,80' W	1823,6	CTD/RO	an Deck	
PS69/551-1	20.09.06	13:16	60° 19,75' S	49° 29,63' W	0,0	ICE	Anlegen an Scholle	

A.4 STATION LIST PS 69

Station	Date	Time	Position Lat	Position Lon	Depth [m]	Gear Abbreviat.	Action	Remarks
PS69/551-1	20.09.06	13:16	60° 19,75' S	49° 29,63' W	0,0	ICE	Eisgangway ausgebracht	
PS69/551-1	20.09.06	13:25	60° 19,71' S	49° 29,63' W	3755,2	ICE	Forscher auf dem Eis	
PS69/551-2	20.09.06	13:42	60° 19,65' S	49° 29,64' W	3731,6	CTD/RO	zu Wasser	
PS69/551-2	20.09.06	14:52	60° 19,46' S	49° 29,67' W	3688,4	CTD/RO	auf Tiefe	EL31 3715meter
PS69/551-1	20.09.06	15:52	60° 19,41' S	49° 29,61' W	3688,5	ICE	Forscher an Bord	
PS69/551-2	20.09.06	15:55	60° 19,41' S	49° 29,60' W	3674,4	CTD/RO	an Deck	
PS69/551-1	20.09.06	15:57	60° 19,41' S	49° 29,60' W	3671,6	ICE	Eisgangway an Bord	
PS69/551-3	20.09.06	19:12	60° 24,96' S	49° 0,82' W	2311,1	EF	Beginn	Frostblumen sammeln
PS69/551-3	20.09.06	19:47	60° 24,91' S	49° 0,63' W	2417,3	EF	Ende	
PS69/551-4	20.09.06	19:58	60° 25,34' S	49° 0,32' W	1924,0	EF	Beginn	
PS69/551-4	20.09.06	20:04	60° 25,33' S	49° 0,28' W	1914,7	EF	Ende	
PS69/552-1	20.09.06	22:54	60° 30,70' S	48° 28,02' W	1813,2	CTD/RO	zu Wasser	
PS69/552-1	20.09.06	23:30	60° 30,67' S	48° 27,90' W	1808,8	CTD/RO	auf Tiefe	EL31 1763meter
PS69/552-1	21.09.06	00:03	60° 30,64' S	48° 27,78' W	1802,0	CTD/RO	an Deck	
PS69/553-1	21.09.06	03:14	60° 19,57' S	48° 20,12' W	4642,1	CTD/RO	zu Wasser	
PS69/553-1	21.09.06	04:41	60° 19,69' S	48° 19,43' W	4691,3	CTD/RO	auf Tiefe	4.655m
PS69/553-1	21.09.06	05:52	60° 19,82' S	48° 18,94' W	4640,8	CTD/RO	an Deck	
PS69/554-3	21.09.06	10:00	0° 0,00' N	0° 0,00' E	0,0	ICE	Anlegen an Scholle	
PS69/554-1	21.09.06	10:10	60° 17,63' S	48° 0,87' W	5628,8	MN	zu Wasser	
PS69/554-1	21.09.06	10:16	60° 17,63' S	48° 0,81' W	5628,8	MN	auf Tiefe	EL 30 107 m
PS69/554-1	21.09.06	10:22	60° 17,63' S	48° 0,75' W	5629,2	MN	an Deck	
PS69/554-2	21.09.06	10:29	60° 17,62' S	48° 0,68' W	5628,8	CTD/RO	zu Wasser	
PS69/554-3	21.09.06	11:00	60° 17,59' S	48° 0,36' W	5629,2	ICE	Eisgangway ausgebracht	
PS69/554-3	21.09.06	11:20	60° 17,55' S	48° 0,15' W	5629,1	ICE	Forscher auf dem Eis	
PS69/554-2	21.09.06	12:13	60° 17,38' S	47° 59,65' W	5650,0	CTD/RO	auf Tiefe	EL31 5580meter
PS69/554-2	21.09.06	13:44	60° 17,02' S	47° 58,95' W	5657,0	CTD/RO	an Deck	
PS69/554-4	21.09.06	14:00	60° 16,94' S	47° 58,80' W	5655,0	MN	zu Wasser	
PS69/554-4	21.09.06	15:15	60° 16,55' S	47° 58,01' W	5647,0	MN	auf Tiefe	2.109m
PS69/554-4	21.09.06	15:16	60° 16,54' S	47° 57,99' W	5648,0	MN	Hieven	
PS69/554-4	21.09.06	16:34	60° 16,18' S	47° 57,03' W	5649,0	MN	an Deck	
PS69/554-5	21.09.06	16:44	60° 16,14' S	47° 56,89' W	5646,0	CTD/RO	zu Wasser	
PS69/554-5	21.09.06	16:58	60° 16,08' S	47° 56,69' W	5641,0	CTD/RO	auf Tiefe	501m
PS69/554-5	21.09.06	17:08	60° 16,03' S	47° 56,55' W	5639,0	CTD/RO	an Deck	
PS69/554-6	21.09.06	17:15	60° 16,00' S	47° 56,45' W	5637,0	MN	zu Wasser	
PS69/554-6	21.09.06	17:34	60° 15,91' S	47° 56,19' W	5630,0	MN	auf Tiefe	544m
PS69/554-6	21.09.06	17:34	60° 15,91' S	47° 56,19' W	5630,0	MN	Hieven	
PS69/554-6	21.09.06	17:57	60° 15,79' S	47° 55,89' W	5619,0	MN	an Deck	
PS69/554-3	21.09.06	18:07	60° 15,72' S	47° 55,77' W	5614,0	ICE	Forscher an Bord	
PS69/554-7	21.09.06	18:13	60° 15,67' S	47° 55,70' W	5606,0	CTD/RO	zu Wasser	
PS69/554-3	21.09.06	18:17	60° 15,64' S	47° 55,65' W	5605,0	ICE	Eisgangway an Bord	
PS69/554-7	21.09.06	19:58	60° 14,58' S	47° 54,76' W	5405,0	CTD/RO	auf Tiefe	5535 m
PS69/554-7	21.09.06	21:25	60° 13,41' S	47° 54,72' W	5113,0	CTD/RO	an Deck	
PS69/555-1	22.09.06	05:56	0° 0,00' N	0° 0,00' E	0,0	CTD/RO	zu Wasser	
PS69/555-1	22.09.06	06:05	60° 20,12' S	47° 28,39' W	3781,0	CTD/RO	Information	Kontext
PS69/555-1	22.09.06	07:08	60° 19,92' S	47° 27,90' W	3740,0	CTD/RO	auf Tiefe	3681 m

A.4 STATION LIST PS 69

Station	Date	Time	Position Lat	Position Lon	Depth [m]	Gear Abbreviat.	Action	Remarks
PS69/555-1	22.09.06	08:47	60° 19,30' S	47° 26,95' W	3734,0	CTD/RO	an Deck	
PS69/556-1	22.09.06	16:06	59° 50,11' S	48° 5,08' W	4472,0	ICE	Anlegen an Scholle	
PS69/556-1	22.09.06	16:09	59° 50,10' S	48° 5,05' W	4473,0	ICE	Eisgangway ausgebracht	
PS69/556-1	22.09.06	16:23	59° 50,05' S	48° 4,90' W	4478,0	ICE	Forscher auf dem Eis	
PS69/556-2	22.09.06	16:30	59° 50,03' S	48° 4,82' W	4474,0	MN	zu Wasser	
PS69/556-2	22.09.06	16:33	59° 50,02' S	48° 4,79' W	4476,0	MN	auf Tiefe	107m
PS69/556-2	22.09.06	16:35	59° 50,01' S	48° 4,77' W	4475,0	MN	Hieven	
PS69/556-2	22.09.06	16:40	59° 49,99' S	48° 4,72' W	4472,0	MN	an Deck	
PS69/556-3	22.09.06	16:53	59° 49,94' S	48° 4,58' W	4476,0	CTD/RO	zu Wasser	
PS69/556-3	22.09.06	18:15	59° 49,58' S	48° 3,72' W	4478,0	CTD/RO	auf Tiefe	4.400m
PS69/556-3	22.09.06	19:28	59° 49,16' S	48° 2,98' W	4479,0	CTD/RO	an Deck	
PS69/556-4	22.09.06	19:47	59° 49,02' S	48° 2,82' W	4482,0	MN	zu Wasser	
PS69/556-4	22.09.06	20:06	59° 48,87' S	48° 2,69' W	4479,0	MN	auf Tiefe	531 m
PS69/556-4	22.09.06	20:26	59° 48,72' S	48° 2,57' W	4475,0	MN	an Deck	
PS69/556-5	22.09.06	20:34	59° 48,66' S	48° 2,54' W	4478,0	MN	zu Wasser	
PS69/556-5	22.09.06	21:46	59° 48,07' S	48° 2,32' W	4478,0	MN	auf Tiefe	2120 m
PS69/556-1	22.09.06	22:25	59° 47,74' S	48° 2,27' W	4473,0	ICE	Forscher an Bord	
PS69/556-1	22.09.06	22:32	59° 47,69' S	48° 2,27' W	4471,0	ICE	Eisgangway an Bord	
PS69/556-5	22.09.06	23:04	59° 47,46' S	48° 2,31' W	4471,0	MN	an Deck	
PS69/556-6	22.09.06	23:10	59° 47,43' S	48° 2,33' W	4464,0	CTD/RO	zu Wasser	
PS69/556-6	22.09.06	23:21	59° 47,37' S	48° 2,36' W	4469,0	CTD/RO	auf Tiefe	EL31 497meter
PS69/556-6	22.09.06	23:33	59° 47,29' S	48° 2,38' W	4466,0	CTD/RO	an Deck	
PS69/557-1	22.09.06	08:55	60° 2,36' S	48° 5,65' W	4259,0	CTD/RO	zu Wasser	
PS69/557-1	23.09.06	10:27	60° 1,70' S	48° 5,65' W	4390,0	CTD/RO	auf Tiefe	4325 m
PS69/557-1	23.09.06	12:03	60° 0,92' S	48° 5,93' W	4541,0	CTD/RO	an Deck	
PS69/558-1	23.09.06	14:16	60° 1,96' S	48° 1,20' W	3517,0	ICE	Anlegen an Scholle	
PS69/558-1	23.09.06	14:17	60° 1,95' S	48° 1,21' W	3528,0	ICE	Eisgangway ausgebracht	
PS69/558-1	23.09.06	14:20	60° 1,93' S	48° 1,25' W	3527,0	ICE	Forscher auf dem Eis	
PS69/558-2	23.09.06	14:40	60° 1,72' S	48° 1,47' W	3632,0	CTD/RO	zu Wasser	
PS69/558-1	23.09.06	15:46	60° 1,05' S	48° 2,12' W	4152,0	ICE	Forscher an Bord	
PS69/558-2	23.09.06	15:54	60° 0,97' S	48° 2,18' W	4194,0	CTD/RO	auf Tiefe	3.952m
PS69/558-1	23.09.06	16:04	60° 0,87' S	48° 2,26' W	4244,0	ICE	Eisgangway an Bord	
PS69/558-2	23.09.06	16:58	60° 0,36' S	48° 2,66' W	4533,0	CTD/RO	an Deck	
PS69/559-1	23.09.06	19:22	60° 6,67' S	47° 53,62' W	2300,0	EF	Beginn	
PS69/559-1	23.09.06	19:48	60° 6,52' S	47° 53,78' W	2368,0	EF	Ende	
PS69/559-2	23.09.06	21:03	60° 11,55' S	47° 55,48' W	3490,0	CTD/RO	zu Wasser	
PS69/559-2	23.09.06	22:29	60° 10,69' S	47° 55,09' W	2750,0	CTD/RO	auf Tiefe	2848 m
PS69/559-2	23.09.06	23:08	60° 10,27' S	47° 55,24' W	2419,0	CTD/RO	an Deck	
PS69/560-1	24.09.06	06:47	0° 0,00' N	0° 0,00' E	0,0	CTD/RO	zu Wasser	
PS69/560-1	24.09.06	06:51	60° 11,73' S	48° 5,37' W	2434,0	CTD/RO	Information	Kontext
PS69/560-1	24.09.06	07:34	60° 11,57' S	48° 5,54' W	2470,0	CTD/RO	auf Tiefe	2375 m
PS69/560-1	24.09.06	08:15	60° 11,41' S	48° 5,59' W	2495,0	CTD/RO	an Deck	
PS69/561-1	24.09.06	14:15	60° 30,07' S	47° 50,86' W	1907,0	CTD/RO	zu Wasser	
PS69/561-2	24.09.06	14:31	60° 30,00' S	47° 50,85' W	1909,0	EF	Beginn	
PS69/561-1	24.09.06	14:52	60° 29,85' S	47° 50,92' W	1875,0	CTD/RO	auf Tiefe	EL31 1820meter

A.4 STATION LIST PS 69

Station	Date	Time	Position Lat	Position Lon	Depth [m]	Gear Abbreviat.	Action	Remarks
PS69/561-2	24.09.06	14:56	60° 29,82' S	47° 50,93' W	1869,0	EF	Ende	
PS69/561-1	24.09.06	15:24	60° 29,63' S	47° 51,03' W	1844,0	CTD/RO	an Deck	
PS69/562-1	24.09.06	20:17	60° 44,96' S	48° 19,51' W	2493,0	ICE	Anlegen an Scholle	
PS69/562-1	24.09.06	20:22	60° 44,94' S	48° 19,53' W	2490,0	ICE	Eisgangway ausgebracht	
PS69/562-1	24.09.06	20:23	60° 44,93' S	48° 19,53' W	2491,0	ICE	Forscher auf dem Eis	
PS69/562-2	24.09.06	20:33	60° 44,89' S	48° 19,56' W	2488,0	MN	zu Wasser	
PS69/562-2	24.09.06	20:38	60° 44,87' S	48° 19,57' W	2486,0	MN	auf Tiefe	103 m
PS69/562-2	24.09.06	20:43	60° 44,85' S	48° 19,58' W	2484,0	MN	an Deck	
PS69/562-3	24.09.06	20:54	60° 44,81' S	48° 19,61' W	2480,0	CTD/RO	zu Wasser	
PS69/562-3	24.09.06	21:40	60° 44,62' S	48° 19,71' W	2461,0	CTD/RO	auf Tiefe	2383 m
PS69/562-3	24.09.06	22:27	60° 44,43' S	48° 19,81' W	2452,0	CTD/RO	an Deck	
PS69/562-4	24.09.06	22:36	60° 44,39' S	48° 19,82' W	2452,0	MN	zu Wasser	
PS69/562-4	24.09.06	22:55	60° 44,32' S	48° 19,85' W	2445,0	MN	auf Tiefe	EL30 530meter
PS69/562-4	24.09.06	23:17	60° 44,23' S	48° 19,88' W	2440,0	MN	an Deck	
PS69/562-5	24.09.06	23:23	60° 44,21' S	48° 19,89' W	2440,0	MN	zu Wasser	
PS69/562-5	25.09.06	00:36	60° 43,93' S	48° 19,96' W	2427,0	MN	auf Tiefe	EL30 2096meter
PS69/562-1	25.09.06	00:46	60° 43,89' S	48° 19,96' W	2424,0	ICE	Forscher an Bord	
PS69/562-1	25.09.06	00:52	60° 43,87' S	48° 19,97' W	2424,0	ICE	Eisgangway an Bord	
PS69/562-5	25.09.06	01:49	60° 43,69' S	48° 20,00' W	2416,0	MN	an Deck	
PS69/562-1	25.09.06	01:55	60° 43,65' S	48° 19,99' W	2418,0	ICE	Verlassen die Scholle	
PS69/563-1	25.09.06	14:07	60° 55,08' S	48° 31,53' W	2375,1	EF	Beginn	Frostblumen sammeln
PS69/563-1	25.09.06	14:32	60° 55,11' S	48° 31,16' W	2394,9	EF	Ende	
PS69/564-1	26.09.06	19:47	61° 11,07' S	48° 54,15' W	2909,9	ICE	Anlegen an Scholle	
PS69/564-1	26.09.06	19:49	61° 11,07' S	48° 54,11' W	2910,1	ICE	Forscher auf dem Eis	
PS69/564-2	26.09.06	20:00	61° 11,09' S	48° 53,88' W	2909,6	CTD/RO	zu Wasser	
PS69/564-2	26.09.06	20:56	61° 11,21' S	48° 52,84' W	2902,4	CTD/RO	auf Tiefe	2829 m
PS69/564-2	26.09.06	21:52	61° 11,36' S	48° 51,91' W	2897,2	CTD/RO	an Deck	
PS69/564-1	26.09.06	23:10	61° 11,60' S	48° 50,86' W	2896,4	ICE	Forscher an Bord	
PS69/564-3	26.09.06	23:29	61° 11,67' S	48° 50,63' W	2897,7	AFLOAT	zu Wasser	
PS69/564-1	26.09.06	23:40	61° 11,71' S	48° 50,49' W	2896,0	ICE	Verlassen die Scholle	
PS69/565-1	28.09.06	15:36	61° 41,87' S	49° 7,07' W	3319,2	ICE	Anlegen an Scholle	
PS69/565-1	28.09.06	15:53	61° 41,94' S	49° 6,80' W	3319,6	ICE	Eisgangway ausgebracht	
PS69/565-2	28.09.06	16:04	61° 41,99' S	49° 6,62' W	3320,8	MN	zu Wasser	
PS69/565-2	28.09.06	16:08	61° 42,01' S	49° 6,55' W	3320,4	MN	auf Tiefe	108m
PS69/565-2	28.09.06	16:09	61° 42,01' S	49° 6,54' W	3320,1	MN	Hieven	
PS69/565-2	28.09.06	16:15	61° 42,04' S	49° 6,44' W	3321,2	MN	an Deck	
PS69/565-3	28.09.06	16:22	61° 42,07' S	49° 6,31' W	3323,6	CTD/RO	zu Wasser	
PS69/565-3	28.09.06	17:28	61° 42,32' S	49° 5,04' W	3323,6	CTD/RO	auf Tiefe	3.259m
PS69/565-3	28.09.06	18:23	61° 42,50' S	49° 3,86' W	3327,6	CTD/RO	an Deck	
PS69/565-4	28.09.06	18:32	61° 42,53' S	49° 3,67' W	3329,6	MN	zu Wasser	
PS69/565-4	28.09.06	19:50	61° 42,74' S	49° 2,03' W	3329,1	MN	auf Tiefe	
PS69/565-4	28.09.06	21:01	61° 42,91' S	49° 0,63' W	3327,6	MN	an Deck	

A.4 STATION LIST PS 69

Station	Date	Time	Position Lat	Position Lon	Depth [m]	Gear Abbreviat.	Action	Remarks
PS69/565-5	28.09.06	21:12	61° 42,93' S	49° 0,43' W	3328,5	CTD/RO	zu Wasser	
PS69/565-5	28.09.06	21:25	61° 42,95' S	49° 0,19' W	3327,2	CTD/RO	auf Tiefe	Winde EL 31 497m gesteckt
PS69/565-5	28.09.06	21:36	61° 42,97' S	49° 0,00' W	3326,8	CTD/RO	an Deck	
PS69/565-1	28.09.06	21:45	61° 42,99' S	48° 59,83' W	3327,6	ICE	Forscher an Bord	
PS69/565-1	28.09.06	21:48	61° 42,99' S	48° 59,78' W	3328,0	ICE	Eisgangway an Bord	
PS69/565-6	28.09.06	21:54	61° 43,00' S	48° 59,67' W	3326,8	MN	zu Wasser	
PS69/565-6	28.09.06	22:15	61° 43,04' S	48° 59,30' W	3328,4	MN	auf Tiefe	532 m
PS69/565-6	28.09.06	22:34	61° 43,08' S	48° 58,97' W	3329,2	MN	an Deck	
PS69/565-7	28.09.06	22:45	61° 43,10' S	48° 58,79' W	3328,3	CTD/RO	zu Wasser	
PS69/565-7	28.09.06	23:46	61° 43,27' S	48° 57,88' W	3330,8	CTD/RO	auf Tiefe	EL 31 3256meter
PS69/565-7	29.09.06	00:33	61° 43,45' S	48° 57,30' W	3332,4	CTD/RO	an Deck	
PS69/566-1	29.09.06	20:06	62° 4,49' S	50° 4,72' W	3387,1	EF	Beginn	
PS69/566-1	29.09.06	20:18	62° 4,46' S	50° 4,66' W	3386,9	EF	Ende	
PS69/567-1	30.09.06	09:43	62° 10,19' S	50° 34,27' W	3446,1	ICE	Anlegen an Scholle	
PS69/567-1	30.09.06	09:58	62° 10,20' S	50° 34,30' W	3446,3	ICE	Forscher auf dem Eis	
PS69/567-2	30.09.06	10:14	62° 10,22' S	50° 34,33' W	3446,8	CTD/RO	zu Wasser	
PS69/567-2	30.09.06	11:18	62° 10,33' S	50° 34,44' W	3451,2	CTD/RO	auf Tiefe	EL31 3380meter
PS69/567-2	30.09.06	12:15	62° 10,49' S	50° 34,30' W	3450,3	CTD/RO	an Deck	
PS69/567-3	30.09.06	12:51	62° 10,58' S	50° 34,12' W	3453,2	AFLOAT	zu Wasser	
PS69/567-1	30.09.06	12:51	62° 10,58' S	50° 34,12' W	3453,2	ICE	Forscher an Bord	
PS69/567-1	30.09.06	13:11	62° 10,64' S	50° 34,08' W	3454,8	ICE	Verlassen die Scholle	
PS69/567-4	30.09.06	13:24	62° 10,68' S	50° 34,07' W	3452,4	EF	Beginn	Eisblumen
PS69/567-4	30.09.06	13:55	62° 10,75' S	50° 33,84' W	3468,4	EF	Ende	
PS69/568-1	01.10.06	10:53	62° 49,68' S	52° 25,04' W	2142,0	ICE	Anlegen an Scholle	
PS69/568-1	01.10.06	11:03	62° 49,70' S	52° 25,13' W	2140,7	ICE	Eisgangway ausgebracht	
PS69/568-2	01.10.06	11:11	62° 49,71' S	52° 25,19' W	2140,8	MN	zu Wasser	
PS69/568-2	01.10.06	11:16	62° 49,73' S	52° 25,23' W	2138,9	MN	auf Tiefe	EL30 107meter
PS69/568-2	01.10.06	11:23	62° 49,74' S	52° 25,28' W	2138,5	MN	an Deck	
PS69/568-1	01.10.06	11:30	62° 49,75' S	52° 25,33' W	2138,0	ICE	Forscher auf dem Eis	
PS69/568-2	01.10.06	11:35	62° 49,76' S	52° 25,36' W	2137,6	CTD/RO	zu Wasser	
PS69/568-2	01.10.06	12:15	62° 49,82' S	52° 25,64' W	2141,2	CTD/RO	auf Tiefe	EL31 2067meter
PS69/568-2	01.10.06	12:54	62° 49,88' S	52° 25,89' W	2130,0	CTD/RO	an Deck	
PS69/568-3	01.10.06	13:04	62° 49,89' S	52° 25,96' W	2122,0	MN	zu Wasser	
PS69/568-3	01.10.06	13:22	62° 49,91' S	52° 26,07' W	2119,2	MN	zu Wasser	EL30 526meter
PS69/568-3	01.10.06	13:43	62° 49,94' S	52° 26,20' W	2122,4	MN	an Deck	
PS69/568-4	01.10.06	13:51	62° 49,95' S	52° 26,25' W	2119,6	EF	Beginn	Frostblumen mit Schlauchboot
PS69/568-5	01.10.06	13:56	62° 49,96' S	52° 26,28' W	2116,0	MN	zu Wasser	
PS69/568-4	01.10.06	14:27	62° 50,01' S	52° 26,46' W	2128,4	EF	Ende	
PS69/568-5	01.10.06	15:06	62° 50,09' S	52° 26,67' W	2122,0	MN	auf Tiefe	2.094m
PS69/568-5	01.10.06	15:07	62° 50,09' S	52° 26,68' W	2120,0	MN	Hieven	
PS69/568-5	01.10.06	16:22	62° 50,23' S	52° 27,04' W	2128,0	MN	an Deck	
PS69/568-4	01.10.06	16:34	62° 50,26' S	52° 27,09' W	2149,2	CTD/RO	zu Wasser	
PS69/568-5	01.10.06	17:17	62° 50,34' S	52° 27,26' W	2132,0	AFLOAT	zu Wasser	
PS69/568-4	01.10.06	17:17	62° 50,34' S	52° 27,26' W	2132,0	CTD/RO	auf Tiefe	2.062m
PS69/568-1	01.10.06	17:36	62° 50,38' S	52° 27,31' W	2132,4	ICE	Forscher an Bord	

A.4 STATION LIST PS 69

Station	Date	Time	Position Lat	Position Lon	Depth [m]	Gear Abbreviat.	Action	Remarks
PS69/568-1	01.10.06	17:47	62° 50,40' S	52° 27,36' W	2131,3	ICE	Eisgangway an Bord	
PS69/568-4	01.10.06	17:50	62° 50,40' S	52° 27,35' W	2125,2	CTD/RO	an Deck	
PS69/569-1	01.10.06	20:28	62° 57,08' S	52° 46,19' W	1130,4	CTD/RO	zu Wasser	
PS69/569-1	01.10.06	20:54	62° 57,02' S	52° 45,89' W	1264,8	CTD/RO	auf Tiefe	1199 m
PS69/569-1	01.10.06	21:16	62° 56,96' S	52° 45,63' W	1169,3	CTD/RO	an Deck	
PS69/569-2	01.10.06	21:30	62° 56,82' S	52° 45,75' W	1377,2	EF	Beginn	
PS69/569-2	01.10.06	21:51	62° 56,74' S	52° 45,48' W	1411,1	EF	Ende	
PS69/570-1	02.10.06	08:15	63° 13,32' S	53° 42,70' W	305,2	CTD/RO	zu Wasser	
PS69/570-1	02.10.06	08:27	63° 13,32' S	53° 42,70' W	0,0	CTD/RO	auf Tiefe	293 m
PS69/570-1	02.10.06	08:38	63° 13,32' S	53° 42,70' W	312,0	CTD/RO	an Deck	
PS69/570-2	02.10.06	08:44	63° 13,32' S	53° 42,70' W	0,0	MN	zu Wasser	
PS69/570-2	02.10.06	08:55	63° 13,32' S	53° 42,70' W	0,0	MN	auf Tiefe	295 m
PS69/570-2	02.10.06	09:09	63° 13,32' S	53° 42,70' W	0,0	MN	an Deck	
PS69/571-1	02.10.06	14:23	63° 35,81' S	53° 56,52' W	290,8	EF	Beginn	Eisberg Beprobung
PS69/571-1	02.10.06	14:36	63° 35,83' S	53° 56,09' W	293,6	EF	Ende	
PS69/572-1	02.10.06	16:26	63° 39,73' S	53° 52,01' W	345,3	ICE	Anlegen an Scholle	
PS69/572-1	02.10.06	16:29	63° 39,71' S	53° 51,91' W	346,8	ICE	Eisgangway ausgebracht	
PS69/572-1	02.10.06	16:30	63° 39,71' S	53° 51,89' W	345,9	ICE	Forscher auf dem Eis	
PS69/572-2	02.10.06	16:42	63° 39,66' S	53° 51,58' W	364,8	CTD/RO	zu Wasser	
PS69/572-2	02.10.06	16:51	63° 39,62' S	53° 51,34' W	358,4	CTD/RO	auf Tiefe	330m
PS69/572-2	02.10.06	17:01	63° 39,57' S	53° 51,08' W	351,1	CTD/RO	an Deck	
PS69/572-3	02.10.06	17:09	63° 39,53' S	53° 50,86' W	352,4	MN	zu Wasser	
PS69/572-3	02.10.06	17:21	63° 39,43' S	53° 50,55' W	353,6	MN	auf Tiefe	341m
PS69/572-3	02.10.06	17:21	63° 39,43' S	53° 50,55' W	353,6	MN	Hieven	
PS69/572-3	02.10.06	17:36	63° 39,31' S	53° 50,18' W	368,1	MN	an Deck	
PS69/572-4	02.10.06	17:45	63° 39,23' S	53° 49,97' W	347,5	BONGO	zu Wasser	
PS69/572-4	02.10.06	17:52	63° 39,15' S	53° 49,81' W	363,6	BONGO	auf Tiefe	100m
PS69/572-4	02.10.06	17:57	63° 39,09' S	53° 49,70' W	347,7	BONGO	an Deck	
PS69/572-5	02.10.06	18:00	63° 39,05' S	53° 49,63' W	349,2	BONGO	zu Wasser	
PS69/572-5	02.10.06	18:06	63° 38,98' S	53° 49,50' W	365,2	BONGO	auf Tiefe	100m
PS69/572-5	02.10.06	18:14	63° 38,88' S	53° 49,33' W	348,7	BONGO	an Deck	
PS69/572-1	02.10.06	18:33	63° 38,64' S	53° 48,94' W	353,5	ICE	Forscher an Bord	
PS69/572-1	02.10.06	18:38	63° 38,59' S	53° 48,88' W	353,7	ICE	Eisgangway an Bord	
PS69/573-1	03.10.06	11:30	64° 22,50' S	54° 24,96' W	605,2	EF	Beginn	Eisblumen
PS69/573-1	03.10.06	11:46	64° 22,35' S	54° 24,73' W	603,1	EF	Ende	
PS69/574-1	03.10.06	15:45	64° 17,79' S	54° 34,70' W	320,4	ICE	Anlegen an Scholle	
PS69/574-1	03.10.06	16:00	64° 17,62' S	54° 34,62' W	639,6	ICE	Eisgangway ausgebracht	
PS69/574-1	03.10.06	16:01	64° 17,61' S	54° 34,61' W	639,6	ICE	Forscher auf dem Eis	
PS69/574-2	03.10.06	16:11	64° 17,49' S	54° 34,56' W	645,6	CTD/RO	zu Wasser	
PS69/574-2	03.10.06	16:21	64° 17,38' S	54° 34,51' W	629,1	CTD/RO	auf Tiefe	304m
PS69/574-2	03.10.06	16:31	64° 17,27' S	54° 34,47' W	631,6	CTD/RO	an Deck	
PS69/574-3	03.10.06	16:38	64° 17,20' S	54° 34,44' W	632,0	MN	zu Wasser	
PS69/574-3	03.10.06	16:49	64° 17,09' S	54° 34,42' W	635,2	MN	auf Tiefe	292m
PS69/574-3	03.10.06	16:50	64° 17,08' S	54° 34,41' W	634,0	MN	Hieven	
PS69/574-3	03.10.06	17:03	64° 16,95' S	54° 34,38' W	635,2	MN	an Deck	
PS69/574-4	03.10.06	17:10	64° 16,88' S	54° 34,37' W	628,4	BONGO	zu Wasser	

A.4 STATION LIST PS 69

Station	Date	Time	Position Lat	Position Lon	Depth [m]	Gear Abbreviat.	Action	Remarks
PS69/574-4	03.10.06	17:16	64° 16,83' S	54° 34,37' W	638,5	BONGO	auf Tiefe	100m
PS69/574-4	03.10.06	17:21	64° 16,78' S	54° 34,36' W	635,1	BONGO	an Deck	
PS69/574-5	03.10.06	17:24	64° 16,75' S	54° 34,36' W	626,4	BONGO	zu Wasser	
PS69/574-5	03.10.06	17:30	64° 16,70' S	54° 34,36' W	628,8	BONGO	auf Tiefe	100m
PS69/574-5	03.10.06	17:37	64° 16,65' S	54° 34,36' W	316,8	BONGO	an Deck	
PS69/574-1	03.10.06	18:10	64° 16,51' S	54° 34,65' W	317,7	ICE	Forscher an Bord	
PS69/574-1	03.10.06	18:13	64° 16,51' S	54° 34,65' W	317,6	ICE	Eisgangway an Bord	
PS69/574-1	03.10.06	18:13	64° 16,51' S	54° 34,65' W	317,6	ICE	Verlassen die Scholle	
PS69/575-1	04.10.06	11:27	64° 24,86' S	55° 10,36' W	353,2	EF	Beginn	
PS69/575-1	04.10.06	12:23	64° 24,44' S	55° 9,25' W	350,4	EF	Ende	
PS69/576-1	04.10.06	16:25	0° 0,00' N	0° 0,00' E	0,0	ICE	Anlegen an Scholle	
PS69/576-1	04.10.06	16:29	0° 0,00' N	0° 0,00' E	0,0	ICE	Eisgangway ausgebracht	
PS69/576-1	04.10.06	16:33	0° 0,00' N	0° 0,00' E	0,0	ICE	Forscher auf dem Eis	
PS69/576-1	04.10.06	16:37	64° 24,95' S	55° 16,06' W	367,2	ICE	Information	Kontext
PS69/576-2	04.10.06	16:50	64° 24,86' S	55° 16,24' W	360,4	CTD/RO	zu Wasser	
PS69/576-2	04.10.06	17:00	64° 24,79' S	55° 16,39' W	352,0	CTD/RO	auf Tiefe	337m
PS69/576-2	04.10.06	17:09	64° 24,74' S	55° 16,52' W	355,5	CTD/RO	an Deck	
PS69/576-2	04.10.06	17:21	64° 24,67' S	55° 16,72' W	356,0	MN	zu Wasser	
PS69/576-2	04.10.06	17:32	64° 24,61' S	55° 16,91' W	357,3	MN	auf Tiefe	338m
PS69/576-2	04.10.06	17:33	64° 24,60' S	55° 16,93' W	356,8	MN	Hieven	
PS69/576-2	04.10.06	17:50	64° 24,52' S	55° 17,23' W	353,2	MN	an Deck	
PS69/576-2	04.10.06	18:00	64° 24,47' S	55° 17,42' W	364,5	BONGO	zu Wasser	
PS69/576-2	04.10.06	18:07	64° 24,44' S	55° 17,55' W	373,1	BONGO	auf Tiefe	100m
PS69/576-2	04.10.06	18:13	64° 24,42' S	55° 17,66' W	376,0	BONGO	an Deck	
PS69/576-1	04.10.06	18:24	64° 24,37' S	55° 17,87' W	362,1	ICE	Forscher an Bord	
PS69/576-1	04.10.06	18:24	64° 24,37' S	55° 17,87' W	362,1	ICE	Eisgangway an Bord	
PS69/576-1	04.10.06	18:24	64° 24,37' S	55° 17,87' W	362,1	ICE	Verlassen die Scholle	
PS69/577-1	05.10.06	12:58	64° 43,55' S	57° 19,90' W	339,3	ICE	Anlegen an Scholle	
PS69/577-1	05.10.06	13:03	64° 43,55' S	57° 19,87' W	338,1	ICE	Eisgangway ausgebracht	
PS69/577-1	05.10.06	13:04	64° 43,55' S	57° 19,86' W	337,6	ICE	Forscher auf dem Eis	
PS69/577-2	05.10.06	13:13	64° 43,55' S	57° 19,83' W	337,6	CTD/RO	zu Wasser	
PS69/577-2	05.10.06	13:22	64° 43,56' S	57° 19,82' W	337,1	CTD/RO	auf Tiefe	EL31 315
PS69/577-2	05.10.06	13:32	64° 43,56' S	57° 19,83' W	336,0	CTD/RO	an Deck	
PS69/577-3	05.10.06	13:38	64° 43,56' S	57° 19,83' W	338,8	MN	zu Wasser	
PS69/577-3	05.10.06	13:50	64° 43,56' S	57° 19,83' W	335,1	MN	auf Tiefe	EL30 328meter
PS69/577-3	05.10.06	14:05	64° 43,56' S	57° 19,84' W	335,2	MN	an Deck	
PS69/577-1	05.10.06	14:29	64° 43,56' S	57° 19,84' W	338,9	ICE	Forscher an Bord	
PS69/577-1	05.10.06	14:29	64° 43,56' S	57° 19,84' W	338,9	ICE	Eisgangway an Bord	
PS69/577-1	05.10.06	14:34	64° 43,56' S	57° 19,84' W	336,8	ICE	Verlassen die Scholle	

A.4 STATION LIST PS 69

Station	Date	Time	Position Lat	Position Lon	Depth [m]	Gear Abbreviat.	Action	Remarks
PS69/578-1	08.10.06	12:50	65° 6,62' S	57° 24,34' W	460,1	ICE	Anlegen an Scholle	
PS69/578-1	08.10.06	12:59	65° 6,60' S	57° 24,24' W	478,4	ICE	Eisgangway ausgebracht	
PS69/578-2	08.10.06	13:19	65° 6,57' S	57° 24,07' W	468,8	CTD/RO	zu Wasser	
PS69/578-1	08.10.06	13:22	65° 6,57' S	57° 24,04' W	476,8	ICE	Forscher auf dem Eis	
PS69/578-2	08.10.06	13:32	65° 6,55' S	57° 23,95' W	464,5	CTD/RO	auf Tiefe	EL31 430meter
PS69/578-2	08.10.06	13:48	65° 6,51' S	57° 23,82' W	0,0	CTD/RO	an Deck	
PS69/578-3	08.10.06	13:55	65° 6,49' S	57° 23,77' W	464,9	BONGO	zu Wasser	
PS69/578-3	08.10.06	14:02	65° 6,48' S	57° 23,72' W	457,2	BONGO	auf Tiefe	SE32.2 100meter
PS69/578-3	08.10.06	14:10	65° 6,45' S	57° 23,65' W	462,1	BONGO	an Deck	
PS69/578-4	08.10.06	14:15	65° 6,44' S	57° 23,62' W	465,1	BONGO	zu Wasser	
PS69/578-4	08.10.06	14:20	65° 6,43' S	57° 23,60' W	0,0	BONGO	auf Tiefe	SE32.2 100meter
PS69/578-4	08.10.06	14:28	65° 6,41' S	57° 23,55' W	460,7	BONGO	an Deck	
PS69/578-5	08.10.06	14:29	65° 6,41' S	57° 23,55' W	473,6	BONGO	zu Wasser	
PS69/578-5	08.10.06	14:36	65° 6,39' S	57° 23,52' W	460,8	BONGO	auf Tiefe	SE32.2 100meter
PS69/578-5	08.10.06	14:43	65° 6,38' S	57° 23,49' W	456,8	BONGO	an Deck	
PS69/578-6	08.10.06	14:47	65° 6,37' S	57° 23,48' W	0,0	BONGO	zu Wasser	
PS69/578-6	08.10.06	14:52	65° 6,35' S	57° 23,46' W	458,0	BONGO	auf Tiefe	SE32.2 100meter
PS69/578-6	08.10.06	14:59	65° 6,33' S	57° 23,45' W	453,2	BONGO	an Deck	
PS69/578-7	08.10.06	15:01	65° 6,33' S	57° 23,44' W	0,0	BONGO	zu Wasser	
PS69/578-7	08.10.06	15:07	65° 6,31' S	57° 23,43' W	0,0	BONGO	auf Tiefe	100m
PS69/578-7	08.10.06	15:14	65° 6,30' S	57° 23,42' W	0,0	BONGO	an Deck	
PS69/578-8	08.10.06	15:29	65° 6,26' S	57° 23,41' W	0,0	MN	zu Wasser	
PS69/578-8	08.10.06	15:43	0° 0,00' N	0° 0,00' E	0,0	MN	auf Tiefe	423m
PS69/578-8	08.10.06	15:44	65° 6,22' S	57° 23,42' W	452,8	MN	Hieven	
PS69/578-8	08.10.06	16:01	65° 6,18' S	57° 23,45' W	0,0	MN	an Deck	
PS69/578-9	08.10.06	16:14	65° 6,15' S	57° 23,49' W	452,3	MN	zu Wasser	
PS69/578-9	08.10.06	16:20	65° 6,14' S	57° 23,51' W	450,8	MN	auf Tiefe	160m
PS69/578-9	08.10.06	16:21	65° 6,13' S	57° 23,52' W	450,3	MN	Hieven	
PS69/578-9	08.10.06	16:29	65° 6,12' S	57° 23,55' W	450,0	MN	an Deck	
PS69/578-10	08.10.06	16:36	65° 6,10' S	57° 23,58' W	450,4	CTD/RO	zu Wasser	
PS69/578-10	08.10.06	16:46	65° 6,08' S	57° 23,63' W	466,4	CTD/RO	auf Tiefe	422m
PS69/578-10	08.10.06	16:57	65° 6,06' S	57° 23,69' W	449,3	CTD/RO	an Deck	
PS69/578-11	08.10.06	17:05	65° 6,05' S	57° 23,73' W	449,2	BONGO	zu Wasser	
PS69/578-11	08.10.06	17:10	65° 6,04' S	57° 23,75' W	448,9	BONGO	auf Tiefe	100m
PS69/578-11	08.10.06	17:17	65° 6,02' S	57° 23,79' W	0,0	BONGO	zu Wasser	
PS69/578-11	08.10.06	17:17	65° 6,02' S	57° 23,79' W	0,0	BONGO	an Deck	
PS69/578-12	08.10.06	17:18	65° 6,02' S	57° 23,79' W	448,0	BONGO	zu Wasser	
PS69/578-12	08.10.06	17:26	65° 6,00' S	57° 23,85' W	447,2	BONGO	auf Tiefe	105m
PS69/578-12	08.10.06	17:33	65° 5,99' S	57° 23,89' W	455,6	BONGO	an Deck	
PS69/578-13	08.10.06	17:34	65° 5,99' S	57° 23,90' W	0,0	BONGO	zu Wasser	
PS69/578-13	08.10.06	17:41	65° 5,97' S	57° 23,95' W	0,0	BONGO	auf Tiefe	100m
PS69/578-13	08.10.06	17:48	65° 5,96' S	57° 24,00' W	448,3	BONGO	an Deck	
PS69/578-14	08.10.06	17:49	65° 5,96' S	57° 24,00' W	448,0	BONGO	zu Wasser	
PS69/578-14	08.10.06	17:55	65° 5,94' S	57° 24,04' W	448,4	BONGO	auf Tiefe	100m
PS69/578-14	08.10.06	18:01	65° 5,93' S	57° 24,08' W	449,2	BONGO	an Deck	
PS69/578-15	08.10.06	18:03	65° 5,93' S	57° 24,09' W	447,2	BONGO	zu Wasser	
PS69/578-15	08.10.06	18:09	65° 5,92' S	57° 24,13' W	0,0	BONGO	auf Tiefe	100m
PS69/578-15	08.10.06	18:16	65° 5,90' S	57° 24,19' W	450,4	BONGO	an Deck	
PS69/578-1	08.10.06	19:56	65° 5,72' S	57° 24,91' W	446,8	ICE	Forscher an Bord	
PS69/578-1	08.10.06	20:08	65° 5,70' S	57° 24,98' W	446,4	ICE	Eisgangway an Bord	
PS69/578-1	08.10.06	20:08	65° 5,70' S	57° 24,98' W	446,4	ICE	Verlassen die Scholle	

A.4 STATION LIST PS 69

Station	Date	Time	Position Lat	Position Lon	Depth [m]	Gear Abbreviat.	Action	Remarks
PS69/579-1	09.10.06	16:13	65° 3,11' S	57° 20,58' W	363,9	ICE	Anlegen an Scholle	
PS69/579-1	09.10.06	16:19	65° 3,13' S	57° 20,62' W	359,2	ICE	Eisgangway ausgebracht	
PS69/579-1	09.10.06	16:22	65° 3,13' S	57° 20,63' W	356,4	ICE	Forscher auf dem Eis	
PS69/579-2	09.10.06	16:42	65° 3,17' S	57° 20,77' W	363,2	CTD/RO	zu Wasser	
PS69/579-2	09.10.06	16:51	65° 3,19' S	57° 20,83' W	372,8	CTD/RO	auf Tiefe	339m
PS69/579-2	09.10.06	17:07	65° 3,23' S	57° 20,95' W	369,1	CTD/RO	an Deck	
PS69/579-3	09.10.06	17:14	65° 3,24' S	57° 21,00' W	0,0	MN	zu Wasser	
PS69/579-3	09.10.06	17:28	65° 3,27' S	57° 21,10' W	379,2	MN	auf Tiefe	348m
PS69/579-3	09.10.06	17:29	65° 3,28' S	57° 21,11' W	383,6	MN	Hieven	
PS69/579-3	09.10.06	17:47	65° 3,31' S	57° 21,26' W	388,0	MN	an Deck	
PS69/579-4	09.10.06	17:54	65° 3,32' S	57° 21,33' W	381,2	BONGO	zu Wasser	
PS69/579-4	09.10.06	18:04	65° 3,34' S	57° 21,41' W	383,6	BONGO	auf Tiefe	150m
PS69/579-4	09.10.06	18:13	65° 3,36' S	57° 21,48' W	387,2	BONGO	an Deck	
PS69/579-5	09.10.06	18:15	65° 3,36' S	57° 21,50' W	388,8	BONGO	zu Wasser	
PS69/579-5	09.10.06	18:26	65° 3,39' S	57° 21,59' W	397,6	BONGO	auf Tiefe	150m
PS69/579-5	09.10.06	18:35	65° 3,41' S	57° 21,67' W	389,9	BONGO	an Deck	
PS69/579-1	09.10.06	18:43	65° 3,41' S	57° 21,75' W	397,5	ICE	Forscher an Bord	
PS69/579-1	09.10.06	18:48	65° 3,42' S	57° 21,79' W	391,2	ICE	Eisgangway an Bord	
PS69/579-1	09.10.06	18:48	65° 3,42' S	57° 21,79' W	391,2	ICE	Verlassen die Scholle	
PS69/580-1	11.10.06	09:53	64° 24,26' S	55° 10,29' W	352,8	EF	Beginn	
PS69/580-1	11.10.06	10:22	64° 24,07' S	55° 10,60' W	0,0	EF	Ende	
PS69/581-1	11.10.06	18:03	64° 11,18' S	54° 23,53' W	318,4	ICE	Anlegen an Scholle	
PS69/581-1	11.10.06	18:09	64° 11,21' S	54° 23,64' W	0,0	ICE	Eisgangway ausgebracht	
PS69/581-1	11.10.06	18:16	64° 11,25' S	54° 23,77' W	318,4	ICE	Forscher auf dem Eis	
PS69/581-2	11.10.06	19:13	64° 11,71' S	54° 24,79' W	313,2	CTD/RO	zu Wasser	
PS69/581-2	11.10.06	19:23	64° 11,82' S	54° 24,94' W	310,0	CTD/RO	auf Tiefe	289 m
PS69/581-2	11.10.06	19:35	64° 11,96' S	54° 25,12' W	314,5	CTD/RO	an Deck	
PS69/581-3	11.10.06	19:41	64° 12,03' S	54° 25,20' W	0,0	MN	zu Wasser	
PS69/581-3	11.10.06	19:53	64° 12,19' S	54° 25,37' W	313,2	MN	auf Tiefe	297 m
PS69/581-3	11.10.06	20:06	64° 12,37' S	54° 25,53' W	303,6	MN	an Deck	
PS69/581-4	11.10.06	20:13	64° 12,47' S	54° 25,62' W	304,8	BONGO	zu Wasser	
PS69/581-4	11.10.06	20:20	64° 12,57' S	54° 25,69' W	304,4	BONGO	auf Tiefe	100 m
PS69/581-4	11.10.06	20:27	64° 12,67' S	54° 25,77' W	309,2	BONGO	an Deck	
PS69/581-1	11.10.06	20:34	64° 12,78' S	54° 25,84' W	0,0	ICE	Forscher an Bord	
PS69/581-1	11.10.06	20:37	64° 12,83' S	54° 25,88' W	305,2	ICE	Eisgangway an Bord	
PS69/581-1	11.10.06	20:39	64° 12,86' S	54° 25,91' W	310,4	ICE	Verlassen die Scholle	
PS69/582-1	11.10.06	21:56	64° 11,10' S	54° 11,59' W	0,0	CTD/RO	zu Wasser	
PS69/582-1	11.10.06	22:13	64° 11,05' S	54° 11,53' W	782,0	CTD/RO	auf Tiefe	EL31 742meter
PS69/582-1	11.10.06	22:34	64° 11,14' S	54° 11,52' W	784,8	CTD/RO	an Deck	
PS69/582-2	11.10.06	22:43	64° 11,20' S	54° 11,51' W	778,0	MN	zu Wasser	
PS69/582-2	11.10.06	23:10	64° 11,34' S	54° 11,38' W	0,0	MN	auf Tiefe	EL30 768meter
PS69/582-2	11.10.06	23:41	64° 11,71' S	54° 11,19' W	806,0	MN	an Deck	
PS69/583-1	12.10.06	02:40	64° 14,00' S	53° 51,62' W	1480,3	CTD/RO	zu Wasser	

A.4 STATION LIST PS 69

Station	Date	Time	Position Lat	Position Lon	Depth [m]	Gear Abbreviat.	Action	Remarks
PS69/583-1	12.10.06	03:10	64° 14,10' S	53° 51,26' W	1493,2	CTD/RO	auf Tiefe	1.435m
PS69/583-1	12.10.06	03:39	64° 14,18' S	53° 50,94' W	1505,2	CTD/RO	an Deck	
PS69/583-2	12.10.06	03:48	64° 14,21' S	53° 50,84' W	1503,6	MN	zu Wasser	
PS69/583-2	12.10.06	04:36	64° 14,36' S	53° 50,32' W	1520,3	MN	auf Tiefe	1.486m
PS69/583-2	12.10.06	04:37	64° 14,36' S	53° 50,31' W	1523,2	MN	Hieven	
PS69/583-2	12.10.06	05:28	64° 14,54' S	53° 49,72' W	1540,9	MN	an Deck	
PS69/583-3	12.10.06	05:41	64° 14,58' S	53° 49,58' W	1543,1	MN	zu Wasser	
PS69/583-3	12.10.06	06:00	64° 14,64' S	53° 49,37' W	1551,6	MN	auf Tiefe	537m
PS69/583-3	12.10.06	06:00	64° 14,64' S	53° 49,37' W	1551,6	MN	Hieven	
PS69/583-3	12.10.06	06:20	64° 14,70' S	53° 49,16' W	1557,9	MN	an Deck	
PS69/584-1	12.10.06	16:40	0° 0,00' N	0° 0,00' E	0,0	ICE	Anlegen an Scholle	
PS69/584-1	12.10.06	16:42	0° 0,00' N	0° 0,00' E	0,0	ICE	Eisgangway ausgebracht	
PS69/584-1	12.10.06	16:46	0° 0,00' N	0° 0,00' E	0,0	ICE	Forscher auf dem Eis	
PS69/584-1	12.10.06	16:55	64° 22,84' S	52° 53,52' W	2465,0	ICE	Information	
PS69/584-2	12.10.06	17:23	64° 22,96' S	52° 53,32' W	2466,0	CTD/RO	zu Wasser	
PS69/584-2	12.10.06	18:12	64° 23,13' S	52° 52,80' W	2469,0	CTD/RO	auf Tiefe	2.403m
PS69/584-2	12.10.06	18:51	64° 23,24' S	52° 52,39' W	2474,0	CTD/RO	an Deck	
PS69/584-3	12.10.06	19:05	64° 23,28' S	52° 52,30' W	2474,0	MN	zu Wasser	
PS69/584-3	12.10.06	20:46	64° 23,37' S	52° 51,12' W	2480,0	MN	auf Tiefe	2565 m
PS69/584-1	12.10.06	20:53	64° 23,38' S	52° 51,03' W	2484,0	ICE	Forscher an Bord	
PS69/584-3	12.10.06	22:15	64° 23,36' S	52° 49,83' W	2490,0	MN	an Deck	
PS69/584-1	12.10.06	22:16	64° 23,36' S	52° 49,81' W	2493,0	ICE	Verlassen die Scholle	
PS69/584-4	12.10.06	22:30	64° 23,45' S	52° 48,48' W	2501,0	CTD/RO	zu Wasser	
PS69/584-4	12.10.06	22:44	64° 23,52' S	52° 48,32' W	2502,0	CTD/RO	auf Tiefe	520 m
PS69/584-4	12.10.06	22:57	64° 23,45' S	52° 48,05' W	2503,0	CTD/RO	an Deck	
PS69/584-5	12.10.06	22:59	64° 23,45' S	52° 47,95' W	2505,0	AFLOAT	zu Wasser	
PS69/584-6	12.10.06	23:11	64° 23,29' S	52° 47,69' W	2506,0	AFLOAT	zu Wasser	
PS69/584-7	12.10.06	23:21	64° 23,39' S	52° 47,35' W	2509,0	MN	zu Wasser	
PS69/584-7	12.10.06	23:40	64° 23,35' S	52° 47,40' W	2508,0	MN	auf Tiefe	EL30 527meter
PS69/584-7	13.10.06	00:03	64° 23,38' S	52° 47,01' W	2511,0	MN	an Deck	
PS69/584-7	13.10.06	00:13	64° 23,46' S	52° 46,71' W	2514,0	CTD/RO	zu Wasser	
PS69/584-7	13.10.06	01:00	64° 23,33' S	52° 45,92' W	2516,0	CTD/RO	auf Tiefe	EL31 2440meter
PS69/584-7	13.10.06	01:43	64° 23,23' S	52° 45,20' W	2522,0	CTD/RO	an Deck	
PS69/585-1	13.10.06	16:05	63° 51,82' S	54° 9,17' W	355,1	ICE	Anlegen an Scholle	
PS69/585-1	13.10.06	16:12	0° 0,00' N	0° 0,00' E	0,0	ICE	Eisgangway ausgebracht	
PS69/585-1	13.10.06	16:17	0° 0,00' N	0° 0,00' E	0,0	ICE	Forscher auf dem Eis	
PS69/585-2	13.10.06	16:32	63° 51,42' S	54° 8,79' W	346,8	CTD/RO	zu Wasser	
PS69/585-2	13.10.06	16:41	63° 51,29' S	54° 8,67' W	346,5	CTD/RO	auf Tiefe	324m
PS69/585-2	13.10.06	16:49	63° 51,17' S	54° 8,58' W	344,0	CTD/RO	an Deck	
PS69/585-1	13.10.06	18:16	63° 49,86' S	54° 7,81' W	334,9	ICE	Forscher an Bord	
PS69/585-1	13.10.06	18:18	63° 49,83' S	54° 7,82' W	334,1	ICE	Eisgangway an Bord	
PS69/585-1	13.10.06	18:19	63° 49,82' S	54° 7,82' W	333,7	ICE	Verlassen die Scholle	
PS69/586-1	13.10.06	21:36	63° 35,22' S	54° 3,73' W	270,9	EF	Beginn	
PS69/586-1	13.10.06	21:40	63° 35,22' S	54° 3,81' W	272,3	EF	Ende	

A.4 STATION LIST PS 69

Station	Date	Time	Position Lat	Position Lon	Depth [m]	Gear Abbreviat.	Action	Remarks
PS69/587-1	14.10.06	05:57	62° 44,47' S	54° 59,93' W	180,0	CTD/RO	zu Wasser	
PS69/587-1	14.10.06	06:05	62° 44,56' S	54° 59,86' W	182,1	CTD/RO	auf Tiefe	169m
PS69/587-1	14.10.06	06:13	62° 44,64' S	54° 59,78' W	183,4	CTD/RO	an Deck	
PS69/588-1	14.10.06	08:11	62° 31,08' S	54° 59,92' W	269,0	CTD/RO	zu Wasser	
PS69/588-1	14.10.06	08:23	62° 31,13' S	54° 59,91' W	269,3	CTD/RO	auf Tiefe	258 m
PS69/588-1	14.10.06	08:30	62° 31,18' S	54° 59,85' W	270,6	CTD/RO	an Deck	
PS69/588-2	14.10.06	08:37	62° 31,23' S	54° 59,65' W	271,9	MN	zu Wasser	
PS69/588-2	14.10.06	08:47	62° 31,31' S	54° 59,47' W	272,0	MN	auf Tiefe	259 m
PS69/588-2	14.10.06	08:58	62° 31,39' S	54° 59,27' W	272,3	MN	an Deck	
PS69/589-1	14.10.06	11:10	62° 17,55' S	54° 59,89' W	479,8	CTD/RO	zu Wasser	
PS69/589-1	14.10.06	11:23	62° 17,69' S	54° 59,85' W	472,9	CTD/RO	auf Tiefe	EL31 453meter
PS69/589-1	14.10.06	11:37	62° 17,82' S	54° 59,95' W	468,8	CTD/RO	an Deck	
PS69/590-1	14.10.06	13:40	62° 4,19' S	54° 59,88' W	579,0	CTD/RO	zu Wasser	
PS69/590-1	14.10.06	13:49	62° 4,18' S	54° 59,86' W	578,6	CTD/RO	auf Tiefe	Winde EL 31 550m gesteckt
PS69/590-1	14.10.06	14:09	62° 4,31' S	54° 59,75' W	580,4	CTD/RO	an Deck	
PS69/591-1	14.10.06	17:08	61° 50,42' S	55° 0,24' W	2188,0	CTD/RO	zu Wasser	
PS69/591-1	14.10.06	17:50	61° 50,31' S	55° 0,53' W	2176,0	CTD/RO	auf Tiefe	2.097m
PS69/591-1	14.10.06	18:28	61° 50,19' S	55° 0,51' W	2172,0	CTD/RO	an Deck	
PS69/592-1	15.10.06	00:10	61° 16,23' S	55° 0,05' W	259,0	CTD/RO	zu Wasser	
PS69/592-1	15.10.06	00:17	61° 16,24' S	55° 0,06' W	259,8	CTD/RO	auf Tiefe	EL31 241meter
PS69/592-1	15.10.06	00:54	61° 16,32' S	55° 0,19' W	259,3	CTD/RO	an Deck	
PS69/592-2	15.10.06	01:02	61° 16,31' S	55° 0,20' W	259,4	MN	zu Wasser	
PS69/592-2	15.10.06	01:12	61° 16,31' S	55° 0,21' W	259,1	MN	auf Tiefe	EL 30 235meter
PS69/592-2	15.10.06	01:27	61° 16,30' S	55° 0,23' W	258,1	MN	an Deck	
PS69/593-1	15.10.06	02:55	61° 28,03' S	54° 59,96' W	990,7	CTD/RO	zu Wasser	
PS69/593-1	15.10.06	03:17	61° 27,94' S	54° 59,66' W	1008,0	CTD/RO	auf Tiefe	963m
PS69/593-1	15.10.06	03:39	61° 27,91' S	54° 59,53' W	1009,0	CTD/RO	an Deck	
PS69/594-1	15.10.06	04:51	61° 36,14' S	55° 0,02' W	2297,0	CTD/RO	zu Wasser	
PS69/594-1	15.10.06	05:35	61° 36,15' S	55° 0,01' W	2299,0	CTD/RO	auf Tiefe	2.239m
PS69/594-1	15.10.06	06:17	61° 36,12' S	55° 0,23' W	2296,0	CTD/RO	an Deck	
PS69/594-1	15.10.06	06:31	61° 36,09' S	55° 0,08' W	2291,0	MN	zu Wasser	
PS69/594-1	15.10.06	07:46	61° 36,06' S	55° 0,43' W	2275,0	MN	auf Tiefe	2117 m
PS69/594-1	15.10.06	09:06	61° 35,81' S	55° 1,64' W	2141,0	MN	an Deck	
PS69/594-2	15.10.06	09:20	61° 36,15' S	54° 59,96' W	2297,0	CTD/RO	zu Wasser	
PS69/594-2	15.10.06	09:57	61° 36,12' S	55° 0,16' W	2297,0	CTD/RO	auf Tiefe	2243 m
PS69/594-2	15.10.06	10:30	61° 36,04' S	55° 0,50' W	2261,0	CTD/RO	an Deck	
PS69/595-1	16.10.06	11:09	60° 6,76' S	49° 15,94' W	2212,0	AFLOAT	zu Wasser	
PS69/596-1	17.10.06	06:34	60° 19,25' S	45° 4,49' W	2848,0	AFLOAT	zu Wasser	
PS69/597-1	17.10.06	12:04	60° 31,92' S	44° 0,50' W	1872,0	HS_PS	Beginn Track	
PS69/597-1	18.10.06	14:14	60° 32,16' S	42° 11,94' W	4741,0	HS_PS	Profil Ende	
PS69/598-1	19.10.06	14:39	58° 0,13' S	37° 29,97' W	3445,0	CTD/RO	zu Wasser	
PS69/598-1	19.10.06	15:45	58° 0,10' S	37° 29,68' W	3461,0	CTD/RO	auf Tiefe	3.393m
PS69/598-1	19.10.06	16:35	58° 0,10' S	37° 29,91' W	3447,0	CTD/RO	an Deck	
PS69/598-2	19.10.06	16:44	57° 60,00' S	37° 30,03' W	3440,0	MN	zu Wasser	
PS69/598-1	19.10.06	16:44	57° 60,00' S	37° 30,03' W	3440,0	MN	zu Wasser	
PS69/598-2	19.10.06	17:48	57° 59,97' S	37° 29,51' W	3462,0	MN	auf Tiefe	
PS69/598-1	19.10.06	17:48	57° 59,97' S	37° 29,51' W	3462,0	MN	auf Tiefe	2122m
PS69/598-1	19.10.06	19:02	58° 0,11' S	37° 28,36' W	3382,0	MN	an Deck	
PS69/598-2	19.10.06	19:02	58° 0,11' S	37° 28,36' W	3382,0	MN	an Deck	
PS69/598-3	19.10.06	19:14	58° 0,15' S	37° 28,37' W	3378,0	CTD/RO	zu Wasser	
PS69/598-3	19.10.06	19:39	58° 0,29' S	37° 28,28' W	3361,0	CTD/RO	auf Tiefe	999m
PS69/598-3	19.10.06	19:56	58° 0,32' S	37° 28,06' W	3346,0	CTD/RO	an Deck	
PS69/599-1	24.10.06	06:11	52° 30,30' S	1° 24,12' W	2816,0	PIES	Beginn Auslegung	
PS69/599-1	24.10.06	06:17	52° 30,42' S	1° 24,04' W	2823,0	PIES	Ende Auslegung	
PS69/599-2	24.10.06	06:33	52° 30,52' S	1° 24,70' W	2808,0	CTD/RO	zu Wasser	
PS69/599-2	24.10.06	07:25	52° 30,40' S	1° 23,83' W	2832,0	CTD/RO	auf Tiefe	EL31 2772meter
PS69/599-2	24.10.06	08:06	52° 30,08' S	1° 23,66' W	2822,0	CTD/RO	an Deck	

A.4 STATION LIST PS 69

Station	Date	Time	Position Lat	Position Lon	Depth [m]	Gear Abbreviat.	Action	Remarks
PS69/600-1	24.10.06	20:17	50° 15,90' S	1° 26,00' E	3884,1	PIES	Beginn Auslegung	
PS69/600-1	24.10.06	20:19	50° 15,82' S	1° 25,91' E	3886,4	PIES	Information	Bendos zu Wasser
PS69/600-1	24.10.06	20:24	50° 15,73' S	1° 25,95' E	3889,2	PIES	Ende Auslegung	
PS69/600-2	24.10.06	20:43	50° 15,49' S	1° 25,42' E	3898,0	CTD/RO	zu Wasser	
PS69/600-2	24.10.06	21:52	50° 15,46' S	1° 25,86' E	0,0	CTD/RO	auf Tiefe	EL31 3832meter
PS69/600-2	24.10.06	22:49	50° 15,31' S	1° 26,10' E	0,0	CTD/RO	an Deck	

Die "**Berichte zur Polar- und Meeresforschung**" (ISSN 1866-3192) werden beginnend mit dem Heft Nr. 569 (2008) ausschließlich elektronisch als Open-Access-Publikation herausgegeben. Ein Verzeichnis aller Hefte einschließlich der Druckausgaben (Heft 377-568) sowie der früheren "**Berichte zur Polarforschung**" (Heft 1-376, von 1982 bis 2000) befindet sich im Internet in der Ablage des electronic Information Center des AWI (**ePIC**) unter der URL <http://epic.awi.de>. Durch Auswahl "Reports on Polar- and Marine Research" auf der rechten Seite des Fensters wird eine Liste der Publikationen in alphabetischer Reihenfolge (nach Autoren) innerhalb der absteigenden chronologischen Reihenfolge der Jahrgänge erzeugt.

To generate a list of all Reports past issues, use the following URL: <http://epic.awi.de> and select the right frame to browse "Reports on Polar and Marine Research". A chronological list in declining order, author names alphabetical, will be produced, and pdf-icons shown for open access download.

Verzeichnis der zuletzt erschienenen Hefte:

Heft-Nr. 573/2008 — "Reactions on surfaces of frozen water: Importance of surface reactions for the distribution of reactive compounds in the atmosphere", by Hans-Werner Jacobi

Heft-Nr. 574/2008 — "The South Atlantic Expedition ANT-XXIII/5 of the Research Vessel 'Polarstern' in 2006", edited by Wilfried Jokat

Heft-Nr. 575/2008 — "The Expedition ANTARKTIS-XXIII/10 of the Research Vessel 'Polarstern' in 2007", edited by Andreas Macke

Heft-Nr. 576/2008 — "The 6th Annual Arctic Coastal Dynamics (ACD) Workshop, October 22-26, 2006, Groningen, Netherlands", edited by Pier Paul Overduin and Nicole Couture

Heft-Nr. 577/2008 — "Korrelation von Gravimetrie und Bathymetrie zur geologischen Interpretation der Eltanin-Impaktstruktur im Südpazifik", von Ralf Krockner

Heft-Nr. 578/2008 — "Benthic organic carbon fluxes in the Southern Ocean: regional differences and links to surface primary production and carbon export", by Oliver Sachs

Heft-Nr. 579/2008 — "The Expedition ARKTIS-XXII/2 of the Research Vessel 'Polarstern' in 2007", edited by Ursula Schauer.

Heft-Nr. 580/2008 — "The Expedition ANTARKTIS-XXIII/6 of the Research Vessel 'Polarstern' in 2006", edited by Ulrich Bathmann

Heft-Nr. 581/2008 — "The Expedition of the Research Vessel 'Polarstern' to the Antarctic in 2003 (ANT-XX/3)", edited by Otto Schrems

Heft-Nr. 582/2008 — "Automated passive acoustic detection, localization and identification of leopard seals: from hydro-acoustic technology to leopard seal ecology", by Holger Klinck

Heft-Nr. 583/2008 — "The Expedition of the Research Vessel 'Polarstern' to the Antarctic in 2007 (ANT-XXIII/9)", edited by Hans-Wolfgang Hubberten

Heft-Nr. 584/2008 — "Russian-German Cooperation SYSTEM LAPTEV SEA: The Expedition Lena - New Siberian Islands 2007 during the International Polar Year 2007/2008", edited by Julia Boike, Dmitry Yu. Bolshiyakov, Lutz Schirrmeyer and Sebastian Wetterich

Heft-Nr. 585/2009 — "Population dynamics of the surf clams *Donax hanleyanus* and *Mesodesma mactroides* from open-Atlantic beaches off Argentina", by Marko Herrmann

Heft-Nr. 586/2009 — "The Expedition of the Research Vessel 'Polarstern' to the Antarctic in 2006 (ANT-XXIII/7)", edited by Peter Lemke